2017-04-01

Seismic Analysis of and Provisions for Dry-Stack Concrete Masonry Wall Systems with Surface Bond in Low-Rise Buildings

Joseph G. Eixenberger
Brigham Young University

Seismic Analysis of and Provisions for Dry-Stack Concrete Masonry Wall Systems with Surface Bond in Low-Rise Buildings

Joseph G. Eixenberger

A dissertation submitted to the faculty of
Brigham Young University
in partial fulfillment of the requirements for the degree of

Doctor of Philosophy

Fernando S. Fonseca, Chair
Richard J. Balling
Clifton B. Farnsworth
Kevin W. Franke
Paul W. Richards

Department of Civil and Environmental Engineering

Brigham Young University

ABSTRACT

Seismic Analysis of and Provisions for Dry-Stack Concrete Masonry
Wall Systems with Surface Bond on Low-Rise Buildings

Joseph G. Eixenberger
Department of Civil and Environmental Engineering, BYU
Doctor of Philosophy

Masonry is one of the oldest forms of construction materials that is still in use today. However, construction practices in the modern age demand faster and more economical practices. Dry-stack masonry, or masonry that doesn't use mortar to bind the blocks together, is a unique system to make masonry more economical. Though several systems of dry-stack masonry have been suggested little to no data exists as most of these systems are patented.

This research used dry-stacked normal weight concrete masonry units with an eccentrically placed reinforcement. The wall system is connected through a surface bond and lacks any geometric connection. Previously, research has been conducted on the wall system for its axial compressive capacity, but little information is known about its ability to withstand lateral forces such as earthquakes.

Research was conducted on the wall system in order to determine the seismic parameters, including the force reduction factor, overstrength factor, and the displacement amplification factor. To determine these factors the guidelines from the Federal Emergency Management Agency (FEMA) Quantification of Building Seismic Performance Factors 2009 were followed. The guidelines are explicit that both experimental data and computer modeling are needed to quantify these parameters.

Experimental data was obtained from a diagonal tension test, and an in-plane shear test. The diagonal tensions test provided preliminary values on the shear modulus and shear resistance. The in-plane shear test was of primary interest and what would be used to verify the computer model.

Computer modeling of the wall system was accomplished with Vector 2. Initially the computer modeling was done to reproduce experimental data. Then, a parametric study was performed using the model to see what component of the wall most effected its capacity. This analysis showed that the surface bond was the component of the wall that most affects its capacity.

Finally, the computer model was run through the FEMA Far-Field earthquake suite to gather data on the strength and ductility. Values of the force reduction factor, overstrength factor, and displacement amplification factor were determined based on the time history analysis and pushover analysis on the computer model.

Keywords: masonry, dry-stack, seismic design, shear walls

ACKNOWLEDGEMENTS

I wish to thank the ENDURA Company for providing me with the funds and materials to allow this testing to occur. Specifically, I would like to thank Brent Ostler for his help during the construction and testing of the walls. Also, thank you to PEER for their use of the time history records that were used for this research.

Thank you to the workers in the structures lab for all their work and ideas as the work progressed. Especially thank you to Kyle Chavez, Rawley Selk, Dave Anderson, and Rodney Mayo for all their work.

I would like to thank my committee and all the efforts they have made to make this research possible. In specific, thank you to Dr. Fonseca for his time, effort, and council throughout the whole research process.

I also appreciate the love and support of my family. To my wonderful wife Amy, who has been there to support and encourage me throughout the last 3 years, I love you and appreciate all that you do. To my parents, thank you for always pushing me to ask questions. To my son Peter, your life and smile has reminded me constantly that research that is being conducted now is to ensure a better world for the next generation.

TABLE OF CONTENTS

LIST OF TABLES

LIST OF FIGURES

1 INTRODUCTION

1.1 Background

Masonry is one of the oldest building methods, and is still in use today. Part of the reason that masonry is still in use is that it requires less energy to produce than other construction materials such as structural steel, requires less specialized labor, and is multifunctional in that it is the enclosure, structure, and finish all in one. However, the construction of masonry systems is slow and limited to the number of blocks a masonry crew can lay (Hines 1995).

Several attempts have been made to speed up the process of masonry construction. One of the early attempts was to increase the size of the masonry units, or to use concrete blocks instead of bricks. Other construction methods such as not using bedding mortar, i.e., dry stack masonry, has been investigated to speed up the process even more (Ramamurthy et al. 2004).

Mortarless or dry-stack systems are categorized by how the system connects together, and the two sub-systems are interlocking and surface bonded. Interlocking systems are connected by the geometry of the block, while surface bonded systems are held together by a face coating on the blocks that is usually cementitious in nature (Anand et al. 2000).

Currently in the United States, dry-stack systems are designed using the empirical design method, or a prescriptive method that has been approved by the international code council (International 2011). Several patents have been issued on dry-stack wall systems (Ramaurthy et al. 2004). The evaluations of these patented systems have only been conducted by the developers

themselves; thus, the information shared has been limited. To become used wide-spread, dry-stack systems must be evaluated according to acceptable standards and in a way similar to that used for typical masonry.

This research investigates a surface bonded dry-stack masonry system in a systematic way, according to acceptable standards, and in the way a typical masonry system would be evaluated. The system utilizes dry-stacked concrete masonry units (CMUs) with eccentrically placed reinforcement. The CMUs are bonded together by a surface coating and lack any geometric connection between them. The system uses non-structural polystyrene insulation inserts that are placed in cells of the CMUs to provide additional insulation, except in cells that are utilized for placement of reinforcement and grout. Research has been conducted on this surface bonded dry-stack system for its axial compression capacity (Fonseca et al. 2012). However, little information is available on this or any dry-stack system for its resistance to lateral forces such as those resulting from earthquakes.

1.2 Objective

The objective of this research was to develop the seismic design parameters for surface bonded dry-stack masonry following the Federal Emergency Management Agency (FEMA) *Quantification of Building Seismic Performance Factors 2009* guidelines hereafter known as the FEMA P-695 (FEMA 2009). The results of this research may allow the wide spread use of surface bonded dry-stack systems and provide a basis for the seismic design of low-rise buildings using the system. As dry-stack systems are currently limited to low-rise buildings (MSJC 2013), this research did not involve mid to high-rise buildings.

1.3 Research Phases

The development of the seismic parameters of a new structural system involves an experimental phase and a computer modeling phase (FEMA 2009). The experimental phase is necessary for characterizing the strength, stiffness, and ductility of materials, elements, and connections of the proposed system. Thus, the blocks, surface bond, grout, mortar, and reinforcement used in the structural system as well as walls were characterized.

In the experimental phase, preliminary testing was done using the diagonal-tension test following ASTM E519 (Standard Test Method for Diagonal Tension (Shear) in Masonry Units and Related Units). However, research shows the diagonal tension test is unreliable for reinforced masonry and the values obtained were preliminary (Bosiljkov 2005). Additional testing was done on 8 ft. x 8 ft. walls, which were tested for their in-plane shear capacity. Results from this testing were used to calibrate the computer models.

The computer modeling is done for two reasons. The first reason is that any experimentation has the cost of materials, labor, and testing, which usually limits the amount of experimental data that can be obtained (FEMA 2009). Secondly, a computer model can be subjected to actual earthquake accelerations, which can better predict how the system will react in an earthquake.

The computer modeling was done using VecTor 2, a two-dimensional finite element program. First, the model was calibrated to experimental data. Then, three building archetypes were studied. The shear walls for these buildings were designed assuming an initial response modification factor, R. The computer model of the walls was then subjected to an earthquake suite, and the results from the analysis were used to validate the assumed R factor and determine

the other seismic parameters. This process is iterative since the likelihood of the first assumed response modification factor, R, being appropriate is very small.

1.4 Outline

The remainder of this dissertation presents a more in-depth discussion of the research that was conducted. Chapter 2 summarizes the FEMA P-695 procedure and discusses its limitations. Chapter 3 discusses the preliminary research from the diagonal-tension test and background information on dry-stack systems. Chapter 4 discusses the experimental research from the in-plane shear test. This includes a statistical analysis of the various components of the wall system and predictive models to determine the wall shear capacity. Chapter 5 presents background information on the finite element program, VecTor 2, and the assumptions made during modeling. Chapter 6 presents the calibration of the computer model with the experimental data. It also contains a sensitivity analysis of the model. Chapter 7 outlines the time history analysis including the design and layout of the 3 building archetypes, the shear wall design requirements, the methodology in determining the seismic parameters, and the suite of earthquakes used. Chapter 8 contains the results of the seismic analysis. Chapter 9 presents the conclusions from the research presented herein, outlines the contribution of the research, and presents recommendations for future research.

2 QUANTIFICATION OF BUILDING SESIMIC PERFORMANCE FACTORS

The objective of the FEMA P-695 procedure is to establish a consistent and rational methodology for determining the response parameters used in the linear design methods traditionally utilized in building codes (FEMA 2009). These parameters are used to transform a complicated nonlinear dynamic behavior to an equivalent linear problem. The different seismic parameters are defined by idealizing the structural response curve by a linearly elastic-perfectly plastic curve. This idealized curve is shown in Figure 2-1 (Uang 1991). In this curve, C represents the base shear divided by the reactive weight, if the structure were to remain in its elastic range, and Δ is the story drift of the structure.

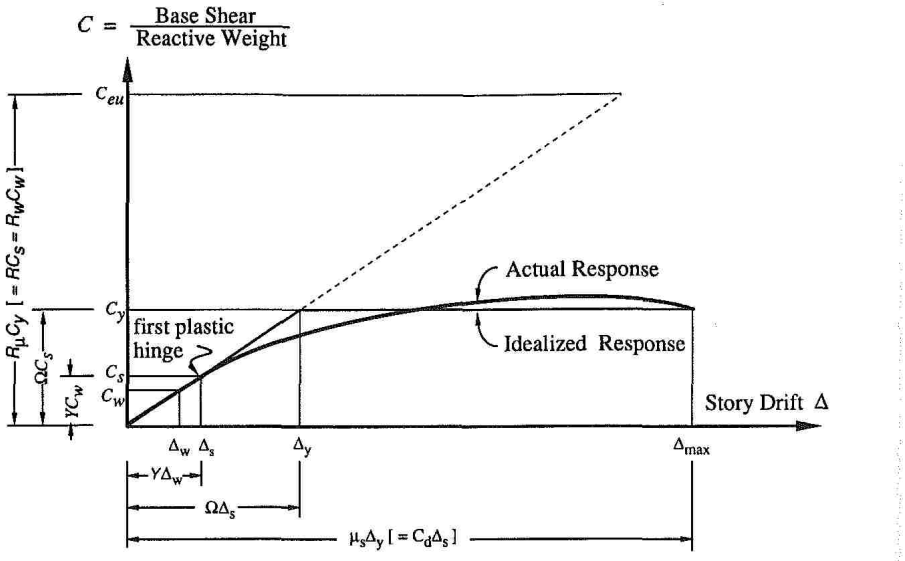

Figure 2-1 Structural response of a linearly elastic-perfectly plastic curve (Uang 1991)

Using Figure 2-1, the structural ductility ratio, μ_s, ductility reduction factor, R_μ, overstrength factor, Ω, allowable stress factor, Y, total force reduction factor, R or R_w, and the displacement amplification factor, C_d, are defined by equations 2-1 through 2-7.

$$\boldsymbol{\mu_s = \frac{\Delta_{max}}{\Delta_y}} \tag{2-1}$$

$$\boldsymbol{R_\mu = \frac{C_{eu}}{C_y}} \tag{2-2}$$

$$\boldsymbol{\Omega = \frac{C_y}{C_s}} \tag{2-3}$$

$$\boldsymbol{Y \approx 1.4} \tag{2-4}$$

$$\boldsymbol{R = R_\mu * \Omega} \tag{2-5}$$

$$\boldsymbol{R_w = R_\mu * \Omega * Y} \tag{2-6}$$

$$\boldsymbol{C_d = \mu_s * \Omega} \tag{2-7}$$

Using these response parameters to account for the ductility and for the additional strength in the system after yield, a system can be designed as if it stayed in the linear region. The problem with many of the seismic response parameters that are in use today is that they were defined somewhat arbitrarily based on the experience of engineers and observations of the system in previous earthquakes (FEMA 2009). The methodology presented in FEMA P-695 was developed to validate these seismic parameters for existing systems and determine the parameters for new systems.

To be consistent with the linear design method, the FEMA P-695 procedure is used to determine these seismic parameters while accounting for low probability of structural collapse. Uncertainty from experimental data, computer modeling, earthquake variability, and design requirements are also accounted for in the methodology.

2.1 Overview of Methodology

The methodology is divided into 6 different parts to develop or confirm the seismic parameters for the system studied. These parts include obtaining required information, characterizing the behavior of the system, developing models, analyzing models, evaluating the performance of the system, and documenting the results. A flowchart of the general procedure is shown in Figure 2-2 (FEMA 2009). Each part is explained in the following sections.

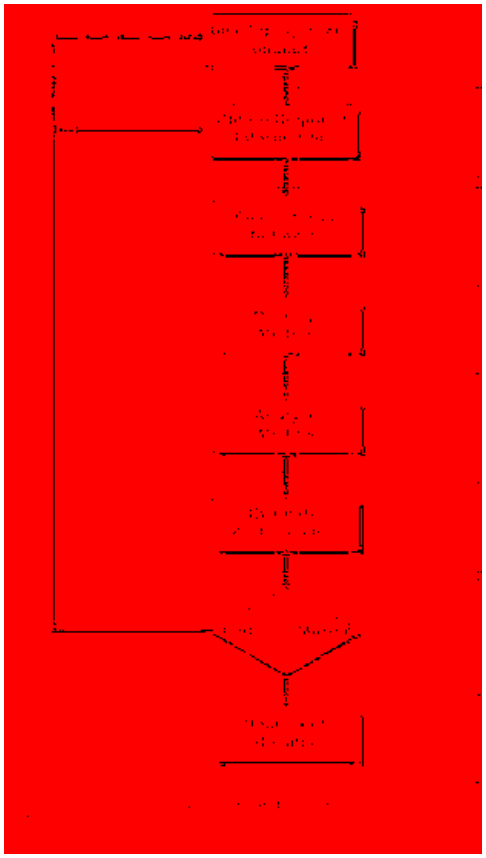

Figure 2-2 Process of establishing seismic parameters (FEMA 2009)

2.2 Obtain Required Information

This part of the methodology is from the experimental phase. It is used to state the design requirements of the system and details the results from material, component, and system testing. The design requirements are the design rules and predictive models for determining the capacity of the system. The test results are the material properties of the various components of the system, the force-deformation behavior of the system, and the nonlinear response of the system.

2.3 Characterize Behavior

Characterizing the behavior is done by creating system archetypes. Archetypes are created by identifying characteristics and limits of the seismic resisting system and by utilizing the design requirements. The archetypes represent typical applications of the system, while having them general enough to reflect the irregularities that are permitted in the building code. Some of the characteristics that should be reflected are building height, varying fundamental period, framing configurations, aspect ratio, and magnitude of gravity loads. To design these archetypes, a trial value of the response modification factor, R, is used. The trial value should be based on an existing system that is similar to the new proposed system. The trial value is evaluated to determine if it is sufficient for the new system.

2.4 Develop Models

Nonlinear models are developed to represent the range on intended applications for the proposed system. These models must be robust enough to simulate significant deterioration mechanisms that lead to structural collapse. When it is not possible to simulate all collapse modes, provisions should be defined to account for the effects and behaviors that are not

explicitly simulated in the model. These models should be collaborated using the experimental data and verified as to their ability to assess the nonlinear behavior of the proposed system.

2.5 Analyze Models

The collapse assessment is done using both nonlinear static (pushover) and nonlinear dynamic (time history) analyses. The pushover analysis is performed to provide statistical data on the system overstrength and ductility capacity. The time history analysis is done to determine the median collapse capacities and collapse margin ratios.

The time history analysis is evaluated using a set of ground motions, known as the Far-Field record set. These records were selected to meet a variety of objectives that are sometimes conflicting. These objectives include being consistent with code requirements, having very strong ground motions, having a large number of records, being independent of structure type, and being independent of site hazards.

To assess the collapse of the system, the ground motions are systematically scaled to increase the earthquake intensities until half of the records in the set cause collapse of the finite element model of the seismic resisting system. The median earthquake intensity is known as the median collapse intensity. The collapse margin ratio is the ratio between the median collapse intensity and the maximum considered earthquake intensity used for design.

2.6 Evaluate Performance

The results from the pushover analysis are used to determine an appropriate value for the system overstrength factor, Ω_0, and the results from the response history analysis are used to

evaluate the acceptability of the trial value of the response modification factor, R. The deflection amplification factor, C_d, is derived from the acceptable value of R.

The trial value of R is evaluated by comparing the collapse margin ratio, with some adjustments, to an acceptable collapse margin ratio. The acceptable collapse margin ratio is determined based on the quality of the information used in defining the system, the total system uncertainty from modeling and experimental data, and established limits on probabilities of collapse. Adjustments to the collapse margin ratio are made based on the shape of the spectrum of rare ground motions, the structure ductility, and the period of vibration. The probability of collapse due to the maximum considered earthquake ground motion is limited to 10% for a population of archetypes and limited to 20% for each individual archetype.

If the adjusted collapse margin ratio is larger than the acceptable collapse margin ratio, then the trail value of R is acceptable. If not, the system must be redefined with a new trial value, either adjusting the design requirements, or re-characterizing the system behavior. Sometimes, if a trial value is not adequate, revisions to the system concept are required.

2.7 Document Results

Documentation is required throughout each part of the methodology. The documentation should lay out the seismic design rules, applicability of the system, testing methodology and results, rationale for the archetypes selection, results of the nonlinear analysis, evaluation of the quality of information, uncertainties that exists, and proposed seismic performance factors. The documentation needs to be detailed enough to give an unfamiliar structural engineer sufficient information to review the quality of the seismic parameters and the system in general.

2.8 Limitations

The FEMA P-695 procedure was developed to apply to all buildings. To achieve this goal, some assumptions were made that were deemed appropriate for the evaluation of the seismic performance.

2.8.1 Record Set

The Far-Field record set was chosen for the collapse performance evaluation of all systems, however this record set is not appropriate for assessing buildings sites near active faults. In addition to the Far-Field record set, a Near-Field record set was developed. An internal study of the P-695 procedure determined that the collapse margin ratio was smaller for a system when evaluated using the Near-Field record set (FEMA 2009). This shows the need for smaller values for the response modification factor for building sites near active faults. To be consistent with the American Society of Civil Engineering (ASCE) design standards the Far-Field record set was the only set used for evaluating the seismic parameters of the system presented herein. This implicitly accepts somewhat greater risk for buildings located near active faults (FEMA 2009). This limitation is considered a flaw that needs to be addressed in the future.

2.8.2 Fundamental Period

Currently in the ASCE procedures, the seismic parameters are defined for the system regardless of the fundamental period (ASCE 2010). The National Institute of Standards and Technology (NIST) performed an evaluation of current systems' seismic parameters as listed in ASCE 7. This evaluation showed that current systems do not meet collapse performance criteria for the FEMA P-695 procedure for low-rise buildings (NIST 2010). That study suggests a need

for period-dependent seismic parameters, as the shorter period buildings have smaller values for the collapse margin ratio (FEMA 2009).

The research presented in this dissertation only concentrated on low-rise buildings. As low-rise buildings have a shorter fundamental periods, the values obtained for the seismic parameters are expected to be lower than if research had been conducted on mid- and high-rise buildings.

3 DRY-STACK MASONRY AND PRELIMINARY TESTING

3.1 Dry-Stack Masonry

Dry-stack masonry systems were developed to improve the speed of construction and eliminate perceived weaknesses in traditional masonry. Often times, the greatest weakness in traditional masonry construction is the speed of construction. Dry-stack masonry has been shown to increase productivity over traditional masonry by 80 to 120%, and reduce indirect work by 30 to 50% (Anand 2003). That study was conducted using interlocking blocks instead of surface bonded blocks. The increase in production and reduction in indirect labor were attributed to easier alignment created by the interlocking geometry of the block, the elimination of vertical joints, and the non-use of mortar. Though surface bonded dry-stack systems do not use the geometry of the block to ease alignment, the elimination of vertical joints and mortar will still increase production and reduce indirect labor when constructing these systems.

Dry-stack masonry has other advantages besides the construction speed. Some of these advantages include: elimination of problems with mortar joints, quality control lies in the manufacturing of the blocks and not on the work at the jobsite, reduction of labor costs, and construction without waiting for a cure time (Hines 1994). However, some disadvantages exist in these systems. The disadvantages of dry-stack systems are: stringent dimensional tolerance are required for the blocks as mortar is not used to compensate for irregularities and insure uniform load transfer, manufacturing costs of the blocks are usually higher, and careful planning and detailing are required as there is less tolerance for adjustments to dry-stack blocks (Anand 2000).

Due to the advantages of dry-stack masonry, several systems have been developed over the years. These systems include but are not limited to: PUTRA Block, R. Thallon Interlocking Block, Haenar Interlocking system, Mecano Interlocking System, and modified H and W Block Masonry System (Thanoon 2004). Most of these systems have been investigated for their axial compression capacity, and been shown to have similar axial capacity to that of traditional masonry (Marzahn 1999; Marzahn and König 2002). Unfortunately, little to no research exists on the shear capacity of these systems and how they behave when subjected to lateral forces such as seismic or wind forces. The lack of existing research on their different behaviors limits the design of dry-stack systems to the empirical design method, which is a non-engineering design method that is highly conservative and can only be used in certain locations (ICC 2012).

3.2 New Dry-Stack System

The dry-stack wall system in this research utilizes concrete masonry blocks similar to traditional CMUs that are 8 in x 8 in x 16 in, but the interior of the block is quite different. There are 5 different blocks in this system, as shown in Figure 3-1. There are three faces in the block, instead of the traditional two, creating two rows of cells with offset webs for grout, reinforcement, insulation inserts, or electrical or plumbing ducts. Only the stretcher and half stretcher blocks were used in this research because the other blocks are used almost exclusively around corners. Stretchers are the blocks primarily used when constructing a wall.

Expanded polystyrene (EPS) insulation inserts are used in the cells of the blocks when grout, reinforcement, or electrical or plumbing ducts are not needed. The purpose of these inserts is to insulate the building. These inserts are slightly taller than the blocks, and along with shims help align the blocks in place. There are 2 sizes of inserts: large and small for the differing cell sizes. The large inserts fit in the exterior cells of the stretcher and the small inserts fit in the interior

cells. When needed, grout and reinforcement are placed in the interior cell of the stretcher block, the cell created between 2 stretcher blocks, or the square cells of the right and left corner and ½ square blocks. Due to the offset of the cells, the reinforcement is placed eccentrically.

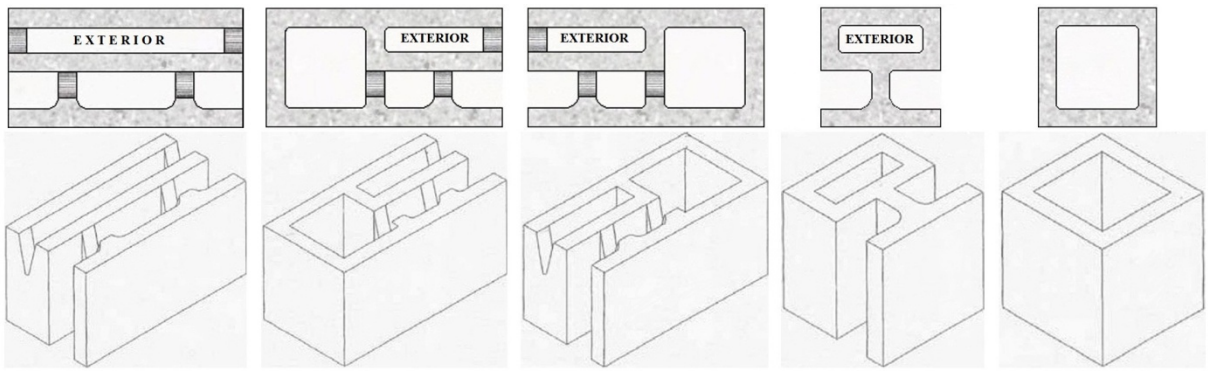

(a) Stretcher (b) Right Corner (c) Left Corner (d) ½ Stretcher (e) ½ Square

Figure 3-1 Concrete blocks used in dry-stack system.

3.3 Diagonal-Tension Test

The diagonal-tension test has been used over the years to determine the mechanical properties of a variety of structures. The diagonal-tension test is used as it can be applied to a variety of masonry, it can be performed in laboratory or in-situ, and it has the capability of being representative of the mechanical parameters in masonry (Calderini et al. 2010). It can even be used on existing structures to help better understand older structures (Dizhur et al. 2013). Another advantage of this test is that finite element modeling has been able to predict reasonable well test results (Gabor et al. 2006). Despite all these advantages, the diagonal-tension test has been shown to be unreliable for reinforced masonry, as the values of the shear modulus determined from test results are generally higher than that for unreinforced masonry (Bosiljkov 2005).

Due to the unreliability of the diagonal-tension test, this test was used as preliminary testing. By conducting this preliminary testing, some mechanical properties of the wall system could be gathered such as the shear modulus. Also, the results of the testes were used to further validate the finite element model.

3.3.1 Grout

The grout was made from a bagged high strength concrete mix, as shown in Figure 3-2. The mix was put in a high capacity mixer unit and water was added to reach between a 9 to 11 inch slump. After the grout was mixed, it was tested according to ASTM C1019 (Standard Test Method for Sampling and Testing Grout), ASTM C143 (Standard Test Method for Slump of Hydraulic-Cement Concrete), and ASTM C 1552 (Standard Practice for Capping Concrete Masonry Units, Related Units and Masonry Prims for Compression Testing).

Figure 3-2 Grout mix.

Once the grout mix was ready, it was transported via a wheelbarrow to the specimens to complete a lift. During one of the two lifts, while constructing the specimens, a portion of the grout was used to make grout prisms. Following ASTM standards, grout molds were made by laying 8 blocks around 3, 3 in. by 3 in., plastic squares as shown in Figure 3-3. The sides of the

blocks were covered with a paper towels to allow moisture to be absorbed by the blocks and insure that the grout did not adhere to the blocks. The grout was then placed in the grout mold in 2 lifts and each lift was rodded 15 times each. The grout prisms were then allowed to sit out for 48 hours before they were placed in a fog room until they were tested.

Figure 3-3 Grout prism apparatus.

The grout prisms were allowed to cure in the fog room for 26 days; the total curing time was 28 days. When the prisms were tested, they were removed from the fog room and the width, length, and height of all specimens were measured with a caliper accurate to within 0.01 in. The prisms were capped with gypsum on top and bottom. The prisms were then tested using a Forney Testing Machine. A picture of the Forney Testing Machine is shown in Figure 3-4. The prisms were tested at a displacement rate of 0.05 in. per min. until failure occurred. A picture of the typical failure of the grout prisms is shown in Figure 3-5. Table 3-1 summarizes the results from the compression test of the grout specimens.

Figure 3-4 Forney Testing Machine.

Figure 3-5 Typical failure of grout prisms.

Table 3-1 Results from Grout Prism Test

Prism	Area (in^2)	Max Force (lbs.)	Compressive Strength (psi)
1	17.1	66885	3924
2	16.7	59550	3560
3	16.9	67020	3978

3.3.2 Mortar

Though the system is a dry-stack system and does not traditionally use mortar, this research investigated the effect of a thin mortar layer between courses. Therefore, a set of specimens were constructed using a thin mortar layer, about 1/8 inch thick, between courses.

The mortar used was a bagged mortar mix. The mortar was tested in accordance with ASTM C230 (Standard Specification for Flow Table for Use in Tests of Hydraulic Cement), ASTM 1437 (Standard Test Method for Flow of Hydraulic Cement Mortar), and ASTM C109 (Standard Test Method for Compressive Strength of Hydraulic Cement Mortars (Using 2-in or Cube Specimens)).

The mortar was made by mixing the bagged mortar with water. Additional water was added until the mortar doubled in diameter when being tested on the flow table.

A portion of the mortar was used to making 2 inch by 2 inch cubes for compressive strength testing. This was done by placing mortar in an oiled mold in 2 lifts. During each lift, the mortar was tamped 32 times. Once complete, the mold with the mortar was placed in the fog room for 24 hours, after which the mortar was removed from the mold. The mortar then cured for 27 days in a lime bath, for a total cure time of 28 days. A picture of the mold that was used is shown in Figure 3-6.

Figure 3-6 Mortar cube mold.

After the cubes were cured, they were tested using a Forney Testing Machine; they were tested at a displacement rate of 0.05 in. per min. until failure. A picture of the typical failure of the mortar cubes is shown in Figure 3-7. Table 3-2 summarizes the results of the mortar cube compressive strength test.

Figure 3-7 Typical failure of mortar cube.

Table 3-2 Results from Mortar Cube Test

Cube	Area (in^2)	Max Force (lbs.)	Compressive Strength (psi)
1	4.02	28610	7116.9
2	4.06	25480	6275.6
3	4.04	26970	6675.6

3.3.3 Surface Bond

The surface bond is essential a mortar mix with glass fibers embedded in the mix, and it was prepared by adding water to it and mixing. Two consistencies were prepared: one for the structural layer, or first layer, and one for the outer, or second layer. During the Flow Table Tests, the diameter of the structural layer material about doubled, whereas for the surface layer material the diameter was around 2.5 times the original diameter. As most of the surface bonding material is made up from the structural layer, testing specimens were built using only the structural layer mix.

The surface coating specimens were built in the same manner as the mortar cubes. After the specimens were made, there were placed in the fog room for 24 hours before they were removed from their mold. They were then cured for 27 days in a lime bath, for a total cure time of 28 days.

After the cubes were cured they were tested using a Forney Testing Machine at a rate of 0.05 in./min. until failure. A picture of the typical failure of the surface bond cubes is shown in Figure 3-8. Table 3-3 summarizes the results obtained from the surface coating material.

Though several batches of the surface bond were used, only 3 cubes were made, as the batches were essentially the same because they were from the same mix and prepared by the same mason.

3.3.4 Concrete Masonry Units (CMUs)

The blocks were tested in accordance to ASTM C1314 (Standard Test Method for Compressive Strength of Masonry Prisms), ASTM C140 (Standard Test Methods for Sampling and Testing Concrete Masonry Units and Related Units), and ASTM C1552.

Figure 3-8 Typical failure of surface bond cubes.

Table 3-3 Results from Surface Bond Test

Cube	Area (in^2)	Max Force (lbs.)	Compressive Strength (psi)
a	4.0	27830	6958
b	4.1	27060	6632
c	4.1	25610	6308

Following ASTM standards, six blocks were tested for their compressive strength. Due to load limitations on the equipment, blocks were cut in half. The area of the blocks was measured with a caliper to the nearest 0.01 in. and the blocks were capped with gypsum. The blocks were tested using a Baldwin-Tate-Emery Testing Machine. A picture of the Baldwin Testing Machine is shown in Figure 3-9 and a picture of a block being tested is shown in Figure 3-10. Results from the block tests are summarized in Table 3-4.

Figure 3-9 Baldwin-Tate-Emery Testing Machine.

Figure 3-10 Block specimen being tested.

Table 3-4 Block Compressive Strength Test Results

Block	Area (in.^{2})	Max Force (lbs.)	Compressive Strength (psi)
1	31.3	65156	2083
2	30.8	78029	2536
3	30.0	43625	1455
4	30.6	54917	1794
5	31.0	52884	1708
6	30.5	37343	1223
		average	1800

3.3.5 CMU Absorption

The absorption of the CMUs was determined following ASTM C140. To determine the absorption, four half blocks were weighed and then placed in a bucket filled with water. The blocks were suspended ½ in. from the bottom of the bucket by using tie wire wrapped around a wood board on top of the bucket. After 24 hours of being in the bucket, the blocks were weighed while in the water, and then removed from the water, surface dried, and weighed again. The blocks were then placed in an oven and dried 24 hours. After 24 hours, the blocks were weighed again, and then placed back in the oven for 2 hour increments until a constant weight was reached. The absorption was then determined using equation 3-1.

$$\textbf{absorption} = \frac{\mathbf{S - O}}{\mathbf{S - S_b}} * \boldsymbol{\rho} \tag{3-1}$$

where S is the saturated weight, O is the oven dry weight, S_b is the submerged weight, and ρ is the density of water.

The moisture content was determined using equation 3-2.

$$\boldsymbol{moisture\ content}(\%) = \frac{\boldsymbol{I - O}}{\boldsymbol{S - O}} * \mathbf{100} \tag{3-2}$$

where I is the initial weight.

Finally, the density of the blocks was determined using equation 3-3. Results from the absorption test are shown in Table 3-5.

$$\textbf{Density} = \frac{\mathbf{O}}{\mathbf{S} - \mathbf{S_b}} * \boldsymbol{\rho} \tag{3-3}$$

3.3.6 CMU Net Area

Due to the manufacturing process, the walls of the CMUs are tapered to facilitate demolding, thus the top surface, with a smaller net area is used in the calculations. As the specimens are partially grouted, it was important to determine the net area of the blocks and the cells that could potentially be grouted. Table 3-6 shows the areas that were determined.

Table 3-5 Absorption Test Results

Specimen	**1**	**2**	**3**	**4**
Initial Weight, lbs.	12.0	12.0	12.3	11.8
Date/time immersed	2/17/2015 9:20	2/17/2015 9:20	2/17/2015 9:21	2/17/2015 9:21
Date/time removed	2/18/2015 12:32	2/18/2015 12:32	2/18/2015 12:32	2/18/2015 12:32
Submerged weight, lbs.	5.1	5.0	5.7	5.2
Saturated weight, lbs.	12.8	12.7	13.1	12.6
Dry Weight 1, lbs.	12.2	12.1	12.4	12.0
Dry Weight 2, lbs.	12.5	12.1	12.4	11.9
Dry Weight 3, lbs.	12.1	12.0	12.3	11.9
Dry Weight 4, lbs.	11.9	11.8	12.1	11.7
Oven Dry Weight, lbs.	11.9	11.8	12.1	11.7
Absorption, lbs./ft.^{3}	7.2	7.0	7.7	7.6
Absorption, %	7.5	7.3	7.6	7.6
Moisture Content, %	11.8	15.9	13.6	12.8
Density, lbs./ft.^{3}	96.1	95.4	102.2	99.5
Net Volume, ft.^{3}	0.12	0.12	0.12	0.11
Average Net Area, in.^{2}	26.84	26.82	25.67	25.36

Table 3-6 Area Calculations

Sample	Top Net Area (in.^{2})	Top Grout Cell Area (in.^{2})	Top Gross Area (in.^{2})
1	61.33	14.97	126.64
2	62.13	14.34	126.64
3	59.90	14.66	126.64
Average	61.12	14.66	126.64

From these, the net area as a fraction of the gross area was determined using equation 3-4.

$$\mathbf{n} = \frac{\mathbf{TA} + \mathbf{G} * \mathbf{\#\ of\ cells}}{\mathbf{GA}} \tag{3-4}$$

where TA is the top area, G is the average grout cell area, and GA is the average gross area. When a block is grouted, only one cell is grouted, so the net area of the grouted block is 0.60 of the gross area and the net area of ungrouted blocks is 0.48 of the gross area.

3.3.7 Prism

As the specimens built were partially grouted, both ungrouted and grouted prisms were constructed. The ungrouted prisms were built and had all cells filled with the EPS inserts. The surface coating was then applied. For the grouted prisms, only the inner cells were grouted and the outer cells were filled with the EPS inserts. After the prisms were built, they were allowed to cure for 28 days. After the curing period, the prisms were tested for their compressive strength in the Baldwin Testing Machine shown in Figure 3-9. The prisms were tested at a displacement rate of 0.1 in. per min. Results from the prism testing are summarized in Table 3-7.

Table 3-7 Results of Masonry Prism Test

Prism	Area (in.^{2})	Max Force (lbs.)	Compressive Strength (psi)
A	51.7	91722	1774
B	53.9	94107	1745
C	54.4	94363	1733
D	35.7	45390	1271
E	36.1	53596	1485
F	36.1	53342	1479

3.3.8 Wallette Construction

Specimens were built to be four ft. long by four ft. tall. Specimen construction consisted of block placement, grouting, and application of the surface coating. Block placement was simply laying the block on a steel channel, which was used to simply secure the specimen during its rotation, before testing and then adding blocks on top of the previously laid blocks. After each course was laid, EPS inserts were placed in the cells of the blocks before the next course was laid. In the case of the thin mortar specimens set, a thin layer of mortar was placed on top of each course before the next course was laid.

The cells that were to be grouted did not have foam inserts placed in them. After four courses, a horizontal grout layer was poured as well as all vertical grout cells.

After the blocks were laid and grouted, the specimens were wetted down with a hose for approximately ten minutes to prepare the wallettes for the application of the surface coating. The surface coating was prepared as previously outlined for both the structural coat and the surface coat. The structural coat was applied using a hawk and trowel. Once a sufficient amount of the structural coat was applied it was spread out using a Darby. The thickness of the structural layer was measured to make sure that they were at least 1/8 in. but no more than 3/16 in. Once the

structural layer began to set up, the outer or second layer was applied using the hawk and trowel and the surface was troweled until smooth. The thickness of the outer layer was not measured but it was essentially a very thin layer only to cover the structural layer and provide a smooth finish to the specimens. The specimens were kept wet over the next 24 hours. They were allowed to cure in the laboratory for 28 days. Pictures of the construction process are shown in Figure 3-11.

(a) Stacking the wallettes. (b) application of structural coat (c) Finished wallettes

Figure 3-11 Construction of wallettes.

3.3.9 Testing Matrix

Diagonal tension testing was performed on eight specimens. The specimens were built on a ten in. wide steel channels to facilitate the moving and rotation of the walls during testing. There were four configurations tested: ungrouted, grouted vertically every two ft. with one horizontal bond beam (2' x 4'), one vertical grouting and one horizontal grouting (4' x 4'), and grouted vertically every two ft. with one bond beam and a thin mortar between every course. The test matrix is given in Table 3-8, and the layout of the specimens is shown in Figure 3-12. The grout pattern was labeled to match that of the full size walls.

Table 3-8 Testing Matrix for the Diagonal-Tension Test

Wall	Grout Pattern	Thin Mortar
#1	Ungrouted	
#2	Ungrouted	
#3	2'x4'	
#4	2'x4'	
#5	4'x4'	
#6	4'x4'	
#7	2'x4'	X
#8	2'x4'	X

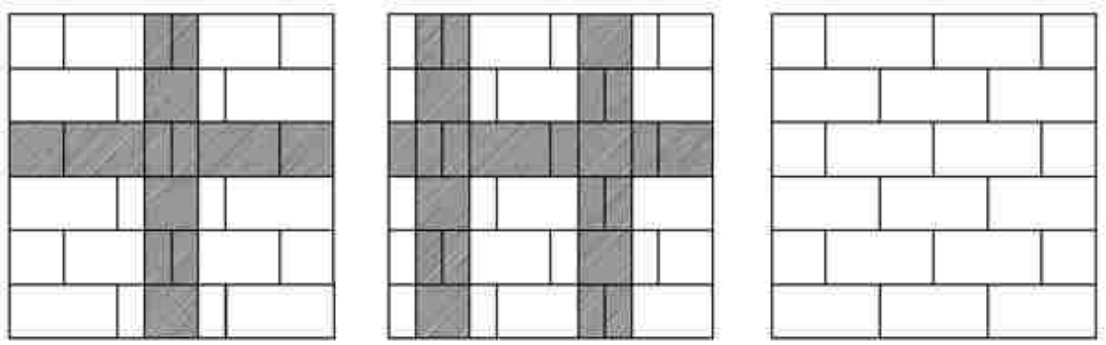

(a) 4' x 4' **(b) 2' x 4'** **(c) ungrouted**

Figure 3-12 Grout configuration.

3.3.10 Instrumentation

In addition to the readings from the internal instruments of the testing machine, four string potentiometer (string pots) were placed on the wallette to measure its deformation. Two string pots were placed on each face of the wall: one to measure the vertical deformation and the other to measure the horizontal deformation. The data was recorded every 0.5 seconds.

3.3.11 Testing Procedures

Testing was conducted in accordance to ASTM E519 (Standard Test Method for Diagonal Tension (Shear) in Masonry Assemblages). Steel shoes were manufactured to be

placed at the corners of the specimens and are shown in Figure 3-13. To insure uniform distribution of the load, the shoes were filled with gypsum before each test. These steel shoes were also used during transportation of the specimens from the construction location to the testing machine. The shoes were placed on the corners of the specimens and connected with a steel channel. Then, the specimens were moved with a forklift to the Baldwin Testing Machine as shown in Figure 3-14. Figure 3-15 shows the test setup.

During testing, the specimens were placed in a diagonal direction resting in the shoe supports and the steel channels that were used for moving the walls were removed. The specimens were tested using a displacement rate of 0.1 in. per min. until failure. Results from the tests are summarized Table 3-9.

Figure 3-13 Steel shoes.

Figure 3-14 Transportation of walls during diagonal-tension test.

Figure 3-15 Diagonal-tension test setup.

Table 3-9 Results from Diagonal-Tension Test

Test	Wall Configuration	Max Force (lbs.)	Thickness (in.)	n	A_n (in.^{2})	S_s (psi)	1/3 S_s max	Strain at 1/3 S_s	G (ksi)
1	ungrouted	23814	8	0.48	185	91	30	0.00014	210
2	ungrouted	19239	8	0.48	185	73	24	0.00024	102
3	2'x4'	28141	8	0.56	215	93	31	0.00016	195
4	2'x4'	31237	8	0.56	215	103	34	0.00044	77
5	4'x4'	16045	8	0.52	200	57	19	0.00014	135
6	4'x4'	22246	8	0.52	200	79	26	0.00024	111
7	2'x4' thin mortar	37487	8	0.56	215	123	41	0.00018	227
8	2'x4' thin mortar	53270	8	0.56	215	175	58	0.00074	79

The value of n was calculated using equation 3-4 and it represents the net area as a fraction of the gross area. The net area was determined using equation 3-5.

$$\mathbf{A_n = \frac{w + h}{2} * t * n} \tag{3-5}$$

where w is the width of the wallette in inches, h is the height of the wallette in inches, and t is the thickness of the wallette in inches

The shear strength of the wallette, S_s, was calculated using equation 3-6.

$$\mathbf{S_s = \frac{0.707 * F}{A_n}} \tag{3-6}$$

where F is the maxium force the wallette resisted.

The shear modulus, G, was calculated using 1/3 of the maximum shear strength and the corresponding strain to insure it corresponds to the linear deformation of shear failure. The shear modulus was then calculated by dividing the shear strength by the strain. For these tests, a mean

shear modulus of 142 ksi was determined with a coefficient of variation of 0.42. This is a large variation, which was expected and has been observed by other researchers (Bosiljkov 2005).

An unexpected result is that of the ungrouted wallette which, on average, were able to resist a higher load than the two ft. by two ft. wallette. This may be due to the fact that wallette 5 was bowed slightly and not straight. The bowing may have caused the load to be applied eccentrically, lowering the strength of the wallette.

3.3.12 Wallette 1

Wallette 1 was ungrouted and with no apparent defects in either the blocks or the surface coating. When the load reached about 11,000 lbs. the outside webs had visible cracking. Even with the major cracking of the outside webs, the surface coating held the wallette together and load continued to increase. Around 20,000 lbs., small cracks along the center of the face of the wallette appeared and continued to increase until complete failure occurred at 23,804 lbs. Though the wallette's ability to resist the load was compromised at this point, the wallette still held together. Figure 3-16 shows pictures of the wall after failure. From the data collected, a stress vs strain graph was generated and is shown in Figure 3-17. In generating the graph, a 3 point low pass filter was applied to the data. The wavering lines are attributed to small internal cracks and settling of the blocks during testing.

3.3.13 Wallette 2

Wallette 2 was also ungrouted and with no apparent defects. When loading reached around 13,000 lbs., cracking was seen on the outside cell webs. The webs then completely failed around 14,000 lbs. After the failure, the load decreased but began to climb again.

(a) Wallette at failure. **(b) Crack of outside webs.** **(c) Crack down center of wallette.**

Figure 3-16 Wallette 1 after failure.

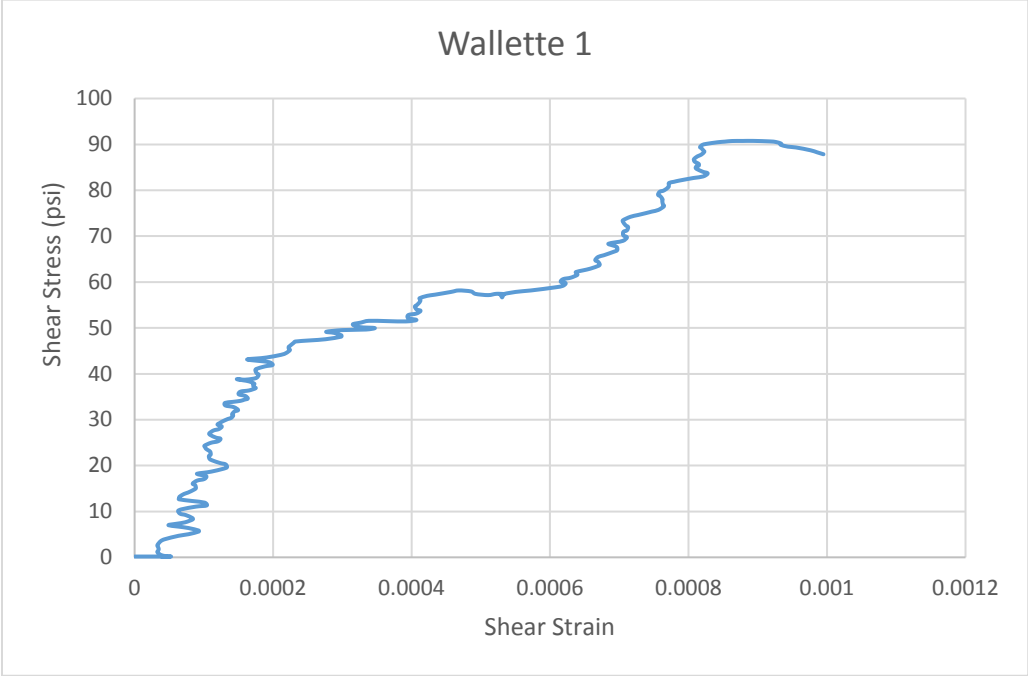

3-17 Stress-strain curve of wallette 1.

At about 17,000 lbs., cracks started to form on the face of the wallette. Total failure occurred at 19,239 lbs. Even after failure, the wallette held together. Figure 3-18 shows the stress vs strain curve for wallette 2. Figure 3-19 shows the wallette after failure.

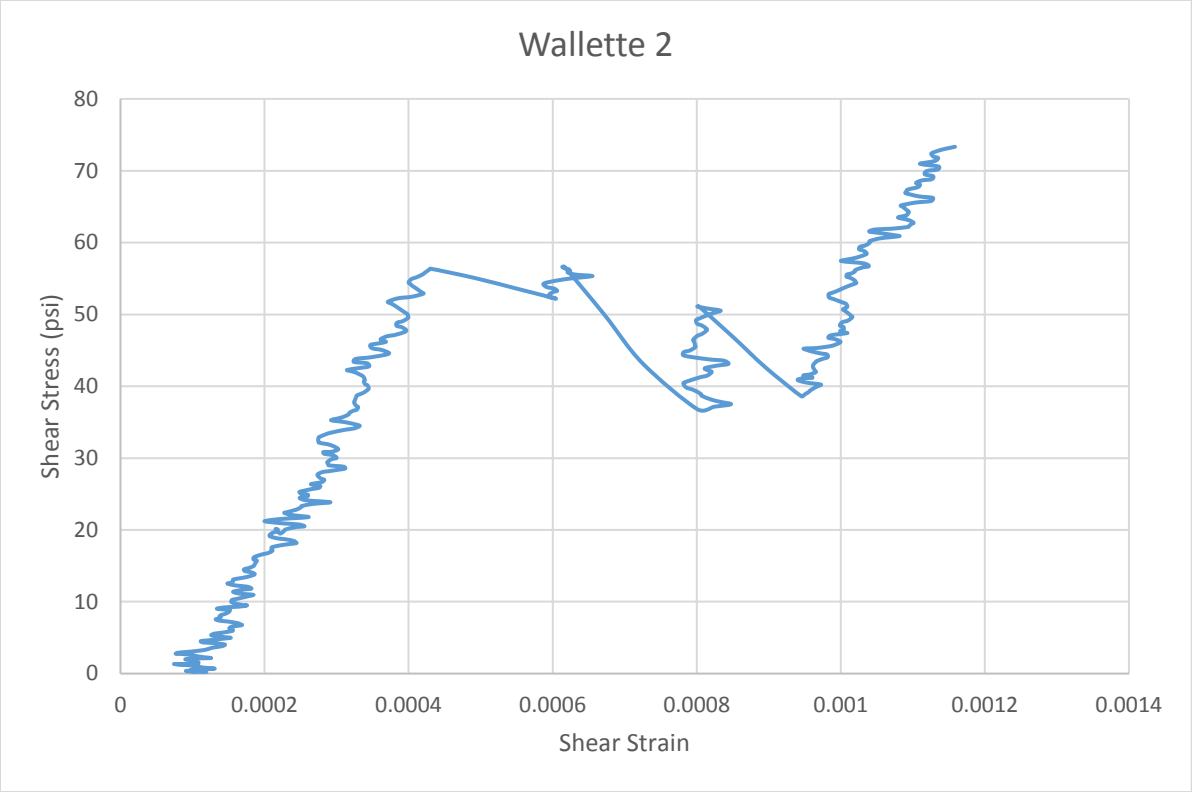

Figure 3-18 Wallette 2 stress-strain curve.

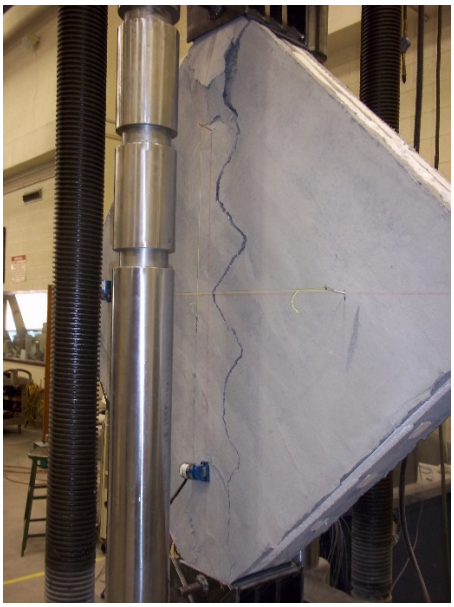

(a) Cracking of face of wallette. **(b) Cracking through webs.**

Figure 3-19 Wallette 2 after failure.

3.3.14 Wallette 3

Wallette three was grouted vertically every two ft. and had a single horizontal bond beam. During testing, no failure in the webs of the blocks occurred as it had happened during the tests of the ungrouted wallettes. The load continued to increase steadily up to about 16,000 lbs. and then continued to increase but at a slower rate. At around 25,000 lbs., small cracks started to appear on the face of the wallette. Final failure occurred at 28,141 lbs. with the small cracks on the face of the wallette opening up slightly. No major crack was observed, and the wall continued to hold together but was unable to support the same load. Figure 3-20 shows the stress vs strain curve for wallette 3, and Figure 3-21 shows the wallette after failure.

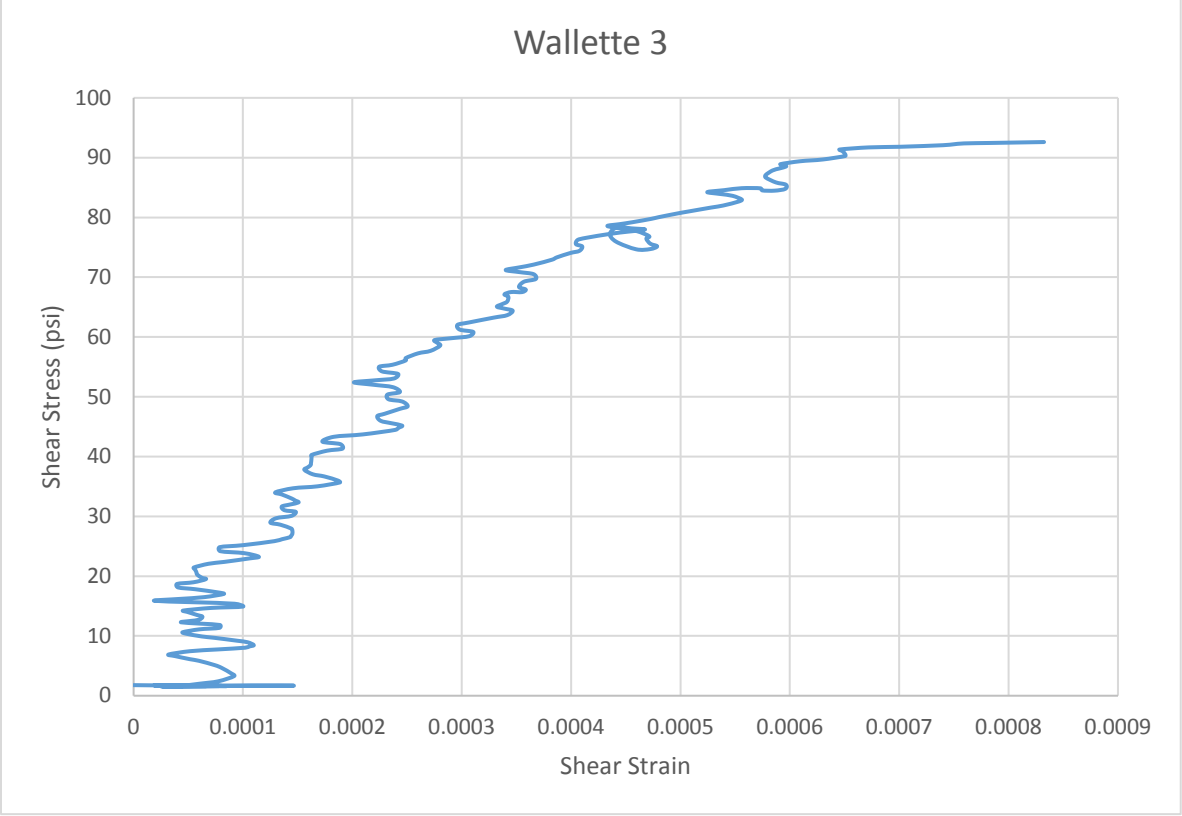

Figure 3-20 Wallette 3 stress-strain curve.

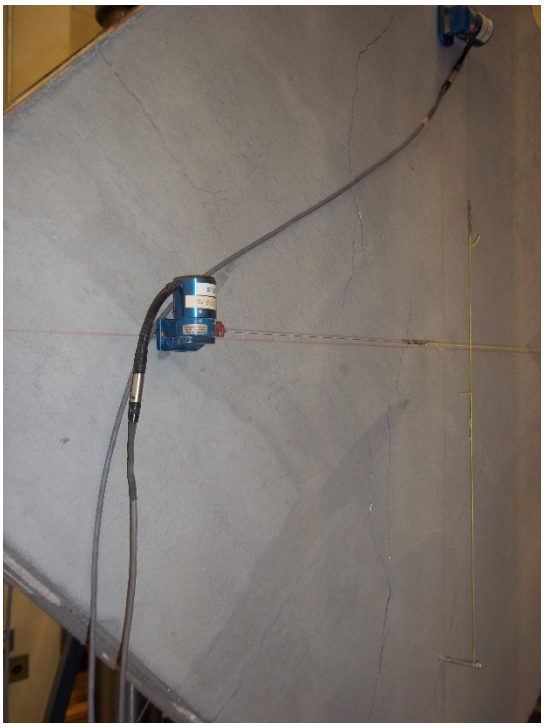

(a) Wallette 3 face after failure. **(b) Close up view of crack on wallette face.**

Figure 3-21 Wallette 3 after failure.

3.3.15 Wallette 4

Wallette 4 was also grouted every two ft. vertically and had one horizontal bond beam. Before testing minor cracks were observed in the web of one of the blocks and on the faces of the wallette. These cracks were minor in nature and may not have impacted the results of the testing. During the test, at around 11,000 lbs., the outside webs of the blocks cracked. The load remained steady for a while and then continued to increase. At around 20,000 lbs., a crack from the top corner to the bottom corner appeared on the face of the wallette. This crack continued to widen until failure occurred at 30,231 lbs. Though severely cracked the wallette continued to hold together. Figure 3-22 shows the stress vs strain relationship of wallette 4, and Figure 3-23 shows wallette 4 after failure.

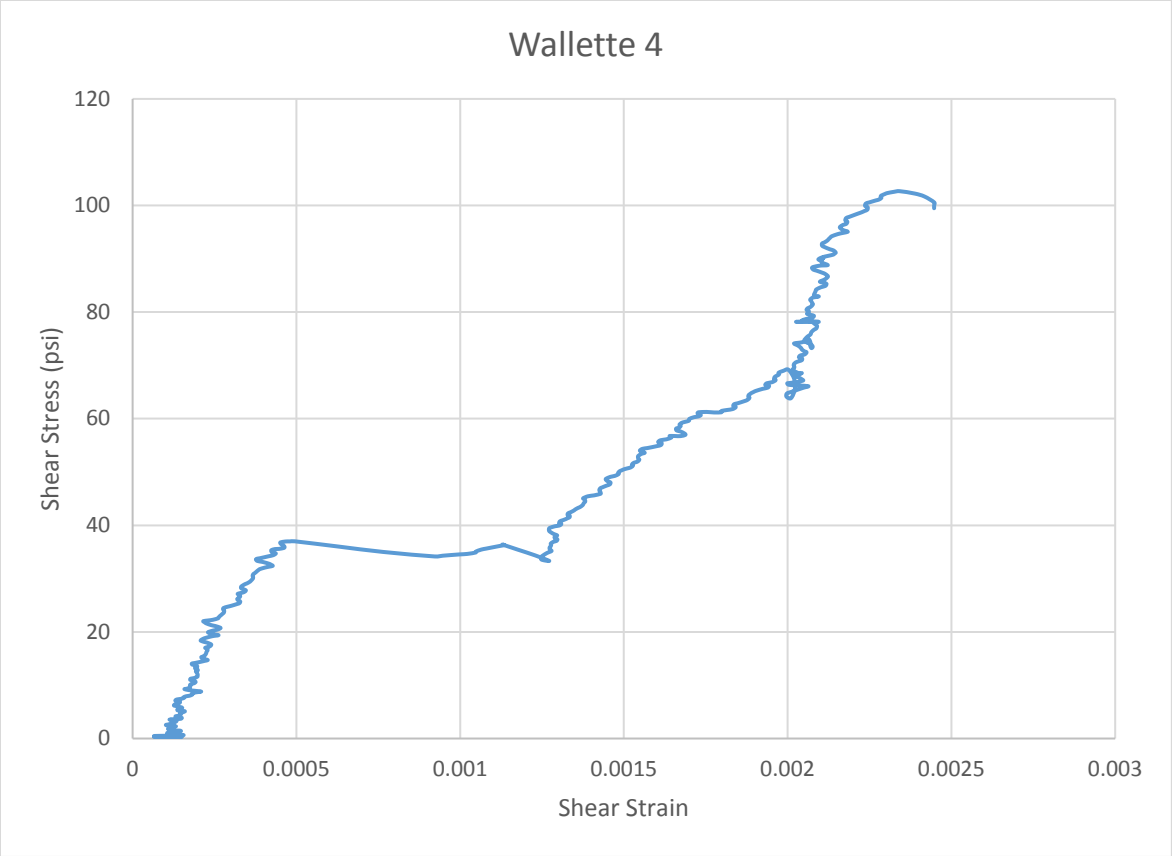

Figure 3-22 Wallette 4 stress-strain curve.

(a) Crack in block prior to testing. **(b) Cracks in web after testing.** **(c) Crack on face.**

Figure 3-23 Wallette 4 after failure.

3.3.16 Wallette 5

Wallette 5 had one vertical grout lift and one horizontal bond beam. This wallette was bowed out-of-plane slightly. Due to the low load that this wallette resisted, in comparison to the wallette of the same configuration and to the ungrouted wallettes this bowing is considered to have had a major impact on the capacity of the wallette. The bowing caused the load to be applied eccentrically generating tension in the blocks and on the surface coating on one side of the wallette. At the end of the testing, the surface coating was peeling from the wallette due to additional compression forces from the bowing.

During the test, small cracks started to appear near the bottom shoe on the inside face of the blocks around 10,000 lbs. At around 13,000 lbs., the structural coat started to peel away from the blocks on the inside face. Final failure occurred at 16,045 lbs. All visible damage occurred on the inside part of the block, which is considered to have happen due to the bowing of the wallette and the eccentricity this caused. The stress vs strain relationship for the wallette is shown in Figure 3-24, and Figure 3-25 shows the wallette after failure.

3.3.17 Wallette 6

Wallette 6 was also grouted with a single vertical lift and a single horizontal bond beam. No defects were observed in the wallette before testing. At around 10,000 lbs., the webs of the outside cell cracked and the load decreased. Then, the load began to increase again. At around 18,000 lbs., a crack on both faces of the wallette was observed going from the top corner to the bottom corner. At 22,079 lbs., final failure occurred, and the crack on the outside face of the wall widened substantially. On the outside face, small pieces of blocks became loose and fell away from the wall, but the majority of the wall held together. Cracks through the webs of the

inside cells were observed at failure. The stress vs. strain relationship for wallette 6 is shown in Figure 3-26, and Figure 3-27 shows wallette six after failure.

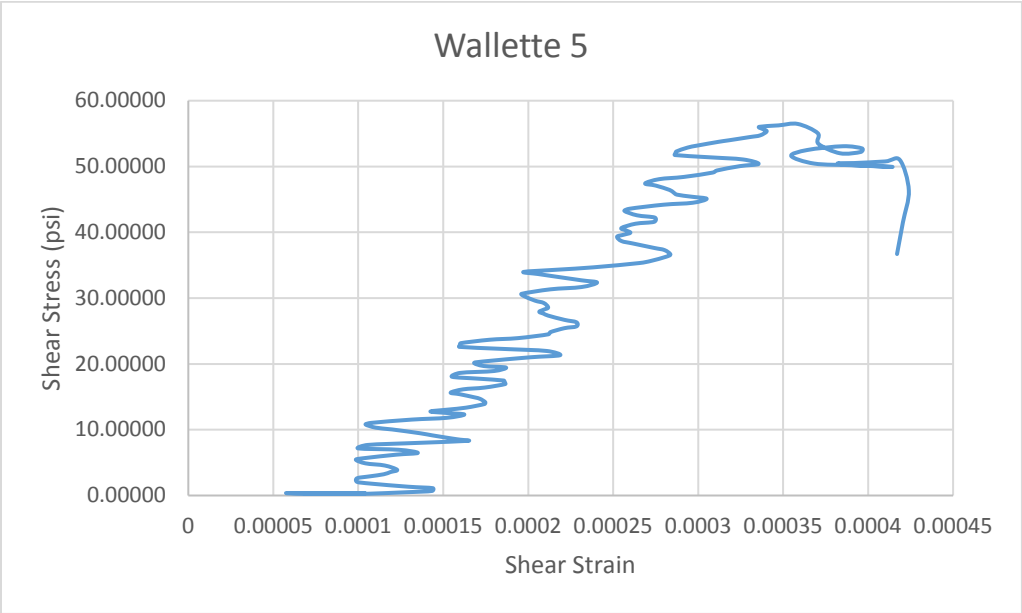

Figure 3-24 Wallette 5 stress-strain curve.

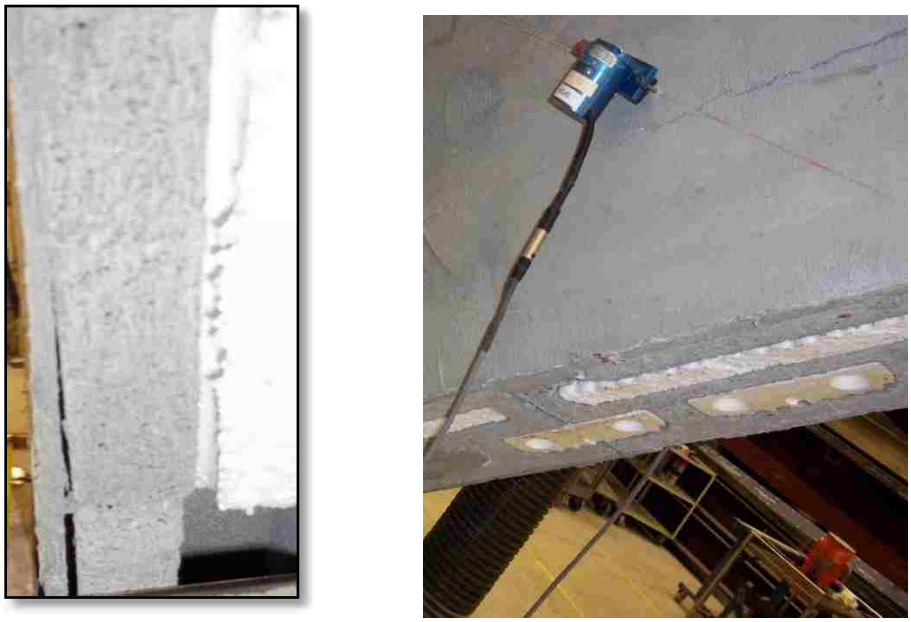

(a) Delamination of surface bond. **(b) Typical cracks in face of wallette.**

Figure 3-25 Failure in wallette 5.

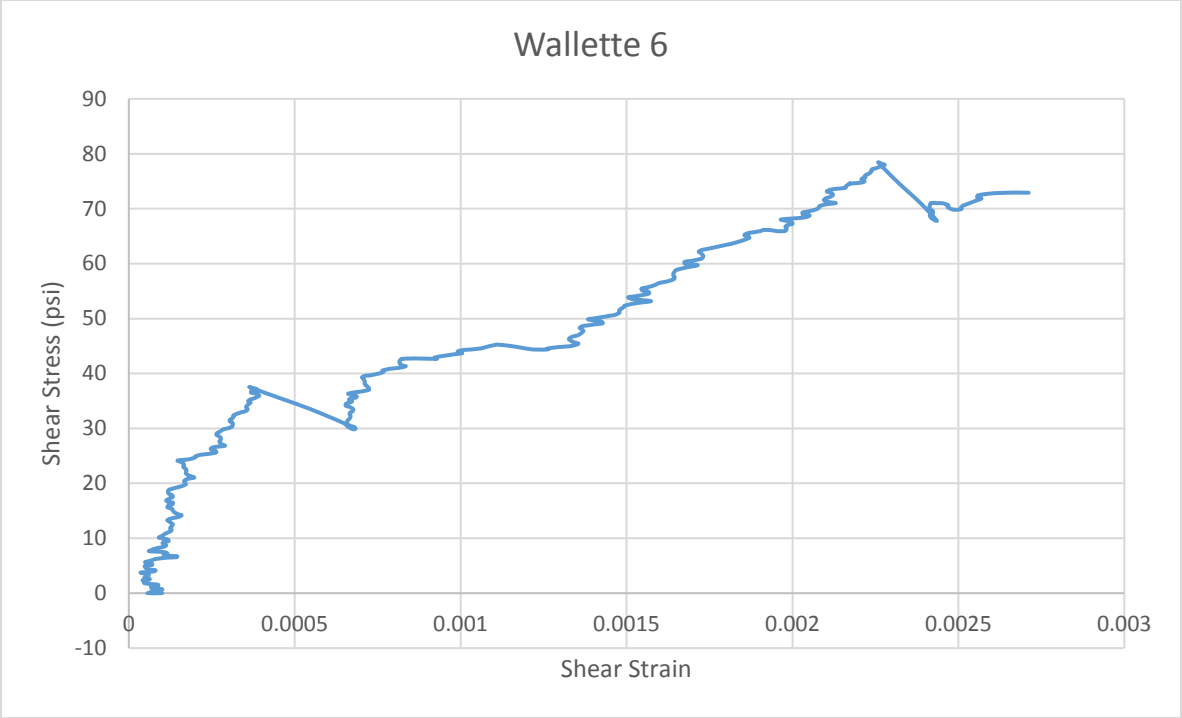

Figure 3-26 Wallette 6 stress-strain curve.

(a) Crack through webs.

(b) Crack through face of wallette.

Figure 3-27 Wallette 6 after failure.

3.3.18 Wallette 7

Wallette 7 was grouted vertically every two ft. and had a single horizontal bond beam. This wallette had a thin mortar layer between courses. No defects were noticed in the wallette prior to testing. During testing, around a load of 16,000 lbs., the webs for the outside cells cracked. Around 35,000 lbs., cracks began to form on the face of the wallette propagating from the top corner to the bottom corner. Cracking noises could also be heard coming from within the wallette about this load. Around 36,000 lbs., the foam inserts on the outside cell fell out and cracking was visible through the webs of the inside cells. After which, the load began to decrease gradually until failure occurred at 32,016 lbs. At the failure the wallette split in half and half the wallette fell to the ground. The stress vs strain relationship for wallette 7 is shown Figure 3-28, and Figure 3-29 shows wallette 7 after failure.

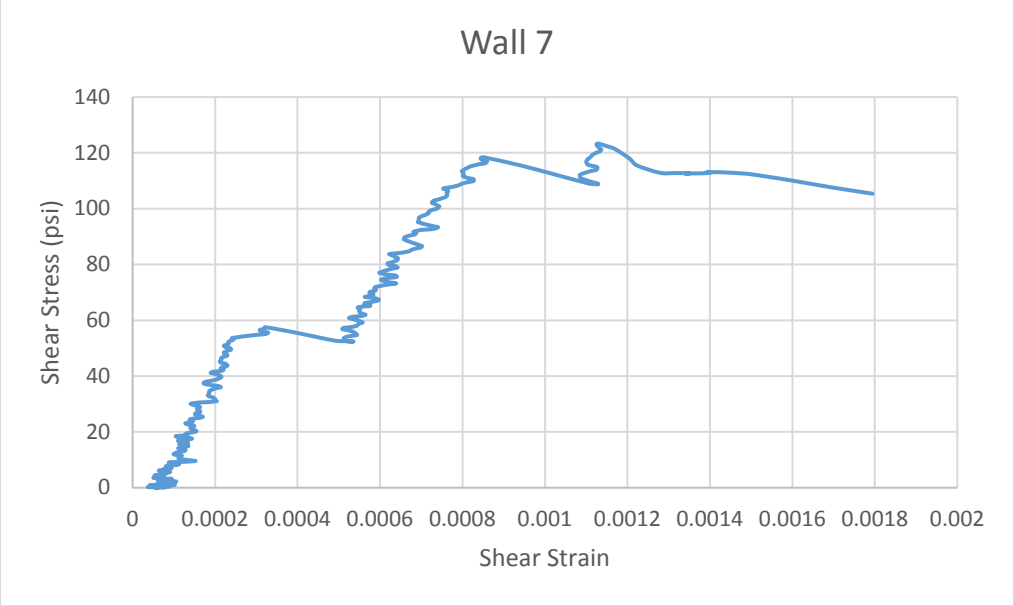

Figure 3-28 Wall 7stress-strain curve.

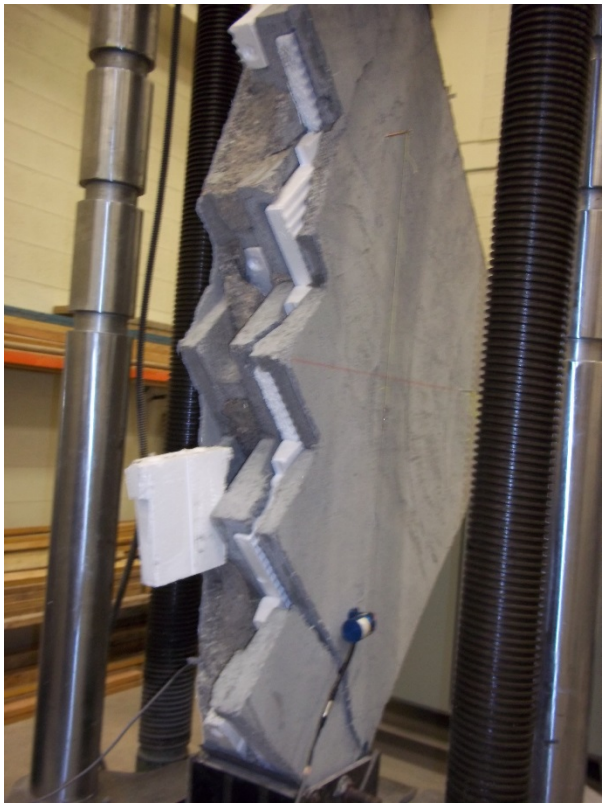

Figure 3-29 Wallette 7 after failure.

3.3.19 Wallette 8

Wallette 8 was grouted the same way as wallette 7, and had a thin mortar layer between courses. No apparent defects were noted in the wall prior to testing. At around 14,500 lbs., cracking of the outside cell webs was noticed, lowering the load resistance for a while. The load then continued to increase until around 36,000 lbs. when cracking noises from the inside of the wallette could be heard and the foam inserts fell out revealing cracking of the webs of the inside cells. Load began to decrease for a while but then continued to increase. At around 45,000 lbs., cracks started to appear on the face of the wallette. The widest of these cracks went from the top corner to the bottom corner of the wallette. Failure occurred at 53,270 lbs. when the wall split in

half. The stress vs strain relationship is shown in Figure 3-30, and Figure 3-31 shows wallette 8 after failure.

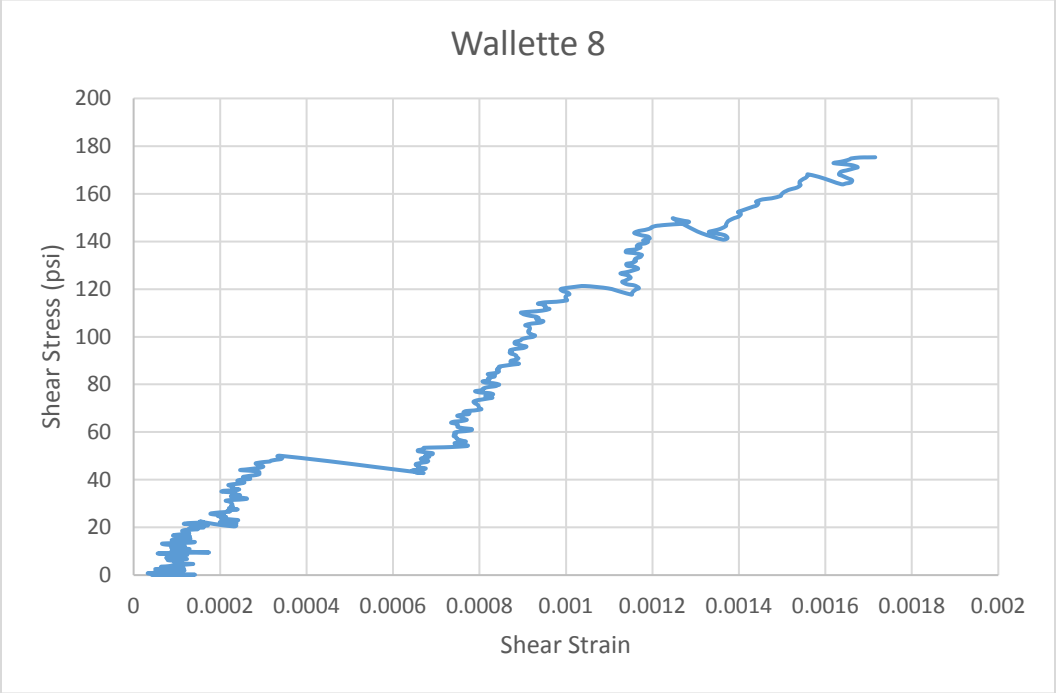

Figure 3-30 Wall 8 stress-strain curve.

3.3.20 Discussion of Diagonal Tension Test

Though the diagonal-tension test was useful in gathering some mechanical properties of the system, much of the data was unreliable as values varied widely from test to test. This is especially seen in the calculation of the shear modulus and shear strength of the wallette. As all the wallettes were built at the same time and with the same materials that were tested, the reason for the variability cannot be ascertained.

As stated before, the diagonal-tension test has shown to be unreliable for typical masonry, and it appears to be similar for dry-stack masonry with surface bond. To verify this, future testing would need to be completed with component testing being done on each wall for

Figure 3-31 Wallette 8 after failure.

statistical comparison. In addition, at least three tests would need to be completed for every variation to allow for the statistical comparison.

4 IN-PLANE SHEAR TEST

Masonry shear walls are designed to resist lateral forces that act on a structure. It has been assumed that if out-of-plane failure is prevented, then in-plane shear walls provide the resistance necessary to prevent collapse (Magnese, 1997). This assumption is continued in this research and out-of-plane failure is not a major consideration. However, research was conducted on the out-of-plane capacity of the dry-stack system considered herein, which is presented in Appendix A. The main consideration is therefore the in-plane lateral forces acting on the shear walls. To assess the capabilities of the dry-stack system, in-plane shear wall tests were conducted.

4.1 Background

The in-plane shear test is utilized as it is the basis of the current nominal shear strength in the masonry design code (ACI 2013). In addition, it has been used to test masonry walls for their seismic resistance (Magenes 1997). The design equations currently used were empirically derived from research that used in-plane shear test of masonry walls (Shing et al. 1990a and Shing et al. 1990b). The design equations were originally based on fully grouted shear wall tests, and later research has shown that partially grouted shear walls are practical lateral load-resisting systems under seismic loading (Schultz et al. 1998). However, partially grouted shear walls have a smaller resistance than fully grouted shear walls (Elmapruk 2010, Minaie 2009, Nolph, 2010). Due to this smaller resistance, a grouted shear wall factor, γ_g, is used in the masonry design code.

Research over the years has shown that many failure modes can occur when the in-plane shear test is used. Two distinct failure modes are usually seen in shear walls: a flexural mode and a shear mode (Gabor et al. 2005). The flexural mode is characterized by horizontal cracks in the bottom courses, yielding of vertical reinforcement, and toe crushing. This failure mode is more ductile as the steel reinforcement yields before failure. In extreme cases, this failure mode can lead to rocking. Rocking failure occurs when there is a continuous flexural crack in one or more bed joints along the entire length of the wall. The wall is essentially split into two parts connected only by the vertical reinforcement, and as the lateral load reverses the wall rocks back and forth. Shear failure is characterized by diagonal cracking of the wall, usually at a 45° angle. This failure occurs suddenly, but effort is made to increase the ductility of shear failures. In some instances, sliding shear failure can occur. This is characterized by the upper segment of the wall sliding along the bottom segment with the vertical reinforcement acting as the only lateral force resisting mechanism (Sveinsson et al 1985).

Several mechanisms influence the failure mode of shear walls. The span ratio, or the height to length ratio has a significant influence on the failure mode of masonry walls (Matsumura 1987, Schultz 1996a&b, Maleki 2008). Reinforcement also contributes to the failure mode of shear walls. Shear reinforcement, or horizontal reinforcement, increases additional shear resistance and improves the post cracking performance of masonry walls when the reinforcement is uniformly distributed up the height of the walls (Voon 2006). However, reinforcement is not engaged until the masonry cracks, so it is not effective in increasing the cracking strength of the wall (Matsumura 1987). In addition, vertical reinforcement is also effective in keeping the shear cracks from opening (Ghanem et al. 1992). Any axial load acting on the wall can also influence

the failure mode. As the axial load increases so does the shear resistance; however, the ductility is decreased as the axial load increases (Voon 2006).

4.2 Component Testing

The same component testing that was done for the diagonal-tension test was also done for the in-plane shear test.

4.2.1 Grout

The grout was made and tested in the same manner as outlined in the Diagonal-Tension test section. Results from the compression testing are summarized in Table 4-1, which also lists the corresponding walls.

Table 4-1 Grout Compressive Strength

Wall	Prism	Area (in^2)	Max Force (lbs.)	Compressive Strength (psi)
3&4	7	16.8	56130	3339
	8	17.1	62045	3620
	9	16.8	59955	3575
5&6	10	17.7	66325	3742
	11	16.5	58540	3543
	12	16.9	67375	3989
7&8	13	17.1	69656	4084
	14	17.1	62285	3652
	15	16.9	61385	3625
9&10	16	17.1	64535	3784
	17	16.8	66872	3988
	18	16.9	67680	4007
11&12	19	17.1	60685	3558
	20	16.9	61245	3617
	21	17.6	61635	3494

ANOVA testing was conducted to determine if there was a statistically significant difference in the 28 day compressive strength of any of the grout with a 95% certainty level. All

specimens were compared to the specimens corresponding to walls three and four. This resulted in a p-value of 0.75, 0.87, 0.51, and 0.12 for the grout used in walls five, six, seven, eight, nine, ten, 11, and 12 respectively. These values indicate that the null hypothesis of equal means was accepted, or in other words, there was no statistical evidence suggesting a difference in 28-day strength between the grout prisms. This indicates that the grout used in all the walls was essentially the same.

4.2.2 Mortar

The mortar was made and tested in the same manner as outlined in the Diagonal-Tension test section. Results from the compression testing are summarized in Table 4-2. The mortar was only used on walls seven and eight.

Table 4-2 Mortar Compressive Strength

Cube	Area (in^2)	Max Force (lbs.)	Compressive Strength (psi)
4	4.1	29335	7155
5	4.2	31340	7458
6	4.2	30705	7343

4.2.3 Surface Coating

The surface coating was made and tested in the same manner as outlined in the Diagonal-Tension test section. Results from the compression testing are summarized in Table 4-3 along with their corresponding walls.

ANOVA testing was conducted to determine if there was a statistically significant difference in the 28 day compressive strength of any of the surface bond with a 95% certainty level. All specimens were compared to the specimens corresponding to walls one and two. This resulted in a p-value of 0.052, 0.003, 0.001, 0.95, and 0.003 for walls three, four, five, six, seven,

eight, nine, ten, 11, and 12 respectively. This indicates that the null hypothesis of equal means was rejected for walls five, six, seven, eight, 11 and 12, but was accepted for walls three, four, nine and ten. In other words, there was a statistically significant difference in the surface coating used on walls five, six, seven, eight, 11, and 12 compared to walls one and two and no statistically significant difference between the surface coatings used on walls three, four, nine, and ten. Additional, ANOVA testing was conducted comparing surface coating used on walls five and six to that used on walls seven, eight, 11, and 12. This resulted in a p-value of 0.155 and 0.247 respectively. This indicates there was no statistically significant difference between the surface coatings used on these walls.

Table 4-3 Surface Coating Compression Strength

Wall	Cube	Area (in^2)	Max Force (lbs.)	Compressive Strength (psi)
1 & 2	D	4.0	24040	5951
	E	4.0	23435	5830
	F	4.0	23850	5903
3 & 4	G	4.1	25030	6074
	H	4.1	27455	6631
	I	4.2	28420	6796
5 & 6	J	4.1	33800	8243
	K	4.0	29200	7228
	L	4.1	32672	8047
7 & 8	M	4.1	29440	7251
	N	4.1	28320	6941
	O	4.1	30720	7492
9 & 10	P	4.1	22190	5465
	Q	4.1	25670	6229
	R	4.0	23925	5951
11 & 12	S	4.1	38215	9274
	T	4.2	33130	7961
	U	4.1	33935	8317

4.2.4 Masonry Prisms Compressive Strength

The masonry prisms were made and tested in the same manner as discussed in the Diagonal-Tension test section. Results from the compression testing are summarized in Table 4-4 along with their corresponding walls.

ANOVA testing was conducted to determine if there was a statistically significant difference in the 28 day compressive strength of any of the prisms with a 95% certainty level. All specimens were compared to the specimens corresponding to walls three and four. These were also split between the grouted and ungrouted prisms. In all cases the null hypothesis was accepted, or in other words there was no statistically significant difference between the prisms tested.

4.2.5 Discussion

Out of all the components tested, the surface coating was the only one which the results indicated statistically significant differences. There are several possibilities for the difference. First, this could be a result of the manufacturing of the surface coating. It came to the attention of the researcher that there was a recalibration of the manufacturing of the surface coating during testing. Another possibility may be in the mixing process. The surface coating was made by the same masons and water was added until the masons thought it looked “right”. As there is no consistent water-cement ratio or mixing time, the amount of water could have been different and could have led to the statistical difference. Another possibility is that the samples taken from walls 11 and 12 were from the second coating layer and not from the structural layer. This possibility is puzzling, however, since the second layer usually had more water and would have resulted in a lower average compressive strength rather than in a higher compressive strength as measured.

Table 4-4 Masonry Prism Compressive Strength

Wall	Prism	Area (in^2)	Max Force (lbs.)	Compressive Strength (psi)
1 & 2	G	33.0	40011	1211
	H	33.3	47558	1430
	I	32.7	48787	1493
3 & 4	J	32.9	44326	1347
	K	33.0	49878	1511
	L	33.3	42362	1274
	M	52.2	94165	1803
	N	51.3	87754	1710
	O	52.0	85886	1652
5 & 6	P	32.7	44051	1348
	Q	31.6	44980	1422
	R	33.3	39522	1188
	S	50.3	92833	1845
	T	51.5	86769	1686
	U	51.5	84963	1651
7 & 8	V	33.8	45030	1331
	W	32.0	39265	1229
	X	32.8	45427	1385
	Y	53.8	91042	1692
	Z	53.8	86275	1603
	AA	52.8	95555	1809
9 & 10	BB	32.9	41342	1258
	CC	32.7	49356	1511
	DD	31.6	47452	1502
	EE	53.0	94708	1788
	FF	53.1	87554	1647
	GG	52.9	92220	1745
11 & 12	HH	32.5	43883	1349
	II	32.6	43306	1328
	JJ	33.0	44451	1348
	KK	52.6	92238	1755
	LL	51.7	93462	1808
	MM	52.5	88865	1694

Despite the statistical difference in the surface coating used, there was no statistical difference between the results of the masonry prisms tests. This indicates that the surface coating had little to no effect on the compressive strength of the prisms. More testing is needed to either confirm or refute this hypothesis.

4.2.6 Correction Factor

The testing on the components showed that there was a statistical difference between the surface coatings used on the various walls. Though there was no statistical difference in the compressive strength on the prisms, failure occurred primarily through the surface coating for lateral loads. This type of failure would be a shear failure instead of compressive failure. The shear strength of concrete is related to the square root of the compressive strength (ACI 2014). Using the square root of the compressive strength of the surface coating, resulted in a shear strength difference of approximately16 psi, or approximately 400 pound shear strength difference for the full size wall if the 16 psi is multiplied by the area of surface coating in the direction of shear. This was within experimental variation of walls built with the same material and so no correction factor was applied to account for the shear strength difference.

4.3 Testing Matrix

Walls were constructed in a similar manner as described in the diagonal-tension test, and 12 walls were built and tested for their in-plane shear capacity. Each wall was eight ft. by eight ft. and were built upon reinforced concrete footings. A total of three configurations were used: ungrouted, grouted vertically every two ft. and horizontally every four ft. (2’ x 4’), and grouted vertically every four ft. and horizontally every four ft. (4’ x 4’). Additional testing was conducted on 4’ x 4’ walls by testing two walls each with an axial load, with a thin mortar set in the bed joints, and testing cyclically instead of monotonically. The testing matrix is shown in Table 4-5 and a visual representation of the wall configurations is shown in Figure 4-1.

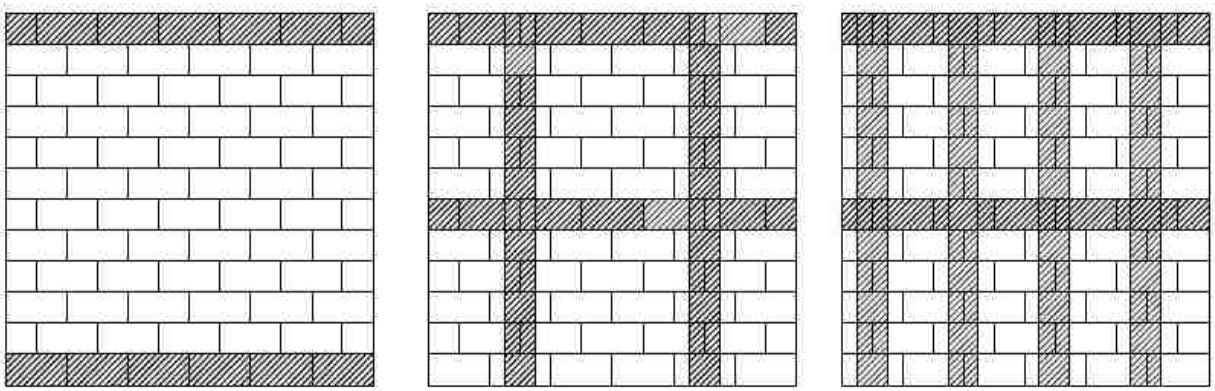

(a) Ungrouted **(b) 4’ x 4’** **(c) 2’ x 4’**

Figure 4-1 Wall configurations

Table 4-5 Testing Matrix

Wall	Grout Pattern	Vertical Reinforcement	Horizontal Reinforcement	Thin Mortar	Cyclic loading	Axial Loaded
#1	Ungrouted	N.A.	N.A.			
#2	Ungrouted	N.A.	N.A.			
#3	4’x4’	2#4 (A_s=0.40 in^2) @ 48” o.c	2#4 (A_s=0.40 in^2) @ 48” o.c			
#4	4’x4’	2#4 (A_s=0.40 in^2) @ 48” o.c	2#4 (A_s=0.40 in^2) @ 48” o.c			
#5	2’x4’	2#4 (A_s=0.40 in^2) @ 24” o.c	2#4 (A_s=0.40 in^2) @ 48” o.c			
#6	2’x4’	2#4 (A_s=0.40 in^2) @ 24” o.c	2#4 (A_s=0.40 in^2) @ 48” o.c			
#7	4’x4’	2#4 (A_s=0.40 in^2) @ 48” o.c	2#4 (A_s=0.40 in^2) @ 48” o.c	X		
#8	4’x4’	2#4 (A_s=0.40 in^2) @ 48” o.c	2#4 (A_s=0.40 in^2) @ 48” o.c	X		
#9	4’x4’	2#4 (A_s=0.40 in^2) @ 48” o.c	2#4 (A_s=0.40 in^2) @ 48” o.c		X	
#10	4’x4’	2#4 (A_s=0.40 in^2) @ 48” o.c	2#4 (A_s=0.40 in^2) @ 48” o.c		X	
#11	4’x4’	2#4 (A_s=0.40 in^2) @ 48” o.c	2#4 (A_s=0.40 in^2) @ 48” o.c			X
#12	4’x4’	2#4 (A_s=0.40 in^2) @ 48” o.c	2#4 (A_s=0.40 in^2) @ 48” o.c			X

The ungrouted walls had the top course and bottom course grouted. The top course was grouted in order to bolt the top cap of the testing frame to the wall, and the bottom course was grouted in order to eliminate the possibility of the wall to simply slide. By grouting the bottom course, failure should have occurred in the wall itself instead of the interface between wall and footing.

4.4 Footing Design

Reinforced concrete footings were 10 ft. long, 18 in. wide, and 12 in. high. Each footing had 2 #6 and 1 #3 reinforcing bars in the top and bottom, and stirrups were #4 bars at 8 in. on center. Each footing was attached to the laboratory strong floor using two 1 in. diameter high strength steel bars. The bars were placed through PVC tubes that had been placed vertically and fixed inside the wood formwork before concrete pouring. In addition, steel plates were bolted on the sides of the footing around the PVC tubes to prevent shear failure in this area. Figure 4-2 shows footing reinforcement.

4.5 Test Setup

The walls were built upon the footings that were then fixed to the laboratory floor. The lateral load was applied to the top course using a 100 kip capacity hydraulic actuator. The actuator was fixed on one end to a steel strong frame and supported underneath by a steel column as shown in Figure 4-3. The actuator was connected to a plate that was then connected to two rectangular tubes that were four in. by two in. in size and 3/8 in. thick. These tubes were inserted through a steel frame and connected to a steel cap with a high strength steel bolt through a vertical slotted hole. The steel cap was attached to the wall with twenty-four 1/2 in. steel bolts. These bolts were placed eight in. on center with 12 bolts on each side of the wall. To minimize

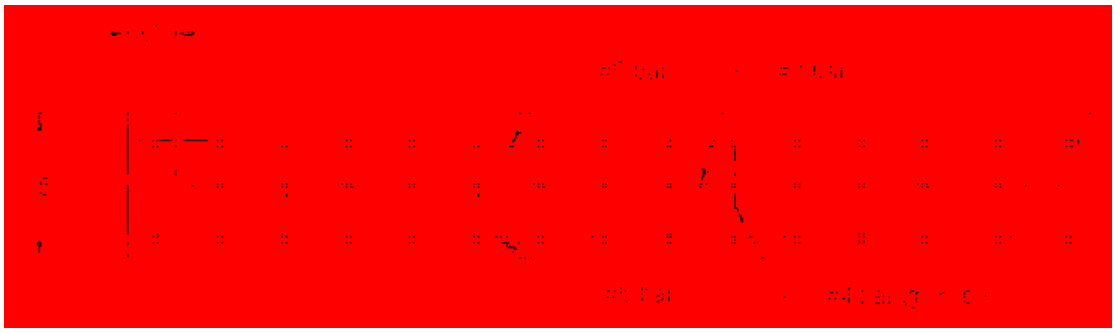

(a) Plan view.

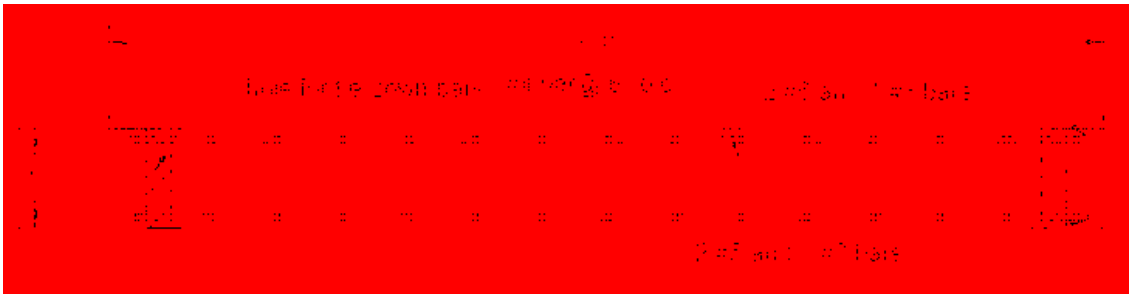

(b) Elevation view.

Figure 4-2 Footing reinforcement.

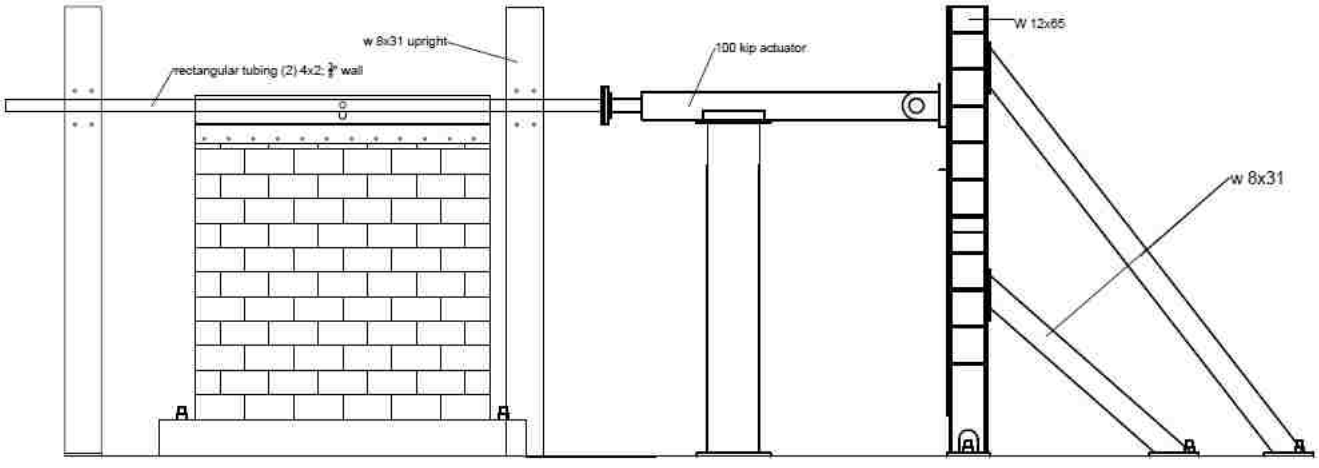

Figure 4-3 In-plane shear test frame design.

the sliding of the footing, two stiff built-up steel angles were post-tensioned to the laboratory strong floor on either side of the wall. Figure 4-4 shows a picture of the test setup.

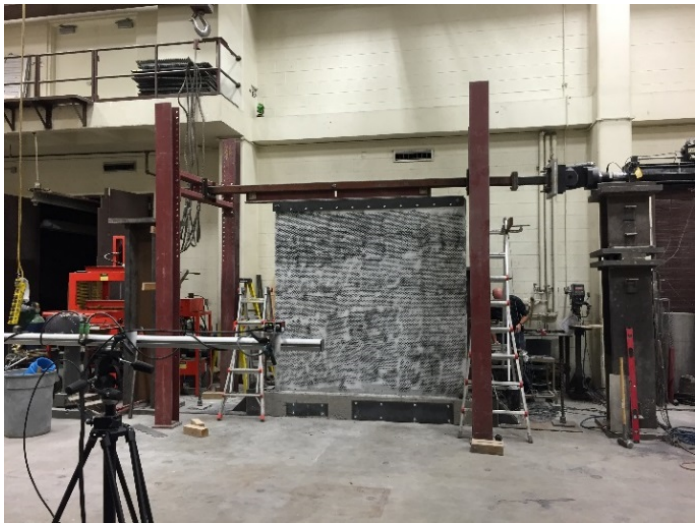

Figure 4-4 Picture of in-plane shear test setup.

4.6 Instrumentation

The applied lateral load and displacements were measured during the testing of the walls. For each wall, string pots were used to measure the displacements of the walls. Two different configurations were used in the placing of the string pots depending on the loading, monotonic or cyclical. For the monotonic loading, one string pot was placed on the top course on the far side from the actuator, one at the bottom course and one at the footing on the far side of the actuator, two on the face of the wall, one on the footing on the actuator side, and one on the bottom of the wall on the actuator side. These are shown in Figure 4-5 (a). The string pot on the far side on the top of the wall measured the lateral displacement of the top of the wall; the string pot on the bottom of the far side of the wall measured the lateral displacement of the bottom of the wall; and string pot on the footing on the far side of the wall measured the lateral displacement of the footing. The two string pots on the face of the wall measured the diagonal contraction or

expansion of the wall; the string pot at the bottom on the actuator side of the wall measured any uplift of the wall during loading, and the string pot on the footing on the actuator side of the wall measured any uplift in the footing during testing.

In addition to the string pots used during monotonic loading, four string pots were used during cyclic loading. One string pot was placed at the top of the wall on the actuator side, one at the bottom of the wall on the actuator side, one at the bottom of the wall on the far side from the actuator, and one on the footing from the far side. The string pots used during the cyclic tests are shown in Figure 4-5 (b). To determine if there was any difference during the pull and push of the wall the string pot at the top of the wall measured the lateral displacement of the top of the wall. The one at the bottom of the actuator side measured the lateral displacement of the bottom of the wall. The other two string pots were used to measure the uplift of the wall and footing. String pots not attached directly to the wall, were attached to an independent frame. Table 4-6 summarizes the string pot information.

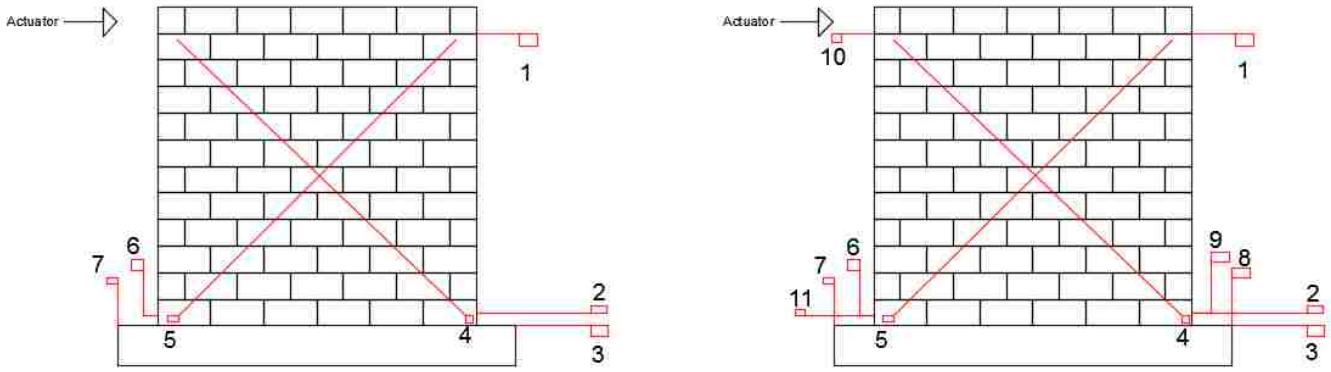

(a) Monotonic loading. **(b) Cyclic loading.**

Figure 4-5 String pot locations.

Table 4-6 String Pot Information

String Pot	Testing		Measurement
	Monotonic	Cyclic	
1	X	X	Lateral displacement at top of wall
2	X	X	Lateral displacement at bottom of wall
3	X	X	Lateral displacement at footing
4	X	X	Diagonal expansion or contraction
5	X	X	Diagonal expansion or contraction
6	X	X	Uplift of wall
7	X	X	Uplift of footing
8		X	Uplift of footing
9		X	Uplift of Wall
10		X	Lateral displacement at top of wall
11		X	Lateral displacement at bottom of wall

In addition to the string pots, a digital image correlation (DIC) camera was set up to measure the displacements throughout the wall. Unfortunately, the data collected was not usable and is not presented in this dissertation.

4.7 Testing Protocol

Specimens were tested using a displacement controlled protocol. The displacement rate was kept constant at 0.1875 in. per min. following the same displacement as other research (Nolph 2010). The majority of the walls were tested monotonically to failure and failure was considered to occur when the load dropped 20% from the peak load.

The walls that were tested cyclically had a slightly different protocol, though the displacement rate was kept the same. The cyclically tested walls used a displacement controlled protocol of 3 cycles at a displacement percentage of the yield displacement. The yield

displacement was calculated using equations 4-1 and 4-2 (Priestley et al 2007). The displacement testing protocol is shown in Figure 4-6.

$$\theta_{y\_mw} = 0.6 * \varepsilon_y * \frac{H_n}{l_w} \quad (4\text{-}1)$$

$$\Delta_y = \boldsymbol{\theta_{y\_mw} * H_e} \quad (4\text{-}2)$$

where H_n is the height of the wall, l_w is the length of the wall, H_e is the effective height of the wall, ε_y is the yield strain of the reinforcing steel, θ_{y_mw} is the yield drift of the masonry wall, and Δ_y is the yield displacement.

The yield displacement was calculated to be 0.1 inches. Displacement levels were set at $0.5\Delta_y$ and increased by $0.5\Delta_y$ until $2.5\Delta_y$. Then displacement started at $4\Delta_y$ and increased by $1\Delta_y$ until $6\Delta_y$. Afterwards, peaks were increased by $2\Delta_y$ until failure occurred.

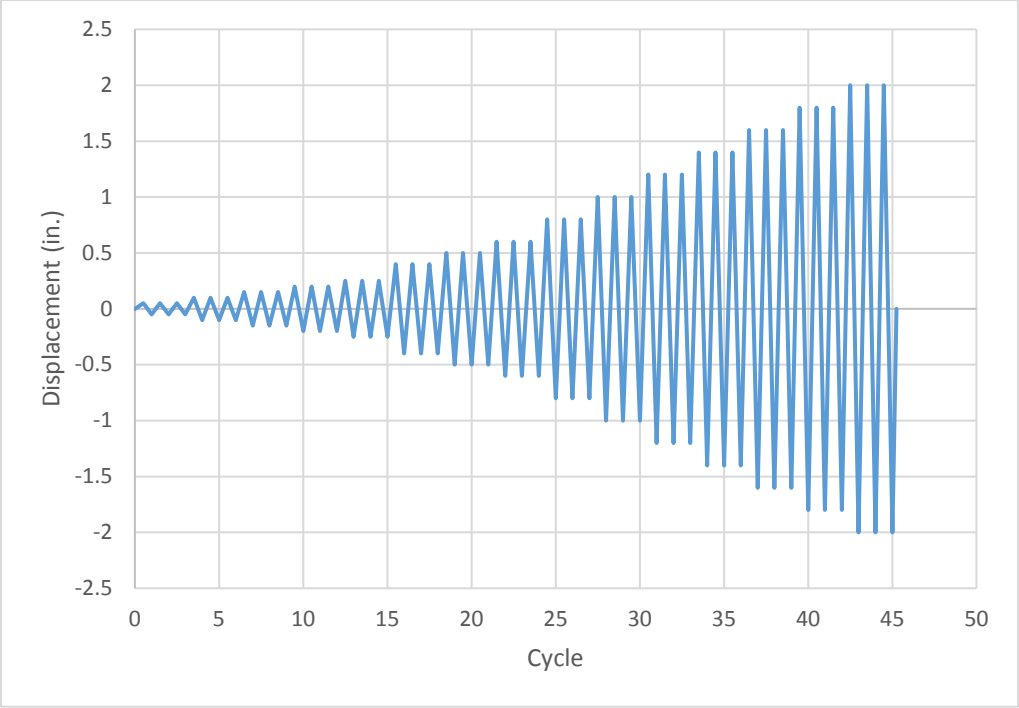

Figure 4-6 Displacement controlled cyclic protocol.

4.8 Results

During testing flexural, shear, sliding, and rocking failure were observed. Sliding was observed between the wall and footing instead of between bed joints as usually occurs. This sliding was attributing to only one #4 bar connecting the footing to the wall whereas there were two #4 vertical reinforcement bars in the wall. Rocking is also assumed to be caused by the limited footing-wall connection capacity compared to the wall capacity.

For each wall the maximum load, maximum displacement, ultimate shear stress, ultimate shear strength, shear modulus, and primary failure mode were determined. The maximum load was taken as the load recorded from the internal instrumentation of the actuator. Table 4-7 summarizes the results from the in-plane shear test, and the primary failure mode for the walls.

Table 4-7 General Results from In-Plane Shear Test

Wall	Configuration	Max Load (lbs.)	Maximum Displacement (in.)	Net area ($in.^2$)	Ultimate Shear Stress (psi)	Ultimate Shear Strength (lbs./ft.)	G (ksi)	Primary Failure Mode
1	ungrouted	2650	0.08	367	7	331	132	Flexural
2	ungrouted	2903	0.03	367	8	363	140	Flexural
3	4'x4'	14730	0.88	405.8	36	1841	118	Shear
4	4'x4'	15982	0.77	405.8	39	1998	23	Rocking
5	2'x4'	22848	1.05	430.1	53	2856	115	Rocking
6	2'x4'	20779	1.08	430.1	48	2597	115	Shear
7	4'x4' thin mortar	12964	0.54	405.8	32	1620	124	Shear
8	4'x4' thin mortar	15057	1.16	405.8	37	1882	133	Rocking
9	4'x4' cyclic loading	11463	0.71	405.8	28	1433	135	Flexural
10	4'x4' cyclic loading	14765	0.94	405.8	36	1846	130	Shear
11	4'x4' axial load	20232	1.02	405.8	50	2529	125	Flexural
12	4'x4' axial load	14258	0.83	405.8	35	1782	130	Rocking

The net area was calculated by finding the average area that resists in-plane shear for each wall, as shown in equation 4-3.

$$\textbf{net area} = \frac{\Sigma(\mathbf{n_1} * \mathbf{GA} * \boldsymbol{n_{b1}} + \mathbf{n_2} * \mathbf{GA} * \boldsymbol{n_{b2}}) * \boldsymbol{C_b}}{\Sigma \boldsymbol{C_b}} \quad (4\text{-}3)$$

where n_1 is the net area as described in the materials section for ungrouted blocks, n_2 is the net area of grouted blocks, GA is the gross area of the block, n_{b1} is the number of ungrouted blocks, n_{b2} is the number of grouted blocks, and C_b is the total number of courses built in that grouting configuration.

The ultimate shear stress was calculated using equation 4-4.

$$\boldsymbol{S} = \frac{\boldsymbol{F}}{\boldsymbol{A}} \quad (4\text{-}4)$$

where S is the ultimate shear stress, F is the max load, and A is the net area.

The ultimate shear strength was calculated using equation 4-5.

$$\boldsymbol{S_s} = \frac{\boldsymbol{F}}{\boldsymbol{d}} \quad (4\text{-}5)$$

where S_s is the ultimate shear strength, F is the max load, and d is the depth in the shear direction, i.e., eight ft.

The shear modulus was determined in same manner as described in Chapter 3. On wall four, string pot four was bumped. If that shear modulus is ignored, the average shear modulus was 128 ksi, which was similar to the shear modulus calculated from the diagonal tension test results; however, the coefficient of variation is only 0.06.

Displacement can be attributed to all four failure modes; however, the finite element model that was used is unable to account for sliding. To eliminate sliding from the displacement,

the displacement was calculated as the difference between the top lateral displacement of the wall and the lateral displacement at the bottom of the wall, or the difference between string pot one and two for monotonic loading and the difference between string pot one and two for pushing of the wall and the difference between string pot ten and 11 for pulling of the wall in cyclic loading. This is shown in equation 4-6.

$$\Delta = \Delta \boldsymbol{h} - \Delta \boldsymbol{h_f} \tag{4-6}$$

where Δ is the deflection, Δh was the horizontal displacement at the top of the wall and Δh_f was the horizontal displacement at the bottom of the wall. The maximum displacement was taken when there was a drop of 20% from peak load.

4.8.1 Wall 1

Wall 1 was ungrouted with minor cracking on part of the web of one block as shown in Figure 4-7. This crack was most likely caused by shrinkage during the manufacturing of the block and was not considered to be a structural problem. At 2,080 lbs. a sudden failure between the bottom two courses occurred as shown in Figure 4-10 b. The wall then began to lift up and separate from these courses. As the only failure that occurred was between the two courses this wall was tested again but to insure the problem occurred elsewhere four steel plates were bolted to the face of the wall between the two courses. A similar sudden failure occurred again at 2,358 lbs. but just slightly above the steel plates as shown in Figure 4-11 a and b. Figure 4-8 shows the load vs deflection curve for the first test and Figure 4-9 shows the load vs deflection curve for the second test. For both cases, the flat part of the curve is representative of the actuator lifting up the rest of the wall and not due to any ductility in the walls themselves. Figure 4-10 shows pictures of the wall after the first test and Figure 4-11 shows pictures of the wall after the second

time testing. In Figure 4-10 and 4-11 the horizontal crack associated with flexural failure can be seen, and toe crushing at the corner can also be seen.

Figure 4-7 Cracking in web prior to testing.

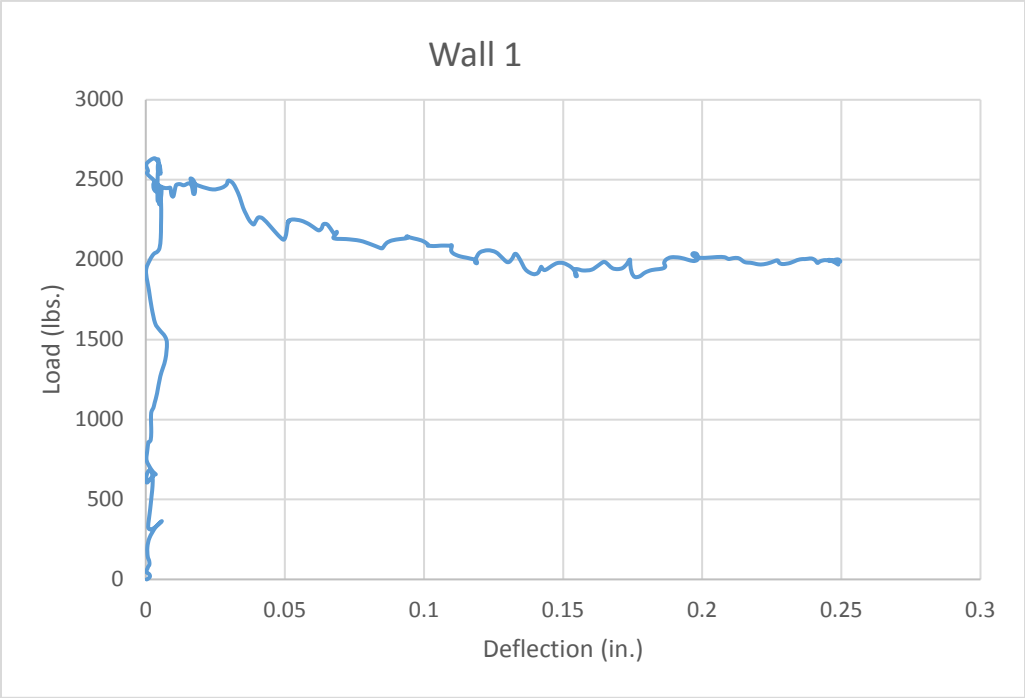

Figure 4-8 Load-deflection curve for Wall 1.

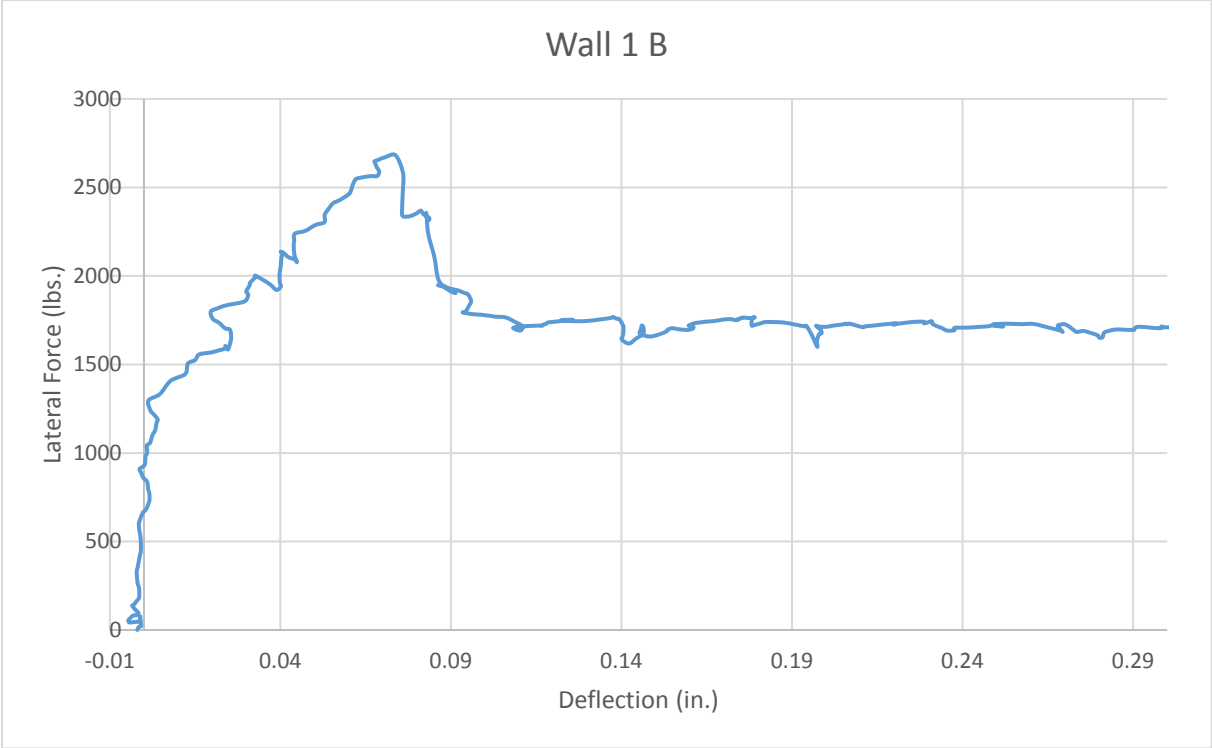

Figure 4-9 Load-deflection curve for wall 1 test 2.

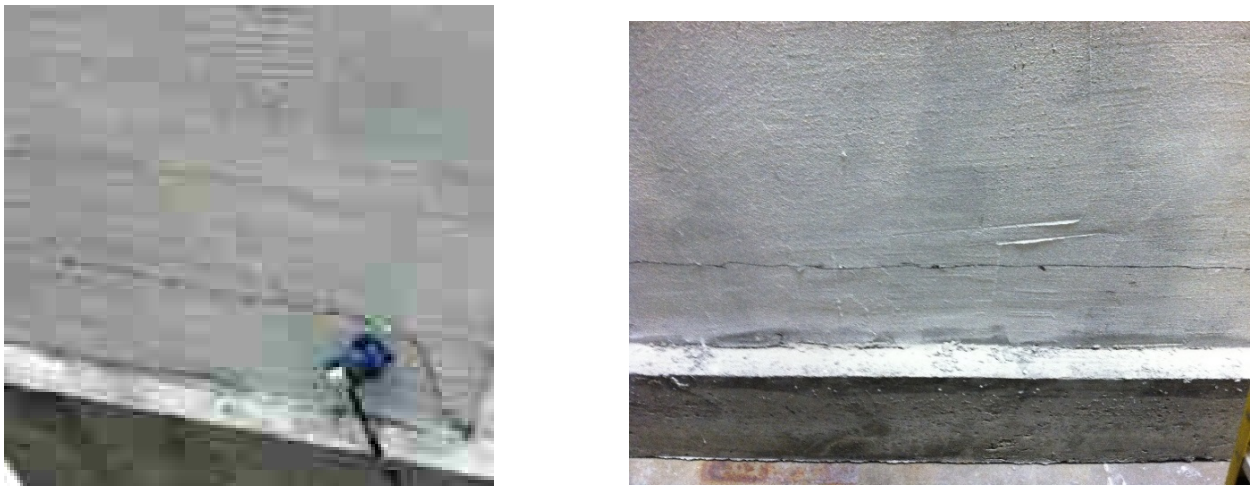

(a) Toe crushing and horizontal crack. **(b) horizontal crack.**

Figure 4-10 Pictures of wall 1 after 1st test.

(a) Failure around steel plate. **(b) Horizontal crack and toe crushing.**

Figure 4-11 Pictures of wall 1 after test 2.

4.8.2 Wall 2

Wall 2 was ungrouted with no apparent defects. At around 2,000 lbs. cracking noises could be heard but no visible damage was observed. At 2,809 lbs. failure occurred, and similar to wall 1, a large crack appeared between the bottom two courses as shown in Figure 4-14 a. As the actuator continued to push, the upper segment of the wall lifted up from the bottom course and initial signs of rocking were observed. Also, similar to wall 1, this wall was tested again by bolting steel plates between the bottom two courses. On the second test, at around 1,500 lbs., cracks formed just above the steel plate. Final failure occurred at 2,582 lbs. At this point the rest of the wall started to lift up from the bottom courses. Figure 4-12 and Figure 4-13 show the load vs deflection curve for test one and test two respectively. The flat parts of the graph after

max load are considered to be the actuator lifting the upper segment of the wall. Figure 4-14 and Figure 4-15 show pictures of the failure of the wall after the 1st and 2nd test, respectively.

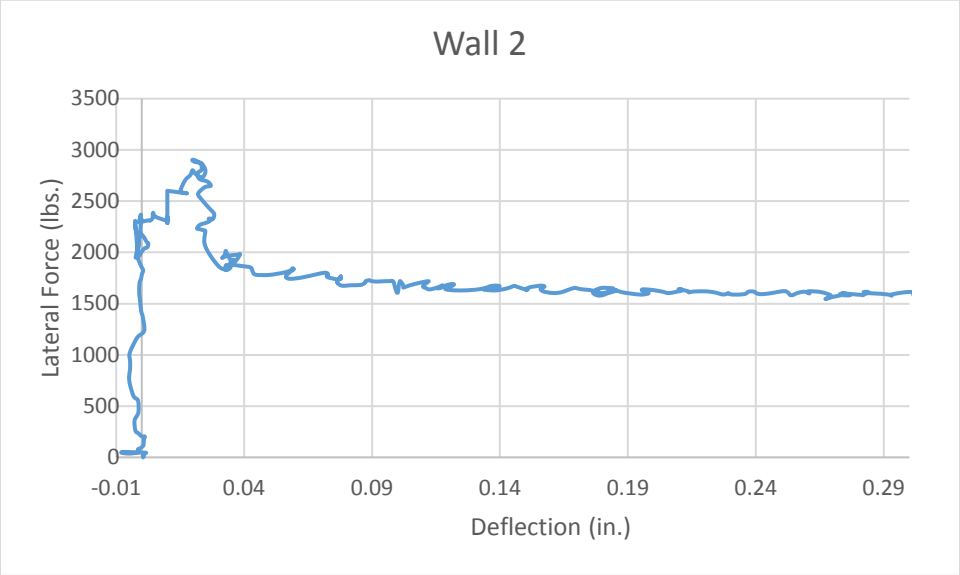

Figure 4-12 Load-deflection curve for wall 2.

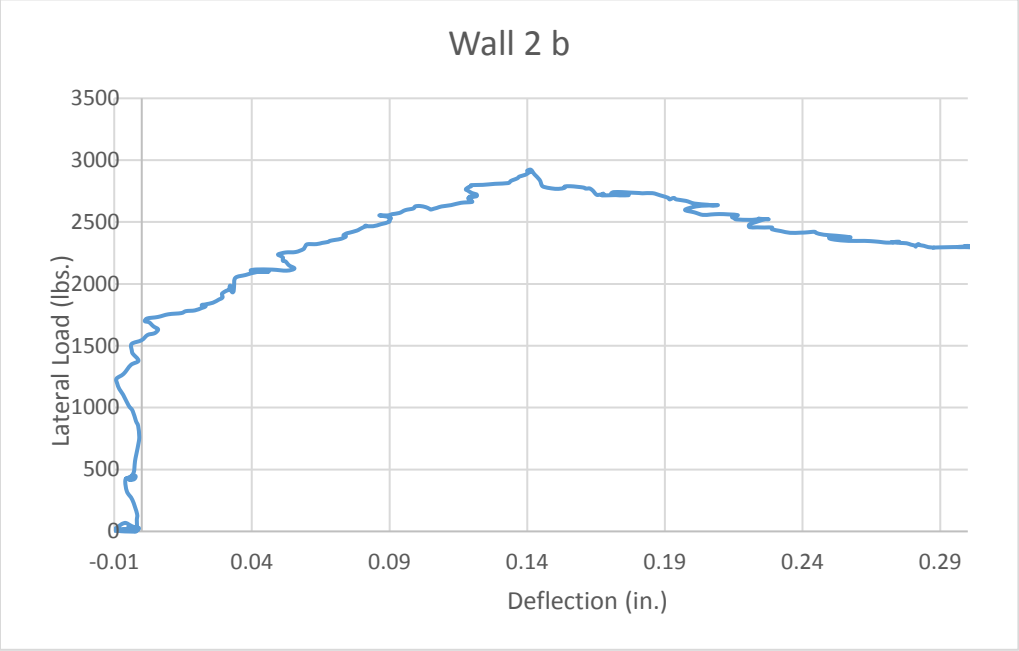

Figure 4-13 Load-deflection curve for wall 2 test 2.

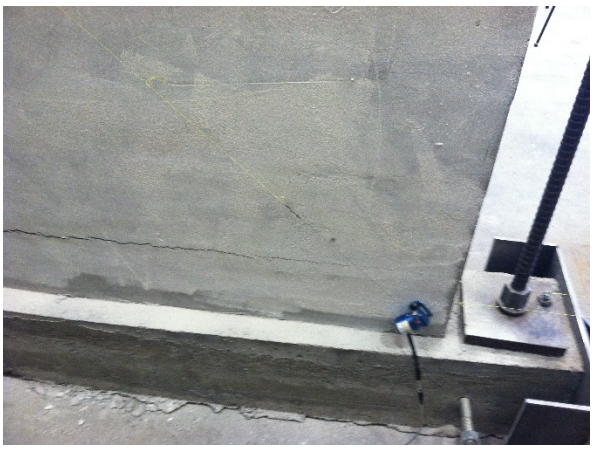

(a) Horizontal crack close to actuator. **(b) Horizontal crack on far side of wall.**

Figure 4-14 Pictures of failure in wall 2.

(a) Horizontal crack above steel plate. **(b) Step down of horizontal crack to existing crack.**

Figure 4-15 Pictures of failure in wall 2 test 2.

4.8.3 Wall 3

Wall 3 was grouted every four ft. vertically and every four ft. horizontally. Before testing, a hairline crack through the surface coating was observed above the horizontal grout layer six courses from the bottom of the wall. This crack was considered to be due to shrinkage and not considered a structural problem. At 6,000 lbs. the wall started to lift slightly on the side closest to the actuator near the footing-to-wall connection as shown in Figure 4-17 a. At 10,000 lbs., cracking noises were heard and minor cracks appeared on the surface. At about 13,000 lbs., the outside cell webs cracked as shown in Figure 4-17 c and large diagonal cracks, as shown in Figure 4-17 b, began to form going from the top corner near the actuator to the bottom of the opposite side of the wall. The load continued to increase to 14,468 lbs., when the diagonal crack widened and the wall was unable to continue resist such a high load. The displacement continued to increase slightly as the load decreased. Figure 4-16 shows the load vs displacement for wall three. Figure 4-17 shows pictures of the wall after failure. As shown in Figure 4-17 the wall failed predominately by shear. However, uplift as well as some signs of toe crushing were observed.

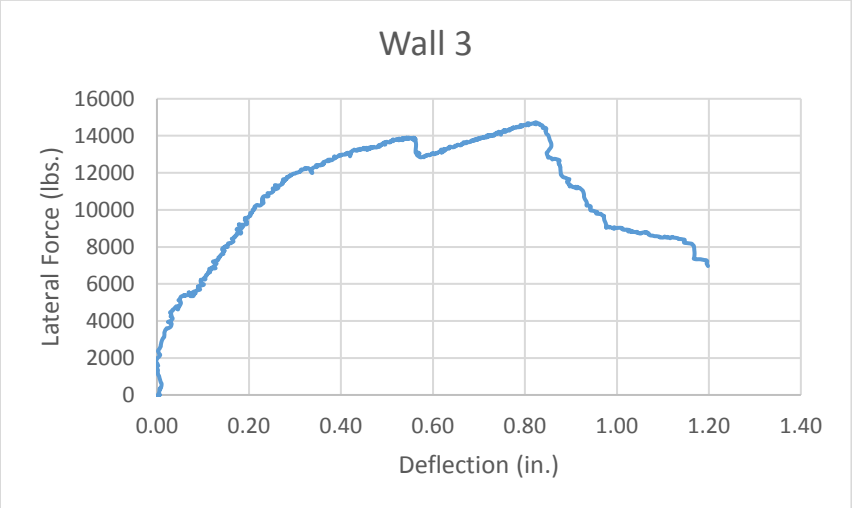

Figure 4-16 Load-displacement curve for wall 3.

(a) Uplift of wall. **(b) Diagonal crack.** **(c) Cracks through webs.**

Figure 4-17 Failure of wall 3.

4.8.4 Wall 4

Wall 4 was grouted every four ft. vertically and every four ft. horizontally, and no visible defects were noticed prior to testing. At around 2,000 lbs., cracking noises could be heard, but with no visible damage was observed. At around 7,000 lbs., the wall began to lift from the footing as shown in Figure 4-19 b. Around 10,000 lbs., a horizontal cracks started to form on the side of the wall closest to the actuator at the third course and sixth course from the bottom of the wall. At around 12,000 lbs., the wall began to experience a large uplift and diagonal shear cracks started to form at the bottom of the wall farthest away from the actuator as shown in Figure 4-19 c. Also, at this load, the outside cell webs started to crack as shown in Figure 4-19 a. Load continued to increase to 15,685 lbs. when a large pop was heard and the wall experienced severe lifting. Later examination showed that the dowel slipped from the grout in the bottom of the wall. After the bond failure of the dowel, the wall started to slide on the footing. Figure 4-18 shows the load displacement curve for wall four. Figure 4-19 shows pictures of the failure.

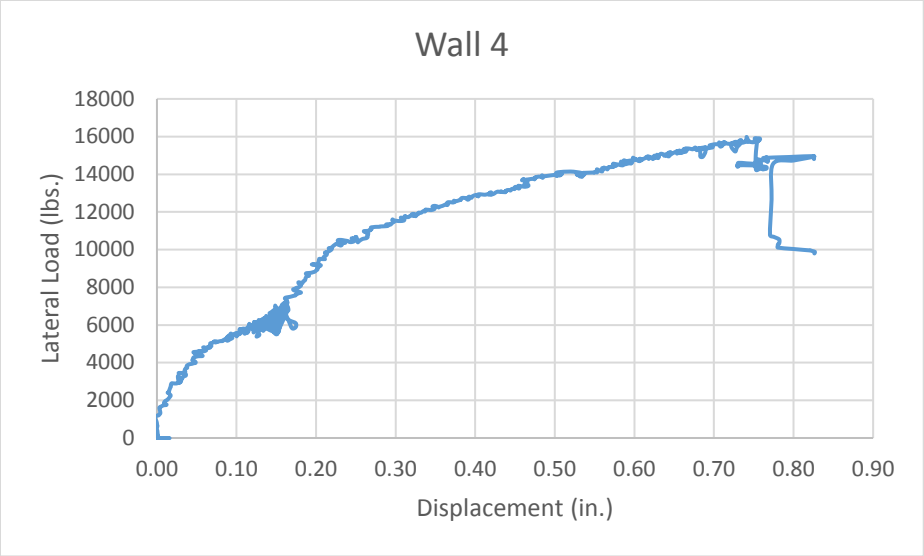

Figure 4-18 Load-displacement curve for wall 4.

(a) Cracking of outside webs. **(b) Uplift of wall.** **(c) Diagonal cracks.**

Figure 4-19 Failure of wall 4.

4.8.5 Wall 5

Wall 5 was grouted every four ft. horizontally and every two ft. vertically, and no apparent defects were observed prior to testing. At around 5,000 lbs., cracking noises could be heard but no visible damage was observed. At around 10,000 lbs., hairline cracks started to appear on the face of the wall in a diagonal direction as shown in Figure 4-21 b. At 16,000 lbs.,

small cracks on the outside cell webs appeared but the webs did not break, and the wall began to experience uplift as shown in Figure 4-21 a. Cracks continued to appear in a shear pattern until failure at 16,945 lbs. Close to the end of the test, a large popping sound was heard and the wall uplifted several inches from the footing. Later investigation showed that the dowel had slipped as shown in Figure 4-21 c. The load vs displacement graph is shown in Figure 4-20. Figure 4-21 shows pictures of the failure in the wall, which show that cracking only occurred in ungrouted blocks.

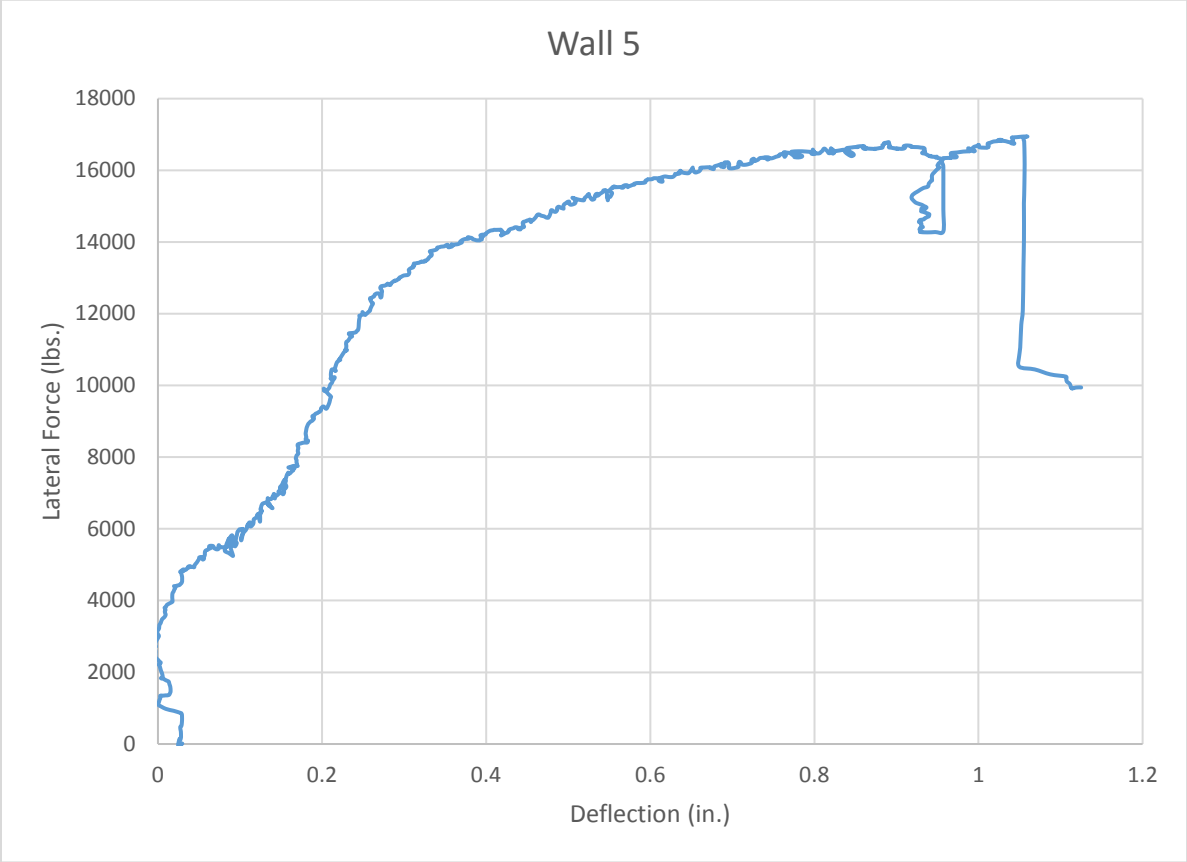

Figure 4-20 Load-deflection curve for wall 5.

(a) Uplift of wall. **(b) Typical diagonal cracks.** **(c) Pullout of dowel from grout.**

Figure 4-21 Failure in wall 5.

4.8.6 Wall 6

Wall 6 was grouted every four ft. horizontally and every two ft. vertically. Before testing, hairline cracks due to shrinkage were noticed between the 6th and 7th course. Around 6,000 lbs., the webs of the outside cells cracked severely as shown in Figure 4-23 c, and cracking noises could be heard. Around 13,000 lbs., diagonal cracks started to become visible on the face of the wall as shown in Figure 4-23 a. More diagonal cracks continued to appear until around 17,000 lbs. when some of them started to widen and the wall experienced slight uplift. The load then continued to increase but no further uplift was observed. The diagonal cracks continued to widen. The ultimate load was reached at 22,848 lbs. when two major cracks, eight courses from the bottom on the actuator side and at the top course in the middle of the wall, widened significantly as shown in Figure 4-23 b. The wall continued to resist some load after the cracks widened but load started to decrease until failure occurred around 12,000 lbs. All cracks were between grouted cells until failure, when the cracks propagated through the grouted cells. Figure

4-22 shows the load vs deflection curve for wall six and Figure 4-23 shows pictures after the wall had failed.

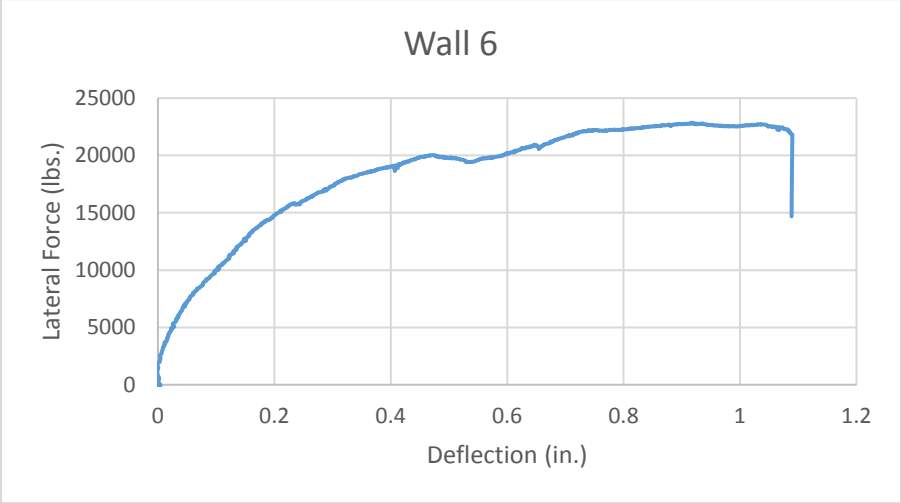

Figure 4-22 Load-displacement graph for wall 6.

(a) Diagonal cracks. **(b) Large shear crack opening.** **(c) Cracking of outside web.**

Figure 4-23 Failure in wall 6.

4.8.7 Wall 7

Wall 7 was grouted every four ft. vertically and every four ft. horizontally. In addition, a thin layer of mortar was placed between each course. No visible damage was observed prior to

testing. Load continued to increase during the test until around 9,000 lbs., when cracking noises could be heard but no visible damage was observed. At 10,000 lbs., hairline cracks were visible throughout the wall as shown in Figure 4-25 b. The wall reached ultimate load at 12,900 lbs. when a sudden crack opened along the top course close to the actuator and propagated diagonally to the bottom far side of the wall as shown in Figure 4-25 a. Failure occurred around 7,000 lbs. when the widening of the cracks continued and the cracks propagated through the grouted cells. Figure 4-24 shows the load vs deflection graph for wall seven and Figure 4-25 shows pictures of the failure in the wall. Wall seven did not experience crack of the webs of the outside cell as previous walls had as shown in Figure 4-25 c. It is believed that there was a problem with data collection at the beginning of the test and for that reason there is little to no deflection until around 6,000 lbs. in the load displacement graph.

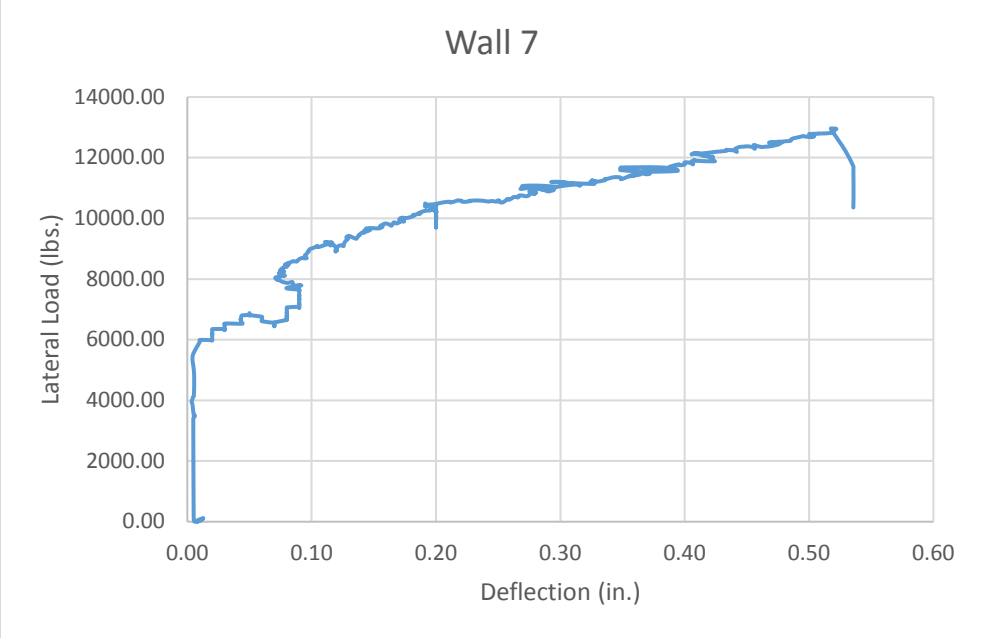

Figure 4-24 Load-displacement curve for wall 7.

(a) Opening in top course. **(b) Typical diagonal cracks.** **(c) Lack of cracks in webs.**

Figure 4-25 Failure in wall 7.

4.8.8 Wall 8

Wall 8 was also grouted every four ft. vertically and every four ft. horizontally, and had a thin layer of mortar placed between each course. A hairline crack was noted between the 7th and 8th course due to shrinkage in the surface bond. Loading was applied until around 5,000 lbs. when cracking noises could be heard no visible damage was observed. Around 7,000 lbs., minor cracking was observed throughout the wall as shown in Figure 4-27 a and the wall began to experience uplift as shown in Figure 4-27 b. At 10,000 lbs., popping noises could be heard and more cracks became visible, but load continued to increase. At 12,000 lbs., a large pop was heard and the wall continued to experience uplift; however, load did continue to increase. Load continued to increase until 14,789 lbs. when failure occurred. At this load, the wall had experienced significant uplift. Figure 4-26 shows the load vs deflection curve for wall 8 and Figure 4-27 shows pictures of the failure in the wall. A vertical crack was observed that can be seen in Figure 4-27 c, which is most likely due to the pulling out of the dowel.

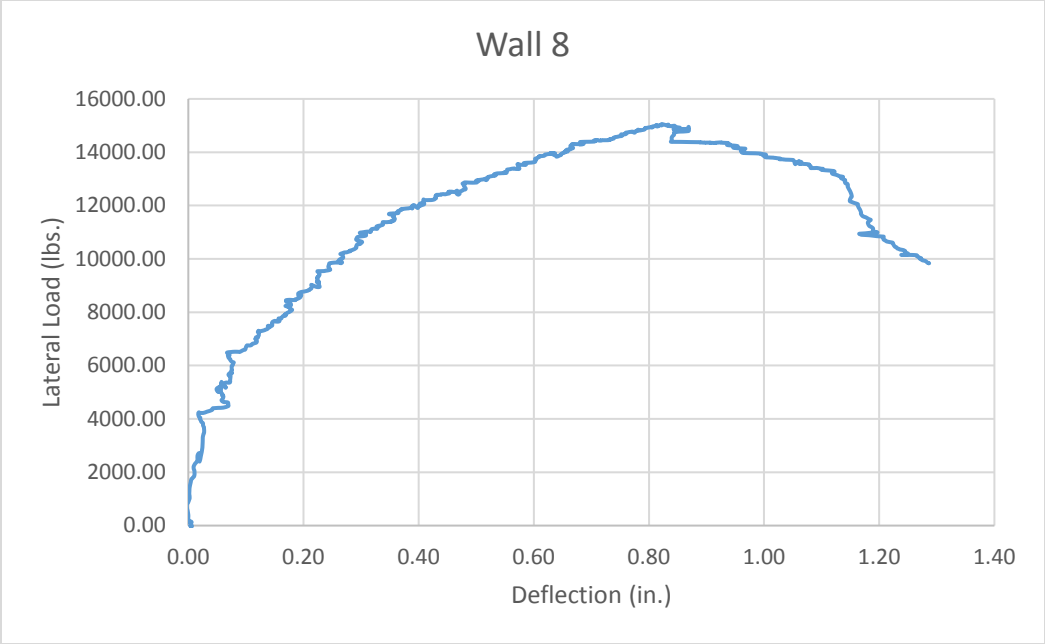

Figure 4-26 Load-displacement curve for wall 8.

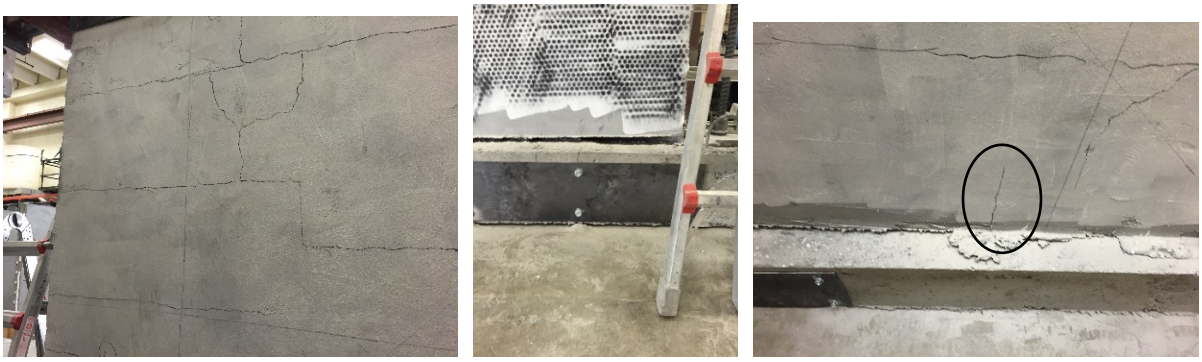

(a) Typical cracking. **(b) Uplift of wall.** **(c) Vertical crack at grout cell.**

Figure 4-27 Failure in wall 8.

4.8.9 Wall 9

Wall 9 was grouted every four ft. vertically and every four ft. horizontally, and a hairline crack was observed between the 6th and 7th course prior to testing. This wall was tested cyclically instead of monotonically. The actuator was set to repeat each cycle three times for a

given displacement. Unfortunately, due to limitations on the frame set up the wall was only pulled up to 0.7 inches. Throughout the test, horizontal cracks appeared first followed by vertical cracks connecting them to the horizontal cracks as shown in Figure 4-29 b. No cracks appeared in the top third of the wall as shown in Figure 4-29 c. This is believed to be due to the damage of the connection between the footing and wall as shown in Figure 4-29 a. The damage also resulted in the wall sliding during the end of the testing. Due to an input error, the loading protocol was not fully run and the wall did not fail. The wall was then pushed until failure in a monotonic manner. Figure 4-28 shows the load vs deflection curve for wall nine. The curves show that the monotonic pushover had just a slightly larger displacement when failure occurred than that of the cyclic testing. Figure 4-29 shows pictures of the failure in the wall.

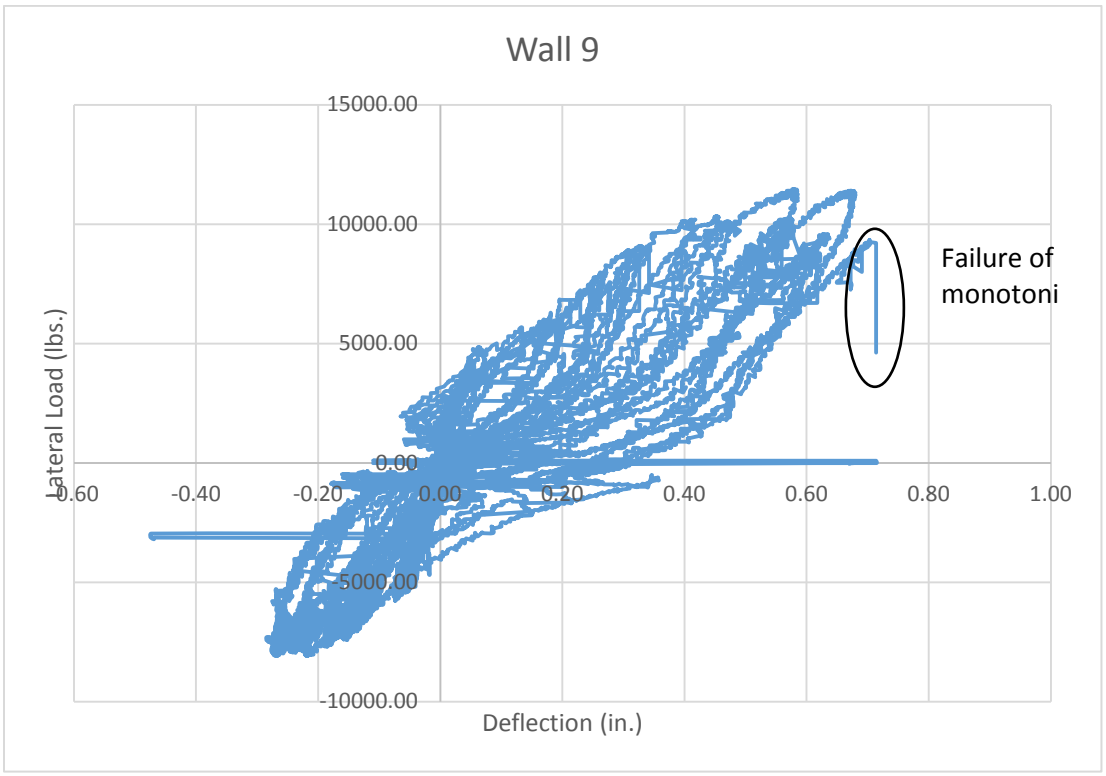

Figure 4-28 Load-displacement curve for wall 9.

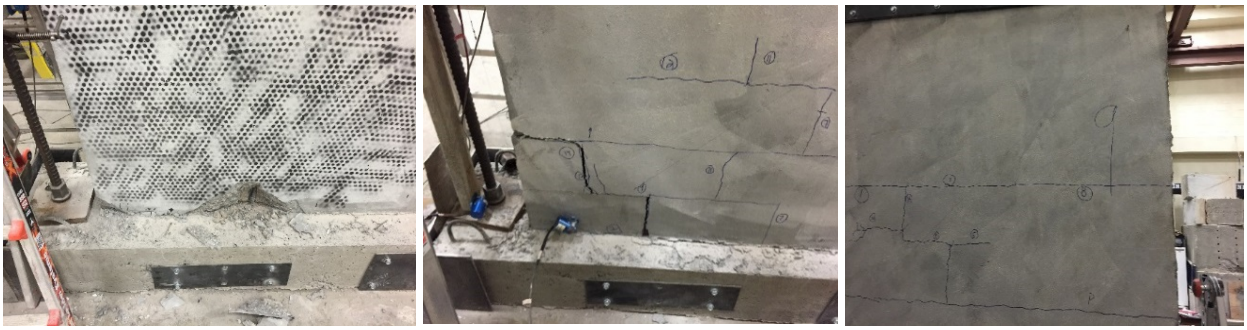

(a) Failure at connection. **(b) Diagonal cracking.** **(c) Lack of cracking in top of wall.**

Figure 4-29 Failure in wall 9.

4.8.10 Wall 10

Wall 10 was grouted every four ft. vertically and every four ft. horizontally, and a hairline crack was noted between the 6th and 7th course prior to testing. This wall was also tested cyclically. The peak displacements used for this test were: 0.05, 0.1, 0.15, 0.2, 0.25, 0.4, 0.5, 0.6, 0.8, 1, 1.2, and 1.4 inches. Unfortunately, due to limitations of the laboratory for frame setup the wall was only able to be pulled up to 0.7 inches. Once the max displacement for pulling was reached the test would increase the displacement for pushing but would maintain the maximum displacement for pulling. Similar to the previous test, cracks would appear horizontally, between the courses, and then vertical cracks would appear connecting the horizontal cracks as shown in Figure 4-31 a. However, in this test, cracks appeared over the entire wall and the connection between the wall and footing did not fail. Failure occurred due to a diagonal crack that appeared at the top of course of the wall and propagated downward to the bottom opposite corner. Figure 4-30 shows the load vs deflection of the wall 10 and Figure 4-31 shows pictures of the failure in the wall.

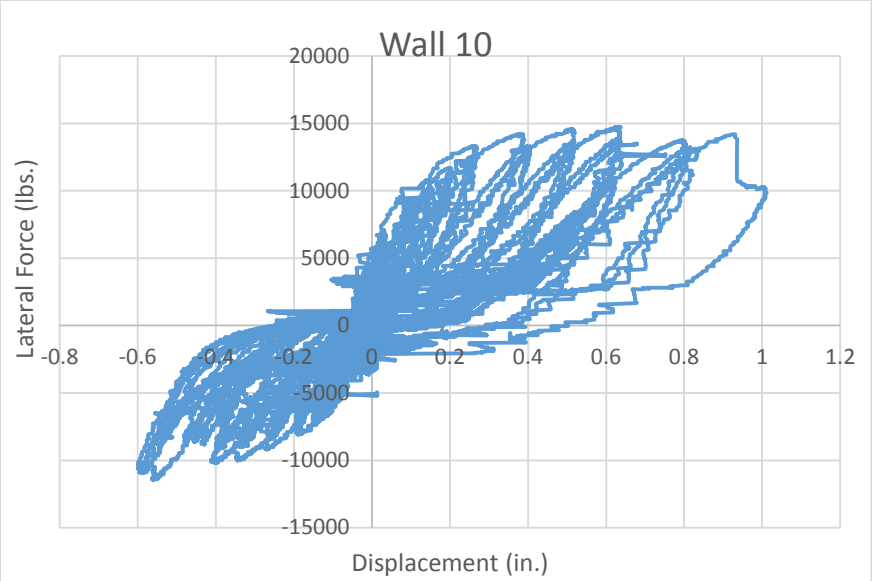

Figure 4-30 Load-displacement curve for wall 10.

(a) Diagonal cracking. **(b) Cracking in web.** **(c) Crushing in bottom of wall.**

Figure 4-31 Failure in wall 10.

4.8.11 Wall 11

Wall 11 was reinforced in the four ft. by four ft. pattern. In addition, this wall was subjected to an axial load. The load was applied as a dead weight. A platform was manufactured and installed above the testing frame and a weight of 15,782 lbs. was placed on the platform. Figure 4-32 shows the axial load setup.

Figure 4-32 Crane counterweight on top of platform above testing frame.

Prior to testing, a hairline crack due to shrinkage of the surface coating was visible between the 6th and 7th course. At around 7,000 lbs., the outside cell webs cracked as shown in Figure 4-34 c. At around 10,000 lbs., a pop was heard and the wall began to experience uplift as shown in Figure 4-34 b. After this load, cracks started to appear at the far side from the actuator at the bottom as shown in Figure 4-34 a. The cracks continued to widen until the load reached about 15,000 lbs. At this load, cracking noises could be heard and cracks appeared throughout the face of the wall. The displacement continued to increase though the load was almost constant. The wall reached its capacity of 20,235 lbs. The cracks at the bottom corner of the wall had widened significantly. The load vs deflection graph for Wall 11is shown in Figure 4-33 and Figure 4-34 shows pictures of the failure of the wall.

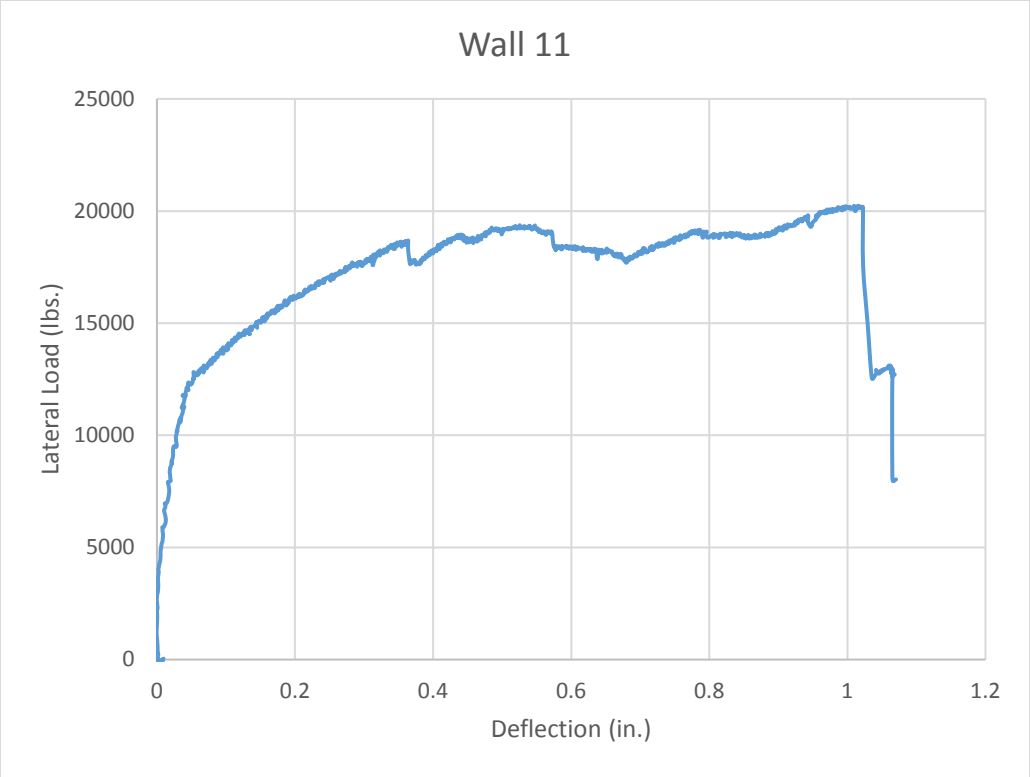

Figure 4-33 Load-displacement curve for wall 11.

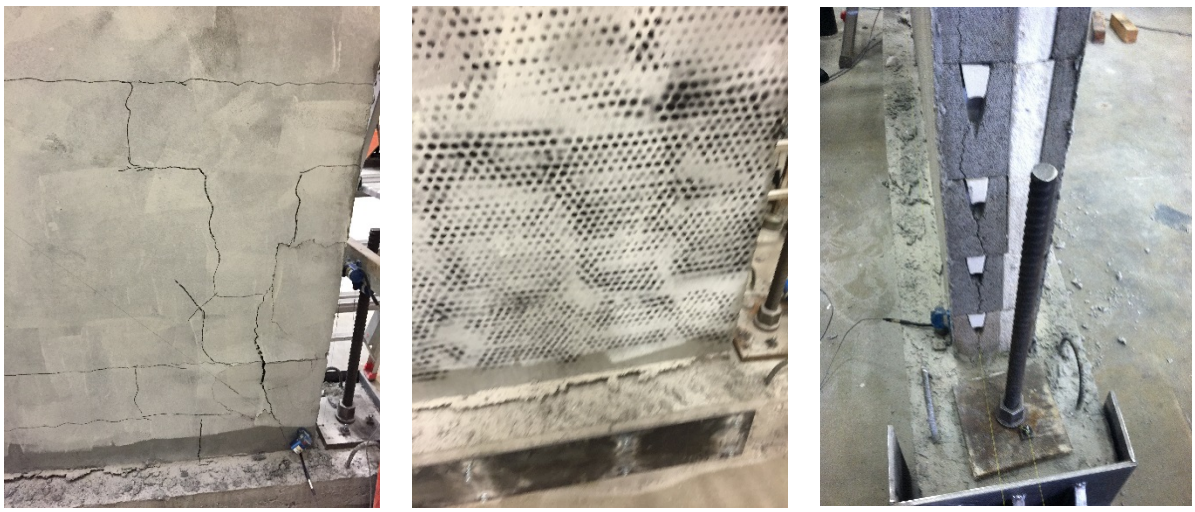

(a) Toe crushing. **(b) Wall uplift.** **(c) Cracking in webs.**

Figure 4-34 Failure in wall 11.

4.8.12 Wall 12

Wall 12 was also grouted every four ft. vertically and every four ft. horizontally, and was also subjected to an axial load. No apparent damage was detected prior to testing. At around 6,000 lbs., the outside webs of the wall cracked as shown in Figure 4-36 c. At 7,000 lbs., the wall began experience uplift as shown in Figure 4-36 a, and cracking started to become visible on the face of the wall. The wall continued to experience uplift with minor cracking appearing until the ultimate load of 14,257 lbs. was reached. At that load, a large popping sound was heard and the wall rotated significantly-the uplift was several inches and toe crushing was seen in the far side of the wall as shown in Figure 4-36b. Figure 4-35 shows the load vs deflection for wall 12 and Figure 4-36 shows pictures of the failures of the wall.

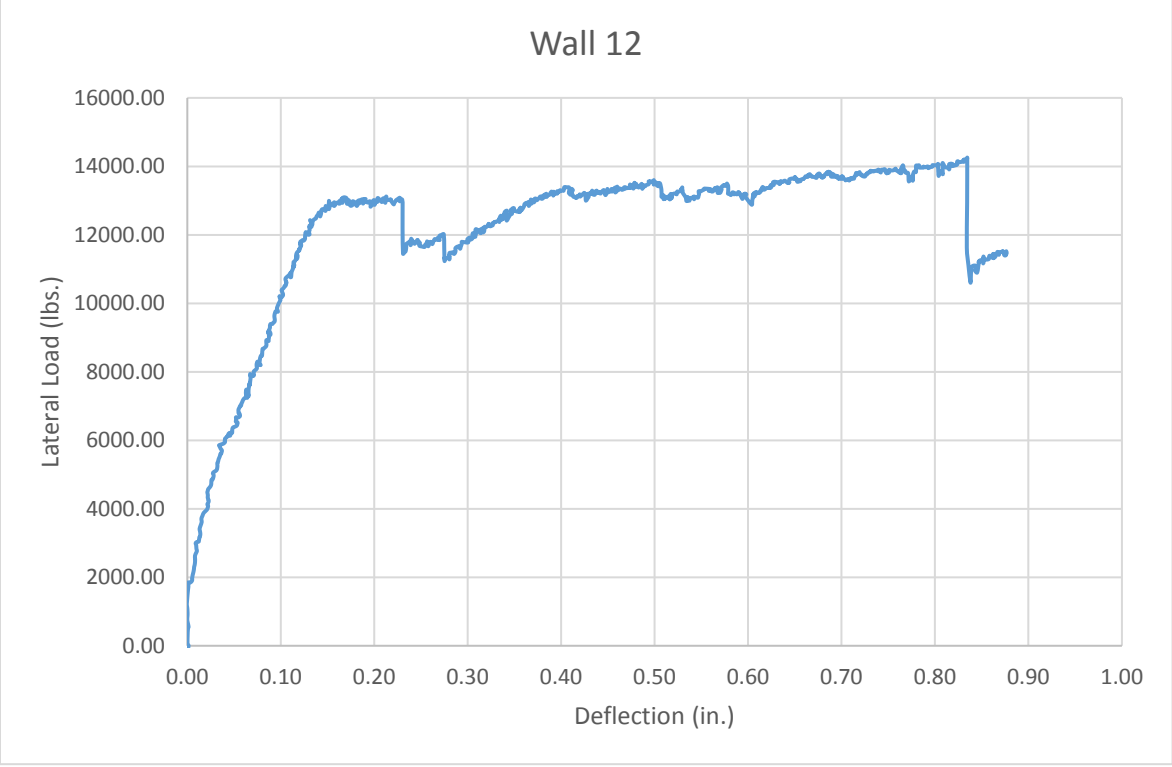

Figure 4-35 Load-displacement curve for wall 12.

(a) Wall uplift.

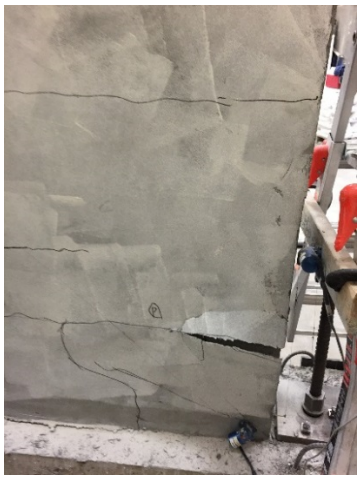

(b) Toe crushing.

(c) Cracks in outer webs.

Figure 4-36 Failure in wall 12.

4.9 Predictive Models

The results of the in-plane shear tests were compared to the results obtained from current design equations. There are three design methods that apply to masonry, the allowable stress design, the strength design, and the empirical design. Currently, dry-stack can only be designed using the empirical design method, however all three methods were used in the comparison. In addition to these design equations, several equations were developed and evaluated by the researcher.

4.9.1 Allowable Stress Design

The goal of the allowable stress design method is to ensure that service loads do not exceed the elastic limit. Currently, a factor of safety of 6.5 is required by code for unreinforced masonry and factor of safety of 2.5 is required for reinforced masonry meet the goal of this method. While using the allowable stress design method the reinforced masonry design

equations were utilized. The allowable shear stress, F_v, is calculated using equations 4-7 to 4-10 (ACI 2013).

$$\boldsymbol{F_v = (F_{vm} + F_{vs})\gamma_g} \tag{4-7}$$

$$\boldsymbol{F_v \leq \left(2\sqrt{f'_m}\right)\gamma_g} \tag{4-8}$$

$$\boldsymbol{F_{vm} = \frac{1}{4}\left(\left(4.0 - 1.75\left(\frac{M}{Vd_v}\right)\right)\sqrt{f'_m}\right) + 0.25\frac{P}{A_n}} \tag{4-9}$$

$$\boldsymbol{F_{vs} = 0.5\left(\frac{A_v F_s d_v}{A_{nv} s}\right)} \tag{4-10}$$

where F_{vm} is the allowable shear stress for masonry, F_{vs} is the allowable shear stress for steel, γ_g is equal to 0.75 if the walls are partially grouted and 1.0 if fully grouted, f'_m is the compressive strength of the masonry, M is the overturning moment, V is the shear force, d_v is the shear depth of the wall, P is the axial load on the wall, A_n is the net area of the wall, A_v is the area of shear reinforcement, F_s is the allowable steel stress, and s is the spacing between shear reinforcement. An example calculation following the allowable stress design method is presented in Appendix B.

Results from the allowable stress design compared to experimental results are summarized in Table 4-8 and Figure 4-37. Though not all walls failed in shear, the results of the testing showed that there was little difference in wall capacity when the wall failed in shear compared to when the walls experienced other failure modes. In Figure 4-37 the line represents if the design values and experimental results were the same. Thus, values below the line are non-conservative and values above the line are conservative. As shown in Figure 4-37 and Table 4-8, the allowable stress design estimates the allowable stress of walls 1 and 2 quite well, however it is highly conservative when compared to the other walls. On average the allowable stress design

method calculated values that were 4.6 times less than what was observed in the experiments. This is similar to what is observed in traditional masonry (Brandow et al. 2015).

Table 4-8 Allowable Stress Design Comparison

Wall	Configuration	Ultimate Shear Stress (psi)	F_v (psi)	$F_{vmeasured}/F_v$
1	ungrouted	7	7	1.04
2	ungrouted	8	7	1.14
3	4'x4'	36	7	5.03
4	4'x4'	39	7	5.45
5	2'x4'	39	7	7.62
6	2'x4'	53	7	6.93
7	4'x4' thin mortar	32	7	4.42
8	4'x4' thin mortar	37	7	5.14
9	4'x4' cyclic loading	28	7	3.91
10	4'x4' cyclic loading	36	7	5.04
11	4'x4' axial load	50	8	6.01
12	4'x4' axial load	35	8	4.24
			Avg.	4.66

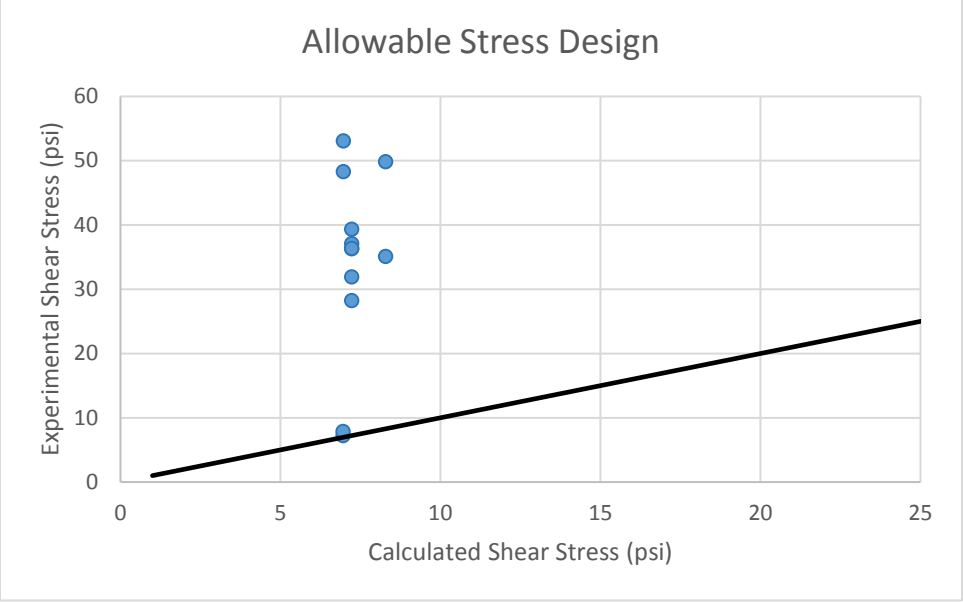

Figure 4-37 Allowable Stress Design comparison to experimental data.

4.9.2 Strength Design

The strength design method is a method where loads are increased by factors, commonly called load factors, and the capacity of the structural element is reduced by factors, commonly called strength reduction factors. The structural element is then designed to reach its ultimate capacity. For earthquake or seismic loads determined by ASCE 7, the load factor is 1.0 and that same load factor was used in this analysis. The reduction factor for shear in masonry is 0.8. In addition, for partially grouted masonry walls there is a further reduction, of 0.75. The calculated shear resistance, φV_n, is calculated using equations 4-11 to 4-14 (ACI 530, 2013).

$$\boldsymbol{\phi V_n = (V_{nm} + V_{ns})\gamma_g * \phi} \tag{4-11}$$

$$\boldsymbol{V_n \leq \left(4 * A_{nv}\sqrt{f'_m}\right)\gamma_g} \tag{4-12}$$

$$\boldsymbol{V_{nm} = \left(4.0 - 1.75\left(\frac{M_u}{V_u d_v}\right)\right)A_{nv}\sqrt{f'_m} + 0.25P_u} \tag{4-13}$$

$$\boldsymbol{V_{ns} = 0.5\left(\frac{A_v}{s}\right)f_y d_v} \tag{4-14}$$

where V_{nm} is the shear resistance from masonry, V_{ns} is the shear resistance from steel, M_u is the factored overturning moment, V_u is the factored shear force, P_u is the factored axial load on the wall, and F_y is the yield stress of steel. In the strength design method, bundled bars are not allowed to be used whereas they are in the allowable stress design method. Therefore, when calculations where done, it was considered that only 1 #4 bar was used instead of the 2 bars that were actually used in construction. An example calculation following the strength design method is presented in Appendix B.

The calculated and measured values are presented in Table 4-9 and Figure 4-38. In Figure 4-38 the line represents if values of the design equations were the same as the experimental results. Thus, values below the line are non-conservative. The results show that the strength design method is non-conservative, and on average calculated a capacity twice of what was observed. This indicates that this methodology should not be used for the design of dry-stack masonry walls.

4.9.3 Empirical Design

The empirical design method is a non-engineering design method and consequently highly conservative. Currently, the design of dry-stack masonry with surface bond is limited to the empirical design method (International 2012). The empirical design method, cannot be used for seismic design in categories C, D, E, or F. This limits dry-stack masonry to seismic

Table 4-9 Strength Design Comparison

Wall	Configuration	Ultimate Shear Resistance (kips)	ϕV_n (kips)	$V_{measured}/ \phi V_n$
1	ungrouted	3	20	0.13
2	ungrouted	3	20	0.14
3	4'x4'	15	27	0.54
4	4'x4'	16	27	0.58
5	2'x4'	17	29	0.80
6	2'x4'	23	29	0.72
7	4'x4' thin mortar	13	27	0.47
8	4'x4' thin mortar	15	27	0.55
9	4'x4' cyclic loading	12	27	0.42
10	4'x4' cyclic loading	15	27	0.53
11	4'x4' axial load	20	30	0.67
12	4'x4' axial load	14	30	0.47
			Avg	0.50

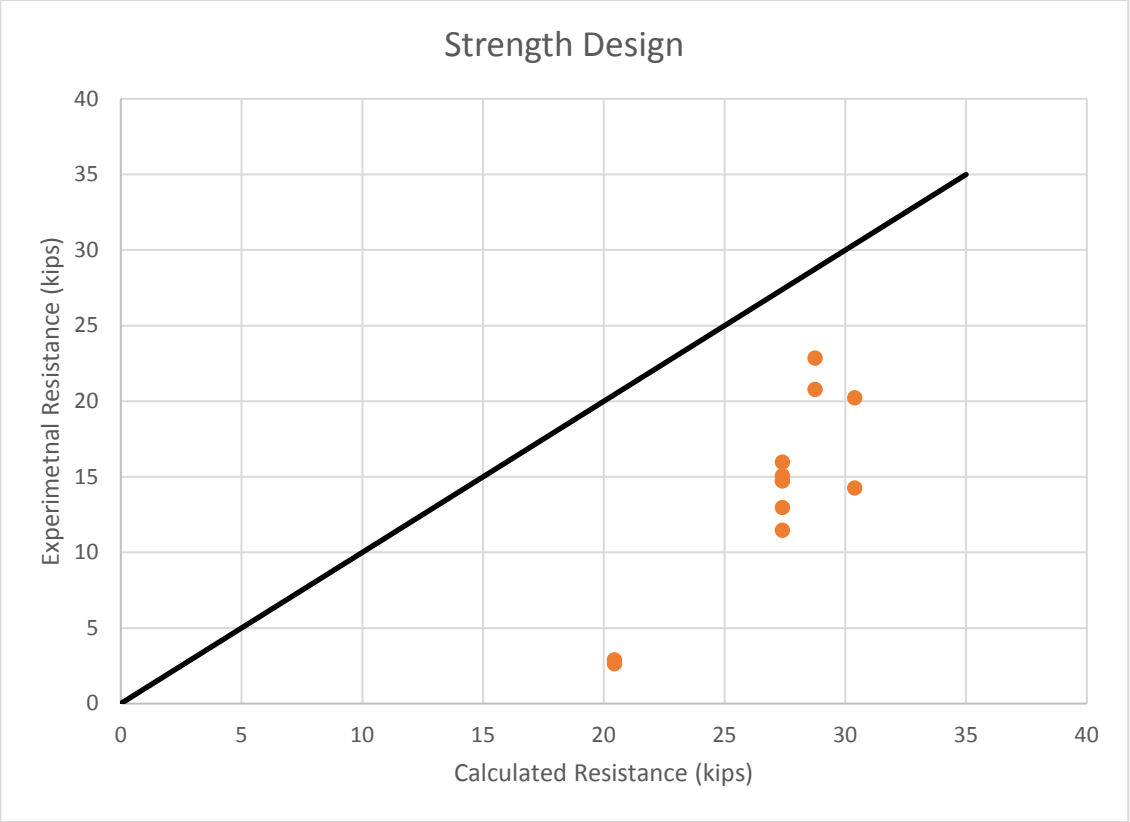

Figure 4-38 Strength Design comparison to experimental data.

categories A and B. In addition, restrictions are given on the allowable stress over the gross area of the wall. Currently, the shear stress is limited to 10 psi (International 2012).

Results from the empirical method and experimental are summarized in Table 4-10 and Figure 4-39. In Figure 4-39 the line represents if experimental results were the same as results calculated from the design equations. Thus, the values below the line are non-conservative and the values above the line are conservative. The results show that the empirical method is non-conservative for the unreinforced walls and highly conservative for the reinforced walls. On average, the empirical design method calculated a capacity almost 3.5 times less than the capacity observed.

Since the current methods are either highly conservative or non-conservative, three methods were developed to predict the capacity of dry-stack surface bonded masonry walls.

Table 4-10 Comparison of Empirical Method

Wall	Configuration	Ultimate Shear Stress (psi)	Fv (psi)	$F_{vmeasured}/F_v$
1	ungrouted	7	10.00	0.72
2	ungrouted	8	10.00	0.79
3	4'x4'	36	10.00	3.63
4	4'x4'	39	10.00	3.94
5	2'x4'	53	10.00	5.31
6	2'x4'	48	10.00	4.83
7	4'x4' thin mortar	32	10.00	3.19
8	4'x4' thin mortar	37	10.00	3.71
9	4'x4' cyclic loading	28	10.00	2.82
10	4'x4' cyclic loading	36	10.00	3.63
11	4'x4' axial load	50	10.00	4.99
12	4'x4' axial load	35	10.00	3.51
			Avg	3.42

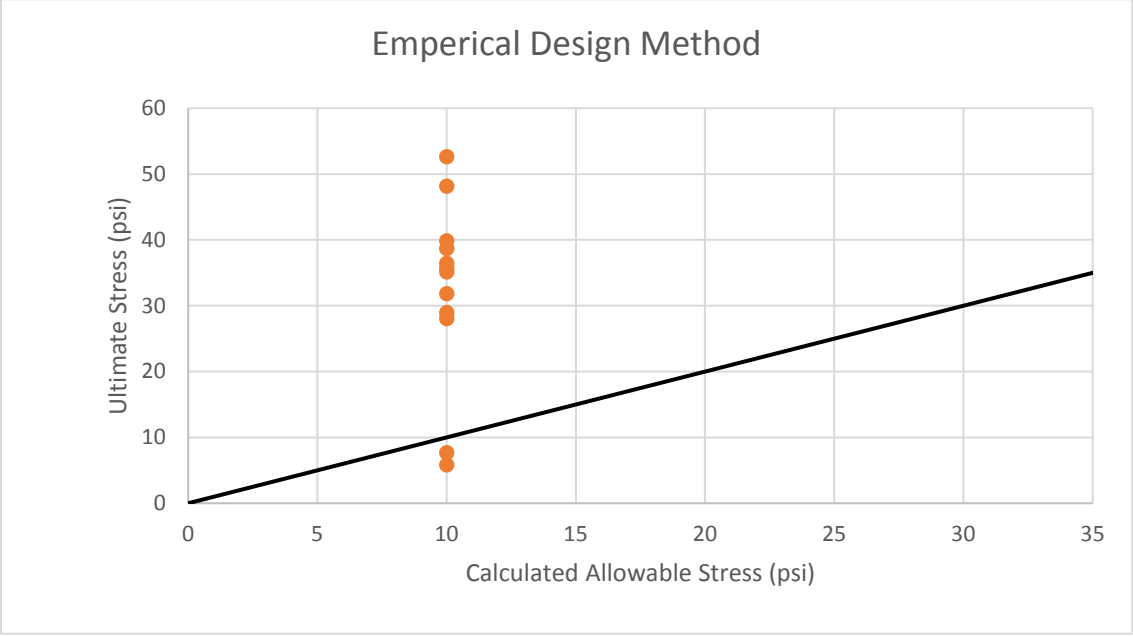

Figure 4-39 Empirical Method compared to experimental data.

4.9.4 Reduction Factor Method

The first method follows the strength design methodology but uses a larger reduction factor on the capacity of the wall, and the proposed reduction factor is 0.3.

Results are summarized in Table 4-11 and Figure 4-40. In Figure 4-40, the line represents if experimental capacities were the same as the capacities calculated by the design equations. Thus, values below the line are non-conservative, while all values above the line are conservative. Using this method the average capacity that was measured was 1.3 times what was calculated. This is a good fit; however, this method has a large reduction factor and still cannot accurately predict the strength of unreinforced walls.

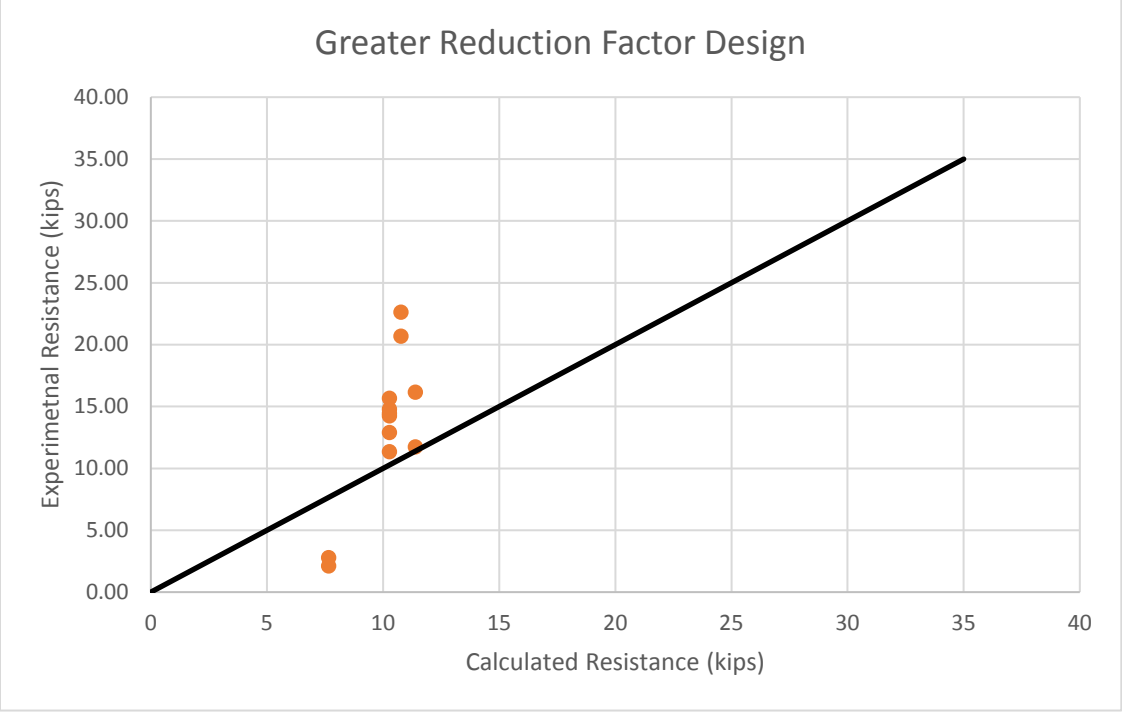

Figure 4-40 Comparison of Greater Reduction Factor Method to experimental data.

Table 4-11 Comparison of Greater Reduction Factor Method

Wall	Configuration	Ultimate Shear Resistance (kips)	ϕV_n (kips)	$V_{measured}/ \phi V_n$
1	ungrouted	3	8	0.35
2	ungrouted	3	8	0.38
3	4'x4'	15	10	1.43
4	4'x4'	16	10	1.56
5	2'x4'	17	11	1.57
6	2'x4'	23	11	2.12
7	4'x4' thin mortar	13	10	1.26
8	4'x4' thin mortar	15	10	1.47
9	4'x4' cyclic loading	11	10	1.12
10	4'x4' cyclic loading	15	10	1.44
11	4'x4' axial load	20	11	1.77
12	4'x4' axial load	14	11	1.25
			Avg.	1.31

4.9.5 Reduced Block Method

In this model the outside cell of the block is considered non-structural so it doesn't contribute to the shear resistance of the wall. This was assumed as most of the initial cracks were observed in the inner part of the block. This method uses the same design equations as the strength design method. In addition, a reduction factor of 0.5 is used. An example calculation following the reduced block method is present in Appendix B.

Results are summarized in Table 4-12 and Figure 4-41. In Figure 4-41, the line represents if experimental capacities were the same as the capacities calculated by the design equations. Thus, values below the line are non-conservative, while all values above the line are conservative. The measured results were 1.02 times what was calculated using this method. This is a very close approximation on average, and this model has an advantage in that there is a smaller reduction factor and less scatter around the calculated design. Unfortunately, the model still is non-conservative for ungrouted and unreinforced walls as well as some reinforced walls. Though the scatter is smaller, it is still prevalent.

Table 4-12 Reduced Block Method Comparison

Wall	Configuration	Proposed Net Area (in^2)	Ultimate Shear Resistance (kips)	ϕV_n (kips)	$V_{measured}$ / ϕV_n
1	ungrouted	250.8	3	8.72	0.30
2	ungrouted	250.8	3	8.72	0.33
3	4'x4'	291.3	15	13.13	1.12
4	4'x4'	291.3	16	13.13	1.22
5	2'x4'	316.6	17	14.01	1.21
6	2'x4'	316.6	23	14.01	1.63
7	4'x4' thin mortar	291.3	13	13.13	0.99
8	4'x4' thin mortar	291.3	15	13.13	1.15
9	4'x4' cyclic loading	291.3	11	13.13	0.87
10	4'x4' cyclic loading	291.3	15	13.13	1.12
11	4'x4' axial load	291.3	20	15.01	1.35
12	4'x4' axial load	291.3	14	15.01	0.95
				Avg.	1.02

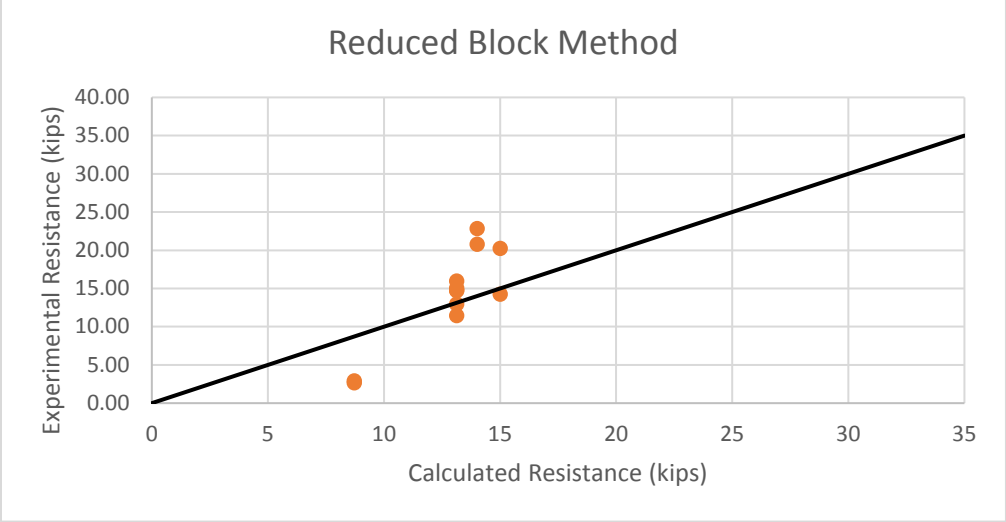

Figure 4-41 Reduced Block Method compared to experimental data.

4.9.6 Surface Bond Method

In this method, the strength design equations that are used in the MSJC Code are used for the steel, and the equations that were used for the block resistance are modified to account for the

surface coating instead of the block resistance. This change was made due to observations during testing. It was observed all failure occurred through the surface coating and little damage was observed in the blocks. In addition, a reduction factor of 0.8 is used and the bundled bars are accounted for. The equations used for this method are given in equations 4-15 to 4-18.

$$\boldsymbol{\phi V_n = (V_{nsb} + V_{ns} + V_{ng})\gamma_g * \phi} \quad (4\text{-}15)$$

$$\boldsymbol{V_{ng} = 2.25 A_{ng}\sqrt{f'_g}} \quad (4\text{-}16)$$

$$\boldsymbol{V_{nsb} = 2.25 A_{nsb}\sqrt{f'_{sb}} + 0.25 P_u} \quad (4\text{-}17)$$

$$\boldsymbol{V_{ns} = 0.5\left(\frac{A_v}{s}\right) f_y d_v} \quad (4\text{-}18)$$

where the variables are the same as outlined for equations 4-11 to 4-14, except that V_{nsb} is the nominal shear resistance from the surface bond, V_{ng} is the nominal shear resistance from the grout, A_{ng} is the net area of the grout, A_{nsb} is the net area of the surface bond, f'_g is the compressive strength of the grout, and f'_{sb} is the compressive strength of the surface bond. Appendix B shows sample calculations for this model.

Results are summarized in Table 4-13 and Figure 4-42. In Figure 4-42, the line represents if experimental capacities were the same as the capacities calculated by the design equations. Thus, values below the line are non-conservative, while all values above the line are conservative. As shown, this method reasonably predicts the strength of the unreinforced and ungrouted walls. Also, the method is conservative. Though some results are only slightly conservative, the corresponding walls failed due to the connection of the wall to the footing. If the connection did not fail, most likely this methodology would be a little more conservative. The measured shear capacity is 1.32 times the calculated capacity using this method.

Of all the design methodologies presented, the surface bond method was the most reasonable while still being conservative. For this reason, this methodology was chosen when designing the archetype walls for the pushover and time history analyses.

Table 4-13 Surface Bond Method Comparison

Wall	Configuration	Ultimate Shear Resistance (kips)	φV_n (kips)	$V_{measured} / \varphi V_n$
1	ungrouted	2.65	2.35	1.13
2	ungrouted	2.90	2.35	1.23
3	4'x4'	14.73	11.35	1.30
4	4'x4'	15.98	11.35	1.41
5	2'x4'	16.95	11.35	1.49
6	2'x4'	22.85	11.35	2.01
7	4'x4' thin mortar	12.96	11.35	1.14
8	4'x4' thin mortar	15.06	11.35	1.33
9	4'x4' cyclic loading	11.46	11.35	1.01
10	4'x4' cyclic loading	14.77	11.35	1.30
11	4'x4' axial load	20.23	14.17	1.43
12	4'x4' axial load	14.26	14.17	1.01
			Avg.	1.32

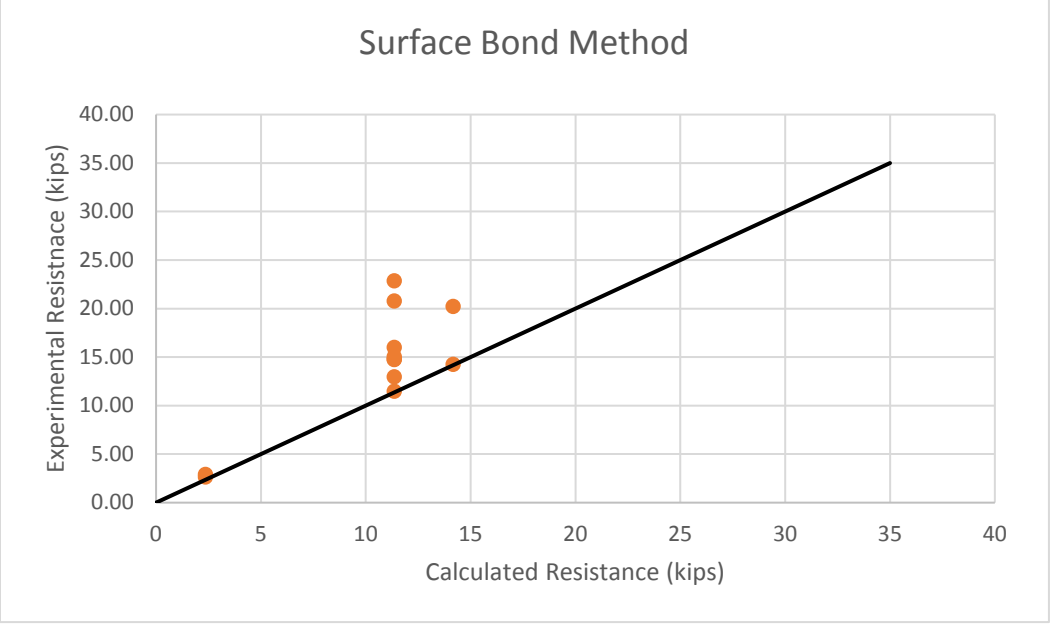

Figure 4-42 Comparison of Surface Bond Method to experimental data.

5 FINITE ELEMENT MODEL

A finite element model was developed using the program VecTor 2 (Computer 2011). This program was developed to model reinforced concrete structures using 2-dimensional finite element analysis. Since its development, it has expanded to model masonry, timber, and steel. The program combines modified compression field theory and the disturbed stress field model for reinforced concrete with the analytical capabilities of finite element analysis. To model the composite nature of concrete, changing material properties due to cracking, and shifting geometries and loadings, VecTor 2 uses an incremental load and iterative secant stiffness algorithm to generate a nonlinear solution.

This chapter gives background on the VecTor 2 program. It then explains the modified compression field theory and disturbed stress field model and how they are implemented in VecTor 2. An overview of how the finite element program is implemented is then given. Then, the elements chosen for the computer model are explained including the shape, size, boundary conditions, and the use of discrete reinforcement over smeared. The values and explanations for the materials properties are outlined. Finally, the models used for second order effects and material properties in the model are explained. Only the material models that were utilized are outlined here in. To be consistent throughout, the nomenclature of the VecTor 2 manual is used even when the original literature uses different terms. Additional information can be found in the relevant literature (Wong 2012)

5.1 Background

VecTor 2 is a nonlinear finite element program that was originally developed for the analysis of 2-dimensional reinforced concrete membrane structures. Experimental test results were used to corroborate the ability of the software to predict the load-deformation response for a range of reinforced concrete structures loaded monotonically, cyclically, and reverse cyclically (Wong 2002).

VecTor 2 is based on the modified compression field theory and the disturbed stress field model. These models are used to calculate the response of elements subjected to in-plane normal and shear stresses. After cracking, concrete is treated as an orthotropic material with smeared, rotation cracks. The nonlinear solution is calculated using incremental total load and an iterative secant stiffness algorithm.

Originally, the constitutive relationships of the modified compression field theory were used in VecTor 2, but later versions have utilized other constitutive models to account for second-order effects such as compression softening and tension stiffening. The later versions were also expanded to model hysteretic response, bond slip, and reinforcement slipping. The program has also been expanded to model different material types including masonry, timber, and steel.

The finite element models in VecTor 2 use a fine mesh of low-powered elements. This is used as reinforced concrete structures require a relatively fine mesh to model reinforcement and local crack patterns. The elements that are included in the program are a 3-node constant strain triangle, a 4-node plane stress rectangular element, and a 4-node quadrilateral element for modeling concrete with or without smeared reinforcement. Discrete reinforcement can be

modeled using a 2-node truss bar, and a 2-node link. A four-node contact element can be utilized for bond-slip mechanisms.

5.2 Modified Compression Field Theory

The Modified Compression Field Theory is used for determining the load-deformation response of reinforced concrete membrane elements subjected to shear and normal stresses. (Vecchio and Collins, 1986). This theory calculates the average local strains and stresses on the concrete and reinforcement, in addition to widths and orientation of cracks. The theory assumes that reinforcement and cracks are uniformly distributed; shear and normal stresses are uniformly applied; there is a unique stress state for each strain state; without considering strain history, the orientation of the principal strain and stress are the same; there is a perfect bond between reinforcement and concrete; the shear stresses in reinforcement are negligible; and there are independent constitutive relationships for concrete and reinforcement. The equilibrium equations are based on average stresses in the concrete and reinforcement, the compatibility relationships are based on the average strains of reinforcement and concrete, and the constitutive relationship is based on the results from testing of reinforced concrete panels (Vecchio and Collins, 1986).

5.2.1 Compatibility Relationships

The assumption of a perfect bond implies that the average strain in the concrete is the same as the average strain in the reinforcement. This relationship is expressed by equations 5-1 and 5-2.

$$\boldsymbol{\varepsilon_x = \varepsilon_{cx} = \varepsilon_{sx}} \tag{5-1}$$

$$\boldsymbol{\varepsilon_y = \varepsilon_{cy} = \varepsilon_{sy}} \tag{5-2}$$

where ε_x and ε_y are the strains in the x and y direction respectively, ε_{cx} is the average strain in the concrete in the x direction, ε_{sx} is the average strain in the reinforcement in the x direction, ε_{cy} is the average strain in the concrete in the y direction, and ε_{sy} is the strain in the reinforcement in the y direction.

Using the shear strain, γ_{xy}, and Mohr's Circle, the principal concrete tensile strain, ε_{c1}, and the average principal concrete compressive strain, ε_{c2}, are determined from equation 5-3.

$$\boldsymbol{\varepsilon_{c1}, \varepsilon_{c2} = \frac{1}{2}(\varepsilon_x + \varepsilon_y) \pm \frac{1}{2}\left((\varepsilon_x + \varepsilon_y)^2 + \gamma_{xy}{}^2\right)^{\frac{1}{2}}} \tag{5-3}$$

Mohr's circle is used to calculate the orientation of the average principal tensile strain axis, θ_ε, and the stress axis, θ_σ, with respect to the x-axis as given in equation 5-4.

$$\boldsymbol{\theta = \theta_\varepsilon = \theta_\sigma = \frac{1}{2} tan^{-1}\left(\frac{\gamma_{xy}}{\varepsilon_x - \varepsilon_y}\right)} \tag{5-4}$$

5.2.2 Equilibrium Relationships

The equilibrium relationship can be described by Figure 5-1 (Wong 2012). The normal stresses, σ_x and σ_y, are set equal to the concrete stresses, f_{cx} and f_{cy} and the reinforcement stresses, f_{sx} and f_{sy}. Assuming that the reinforcement does not have any dowel action, the applied shear stresses are equal to the average shear stress in the concrete, v_{cxy}. This leads to equations 5-5 to 5-7.

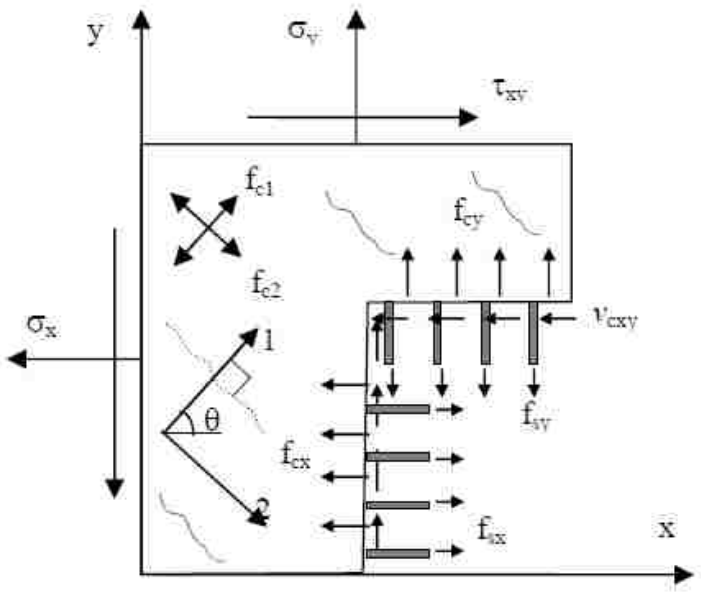

Figure 5-1 Diagram of reinforced concrete element average stresses (Wong et al. 2012).

$$\boldsymbol{\sigma_x = f_{cx} + \rho_{sx} f_{sx}} \quad (5\text{-}5)$$

$$\boldsymbol{\sigma_y = f_{cy} + \rho_{sy} f_{sy}} \quad (5\text{-}6)$$

$$\boldsymbol{\tau_{xy} = v_{cxy}} \quad (5\text{-}7)$$

where ρ_{sx} and ρ_{sy} are the reinforcement ratios in the x direction and y direction, respectively.

The relationship between average concrete stresses, f_{cx} and f_{cy}, to the average principal concrete tensile stress, f_{c1}, are determined using Mohr's Circle and the assumption that cracked concrete is orthotropic with respect to the principal stress direction. This relationship is described in equations 5-8 and 5-9.

$$\boldsymbol{f_{cx} = f_{c1} - v_{cxy} * cot(90 - \theta_\sigma)} \quad (5\text{-}8)$$

$$\boldsymbol{f_{cy} = f_{c1} - v_{cxy} * tan(90 - \theta_\sigma)} \quad (5\text{-}9)$$

5.2.3 Constitutive Relationships

The constitutive relationships were based on the results of tests conducted on 30 reinforced concrete panels that were 890x890x70 mm (Vecchio and Collins, 1986). The constitutive relationships relate the strains in the compatibility relationships with the stresses in the equilibrium relationships. The principal compressive stress, f_{c2}, is related to the principal compressive strain, ε_{c2}, by equation 5-10.

$$f_{c2} = \frac{f'_c\left(2\left(\frac{\varepsilon_{c2}}{\varepsilon_0}\right) - \left(\frac{\varepsilon_{c2}}{\varepsilon_0}\right)^2\right)}{0.8 - 0.34\left(\frac{\varepsilon_{c1}}{\varepsilon_0}\right)} \tag{5-10}$$

where f'_c is the peak compressive stress, ε_0 is the concrete cylinder strain, and ε_{c1} is the principal tensile strain. The denominator of equation 5-10 accounts for the decrease in strength and stiffness as the principal tensile strains increases.

A relationship between the principal stresses, f_{c1}, to the principal tensile strain, ε_{c1}, is required as concrete acts differently in tension than in compression. To relate these two variables, a relationship between the uniaxial cracking strength, f'_t, and the cracking strain, ε_{cr}, to the strength is needed. This is done using equations 5-11 to 5-13.

$$f'_t = 0.33\sqrt{f'_c} \quad (in\ MPa) \tag{5-11}$$

$$\varepsilon_{cr} = \frac{f'_t}{E_c} \tag{5-12}$$

$$E_c = 5000\sqrt{f'_c} \quad (in\ MPa) \tag{5-13}$$

where E_c is the initial tangent stiffness of the concrete. In the linear-elastic range, the concrete is modeled in tension by equation 5-14, until cracking occurs.

$$f_{c1} = E_c * \varepsilon_{c1} \tag{5-14}$$

After cracking, the principal concrete stresses are calculated by equation 5-15.

$$f_{c1} = \frac{f'_t}{1 + \sqrt{200\varepsilon_{c1}}} \tag{5-15}$$

The stresses in the reinforcement in compression and tension are determined using the bilinear relationship between the average stress, f_s, and average strain, ε_s, as shown in equations 5-16 and 5-17.

$$f_{sx} = E_s * \varepsilon_{sx} \leq f_{sxyield} \tag{5-16}$$

$$f_{sy} = E_s * \varepsilon_{sy} \leq f_{syyield} \tag{5-17}$$

where E_s is the elastic modulus of the reinforcement, and $f_{sxyield}$ and $f_{syyield}$ are the yield stresses of the reinforcement in the x and y direction.

5.3 Disturbed Stress Field Model

The disturbed stress field model is used to account for some of the deficiencies that exist in the modified compression field theory (Vecchio, 2000). These deficiencies include an overestimation of shear stiffness and strength in lightly reinforced elements, when crack shear slip becomes important. For heavily reinforced elements with limited rotation, the modified compression field theory underestimates the shear stiffness and strength. To account for these deficiencies, the disturbed stress field model augments the compatibility relationships to include crack shear slip deformations by decoupling the orientation of the principal stress field from the principal strain field.

5.3.1 Compatibility Relationships

The disturbed stress field model does not assume that the principal strain and principal stress axes remain linked. It assumes that the principal strain field changes inclination at a greater rate than the principal stress field. To account for this difference, the disturbed stress field model equates the total strains ε_x, ε_y, and γ_{xy}, as the sum of net concrete strains, ε_{cx}, ε_{cy}, and $\gamma_{cxy,}$ and strain due to shear slip, ε^s_x, ε^s_y, and γ^s_{xy} as shown in equations 5-18 to 5-20.

$$\boldsymbol{\varepsilon_x = \varepsilon_{cx} + \epsilon^s{}_x} \tag{5-18}$$

$$\boldsymbol{\varepsilon_y = \varepsilon_{cy} + \epsilon^s{}_y} \tag{5-19}$$

$$\boldsymbol{\gamma_y = \gamma_{cxy} + \gamma^s{}_{xy}} \tag{5-20}$$

The principal net concrete tensile strain, ε_{c1}, and the principal net concrete compressive strain, ε_{c2}, are related using Mohr's circle as shown in equation 5-21.

$$\boldsymbol{\varepsilon_{c1}, \varepsilon_{c2} = \frac{1}{2}(\varepsilon_{cx} + \varepsilon_{cy}) \pm \frac{1}{2}((\varepsilon_{cx} - \varepsilon_{cy})^2 + \gamma_{cxy}{}^2)^{\frac{1}{2}}} \tag{5-21}$$

The components from crack slip shear strain, ε^s_x, ε^s_y, and γ^s_{xy}, are calculated from the average crack slip shear strain, γ_s, using equation 5-22.

$$\boldsymbol{\gamma_s = \frac{\delta_s}{s}} \tag{5-22}$$

Using the relationship in Mohr's Circle equations 5-23 to 5-25 solve for the components of $\gamma_{s,}$ ε^s_x, ε^s_y, and γ^s_{xy}.

$$\boldsymbol{\varepsilon^s{}_x = -\frac{1}{2}\gamma_s \, sin(2\theta)} \tag{5-23}$$

$$\varepsilon^s{}_y = \frac{1}{2}\gamma_s \sin(2\theta) \tag{5-24}$$

$$\gamma^s{}_{xy} = \gamma_s \cos(2\theta) \tag{5-25}$$

where θ is the orientation of the principal net concrete strains. This orientation and the orientation of the principal concrete stresses, θ_σ, with respect to the x-axis are determined using Mohr's circle as shown in equation 5-26.

$$\theta = \theta_\sigma = \frac{1}{2}\tan^{-1}\left(\frac{\gamma_{cxy}}{\varepsilon_{cx} - \varepsilon_{cy}}\right) \tag{5-26}$$

The orientation of the principal total strain field, θ_ε, is determined in a similar manner using equation 5-27:

$$\theta_\varepsilon = \frac{1}{2}\tan^{-1}\left(\frac{\gamma_{xy}}{\varepsilon_x - \varepsilon_y}\right) \tag{5-27}$$

The rotation lag, $\Delta\theta$, is then the difference between θ_ε and θ_σ.

Assuming a perfect bond, the average strains of the reinforcement components in the x and y direction are the same as the total strains similar to what is shown in equation 5-1 and 5-2.

5.3.2 Equilibrium Relationships

The equilibrium relationships for the disturbed stress field model are the same as those for the modified compression field theory. These are outlined in equations 5-5 to 5-7. In addition to these equilibrium equations, additional relationships for local stresses at the crack are given in equations 5-28 and 5-29.

$$f_{c1} = \rho_x(f_{scrx} - f_{sx})\cos^2\theta_{nx} + \rho_y(f_{scry} - f_{sy})\cos^2\theta_{ny} \tag{5-28}$$

$$v_{c1} = \rho_x(f_{scrx} - f_{sx})\cos\theta_{nx} * \sin\theta_{nx} + \rho_y(f_{scry} - f_{sy})\cos\theta_{ny} * \sin\theta_{ny} \quad (5\text{-}29)$$

where f_{scrx} and f_{scry} are the local reinforcement stress at a crack, and θ_{nx} and θ_{ny} are the angels between the normal to the crack and the reinforcement. However, the average concrete tensile stress is limited to the yield strength of the reinforcement in the crack and is shown by equation 5-30.

$$f_{c1} \leq \rho_x(f_{sxyield} - f_{sx})\cos^2\theta_{nx} + \rho_y(f_{syyield} - f_{sy})\cos^2\theta_{ny} \quad (5\text{-}30)$$

5.3.3 Constitutive Relationships

The constitutive relationships were based on additional test panels (Vecchio and Collins, 1993). From these tests, a reduction factor, β_d, was implemented to account for the softening effect of the coexisting principle tensile strains as shown in equation 5-31.

$$\beta_d = \frac{1}{1 + C_s C_d} \leq 1.0 \quad (5\text{-}31)$$

where C_s is 0.55 when using the disturbed stress field model. C_d, a factor for the softening effect of transverse tensile strains is determined using equation 5-32.

$$C_d = 0.35\left(\frac{-\varepsilon_{c1}}{\varepsilon_{c2}} - 0.28\right)^{0.8} \quad (5\text{-}32)$$

The softening factor in equation 5-31 is applied to the concrete cylinder strength, f'_c, and the corresponding peak strain, ε_0, to determine the peak compressive stress, f_p, and the corresponding peak strain ε_p using equations 5-33 and 5-34.

$$f_p = -\beta_d f'_c \quad (5\text{-}33)$$

$$\varepsilon_p = -\beta_d \varepsilon_0 \quad (5\text{-}34)$$

Using these new parameters, the relationship between principal concrete compressive stress, f_{c2}, and the principal net compressive strain, ε_{c2}, is calculated using equation 5-35.

$$f_{c2} = f_p \frac{n(\frac{\varepsilon_{c2}}{\varepsilon_p})}{n - 1 + (\frac{\varepsilon_{c2}}{\varepsilon_p})^{nk}} \tag{5-35}$$

where:

$$n = 0.8 - \frac{f_p}{17} \quad (in\ MPa) \tag{5-36}$$

$$k = \begin{cases} 1.0 & for\ \varepsilon_p < \varepsilon_{c2} < 0 \\ 0.67 - \frac{f_p}{62} & for\ \varepsilon_{c2} < \varepsilon_p < 0 \end{cases} \tag{5-37}$$

For concrete in tension, the response before cracking is the same as given in equation 5-14. For cracked concrete the average concrete tensile stresses, f^a_{c1}, is modeled using equation 5-38.

$$f^a_{c1} = \frac{f'_t}{1 + \sqrt{c_t \varepsilon_{c1}}} \quad for\ \varepsilon_{cr} < \varepsilon_{c1} \tag{5-38}$$

where:

$$c_t = 2.2m \tag{5-39}$$

$$\frac{1}{m} = \sum_{i=1}^{n} \frac{4\rho_i}{d_{b_i}} |cos\ \theta_{nii}| \qquad (in\ mm) \tag{5-40}$$

where d_{bi} is the bar diameter and ρ_i is the reinforcement ratio for each of the n reinforcement components.

Post-cracking tensile stresses, $f_{c1}{}^{b}$, occurs due to tension softening, and can have a significant affect in lightly reinforced concrete structures. The cracking tensile stress due to tension softening is calculated using equation 5-41.

$$\boldsymbol{f_{c1}{}^{b} = f'_{t}\left(1 - \frac{\varepsilon_{c1} - \varepsilon_{cr}}{\varepsilon_{ts} - \varepsilon_{cr}}\right) \quad for\ \varepsilon_{cr} < \varepsilon_{c1} < \varepsilon_{ts}} \tag{5-41}$$

where ε_{ts} is the terminal strain, or strain at which tensile stresses in plane concrete is reduced to zero. This is determined by equation 5-42.

$$\boldsymbol{\varepsilon_{ts} = 2.0\frac{G_f}{f'_t * L_r}} \tag{5-42}$$

where G_f is the fracture energy parameter, assumed to be 75 N/m, and L_r is the characteristic length. The post-cracking principal tensile stress in the concrete is taken as the larger of the value predicted by tension stiffening or the tension softening as shown in equation 5-43.

$$\boldsymbol{f_{c1} = max(f_{c1}{}^{a}, f_{c1}{}^{b})} \tag{5-43}$$

The constitutive model for reinforcement in tension or compression is accounted for by equation 5-44.

$$\mathbf{f_s} = \begin{cases} \mathbf{E_s\varepsilon_s} & \mathbf{for\ 0 < \varepsilon_s < \varepsilon_{syield}} \\ \mathbf{f_{syield}} & \mathbf{for\ \varepsilon_{syield} < \varepsilon_s < \varepsilon_{sh}} \\ \mathbf{f_{syield} + E_{sh}(\varepsilon_s - \epsilon_{sh})} & \mathbf{for\ \varepsilon_{sh} < \varepsilon_s < \varepsilon_u} \\ \mathbf{0} & \mathbf{for\ \varepsilon_u < \varepsilon_s} \end{cases} \tag{5-44}$$

where E_s is the elastic modulus of the reinforcement, f_{syield} is the yield strength of the reinforcement, ε_{syield}, is the yield strain of the reinforcement, ε_{sh} is the strain at the onset of strain hardening, and ε_u is the ultimate strain of the reinforcement.

5.4 Finite Element Implementation

An overview of the algorithm for nonlinear finite element analysis is summarized in Figure 5-2 (Wong, 2012). The finite element program uses displacement-based methods relating unknown nodal displacements to specified forces by the structure stiffness matrix. The subsequent sections describe in detail the most important steps shown.

5.4.1 Composite Stiffness Matrix

The total strains are a summation of the net concrete strains, ε_c, elastic strain offsets, ε_c^o, plastic strain offsets in the concrete, ε_c^p, and strains due to crack shear slip, ε^s, following the Disturbed Stress Field Model, as shown in equation 5-45.

$$[\boldsymbol{\varepsilon}] = [\boldsymbol{\varepsilon_c}] + [\boldsymbol{\varepsilon_c^o}] + \left[\boldsymbol{\varepsilon_c^p}\right] + [\boldsymbol{\varepsilon^s}] \tag{5-45}$$

The total strains are related to the stresses, σ, by the composite material stiffness matrix, D, as shown in equation 5-46, where σ^0 is the pseudo stress vector.

$$[\boldsymbol{\sigma}] = [\boldsymbol{D}][\boldsymbol{\varepsilon}] - \left[\boldsymbol{\sigma^0}\right] \tag{5-46}$$

The composite material stiffness matrix is created by summing the concrete material stiffness matrix, D_c, and the reinforcement component material stiffness matrix, D_s, as shown in equation 5-47.

$$[\boldsymbol{D}] = [\boldsymbol{D_c}] + \sum_{\boldsymbol{i=1}}^{\boldsymbol{n}} [\boldsymbol{D_s}]_{\boldsymbol{i}} \tag{5-47}$$

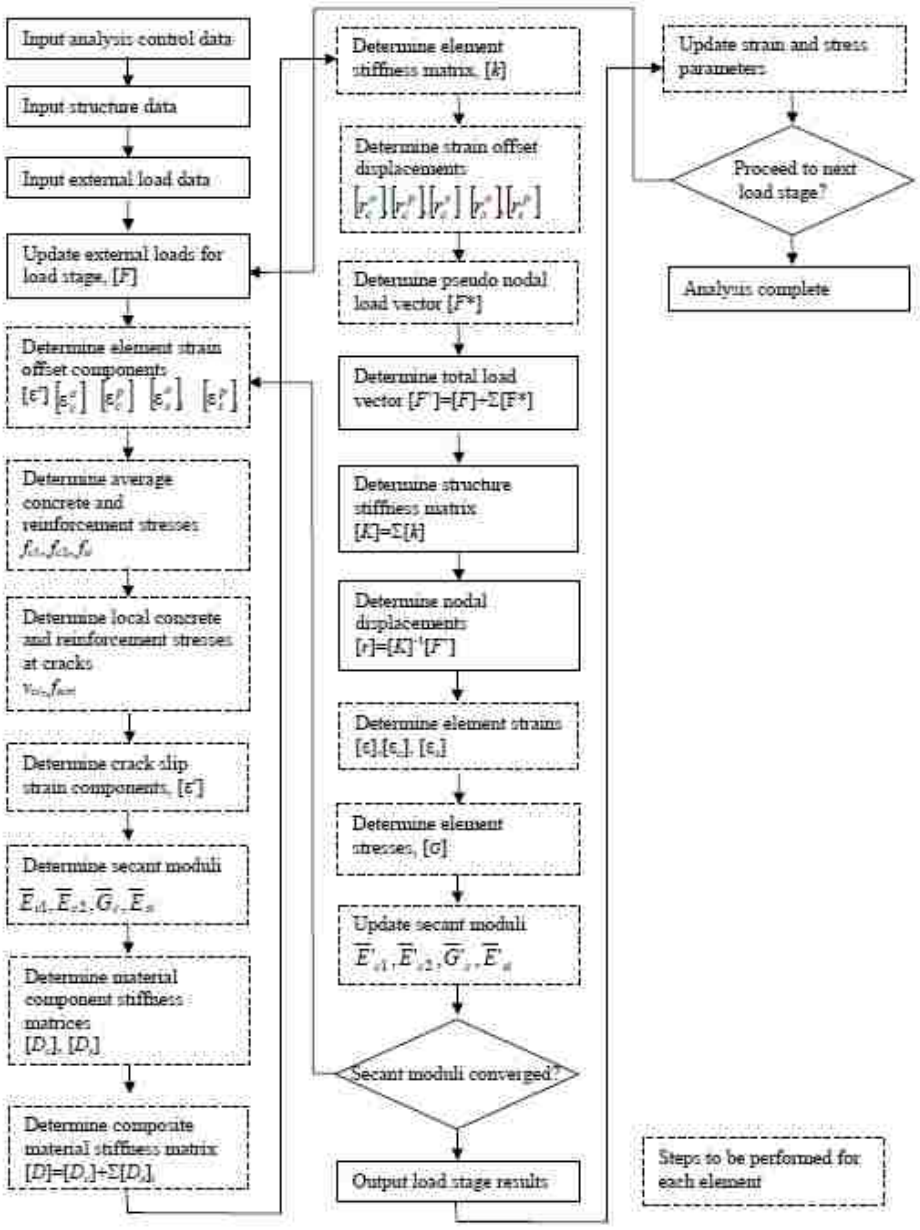

Figure 5-2 VecTor 2 nonlinear finite element analysis algorithm (Wong et al. 2012)

The pseudo stress vector, σ^o, is subtracted from the total stress to account for the stress contribution of strain offsets and shear slip. This vector is calculated using equation 5-48.

$$[\boldsymbol{\sigma^0}] = [\boldsymbol{D_c}]\{[\boldsymbol{\varepsilon_c^0}] + [\boldsymbol{\varepsilon_c^p}] + [\boldsymbol{\varepsilon^s}]\} + \sum_{i=1}^{n} [\boldsymbol{D_s}]_i \left\{[\boldsymbol{\varepsilon_s^0}]_i + [\boldsymbol{\varepsilon_s^p}]_i\right\} \quad (5\text{-}48)$$

The concrete material stiffness matrix, D_c, is assumed to be an orthotropic material in the principal stress directions and the Poisson's effect is negligible. These assumptions allows D_c to be calculated using equation 5-49.

$$[\boldsymbol{D_c}]' = \begin{bmatrix} \bar{E}_{\boldsymbol{c1}} & \mathbf{0} & \mathbf{0} \\ \mathbf{0} & \bar{E}_{\boldsymbol{c2}} & \mathbf{0} \\ \mathbf{0} & \mathbf{0} & \boldsymbol{\bar{G}_c} \end{bmatrix} \tag{5-49}$$

where:

$$\boldsymbol{\bar{E}_{c1}} = \frac{\boldsymbol{f_{c1}}}{\boldsymbol{\varepsilon_{c1}}} \tag{5-50}$$

$$\boldsymbol{\bar{E}_{c2}} = \frac{\boldsymbol{f_{cs}}}{\boldsymbol{\varepsilon_{c2}}} \tag{5-51}$$

$$\boldsymbol{\bar{G}_{c1}} = \frac{\boldsymbol{\bar{E}_{c1}} * \boldsymbol{\bar{E}_{c2}}}{\boldsymbol{\bar{E}_{c1}} + \boldsymbol{\bar{E}_{c2}}} \tag{5-52}$$

The material stiffness matrices, D_s, for each reinforcement component is determined assuming that it only resists uniaxial stresses using equation 5-53.

$$[\boldsymbol{D_s}]_{\boldsymbol{i}}' = \begin{bmatrix} \boldsymbol{\rho_i \bar{E}_{si}} & \mathbf{0} & \mathbf{0} \\ \mathbf{0} & \mathbf{0} & \mathbf{0} \\ \mathbf{0} & \mathbf{0} & \mathbf{0} \end{bmatrix} \tag{5-53}$$

where ρ_i is the reinforcement ratio for the reinforcement component, and the secant modulus $\bar{E}_{si}$, is computed by equation 5-54.

$$\boldsymbol{\bar{E}_{si}} = \frac{\boldsymbol{f_{si}}}{\boldsymbol{\varepsilon_{si}}} \tag{5-54}$$

5.4.2 Element Stiffness Matrix

The element stiffness matrix, k, is calculated by the composite material stiffness matrix using equation 5-55.

$$[\boldsymbol{k}] = \int_{\boldsymbol{vol}} [\boldsymbol{B}]^{\boldsymbol{T}} [\boldsymbol{D}][\boldsymbol{B}] \boldsymbol{dV} \tag{5-55}$$

where B is the strain-displacement matrix. The strain displacement matrix is dependent on the element, and interpolates strains by relating nodal displacements of the element to strain.

5.4.3 Total Iterative Secant Stiffness Solution

The global stiffness matrix, K, is calculated by summing all the element stiffness matrices as shown in equation 5-56.

$$[\boldsymbol{K}] = \sum_{\boldsymbol{i=1}}^{\boldsymbol{m}} [\boldsymbol{k}]_{\boldsymbol{i}} \tag{5-56}$$

The nodal displacement matrix, r, is found by multiplying the total nodal load vector, F', by the inverse of the global stiffness matrix as shown in equation 5-57.

$$[\boldsymbol{r}] = [\boldsymbol{K}]^{\boldsymbol{-1}} [\boldsymbol{F'}] \tag{5-57}$$

Using the nodal displacement matrix the total element strains are determined by equation 5-58.

$$[\boldsymbol{\varepsilon}] = [\boldsymbol{B}][\boldsymbol{r}] \tag{5-58}$$

The normal and shear stresses are then determined by multiplying the element strains by the material stiffness matrices as shown by equation 5-59.

$$[\boldsymbol{\sigma}] = [\boldsymbol{D_c}]\{[\boldsymbol{\varepsilon}] - [\boldsymbol{\varepsilon_c^0}] - [\boldsymbol{\varepsilon_c^p}] - [\boldsymbol{\varepsilon^s}]\} + [\boldsymbol{D_s}]\{[\boldsymbol{\varepsilon}] - [\boldsymbol{\varepsilon_s^0}] - [\boldsymbol{\varepsilon_p^0}]\} \tag{5-59}$$

5.5 Element Library

Several decisions had to be made including what shape and size of the element to use, the boundary conditions, and whether to use discrete or smeared reinforcement.

5.5.1 Element Shape

VecTor 2 library has three type of shapes: rectangular, triangle, and quadrilateral shapes. All of these elements use a minimum number of nodes, straight conforming boundaries, and linear displacement functions (Wong 2012). Using low powered elements allows VecTor 2 to explicitly calculate their stiffness coefficients without resorting to numerical integration, and are not susceptible to behavior such as zero-energy modes or modes which can be activated without any energy in the system.

The rectangular shape was chosen as it has been shown to be the most accurate with concrete structures (Wong, 2012). The accuracy of rectangular elements decreases as it deviates from square and so aspect ratios greater than 3:2 should be avoided.

5.5.2 Element Size

The mesh or element size used can affect the results. When a finer mesh is used, the more rapid the propagation of the softening zone exists, thus lowering the load resistance (Lotfi, 1991). In this research a mesh size of a half unit is used (Lotfi, 1991, and Haach 2014). Using a half unit size uses a mesh that is square, which is the most accurate dimensions using a rectangular element.

5.5.3 Boundary Conditions

Masonry shear walls are often assumed to act as cantilever walls. This means that in most models the boundary condition is usually a fixed based and a free end, usually with an axial load. This assumption has been kept when modeling shear walls using numerical analysis and has been verified by experimental data (Vermeltfoort, 1991, Chaimoon, 2007, and Tomaževic, 1994). During the experimental phase of this research, the walls were built with the bottom of the wall fixed and the top of the wall free. For these reasons the model utilized a cantilevered wall boundary condition.

5.5.4 Discrete vs Smeared Reinforcement

VecTor 2 allows the reinforcement to be modeled as discrete elements, creating reinforcement elements explicitly, or smeared elements, distributing the properties of reinforcement over an existing concrete or masonry element. Literature has shown that the majority of modeling has used discrete modeling of reinforcement (Dhanasekar, 2008; and Marfia, 2001). In addition, to account for reinforcement buckling, discrete method had to be used. Therefore, discrete reinforcement was used for modeling.

5.6 Material Properties

The material properties for the masonry, reinforcement and surface coating were based on the experimental results, and how they were implemented in VecTor 2 is outlined in the subsequent sections.

5.6.1 Masonry

As VecTor 2 is a 2-dimensional finite element program, it was necessary to account for the hollow cells of the masonry blocks. An equivalent thickness or using the average thickness of the concrete face shells of the block was utilized. This methodology has been used to account for the hollow cells (Stavridis, 2010). For the block used, the equivalent thickness was 3.85 inches (97.79 mm) for the ungrouted elements and 4.75 inches (120 mm) for the grouted elements as shown in Figure 5-3. In Figure 5-3 the green colored elements are the grouted elements and the red elements are the ungrouted elements.

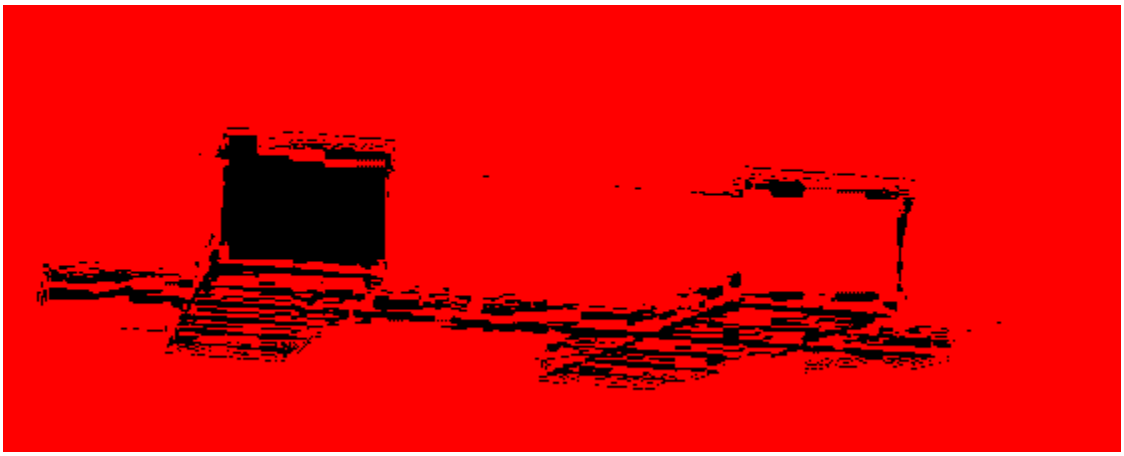

Figure 5-3 Use of equivalent thickness in VecTor 2.

The compressive strength of the masonry units was based on test results from the masonry prisms instead of the masonry blocks. This was done as the interaction of the blocks being stacked resulted in a smaller compressive strength value than the blocks themselves, and were therefore conservative in nature. From the masonry prism tests, an average compressive strength of 1525 psi was calculated.

To account for the joint failure in masonry, VecTor 2 uses a continuum with average properties across a single finite element. To accurately account for the smeared property, joint

spacing and thickness were needed. As the blocks were a nominal 8 inch by 16 inch block, the spacing of the joints were defined in the model using this nominal size. Since dry-stack doesn't utilize mortar between the joints, the joint thickness is dependent on the quality of manufacturing of the block. As the blocks were required to be manufactured to a tolerance of 1/16 of an inch, the maximum joint spacing due to inconsistencies in manufacturing would be 1/8 of an inch, or 1/16 of an inch from each block that makes up the joint. This value of 1/8 of an inch was used for the joint thickness.

5.6.2 Reinforcement

As grade 40 reinforcement steel was used in the experimental phase of this research a yield strength of 40 ksi (280 MPa) and an ultimate strength of 70 ksi (500 MPa) was used. For the walls in the archetypes, grade 60 steel with a yield strength of 60 ksi (400 MPa) and an ultimate strength of 90 ksi (600 MPa) was used, as grade 60 steel is becoming more common in construction.

5.6.3 Surface Coating

VecTor 2 has no explicit way to account for the surface coating, nor is there any literature available on how other researchers have modeled such material. However, observations during testing indicate that the surface coating had little to no damage except at the joints between the blocks. Therefore, it was assumed that the only contribution from the surface coating was at the joints.

Usually, the joint strength is dependent on the mortar strength, and is accounted for in VecTor 2 by a ratio of the shear strength of the joint to the compressive strength of the block.

The shear strength of the joint was calculated based on the maximum shear strength using the strength design technique as shown in equation 5-60 (MSJC 2013).

$$\boldsymbol{V_n \leq 4A_{nv}\sqrt{f'_m}} \tag{5-60}$$

However, the quantity of interest was the shear strength and not the total resistance, so the area in the shear direction, A_{nv}, was dropped from the equation, and the compressive strength of the block was changed to the compressive strength of the surface coating. In addition, it was necessary to account for the thickness difference of the surface coating compared to the block. Making these changes, the joint strength ratio was calculated using equation 5-61.

$$\boldsymbol{joint\ strength\ ratio = \frac{4\sqrt{f'_{sb}}}{f'_m} * \frac{t_{sb}}{t_m}} \tag{5-61}$$

where f'_{sb} is the compressive strength of the surface bond, f'_m is the compressive strength of the block, t_{sb} is the thickness of the surface bond, and t_m is the equivalent thickness of the block.

From the experimental phase of this research, the average compressive strength of the surface coating was 6975 psi. As stated earlier, the compressive strength of the block was 1525 psi. The thickness of the surface coating was assumed to be 0.25 inches or being a nominal 1/8 of an inch thick on both sides, and the equivalent thickness of the block was 3.85 inches. This resulted in a joint strength ratio of 0.015.

5.7 Secondary Models

In addition to the Modified Compression Field Theory and Disturbed Stress Field Model, other models were used to create constitutive and behavior relationships. These models were used to account for the tension stiffening, hysteretic response, and damping. The following

sections give the theoretical background of these models, but don't provide detail on how they are implemented in VecTor 2 nor does it make a comparison with other available models. Additional, information on these subjects can be found in existing literature (Wong 2012).

5.7.1 Hognestad

The Hognestad model is to account for concrete behavior in compression before the pre-peak load is reached (Hognestad, 1951). The parabolic relationship from this model is suitable for normal concrete strengths and is the default choice for VecTor 2. The relationship between the stress and strain is defined using equation 5-62.

$$\boldsymbol{f_c = -f_p\left\{2\left(\frac{\varepsilon_c}{\varepsilon_p}\right) - \left(\frac{\varepsilon_c}{\varepsilon_p}\right)^2\right\} < 0} \tag{5-62}$$

where f_c is the compression in the concrete, f_p is the peak compressive stress in the concrete, ε_c is the current strain in the concrete, and ε_p is the strain at the peak compressive stress in the concrete.

5.7.2 Modified Park-Kent

This stress-strain curve is a linearly descending stress strain curve, which modifies the stress-strain curve originally proposed by Kent and Park (Park 1982). This stress-strain curve was used originally to compute the flexural strength of reinforced concrete columns. The descending stress-strain curve is defined in VecTor 2 using equation 5-63.

$$\boldsymbol{f_c^b = \left[f_p + Z_m f_p(\varepsilon_c - \varepsilon_p)\right] < 0 \quad or -0.2 f_p \; for \; \varepsilon_c < \varepsilon_p < 0} \tag{5-63}$$

where:

$$Z_m = \frac{0.5}{\frac{3 + 0.29|f'_c|}{145|f'_c| - 1000} * (\frac{\varepsilon_0}{-0.002}) + (\frac{|f_{lat}|}{170})^{0.9} + \varepsilon_p} \quad (5\text{-}64)$$

where f_{lat} is the summation of principal stresses transverse to the direction under consideration.

5.7.3 Modified Bentz 2003

This model is used to define the tension stiffening characteristics in cracked concrete (Wong 2012). This particular model accounts for the percentage of reinforcement as well as bond properties between the concrete and reinforcement and is the default value used in VecTor 2. The average concrete tensile stress, f_{c1}, is calculated by equation 5-65.

$$f_{c1} = \frac{f'_t}{1+\sqrt{c_t \varepsilon_{c1}}} \qquad for\ \varepsilon_{c1} > \varepsilon'_t \quad (5\text{-}65)$$

Where:

$$c_t = 3.6 t_d m \quad (5\text{-}66)$$

$$t_d = 0.6 \quad (5\text{-}67)$$

$$\frac{1}{m} = \sum_{i=1}^{n} 4 \frac{\rho_i}{d_{bi}} * |cos(\theta - \alpha_i|| \quad (5\text{-}68)$$

where ρ_i is the reinforcement ratio, d_{bi} is the diameter of the rebar, θ is the inclination of the principle direction, and α_i is the inclination of reinforcement.

5.7.4 Linear Tension Softening

The tension softening stress-strain curve descends linearly from the cracking stress and strain to either zero stress, or to a residual stress (Wong, 2012). This curve is defined by equation 5-69.

$$f_{ts} = f_{cr}\left[1 - \frac{\varepsilon_{c1} - \varepsilon_{cr}}{\varepsilon_{ch} - \varepsilon_{cr}}\right] \geq 0, for\ \varepsilon_{cr} < \varepsilon_1 \quad (5\text{-}69)$$

where ε_{ch} is the characteristic strain, ε_{cr} is the cracking strain, f_{cr}, is the tensile stress when concrete cracks, and ε_{c1} is strain that the concrete is currently experiencing.

5.7.5 Hysteretic Response

Due to the internal damage that occurs in concrete under loading and unloading, the hysteric response can affect dramatically the strength and ductility of reinforced concrete structures. The chosen model that is utilized is based on the work of Palermo and Vecchio (2002). In this model the compression strain and stress are calculated in a similar manner as the tension. As such, only the definition of the stress strain curve for compression is given. When reloading the compressive stress, f_c, is computed using equation 5-70.

$$f_c = f_{ro} + E^{+}_{cm}(\varepsilon_c - \varepsilon_{ro}) \quad (5\text{-}70)$$

where ε_{ro} is the strain in the current hysteretic loop, f_{ro} is the stress in the current hysteretic loop, ε_{cm} is the unloading strain in the current loop and f_{cm} is the corresponding stress. The reloading modulus of elasticity, E^{+}_{cm} is computed using equation 5-71.

$$E^{+}_{cm} = \frac{\beta_d * f_{cm} - f_{ro}}{\varepsilon_{cm} - \varepsilon_{ro}} \quad (5\text{-}71)$$

B_d, the damage indicator is used to degrade the elastic modulus E_{cm}. The damage indicator is calculated by equation 5-72.

$$\beta_d = \begin{cases} \dfrac{1}{1 + 0.1(\frac{\varepsilon_{rec}}{\varepsilon_p})^{0.5}} & for\ |\varepsilon_c| < |\varepsilon_p| \\ \dfrac{1}{1 + 0.175(\frac{\varepsilon_{rec}}{\varepsilon_p})^{0.6}} & for\ |\varepsilon_c| > |\varepsilon_p| \end{cases} \quad (5\text{-}72)$$

where:

$$\boldsymbol{\varepsilon_{rec} = \varepsilon_{cm} - \varepsilon_{ro}} \tag{5-73}$$

where ε_p is the strain at peak stress in the base-curve.

Unloading in compression results in a concrete stress, f_c, at a strain of ε_c modeled using equation 5-74.

$$\boldsymbol{f_c = f_{cm} + E_c(\varepsilon_c - \varepsilon_{cm}) + \frac{E_c(0.071 - 1)(\varepsilon_c - \varepsilon_{cm})^{N_c}}{N_c(\varepsilon_c^p - \varepsilon_{cm})^{N_c - 1}}} \tag{5-74}$$

where ε_c^p is the current plastic offset strain, ε_{cm} is the previously maximum compressive strain, and f_{cm} is the corresponding stress. N_c is the Rasmberg-Osgood term that accounts for the deviation from linear elasticity. N_c is calculated by equation 5-75.

$$\boldsymbol{N_c = \frac{E_c(1 - 0.071)(\varepsilon_c^p - \varepsilon_{cm})}{f_{cm} + E_c(\varepsilon_c^p - \epsilon_{cm})}} \tag{5-75}$$

5.7.6 Reinforcement Buckling

The reinforcement buckling is modeled using the Asatsu Model (Wong et al. 2002). This model required the use of discrete reinforcement connected with a bond element. The criteria for buckling has 3 requirements: the reinforcement is plasticized, is subject to compressive stresses greater than 80% of the yield strength, and the bond deterioration is severe. This model was used as it was the only model that did not require a specified unsupported length to account for buckling.

5.7.7 Bond Relationship

The bond relationship for the reinforcement bars was based on the Eligehausen Model (Eligehausen et al 1983). A confined stress-slip relationship was used, but no confinement pressure was assumed as no testing had been done. With those assumptions the stress-slip relationship is defined by equation 5-76.

$$\tau = \begin{cases} \tau_{p1}\left(\frac{\Delta}{\Delta_{p1}}\right)^{\alpha} & for\ \Delta \leq \Delta_{p1} \\ \tau_{p2} & for\ \Delta_{p1} < \Delta \leq \Delta_{p2} \\ \tau_{p2} - \left[\frac{\Delta - \Delta_{p2}}{\Delta_{p3} - \Delta_{p2}}\left(\tau_{p2} - \tau_{pf}\right)\right] & for\ \Delta_{p2} < \Delta \leq \Delta_{p3} \\ \tau_{pf} & for\ \Delta_{p3} < \Delta \end{cases} \quad (5\text{-}76)$$

where:

$$\tau_{p1} = \left(20 - \frac{d_b}{4}\right)\sqrt{\frac{f'_c}{30}} \quad (5\text{-}77)$$

$$\tau_{p2} = \tau_{p1} \quad (5\text{-}78)$$

$$\tau_{pf} = \left(5.5 - 0.07\frac{S}{H}\right)\sqrt{\frac{f'_c}{27.6}} \quad (5\text{-}79)$$

$$\Delta_{p1} = \sqrt{\frac{f'_c}{30}} \quad (5\text{-}80)$$

$$\Delta_{p2} = 3.0\ mm \quad (5\text{-}81)$$

$$\Delta_{p3} = S \quad (5\text{-}82)$$

$$\alpha = 0.4 \quad (5\text{-}83)$$

where S is the spacing of the bars, and H is the height of the confined bar.

5.7.8 Damping

Damping can dramatically change the results of a time history analysis. VecTor 2 utilizes Rayleigh Damping to account for damping. Rayleigh Damping is defined by equation 5-84.

$$\boldsymbol{c = a_0 m + a_1 k} \tag{5-84}$$

where a_o is the mass proportional damping, and a_1 is the stiffness proportional damping. These are defined by equation 5-85

$$\boldsymbol{a_0 = 2\zeta_i \omega_i \quad and \quad a_1 = \frac{2\zeta_j}{\omega_j}} \tag{5-85}$$

and the damping ratio is defined by equation 5-86.

$$\boldsymbol{\zeta_n = \frac{a_0}{2}\frac{1}{\omega_n} + \frac{a_1}{2}\omega_n} \tag{5-86}$$

where ω is the natural frequency.

The problem with the use of damping is that under certain conditions the damping forces can become unrealistically large resulting in an analysis that is non-conservative (Hall, 2006). This is caused by severe strain softening with negative stiffness, which can be mitigated by using initial stiffness-proportional Rayleigh damping (NIST 2010). VecTor 2 utilizes initial stiffness-proportional Rayleigh damping to reduce this problem. However, even with this precaution, problems can still occur in low-rise buildings, so caution must be used for choosing a damping ratio (NIST 2010). Another method for accounting for the problem with the stiffness proportional damping is ignoring it altogether (Elmenshawi et al 2010). Unfortunately, VecTor 2 does not allow for this possibility.

Commonly, 5% or 2% damping has been used when modeling reinforced masonry (NIST 2010; Bennati et al. 2005). Initially, both values were tried when performing time history analysis. Unfortunately, in both cases the damping forces became too great and results were

unrealistic, as no model failed even with a spectral acceleration up to 5 times the design spectral acceleration. To compensate, a damping ratio of 0.002% was used, which is essentially the same as ignoring damping (Elmenshawi et al 2010).

5.8 Conclusion

VecTor 2 is a very robust finite element program that incorporates several theories to model the behavior of concrete and masonry. The choices of the various models were later calibrated and validated from the experimental data that is detailed in the next chapter.

6 MODEL CALIBRATION AND SENSITIVITY ANALYSIS

The assumptions and finite element model were calibrated and validated with the experimental data that are outlined in Chapters 3 and 4. Numerical results were compared to the results of the diagonal tension test, and then later were validated with the in-plane shear test results. A sensitivity analysis was also conducted to determine the response of the model to different parameters.

6.1 Diagonal Tension Test Calibration

The wallettes were unable to be modeled in the same manner that they were tested, due to boundary conditions. Instead the wallettes were modeled as cantilevered, with a nodal displacement in the x and y direction (Haach 2014).

A comparison of the finite element model response to the experimental data for the wallettes that were representative of the 2'x4' pattern is shown in Figure 6-1. Similar results were obtained for the other wallette patterns. The model was able to only represent one of the two wallettes and this was attributed to the variability of the experimental data and not a fault of the model. The purpose of the comparison with the diagonal tension test results was to show the ability of the model to capture the stress-strain curve of the wallettes. As the model was able to do this, the model was not refined any further.

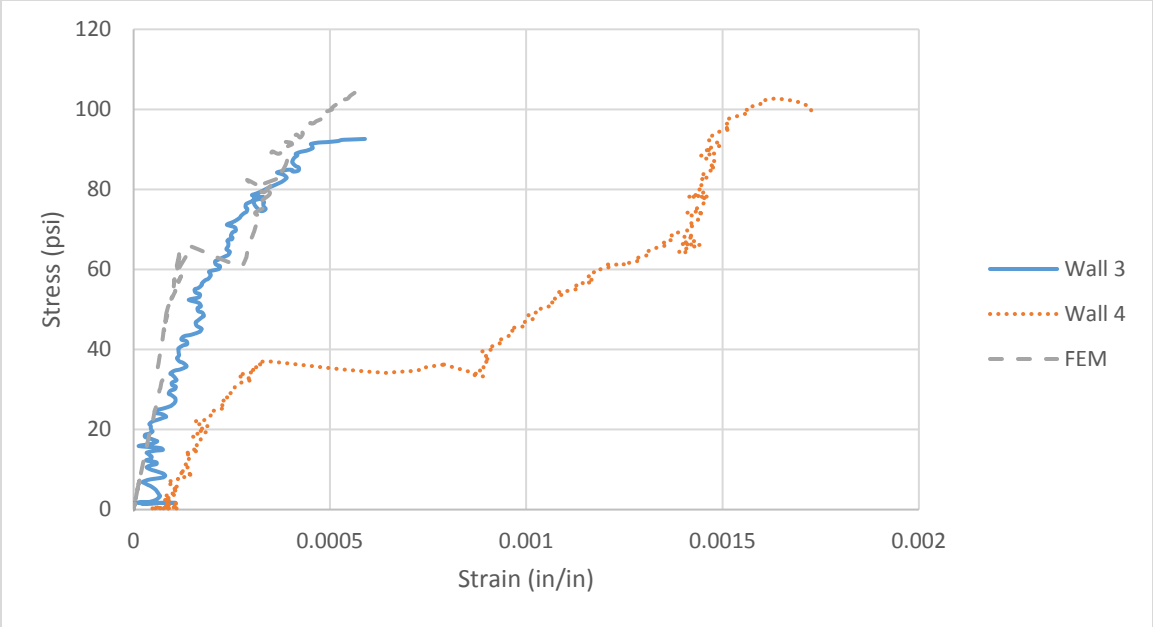

Figure 6-1 Stress-strain comparison of experimental data to finite element model.

6.2 In-Plane Shear Test Calibration

The finite element model was calibrated to the results of the in-plane shear walls. As there was a limited number of experimental results and the goal of the modeling was to capture the resistance and ductility of the walls, the model was calibrated to each set of walls instead of each wall individually. The model used equal nodal displacement for all the nodes on the top of the model wall. In all cases, the finite element model was able to represent the experimental data fairly well, but had especially accurate representation of the walls that were in the 4'x4' configuration. Part of this accuracy was due to the consistency of the experimental data.

6.2.1 Ungrouted and Unreinforced Walls

The response of the finite element model and the experimental data for walls one and two are shown in Figure 6-2. As shown, the finite element model predicts the initial stiffness of the wall, failure load, and displacement of the experimental data reasonably well. In addition, the

finite element model had approximately the same load after failure. This load is attributed to the uplift and rocking of the wall, and shows that finite element model was able to capture this failure mode.

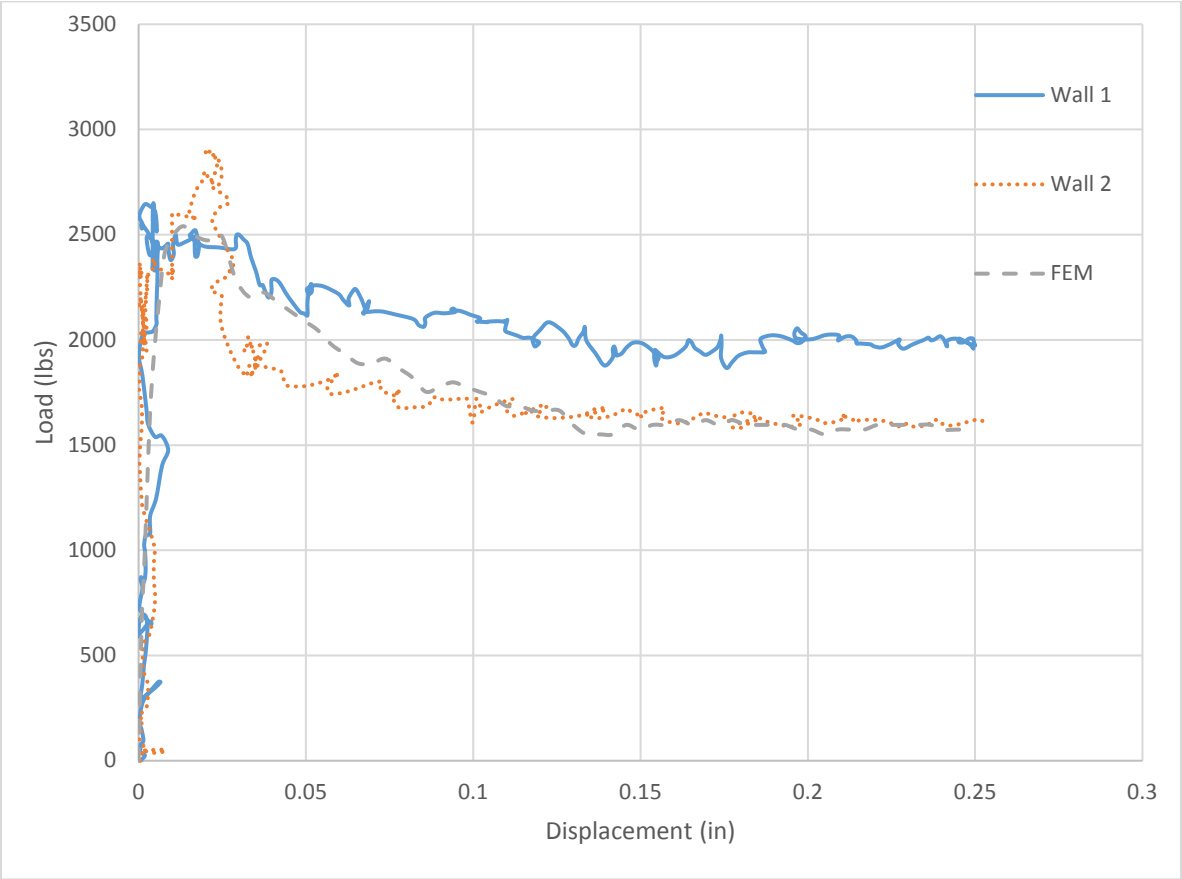

Figure 6-2 Finite element model vs ungrouted experimental wall data.

6.2.2 Grouted and Reinforced 4' by 4' Walls

The response of the finite element model and the experimental data for walls three and four are shown in Figure 6-3. As shown, the finite element model predicts the initial stiffness of the wall, failure load fairly well, and is in between the maximum displacement of the experimental data.

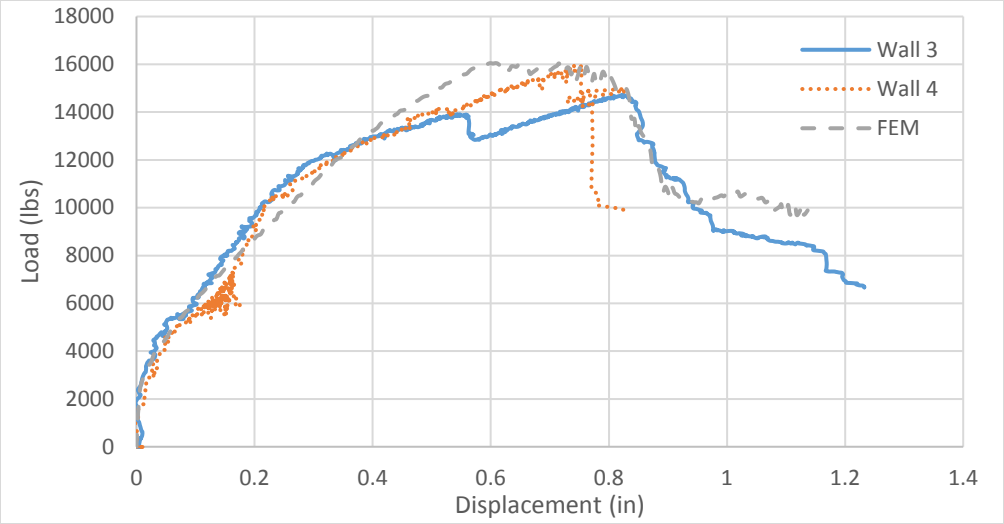

Figure 6-3 Finite element model vs 4'x4' grouted walls.

6.2.3 Grouted and Reinforced 2’ by 4’ Walls

The response of the finite element model and the experimental data for walls five and six is shown in Figure 6-4. As shown, the finite element model predicts the initial stiffness of the wall fairly well, is in between the experimental data for maximum load, and similar maximum displacement before failure.

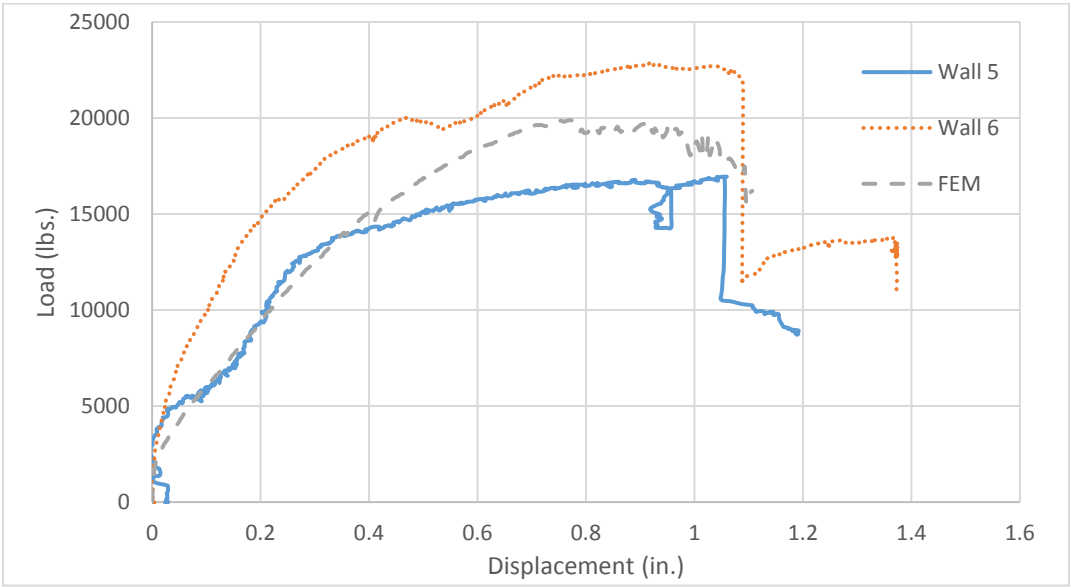

Figure 6-4 Finite element model vs 2'x4' grouted walls.

6.2.4 Thin Mortar Set Walls

To model the walls with a thin mortar set, the joint strength ratio as outlined in 5.6.3 was modified to account for the addition of the mortar. The thickness of the surface bond and mortar was equivalent to the thickness of the block. This resulted in a joint strength ratio of 0.22 instead of 0.015.

The response of the finite element model and the experimental data for walls seven and eight are shown in Figure 6-5. As shown, the finite element model has initial stiffness in between the set of walls, is in between the experimental data for maximum load, and the maximum displacement at failure is in between the two walls.

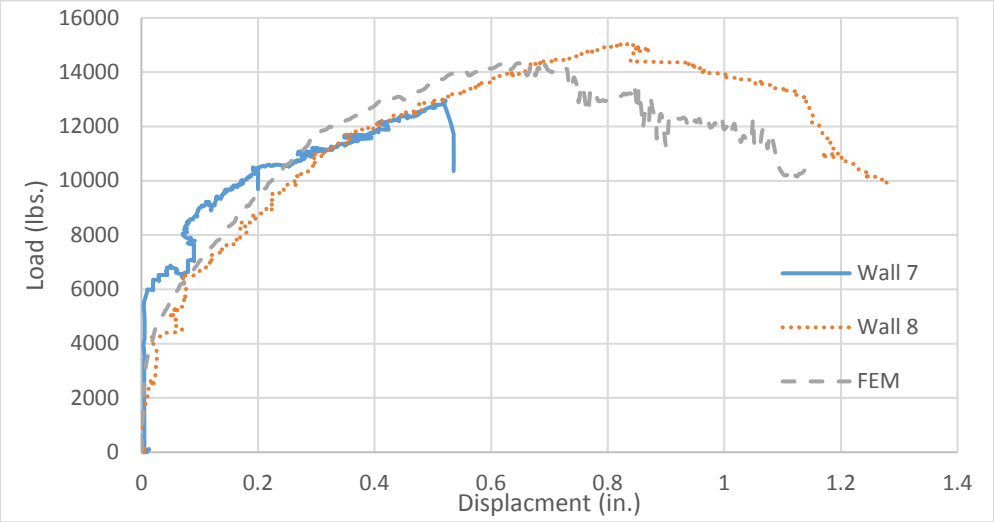

Figure 6-5 Finite element model vs thin mortar set walls.

6.2.5 Cyclically Loaded Walls

As with the other finite element models, cyclically loaded walls used nodal displacement for the nodes at the top of the wall to generate the response. The nodal displacements that were used were the same displacement protocol as is outlined in section 4.7.

The response of the finite element model and the experimental data for walls nine and ten are shown in Figure 6-6 and the backbone curve is presented in Figure 6-7. As shown, the finite element model has the same initial stiffness as the set of walls, is in between the experimental data for maximum load, and the maximum displacement at failure is equal to wall nine.

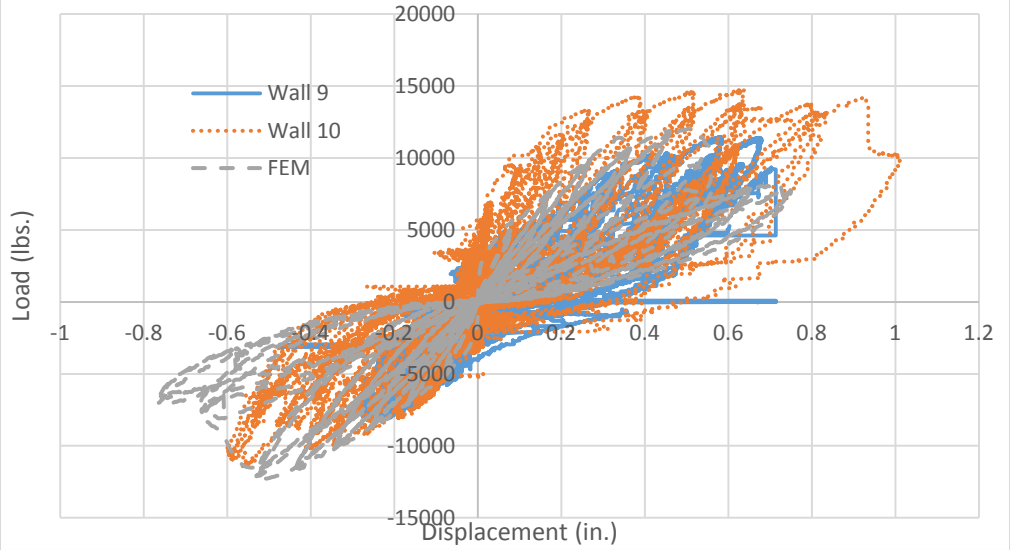

Figure 6-6 Finite element model vs cyclically loaded walls.

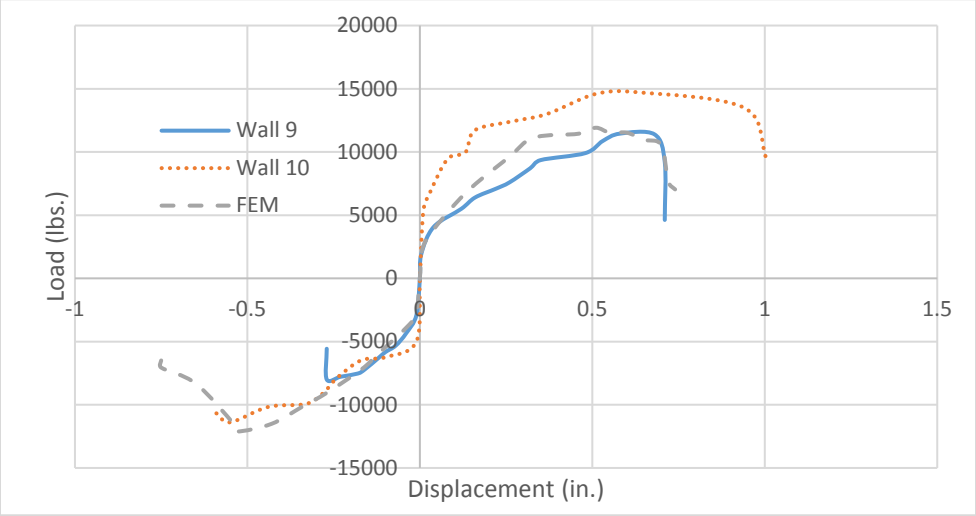

Figure 6-7 Backbone curve of finite element model vs cyclically loaded walls.

6.2.6 Axial Loaded Walls

To model the axial load on the walls, a distributed nodal load was applied to each node on top of the wall. The lateral displacement was again modeled by an equal nodal displacement of all the nodes at the top of the model wall.

The response of the finite element model and the experimental data for walls 11 and 12 are shown in Figure 6-6. As shown, the finite element model has initial stiffness in between that of the set of walls, is in between the experimental data for maximum load, and the maximum displacement at failure is in between the two walls. The major difference from experimental data compared to the finite element model is the model's stiffness degraded quicker than the experimental data, but continued to increase in load where experimental data leveled off quite quickly after reaching its elastic limit. This difference is due to the use of the Hognestad Model which assumes a parabolic relationship prior to the peak load, while the experimental data had an increase in stiffness due to the axial load which caused the quick increase in load and the almost level displacement once the peak load was reached.

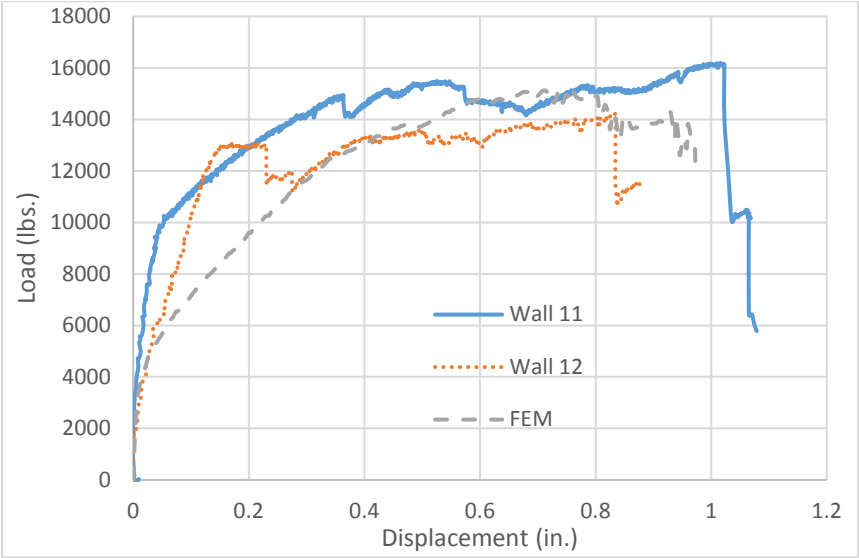

Figure 6-8 Finite element model vs axial loaded walls.

6.3 Sensitivity Analysis

The model predicts reasonable well the response of the walls. To better understand the model, a sensitivity analysis was conducted using the finite element model, using the model for the 4'x 4' set of walls. The following sections explains the sensitivity of the model to several variables, with both an increase and decrease in each variable by 33%. An overview of the results are shown in Table 6-1.

Table 6-1 Overview of Sensitivity Analysis

	Elastic Modulus	Compressive Strength	Joint Strength	Reinforcement Area	Steel Strength
33% Decrease					
% change in displacement	10.2	21.8	7.6	7.6	-0.4
% change in load	-2.2	-5.0	0.3	-9.2	-6.9
33% increase					
% change in displacement	-7.2	13.2	-2.6	2.5	0.00
% change in load	-0.3	4.6	16.5	-2.7	0.00

6.3.1 Elastic Modulus

The elastic modulus was a chosen variable as it controls the stiffness of the wall both initially and as it begins to degrade. The comparison to the original model is shown in Figure 6-9, where original is the finite element model before the elastic modulus was changed. As shown, the elastic modulus has little effect on the maximum load of the model, but did influence the displacement at failure. The difference in displacement is due to the difference in initial stiffness and degradation of the original stiffness. This results in reaching the peak load and maximum displacement sooner as the stiffness increases.

The elastic modulus is usually related to the compressive strength of masonry (DORMS 2012). As the compressive strength of the blocks did not vary greatly during testing, these results cannot be compared to experimental data.

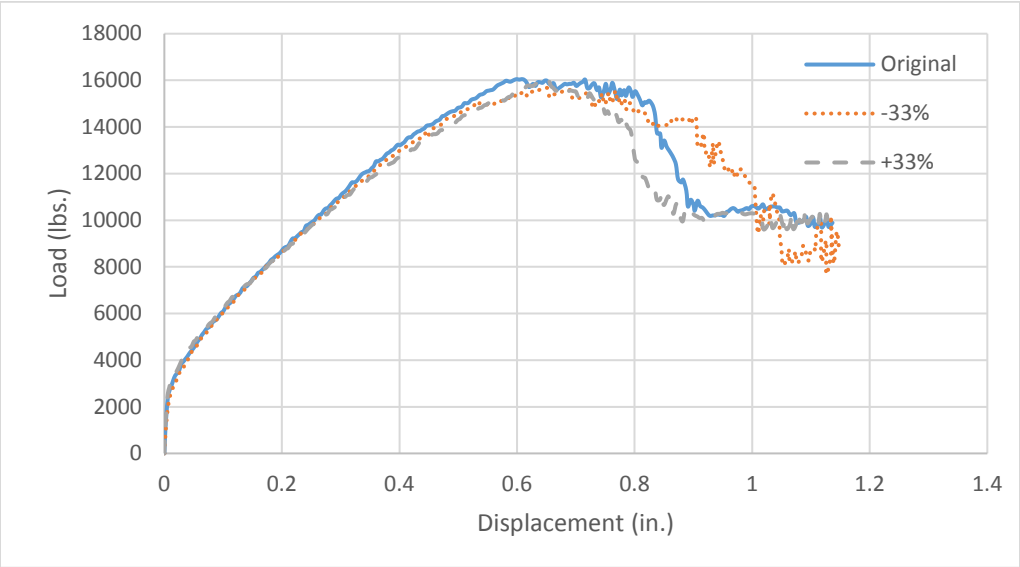

Figure 6-9 Sensitivity analysis of elastic modulus.

6.3.2 Masonry Compressive Strength

The masonry compressive strength was examined as it is one of the main resisting components of the wall. The comparison to the original model is shown in Figure 6-10. As expected decreasing the compressive strength decreased the maximum load and increasing the compressive strength increased the maximum load. Increasing and decreasing the compressive strength increased the maximum displacement at failure. The decreasing of the compressive strength changed the failure mode to more of a flexural failure, which increases the displacement, while the increasing of the compressive strength did not change the shear failure mode but required a higher load and displacement for failure to occur.

Observations during experimental testing showed that failure occurred mainly through the surface coating. This implies that the compressive strength of the blocks would have little

effect on the capacity of the walls, however the model showed it had an impact. This is most likely due to the interaction in the model between the compressive strength and several other variables such as elastic modulus and joint strength. Though care was taken to change these variables to only examine the masonry compressive strength, it is most likely that some variables were missed, resulting in the large influence of the block compressive strength. Future research could examine the influence of different block compressive strength on the shear failure.

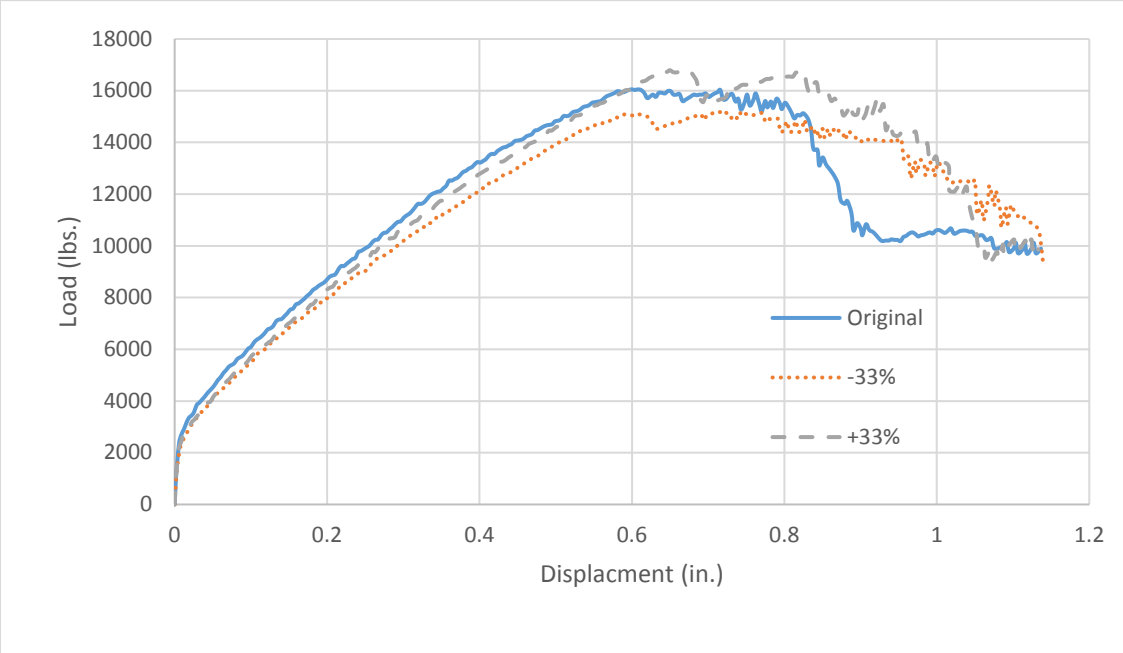

Figure 6-10 Sensitivity analysis of block compressive strength.

6.3.3 Joint Strength

The joint strength is influenced by two parts; the shear capacity and the thickness of the surface coating. As most of the failure in the walls occurred through the joints, this variable was considered important to examine. Figure 6-11 shows the comparison to the original model. As shown, increasing the joint strength increased the capacity, but decreasing the joint strength also

increased the capacity slightly. This is believed to be caused by a change from a shear to a flexural failure, which would also explain why the displacement increased while decreasing the joint strength, but maintained almost the same displacement when the joint strength increased.

As failure occurred primarily through the surface coating at the joints this is considered the main cause of the variability in experimental data. Additionally, statistical analysis showed that there were differences in the compressive strength of the surface coating that was used. However, as discussed in section 4.2.6, there exists a relationship between the compressive strength and shear strength, and the difference in the overall shear strength would be minimal. However, a 33% difference for a nominal 1/8 inch thickness on both sides of the wall is 1/12 inch. While care was taken to insure that 1/8 inch thickness of surface coating was applied to the wall, due to such a small tolerance it is quite likely this caused the difference in failure mode and capacity of the walls.

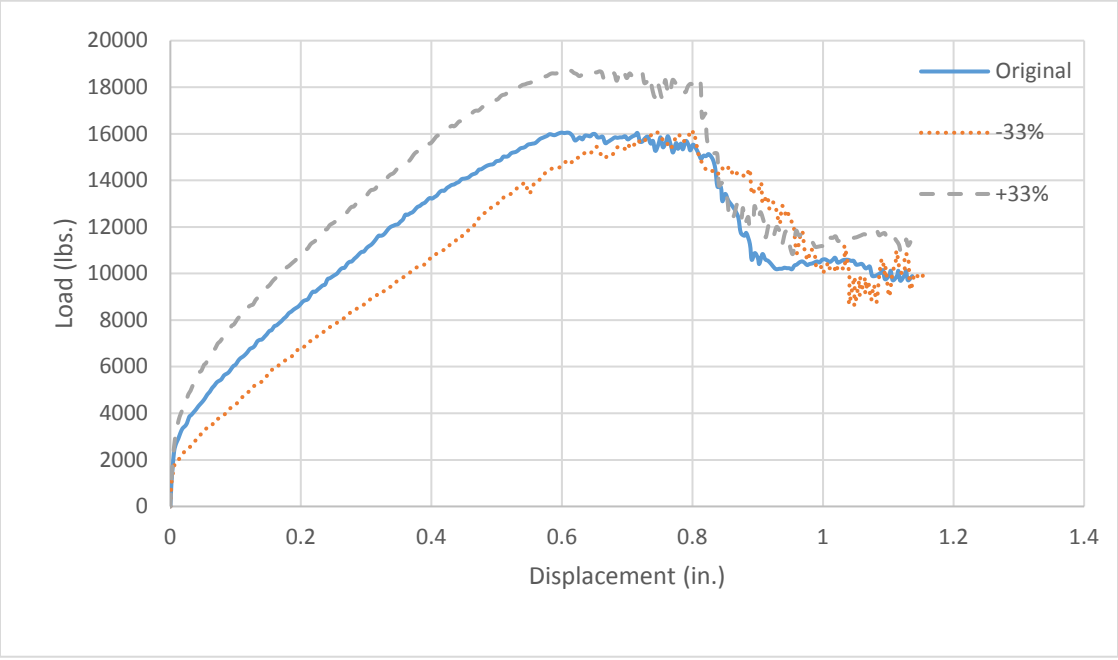

Figure 6-11 Sensitivity analysis of joint strength.

6.3.4 Reinforcement Area

The amount of vertical reinforcement was already shown to increase the capacity of the walls, but this study examined how increasing the amount of horizontal reinforcement affects the walls. Figure 6-12 shows the comparison with the original model. As shown, by increasing and decreasing the reinforcement area the load decreased overall, but by decreasing the reinforcement, the maximum displacement increased slightly. However, the effect of changing the steel area was slight in either case.

As the reinforcement area was the same throughout all experiments these results could not be compared. Future research should be conducted changing amount of horizontal reinforcement to examine its influence.

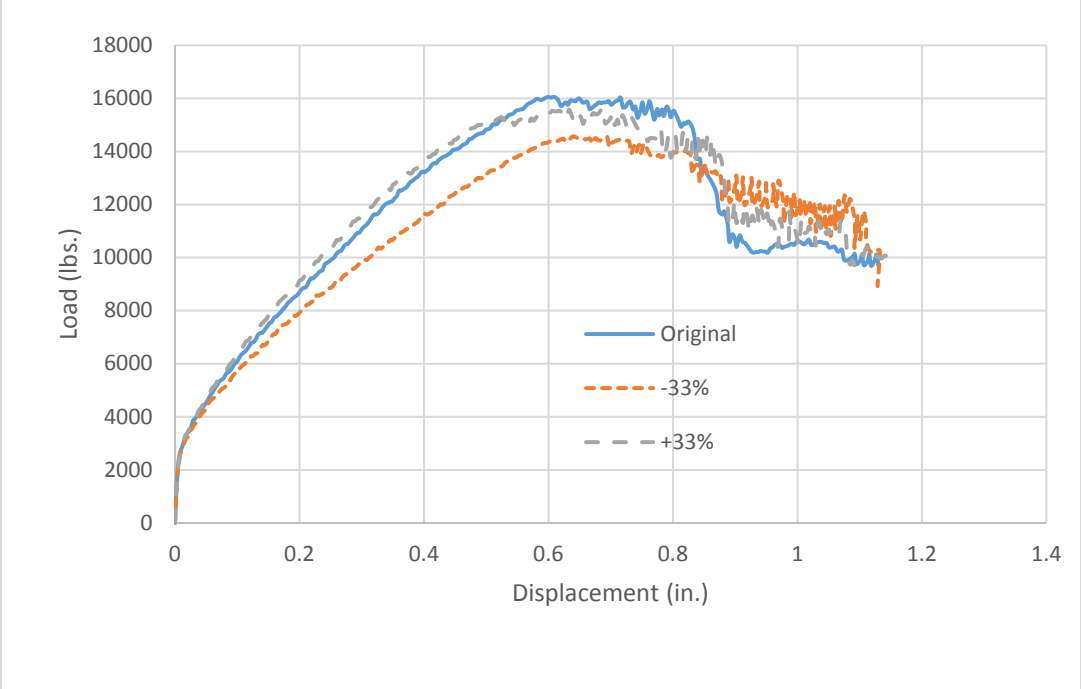

Figure 6-12 Sensitivity analysis of reinforcement area.

6.3.5 Reinforcement Strength

As grade 40 steel was used during the experimentation stage instead of grade 60 as is common in construction, it was decided to investigate how the steel strength would affect the load-displacement relationship. The comparison is shown in Figure 6-13. As shown, decreasing the capacity of the reinforcement decreased the load, however increasing the capacity had no effect. It is believe that by decreasing the reinforcement strength the failure mode is controlled by flexure, while increasing the reinforcement strength the failure is controlled by shear, and therefore, the joint strength and capacity of the blocks are what are most important and increasing the steel strength has no effect.

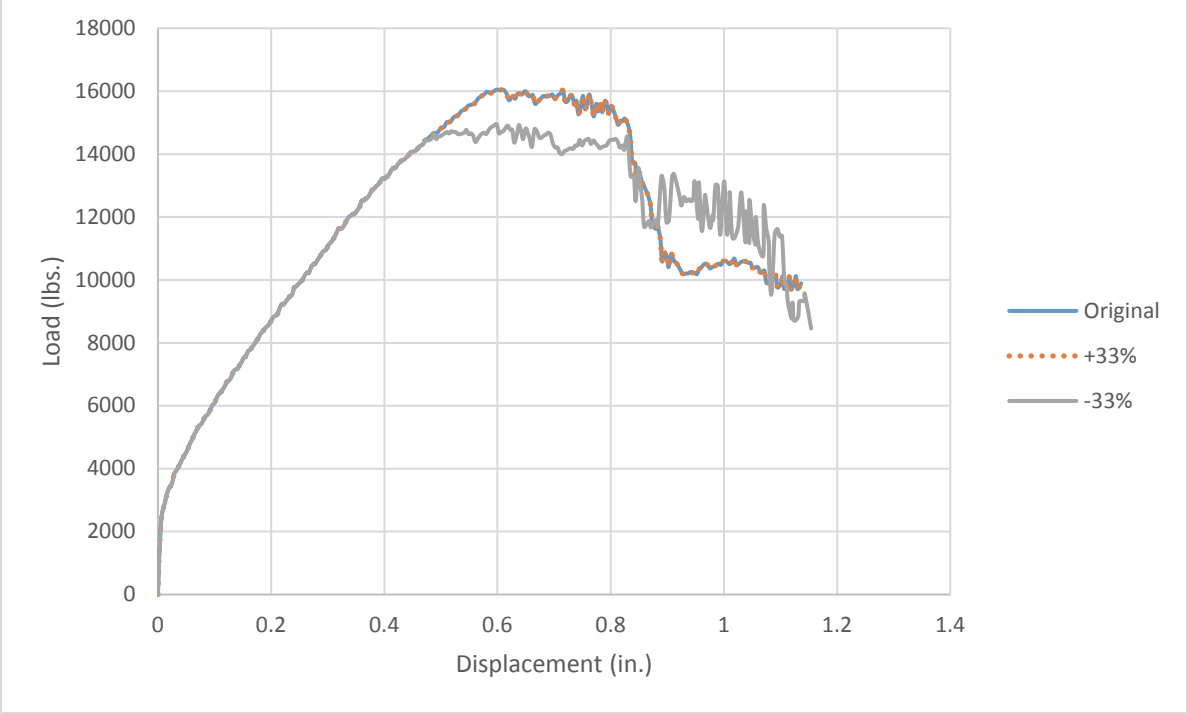

Figure 6-13 Sensitivity analysis of reinforcement strength.

7 SEISMIC ANALYSIS OUTLINE AND METHODOLOGY

A time history and pushover analysis using the finite element model is needed to determine the seismic parameters. To perform these analysis, archetypes are used and designed to represent the variety of structures that may be built using the dry-stack system. This chapter outlines the design requirements, archetypes configurations, earthquake record set, and the methodology for determining the seismic parameters.

7.1 Design Requirements

The walls were designed in accordance with the requirements of a special reinforced masonry shear wall (MSJC 2013). In addition, the walls were detailed for flexural and axial loads following the strength design method with the alterations as outlined in the international code council report for the dry-stack system (ICC-ES 2001). To detail the shear reinforcement, the surface coating method as outlined in Section 4.9.7 was used. For both shear and flexural reinforcement, grade 60 steel is used and the maximum size bar that can be used is a #6 bar due to limited size of the block cells.

To determine the seismic forces acting on the archetype walls, the Equivalent Lateral Force (ELF) Method was utilized following ASCE 7-10 (ASCE 2010). While detailing the archetypes using the ELF method, it was assumed that the walls were rectangular cantilever walls. The dead and live loads were based on loads from the International Building Code and are given in Table 7-1 and used to determine the seismic mass (International 2012).

Table 7-1 Loads Used for Design

Load	Value
Roof Loads	
Dead Load Single Story	30 psf
Dead Load Multistory	85 psf
Live Load	20 psf
Floor Loads	
Dead Load	100 psf
Live Load	28 psf
Corridor Dead Load	73 psf
Corridor Live Load	60 psf

7.2 Archetype Configuration

The archetypes that were used here in were the same as those used when traditional masonry was studied following the FEMA guidelines (NIST 2010). However, more shear walls were needed due to the lower capacity of the dry-stack walls. The plan layouts are shown in Figure 7-1. Layout 1 was selected to represent commercial buildings with large windows and smaller walls. The roof height is 12 ft. high and the shear walls are 24 ft. long. Layout 2 was selected to represent residential occupancies such as hotels and college dorms. Layout 2 was used for both 1 and 2 story archetypes, each with floor height of 10 ft. and wall length of 32 ft. The shear walls in opposing directions were considered independent from each other and not connected structurally.

In all cases the minimum number of walls needed was selected for design. Gravity loads, as stated previously can change the capacity of the shear walls (Voon 2006). As such, archetypes shear walls were analyzed with 2,000 and 4,000 axial load per foot. The 2,000 lbs. was chosen as this is what a wall is typically designed to support, and the 4,000 lbs. load was chosen to determine the affect a higher axial load has on the wall response. These loads are denoted low and high gravity loads respectively. Due to limitations on dry-stack systems, only 1 and 2 story archetypes were considered, making all archetypes have a short period domain. During the

analysis, seismic category B, C, and D were considered. The archetypes were then divided into performance groups based upon their seismic category and gravity load.

Based on the seismic design category, the maximum considered earthquake parameters and the design spectral acceleration are given in Table 7-2. A summary of the design variables stated previously is given in Table 7-3. Table 7-4 summarizes other key design considerations. In Table 7-4 the force reduction factor, R, was initially chosen as 5 similar to special reinforced masonry shear walls. Initial values showed that an R value of 5 would result in a collapse margin ratio below the acceptable collapse margin ratio, or in other words the system would not meet the FEMA P-695 criteria. Therefore, an R value of 2, similar to ordinary reinforced masonry shear walls was used for all future designs. T was the period calculated using an eigenvalue analysis and T_1 was the period using the simplified ASCE method (ASCE 2010).

Table 7-2 Summary of Seismic Design Parameters for Short-Period Spectral Acceleration

Seismic Design Category		Maximum Considered Earthquake			Design
Maximum	Minimum	SS (g)	Fa	SMS (g)	SDS (g)
D		1.5	1.0	1.5	1.0
C	D	0.55	1.36	0.75	0.50
B	C	0.33	1.53	0.50	0.33
	B	0.156	1.6	0.25	0.167

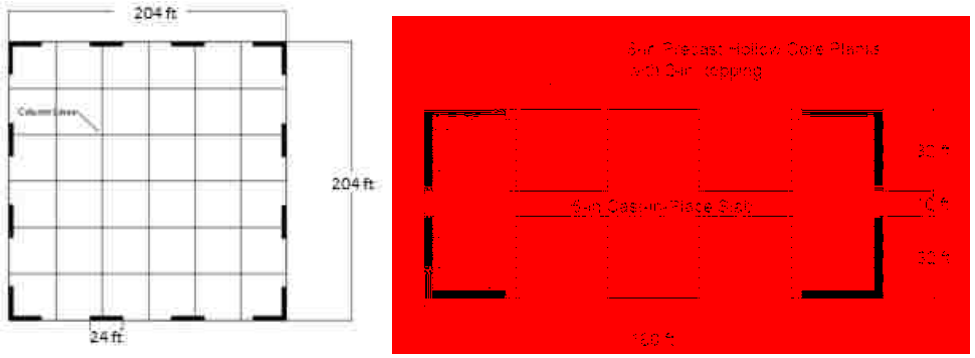

(a) Design layout 1. **(b) Design layout 2.**

Figure 7-1 Archetype layouts.

Table 7-3 Seismic and Gravity Design Parameters

Layout	# of Stories	SDC	Gravity	Archetype ID
1	1	D_{max}	low	11DMAL
			high	11DMAH
		D_{min}	low	11DMIL
			high	11DMIH
		C_{max}	low	11CMAL
			high	11CMAH
		C_{min}	low	11CMIL
			high	11CMIH
		B_{max}	low	11BMAL
			high	11BMAH
		B_{min}	low	11BMIL
			high	11BMIH
2	1	D_{max}	low	21DMAL
			high	21DMAH
		D_{min}	low	21DMIL
			high	21DMIH
		C_{max}	low	21CMAL
			high	21CMAH
		C_{min}	low	21CMIL
			high	21CMIH
		B_{max}	low	21BMAL
			high	21BMAH
		B_{min}	low	21BMIL
			high	21BMIH
2	2	D_{max}	low	22DMAL
			high	22DMAH
		D_{min}	low	22DMIL
			high	22DMIH
		C_{max}	low	22CMAL
			high	22CMAH
		C_{min}	low	22CMIL
			high	22CMIH
		B_{max}	low	22BMAL
			high	22BMAH
		B_{min}	low	22BMIL
			high	22BMIH

Table 7-4 Design Parameters

Archetype ID	# of walls in each direction	Wall height/length (ft)	Seismic Weight Roof (kips/wall)	Seismic Weight floor (kips/wall)	R	T (sec)	T_1 (sec)	V/w	S_{mt} (g)
11DMAL	8	12/24	323	N/A	5,2	0.12	0.25	0.200	1.5
11DMAH	8	12/24	323	N/A	5,2	0.12	0.25	0.200	1.5
11DMIL	8	12/24	323	N/A	2	0.12	0.25	0.100	0.75
11DMIH	8	12/24	323	N/A	2	0.12	0.25	0.100	0.75
11CMAL	8	12/24	323	N/A	2	0.12	0.25	0.250	0.75
11CMAH	8	12/24	323	N/A	2	0.12	0.25	0.250	0.75
11CMIL	8	12/24	323	N/A	2	0.10	0.25	0.165	0.5
11CMIH	8	12/24	323	N/A	2	0.10	0.25	0.165	0.5
11BMAL	8	12/24	323	N/A	2	0.10	0.25	0.165	0.5
11BMAH	8	12/24	323	N/A	2	0.10	0.25	0.165	0.5
11BMIL	8	12/24	323	N/A	2	0.10	0.25	0.084	0.25
11BMIH	8	12/24	323	N/A	2	0.10	0.25	0.084	0.25
21DMAL	4	10/32	516	N/A	2	0.08	0.25	0.200	1.5
21DMAH	4	10/32	516	N/A	2	0.08	0.25	0.200	1.5
21DMIL	4	10/32	516	N/A	2	0.08	0.25	0.100	0.75
21DMIH	4	10/32	516	N/A	2	0.08	0.25	0.100	0.75
21CMAL	4	10/32	516	N/A	2	0.08	0.25	0.250	0.75
21CMAH	4	10/32	516	N/A	2	0.08	0.25	0.250	0.75
21CMIL	4	10/32	516	N/A	2	0.07	0.25	0.165	0.5
21CMIH	4	10/32	516	N/A	2	0.07	0.25	0.165	0.5
21BMAL	4	10/32	516	N/A	2	0.07	0.25	0.165	0.5
21BMAH	4	10/32	516	N/A	2	0.07	0.25	0.165	0.5
21BMIL	4	10/32	516	N/A	2	0.07	0.25	0.084	0.25
21BMIH	4	10/32	516	N/A	2	0.07	0.25	0.084	0.25
22DMAL	8	20/32	258	308.5	2	0.13	0.30	0.200	1.5
22DMAH	8	20/32	258	308.5	2	0.13	0.30	0.200	1.5
22DMIL	8	20/32	258	308.5	2	0.13	0.32	0.100	0.75
22DMIH	8	20/32	258	308.5	2	0.13	0.32	0.100	0.75
22CMAL	8	20/32	258	308.5	2	0.13	0.30	0.250	0.75
22CMAH	8	20/32	258	308.5	2	0.13	0.30	0.250	0.75
22CMIL	8	20/32	258	308.5	2	0.12	0.32	0.165	0.5
22CMIH	8	20/32	258	308.5	2	0.12	0.32	0.165	0.5
22BMAL	8	20/32	258	308.5	2	0.12	0.30	0.165	0.5
22BMAH	8	20/32	258	308.5	2	0.12	0.30	0.165	0.5
22BMIL	8	20/32	258	308.5	2	0.13	0.32	0.084	0.25
22BMIH	8	20/32	258	308.5	2	0.13	0.32	0.084	0.25

7.2.1 Material Properties

The masonry walls were assumed to be constructed with the nominal 8 in. hollow concrete blocks as described in Section 3.2. The walls were assumed to be made with 115 pcf concrete masonry units and a grout density of 140 pcf. The weight of the walls were determined using the ENDURA design tables (SouthWest 2014). The masonry units were assumed to have a compressive strength of 1500 psi, which was similar to what was determined in the experimental phase. The steel reinforcing was assumed to be ASTM A615 Grade 60.

7.2.2 Shear Wall Designs

Table 7-5 outlines the various designs for all the archetypes. The vertical reinforcement was controlled mainly by the requirements of specially reinforced masonry walls or at least 1 #4 bar at 48 inches on center. The horizontal reinforcement was controlled mainly by the lateral forces. In some cases, no design is given as it was already determined that the system would not meet the FEMA P-695 criteria for that seismic category, so the design was stopped.

7.3 Far-Field Record Set

The Far-Field record set includes a set of ground motions recorded at sites greater than 10 km from the fault rupture. Though a Near-Field set exists, a time-history analysis is not required using this set as there is still so much uncertainty and lack of research for seismic events close to the fault rupture (FEMA 2009). The rationale behind the Far-Field set selection, and how the record set is modified is outlined in the following sections (FEMA 2009).

As a case study, archetype 11BMIL was subject to the Near-Field set to compare to the results of the Far-Field set. More information on the Near-Field set can be found in Appendix A of *Quantification of Building Seismic Performance Factors* (FEMA 2009).

Table 7-5 Shear Wall Design

Archetype ID #	t (in.)	f'm (psi)	M_u (kip-ft)	Vert Reinf.	Vu (kips)	Horiz Reinf.	ΦV_n (kips)
11DMAL	8	1500	749	1#4@48"	78	1#6@32"	85
11DMAH	8	1500	749	1#4@48"	78	1#6@32"	85
11DMIL	8	1500	375	1#4@48"	39	1#5@48"	47
11DMIH	8	1500	375	1#4@48"	39	1#5@48"	47
11CMAL	8	1500	936	1#4@48"	78	1#6@32"	85
11CMAH	8	1500	936	1#4@48"	78	1#6@32"	86
11CMIL	8	1500	618	1#4@48"	52	1#5@32"	64
11CMIH	8	1500	618	1#4@48"	52	1#5@32"	64
11BMAL	8	1500	572	1#4@48"	60	1#5@32"	64
11BMAH	8	1500	572	1#4@48"	60	1#5@32"	64
11BMIL	8	1500	290	1#4@48"	30	1#4@48"	35
11BMIH	8	1500	290	1#4@48"	30	1#4@48"	35
21DMAL	8	1500	557	1#4@48"	70	1#4@24"	75
21DMAH	8	1500	557	1#4@48"	70	1#4@24"	75
21DMIL	8	1500	279	1#4@48"	35	1#4@48"	47
21DMIH	8	1500	279	1#4@48"	35	1#4@48"	47
21CMAL	8	1500	697	1#4@48"	87	1#6@40"	94
21CMAH	8	1500	697	1#4@48"	87	1#6@40"	94
21CMIL	8	1500	460	1#4@48"	57	1#4@32"	61
21CMIH	8	1500	460	1#4@48"	57	1#4@32"	61
21BMAL	8	1500	460	1#4@48"	57	1#4@32"	61
21BMAH	8	1500	460	1#4@48"	57	1#4@32"	61
21BMIL	8	1500	232	1#4@48"	29	1#4@48"	47
21BMIH	8	1500	232	1#4@48"	29	1#4@48"	47
22DMAL	8	1500	2913	1#4@48"	204	N/A	N/A
22DMAH	8	1500	2913	1#4@48"	204	N/A	N/A
22DMIL	8	1500	1457	1#4@48"	102	1#6@24"	113
22DMIH	8	1500	1457	1#4@48"	102	1#6@24"	113
22CMAL	8	1500	3641	1#4@48"	255	N/A	N/A
22CMAH	8	1500	3641	1#4@48"	255	N/A	N/A
22CMIL	8	1500	2403	1#4@48"	168	1#6@16"	208
22CMIH	8	1500	2403	1#4@48"	168	1#6@16"	208
22BMAL	8	1500	1202	1#4@48"	105	1#5@24"	107
22BMAH	8	1500	1202	1#4@48"	105	1#5@24"	107
22BMIL	8	1500	608	1#4@48"	53	1#5@48"	62
22BMIH	8	1500	608	1#4@48"	53	1#5@48"	62

7.3.1 Objectives

The records were chosen to meet various and sometimes conflicting objectives. First, it needed to be consistent with ASCE ground motion requirements. In other words, the ground motions "consist of pairs of appropriate horizontal ground motion acceleration components that shall be selected and scaled from individual record events" (ASCE 2010). For this reason, no more than 2 record sets could be chosen from any one earthquake. Second, the records had to represent very strong ground motions, i.e. greater than 6.5 magnitude. Although smaller magnitude earthquakes can cause failure, it is usually larger magnitude earthquakes that cause collapse. In addition, there needed to be a large number of records that are not dependent on the period or other structural properties, and they need to be from a variety of site and source conditions.

7.3.2 Record Set

The record set is shown in Table 7-6 and includes the ID number, earthquake name, year, record sequence number, file names, peak ground acceleration (PGA), and peak ground velocity (PGV) (FEMA 2009). The maximum PGA and PGV is the larger of the two values obtained from the two horizontal ground motions.

7.3.3 Normalization

There is an inherit variability that exists between the records. This can be because of differences in event magnitude, distance to source, source types, and site conditions. To remove some of the unwarranted variability, the records are normalized by their respective peak ground velocities, by applying a normalization factor to the horizontal components of the ground motion. The normalization factor is calculated using equation 7-1.

Table 7-6 Far-Field Record Set (FEMA 2009)

ID No.	Earthquake Name	Year	Record Sequence number	File Names	PGA_{max} (g)	PGV_{max} (cm/s.)
1	Northridge	1994	953	NORTHR/MUL009 & NORTHR/MUL279	0.52	63
2	Northridge	1994	960	NORTHR/LOS000 & NORTHR/LOS270	0.48	45
3	Duzce, Turkey	1999	1602	DUZCE/BOL000 & DUZCE/BOL090	0.82	62
4	Hector Mine	1999	1787	HECTOR/HEC000 & HECTOR/HEC090	0.34	42
5	Imperial Valley	1979	169	IMPVALL/H-DLT262 & IMPVALL/H-DLT352	0.35	33
6	Imperial Valley	1979	174	IMPVALL/H-E11140 & IMPVALL/H-E11230	0.38	42
7	Kobe, Japan	1995	1111	KOBE/NIS000 & KOBE/NIS090	0.51	37
8	Kobe, Japan	1995	1116	KOBE/SHI000 & KOBE/SHI090	0.24	38
9	Kocaeli, Turkey	1999	1158	KOCAELI/DZC180 & KOCAELI/DZC270	0.36	59
10	Kocaeli, Turkey	1999	1148	KOCAELI/ARC000 & KOCAELI/ARC090	0.22	40
11	Landers	1992	900	LANDERS/YER270 & LANDERS/YER360	0.24	52
12	Landers	1992	848	LANDERS/CLW-LN & LANDERS/CLW-TR	0.42	42
13	Loma Prieta	1989	752	LOMAP/CAP000 & LOMAP/CAP090	0.53	35
14	Loma Prieta	1989	767	LOMAP/G03000 & LOMAP/G03090	0.56	45
15	Manjil, Iran	1990	1633	MANJIL/ABBAR—L & MANJIL/ABBAR—T	0.51	54
16	Superstition Hills	1987	721	SUPERST/B-ICC000 & SUPERST/B-ICC090	0.36	46
17	Superstition Hills	1987	725	SUPERST/B-POE270 & SUPERST/B-POE360	0.45	36
18	Cape Mendocino	1992	829	CAPEMEND/RIO270 & CAPEMEND/RIO360	0.55	44
19	Chi-Chi Taiwan	1999	1244	CHICHI/CHY101-E & CHICHI/CHY101-N	0.44	115
20	Chi-Chi Taiwan	1999	1485	CHICHI/TCU045-E & CHICHI/TCU045-N	0.51	39
21	San Fernando	1971	68	SFERN/PEL090 & SFERN/PEL180	0.21	19
22	Friuli, Italy	1976	125	FRIULI/A-TMZ000 & FRIULI/A-TMZ270	0.35	31

$$\boldsymbol{NM = \frac{Median(PGV_{peer})}{PGV_{peer,i}}} \tag{7-1}$$

where NM is the normalization factor, Median (PGV_{peer}) is the median peak ground velocity for the record set, and $PGV_{peer,i}$ is the individual peak ground velocity for the individual record. The

normalization factor, normalized PGA, and normalized PGV for each set of records is given in Table 7-7 (FEMA 2009). Figure 7-2 shows the normalized response spectra of the Far-Field set including the median spectra and 2 standard deviation (FEMA 2009).

Table 7-7 Normalization Factors

ID No.	Normalization Factor	Normalized Motions	
		PGA_{max} (g)	PGV_{max} (cm/s.)
1	0.65	0.34	41
2	0.83	0.40	38
3	0.63	0.52	39
4	1.09	0.37	46
5	1.31	0.46	43
6	1.01	0.39	43
7	1.03	0.53	39
8	1.10	0.26	42
9	0.69	0.25	41
10	1.36	0.30	54
11	0.99	0.24	51
12	1.15	0.48	49
13	1.09	0.58	38
14	0.88	0.49	39
15	0.79	0.40	43
16	0.87	0.31	40
17	1.17	0.53	42
18	0.82	0.45	36
19	0.41	0.18	47
20	0.96	0.49	38
21	2.10	0.44	40
22	1.44	0.50	44

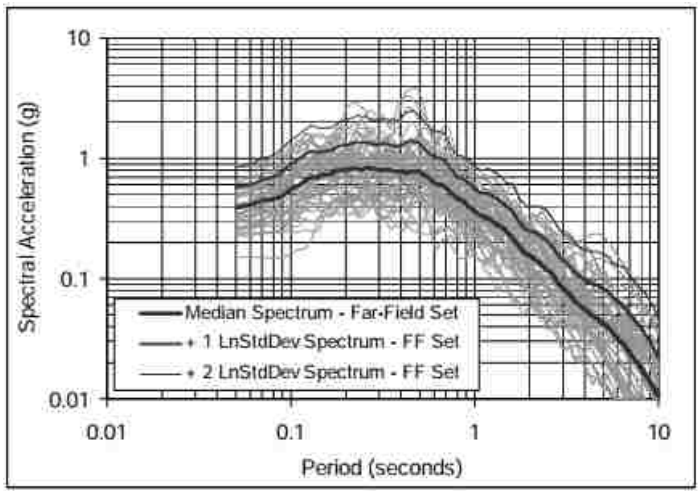

Figure 7-2 Far-Field Set Response Spectra (FEMA 2009).

The FEMA P-695 procedure uses the PGV to normalize the ground motions, but doesn't explain the rationale behind this decision. The PGA and PGV are often used as measures of the intensity of strong ground motion. The PGA is often well correlated with the failure of short period structures and PGV is well correlated with failure in long period structures (Matsumura 1992). It is assumed that PGV was chosen so as to be applicable to a wider range of buildings. Further research should be conducted on using the PGA for normalizing ground motions to evaluate the seismic parameters of low-period structures. For this research the use of the PGV was used to normalize the ground motions.

7.3.4 Scaling

Ground motions are scaled to a higher intensity until the archetype collapses. Instead of scaling each record individually, the ground motion records are collectively scaled until half the ground motions cause the archetype to collapse. This process is done in 2 parts. First, all the ground motions are scaled by their normalization factor. Second, the normalized ground motions are scaled to a specific intensity when the median spectral acceleration of the Far-Field Record set matches the spectral acceleration at the fundamental period for the archetype being analyzed. The scaling factors for a variety of fundamental periods to reach the maximum considered earthquake (MCE) is given in Table 7-8 (FEMA 2009). After the record set is scaled to the MCE, it is collectively scaled upward and downward until half the record set causes the model for the archetype wall being analyzed to collapse.

7.4 Determining the Seismic Parameters

During design, an initial value of the response modification factor is chosen, usually based on other systems of similar nature. Once the design process is done, the finite element

models of the designed shear walls are subject to both a pushover analysis and a time history analysis. The pushover analysis is used to determine the overstrength factor, Ω, and the period based ductility, μ. The time history analysis is used to validate the initial value of R. R is considered acceptable when the average MCE ground motions for each performance group have a 10% collapse probability; however, to account for some archetypes causing outlying data, an individual archetype can have a 20% collapse probability. The deflection amplification factor, C_d, is then calculated using the acceptable R value.

Table 7-8 Scaling Factors for Anchoring the Normalized Far-Field Record Set to MCE Spectral Demand (FEMA 2009)

Period $T = C_u T_a$ (sec.)	Median Value of Normalized Record Set $\hat{S}_{NRT}$ (g)		Scaling Factors for Anchoring Far-Field Record Set to MCE Spectral Demand			
	Near-Field Set	Far-Field Set	SDC D_{max}	SDC C_{max} / SDC D_{min}	SDC B_{max} / SDC C_{min}	SDC B_{min}
0.25	0.936	0.779	1.93	0.96	0.64	0.32
0.3	1.020	0.775	1.94	0.97	0.65	0.32
0.35	0.939	0.761	1.97	0.99	0.66	0.33
0.4	0.901	0.748	2.00	1.00	0.67	0.33
0.45	0.886	0.749	2.00	0.89	0.59	0.30
0.5	0.855	0.736	2.04	0.82	0.54	0.27
0.6	0.833	0.602	2.49	0.83	0.55	0.28
0.7	0.805	0.537	2.40	0.80	0.53	0.27
0.8	0.739	0.449	2.50	0.83	0.56	0.28
0.9	0.633	0.399	2.50	0.83	0.56	0.28
1.0	0.571	0.348	2.59	0.86	0.58	0.29
1.2	0.476	0.301	2.49	0.83	0.55	0.28
1.4	0.404	0.256	2.51	0.84	0.56	0.28
1.6	0.356	0.208	2.70	0.90	0.60	0.30
1.8	0.319	0.168	2.98	0.99	0.66	0.33
2.0	0.284	0.148	3.05	1.02	0.68	0.34
2.2	0.258	0.133	3.08	1.03	0.68	0.34
2.4	0.230	0.118	3.18	1.06	0.71	0.35
2.6	0.210	0.106	3.28	1.09	0.73	0.36
2.8	0.190	0.091	3.53	1.18	0.79	0.39
3.0	0.172	0.080	3.75	1.25	0.83	0.42
3.5	0.132	0.063	4.10	1.37	0.91	0.46
4.0	0.104	0.052	4.29	1.43	0.95	0.48
4.5	0.086	0.046	4.34	1.45	0.96	0.48
5.0	0.072	0.041	4.43	1.48	0.98	0.49

7.4.1 Defining Failure and Collapse

For the pushover analysis, defining ultimate failure, displacement, and yield are important. Though there is significant amount of literature that exists on the subject, there is no consensus on which method is best (Shing et al 1989, Tomazevic 1998, Shedid et al. 2008). For the requirements for the FEMA P695, the effective yield displacement is defined as the displacement needed to reach the maximum shear if the stiffness of the design shear of the wall was constant, failure is when there is a drop of 20% from the maximum shear, and the displacement corresponding to the maximum shear is the ultimate displacement. A visual representation of these variables is shown in Figure 7-3; where V represents the base shear at yield, V_{max} is the maximum base shear, $\delta_{y,eff}$ is the effective yield displacement, and δ_u is the ultimate roof displacement (FEMA 2009). This method is conservative in nature but has been shown to be more consistent with less scatter than some of the other methods (Shedid et al. 2008).

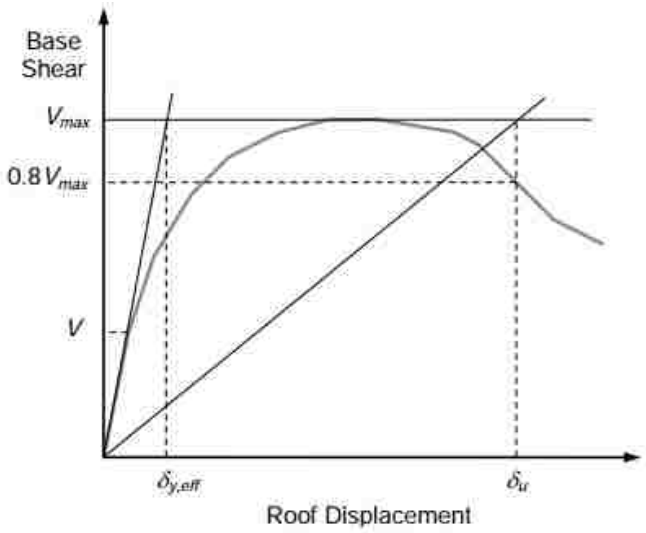

Figure 7-3 Idealized pushover curve (Shedid et al.).

Quantifying when a building collapse is significantly more difficult than establishing a failure criteria. Part of this is due to lack of research of collapse of low-rise buildings, lack of

earthquake data on dry-stack systems, and variety of failure mechanisms that can occur. In low-rise buildings, it has been shown that severe rocking and sliding can occur and collapse still not occur (NIST 2010). Numerical models can capture failure, but after failure, deflection just continues to increase significantly as shown in Figure 7-4. Due to these limitations of numerical models and lack of research to quantify collapse in low-rise buildings, defining collapse is not possible at this time. Instead, provisions are usually assigned to define collapse. One approach is to limit the displacements or deformations (Irtem, 2007). Another approach is to use both limits on displacement and failure definition (Mwafy, 2001). This second approach was used in this research. A building was considered to have collapsed when there was a drop of 20% of the maximum load, which was consistent with the failure criteria from the FEMA P-695, or the story drift reached 1%, which is consistent with ASCE requirements (ASCE 2010). These limits are considered conservative but were used due to lack of research to better define collapse. The criteria for the drop in lateral resistance was used to account for those items that are explicitly modeled, such as shear failure, buckling, rupture, bond slipping, and excessive cracking. The displacement criteria was used to account for failure criteria that cannot be explicitly modeled such as out-of-plane stability. The limit imposed was similar to the displacements observed in the out-of-plane flexure test prior to failure, as shown in Appendix A.

7.4.2 Pushover Analysis

The pushover analysis is used to determine the overstrength factor and the period based ductility. The overstrength factor, Ω, is calculated for each archetype using equation 7-2.

$$\boldsymbol{\Omega} = \frac{\boldsymbol{V_{max}}}{\boldsymbol{V}} \tag{7-2}$$

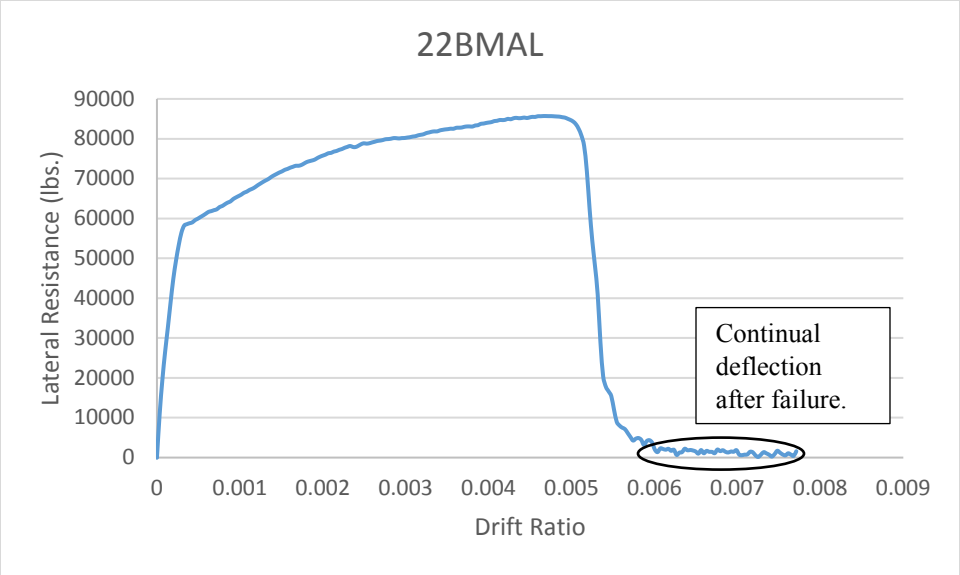

Figure 7-4 Pushover curve showing model's response after failure.

where V_{max} is the maximum shear force obtained from the pushover analysis and V is the design shear force. The system overstrength factor, Ω_o, is the largest average value of calculated overstrength from any performance group, but is limited to 1.5 times R.

The period based ductility, μ_t, for each archetype is calculated using equation 7-3. This value is used later in the time history analysis.

$$\boldsymbol{\mu_T = \frac{\delta_u}{\delta_{y,eff}}} \tag{7-3}$$

7.4.3 Collapse Margin Ratio

The probability of collapse if measured by using the collapse margin ratio (CMR). The CMR is a ratio between the median collapse intensity, S_{CT}, and the maximum considered earthquake ground motion spectral demand, S_{MT}. Therefore, the CMR is defined as shown in equation 7-4.

$$\boldsymbol{CMR = \frac{S_{CT}}{S_{MT}}} \tag{7-4}$$

S_{MT} is as the maximum considered earthquake spectral acceleration at the period of the system (ASCE 2010).

7.4.4 Spectral Shape Factor

The spectral shape of rare ground motions in the Western United States has been shown to be less damaging than other records of less intensity due to their spectral shape (Baker and Cornell, 2006). To account for the less damaging records an adjusted collapse margin ratio (ACMR) is calculated by multiplying the CMR by a spectral shape factor, which is based on the fundamental period of the structure and the period-based ductility calculated from the pushover analysis. Using these variables, the SSF is determined using Table 7-1 of FEMA P695 (FEMA 2009).

7.4.5 Quantifying Uncertainty

An acceptable collapse margin ratio is determined based on the total system collapse uncertainty. Uncertainty in collapse of the system is associated with design requirements, test data, nonlinear models, and record-to-record uncertainty. To quantify the uncertainty, each of these categories are given a quality rating and a total uncertainty is calculated using equation 7-5.

$$\boldsymbol{\beta_{TOT}} = \sqrt{\boldsymbol{\beta_{RTR}^2} + \boldsymbol{\beta_{DR}^2} + \boldsymbol{\beta_{TD}^2} + \boldsymbol{\beta_{MDL}^2}} \tag{7-5}$$

where β_{TOT} is the total structural uncertainty, β_{RTR} is the record-to-record uncertainty, β_{DR} is the design requirements uncertainty, β_{TD} is test data uncertainty, and β_{MDL} is model uncertainty.

The record-to-record uncertainty accounts for the variability in the response of the archetypes to different ground motion records. A fixed value of 0.4 is assumed for systems with a period based ductility, μ_T, greater than 3 as determined from the pushover analysis. For systems with limited ductility, the record-to-record uncertainty is at least 0.2 and calculated by equation 7-6.

$$\boldsymbol{\beta_{RTR} = 0.1 + 0.1\mu_T \leq 0.4} \quad \text{(7-6)}$$

The testing data uncertainty is accounted for by rating the test data. The rating account for the quality of the testing program as well as examination of key parameters and behavioral issues. These ratings vary from superior to poor based on the requirements of P-695 as shown in Table 7-9 (FEMA 2009). For the dry-stack system a rating of poor was given. This was due to the limited number of walls tested and the need for further testing of certain variables. These variables include thickness of the surface coating, axial loads, and spacing and size of horizontal reinforcement. The effects of using bundled bars instead of a single bar, also needs to be studied.

The design requirements uncertainty is accounted for in a similar manner to the test data uncertainty. The requirements for the design requirements as well as the quality rating system is given in Table 7-10 (FEMA 2009). The system was given a rating of good or 0.2, following the same rating system given for special reinforced masonry shear walls (NIST 2010). The basis for this is that special reinforced walls have reasonable safeguards against unanticipated failure modes, with a high confidence in the design requirements.

Finally, the uncertainty that exists in the model is quantified in a similar manner as that of the design requirements and testing data. The quality rating requirements basis is given in Table

Table 7-9 Rating of Test Data (FEMA 2009)

Completeness and Robustness	Confidence in Test Results		
	High	Medium	Low
High. Material, component, connection, assembly, and system behavior well understood and accounted for. All, or nearly all, important testing issues addressed.	(A) Superior $\beta_{TD} = 0.10$	(B) Good $\beta_{TD} = 0.20$	(C) Fair $\beta_{TD} = 0.35$
Medium. Material, component, connection, assembly, and system behavior generally understood and accounted for. Most important testing issues addressed.	(B) Good $\beta_{TD} = 0.20$	(C) Fair $\beta_{TD} = 0.35$	(D) Poor $\beta_{TD} = 0.50$
Low. Material, component, connection, assembly, and system behavior fairly understood and accounted for. Several important testing issues not addressed.	(C) Fair $\beta_{TD} = 0.35$	(D) Poor $\beta_{TD} = 0.50$	--

Table 7-10 Rating of Design Requirements (FEMA 2009)

Completeness and Robustness	Confidence in Basis of Design Requirements		
	High	Medium	Low
High. Extensive safeguards against unanticipated failure modes. All important design and quality assurance issues are addressed.	(A) Superior $\beta_{DR} = 0.10$	(B) Good $\beta_{DR} = 0.20$	(C) Fair $\beta_{DR} = 0.35$
Medium. Reasonable safeguards against unanticipated failure modes. Most of the important design and quality assurance issues are addressed.	(B) Good $\beta_{DR} = 0.20$	(C) Fair $\beta_{DR} = 0.35$	(D) Poor $\beta_{DR} = 0.50$
Low. Questionable safeguards against unanticipated failure modes. Many important design and quality assurance issues are not addressed.	(C) Fair $\beta_{DR} = 0.35$	(D) Poor $\beta_{DR} = 0.50$	--

7-11 (FEMA 2009). The model is considered generally comprehensive and reprehensive of uses of the structural system for design with use of the archetypes, and the model captures behavioral

effects that contribute to collapse. The accuracy and robustness of the model was considered medium, as out-of-plane effects were only accounted for by limiting story drift. This led to a rating of fair or 0.35.

An inherit problem that exists in determining uncertainty in this manner is the subjective nature of rating for the test data, design requirements, and model. While care was given to give ratings consistent with ratings given to other systems it is possible that another perspective would have different rating values. This can lead to significantly different acceptable collapse margin ratio, and change the seismic parameters that are calculated.

Table 7-11 Rating of Model (FEMA 2009).

Representation of Collapse Characteristics	Accuracy and Robustness of Models		
	High	Medium	Low
High. Index models capture the full range of the archetype design space and structural behavioral effects that contribute to collapse.	(A) Superior $\beta_{MDX} = 0.10$	(B) Good $\beta_{MDX} = 0.20$	(C) Fair $\beta_{MDX} = 0.35$
Medium. Index models are generally comprehensive and representative of the design space and behavioral effects that contribute to collapse.	(B) Good $\beta_{MDX} = 0.20$	(C) Fair $\beta_{MDX} = 0.35$	(D) Poor $\beta_{MDX} = 0.50$
Low. Significant aspects of the design space and/or collapse behavior are not captured in the index models.	(C) Fair $\beta_{MDX} = 0.35$	(D) Poor $\beta_{MDX} = 0.50$	--

7.4.6 Acceptable Collapse Margin Ratio

Acceptable values of collapse margin ratio are established values of acceptable probabilities of collapse based on total system collapse uncertainty. Table 7-12 gives the acceptable collapse margin ratio based on the total system collapse uncertainty. Interpolation between uncertainty levels is allowed (FEMA 2009).

Table 7-12 Acceptable Collapse Margin Ratio (FEMA 2009)

Total System Collapse Uncertainty	Collapse Probability				
	5%	10% ($ACMR_{10\%}$)	15%	20% ($ACMR_{20\%}$)	25%
0.275	1.57	**1.42**	1.33	**1.26**	1.20
0.300	1.64	**1.47**	1.36	**1.29**	1.22
0.325	1.71	**1.52**	1.40	**1.31**	1.25
0.350	1.78	**1.57**	1.44	**1.34**	1.27
0.375	1.85	**1.62**	1.48	**1.37**	1.29
0.400	1.93	**1.67**	1.51	**1.40**	1.31
0.425	2.01	**1.72**	1.55	**1.43**	1.33
0.450	2.10	**1.78**	1.59	**1.46**	1.35
0.475	2.18	**1.84**	1.64	**1.49**	1.38
0.500	2.28	**1.90**	1.68	**1.52**	1.40
0.525	2.37	**1.96**	1.72	**1.56**	1.42
0.550	2.47	**2.02**	1.77	**1.59**	1.45
0.575	2.57	**2.09**	1.81	**1.62**	1.47
0.600	2.68	**2.16**	1.86	**1.66**	1.50
0.625	2.80	**2.23**	1.91	**1.69**	1.52
0.650	2.91	**2.30**	1.96	**1.73**	1.55
0.675	3.04	**2.38**	2.01	**1.76**	1.58
0.700	3.16	**2.45**	2.07	**1.80**	1.60
0.725	3.30	**2.53**	2.12	**1.84**	1.63
0.750	3.43	**2.61**	2.18	**1.88**	1.66
0.775	3.58	**2.70**	2.23	**1.92**	1.69
0.800	3.73	**2.79**	2.29	**1.96**	1.72
0.825	3.88	**2.88**	2.35	**2.00**	1.74
0.850	4.05	**2.97**	2.41	**2.04**	1.77
0.875	4.22	**3.07**	2.48	**2.09**	1.80
0.900	4.39	**3.17**	2.54	**2.13**	1.83
0.925	4.58	**3.27**	2.61	**2.18**	1.87
0.950	4.77	**3.38**	2.68	**2.22**	1.90

8 SEISMIC PARAMETERS OF DRY-STACK MASONRY

The following sections detail the results of the pushover and time history analyses at the various seismic categories, and the resulting seismic parameters. Though it is technically required to determine that all seismic design categories meet the requirements, studies have shown that the seismic design category with the highest level of seismicity governs the evaluation of the R factor (NIST 2010). As such, research concentrated on seismic category D and changed to different seismic categories until the system was able to have an ACMR higher than the acceptable collapse margin ratio. The dry-stack system was unable to meet the requirements for seismic categories D or C, but was able to meet the requirements for seismic category B. Possible explanations for this failure are outlined in the subsequent sections.

8.1 Seismic D Category

Initial analyses attempted to show that dry-stack masonry would meet the same seismic design category requirements as that of traditional masonry. As such, an initial R value of 5, the same value used for special reinforced masonry shear walls, was used. From the pushover analysis, a period-based ductility factor of 3.28 was calculated. This resulted in an acceptable collapse margin ratio of 2.65 using equations 7-5 and 7-6. When the time history analysis of archetype ID 11DMAL was conducted, an adjusted collapse margin ratio of 0.63 was calculated. This is well below the acceptable margin ratio of 2.65 and even well below the outlier acceptable

margin ratio of 1.90. Therefore, the dry-stack system could not meet the requirements of the seismic design category D with an R value of 5.

After the initial analyses results, a new R value of 2 was used, which corresponds to the R value for ordinary masonry shear walls. During the redesign of archetype ID 11DMAL, it became apparent that the system would not meet the requirements for seismic design category D category without completely changing the established archetypes. Due to these setbacks, it was determined that the dry-stack system would never meet the requirements of seismic category D.

When similar analyses were conducted using traditional special reinforced masonry shear walls, the archetypes with these walls were also unable to meet the requirements that are outlined by FEMA for low-rise buildings (NIST 2010). In fact, for the same archetype layout and gravity loads, an ACMR of 0.66 was determined, which was just slightly higher than the value that was determined for the dry-stack system. The reasons for this results are the high-ductility demand placed on short-period archetypes, the lower ductility capacity of shorter walls, and the need to be conservative on shorter walls due to the lack of research on collapse mechanisms of low-rise buildings. It is believed that due to the low adjusted collapse margin ratio dry-stack systems with surface bond will not be able to meet the criteria.

8.2 Seismic Category C

Due to the problems encountered in seismic category D, an R value of 2 was used when designing the archetypes for seismic category C; the requirements for special reinforced masonry shear walls were, however, maintained. The pushover and time history analyses were performed on archetype ID 11CMAL. The pushover analysis resulted in a period based ductility of 3.86, which resulted in an acceptable collapse margin ratio of 2.65. The time history analysis on this

archetype resulted in an adjusted collapse margin ratio of 2.12. Again the dry-stack system was unable to meet the requirements for seismic design category C.

When traditional ordinary masonry shear walls were evaluated with the FEMA requirements they were able to meet the requirements for seismic design category C but the acceptable collapse margin ratio was only 1.69, and an ACMR of 1.91 (NIST 2010). It is expected that if future testing is conducted on the dry-stack system, there will be a decrease in the uncertainty, which will result in the dry-stack system meeting the requirements for seismic design category C. For example, if the test data was rated as fair instead of poor this would result in an ACMR of 2.34 for the performance group average and 1.75 for the outlier value. The archetype would meet the criteria for the outlier value and it would be possible that the average adjusted collapse margin ratio for the performance group would be above 2.34.

8.3 Seismic Category B

Similar to what was conducted for seismic design category C, an R value of 2 was used for the seismic design of category B. The requirements for a special reinforced masonry shear wall were also maintained for the design.

8.3.1 Pushover Analysis

A pushover analysis was performed on each archetype. Figure 8-1 shows the results from the pushover analysis of archetype 11BMAH. Similar results were obtained for all archetypes and are presented in Appendix C. From the pushover analysis the overstrength factor, Ω, and the period based ductility, μ_T, were determined and are presented in Table 8-1.

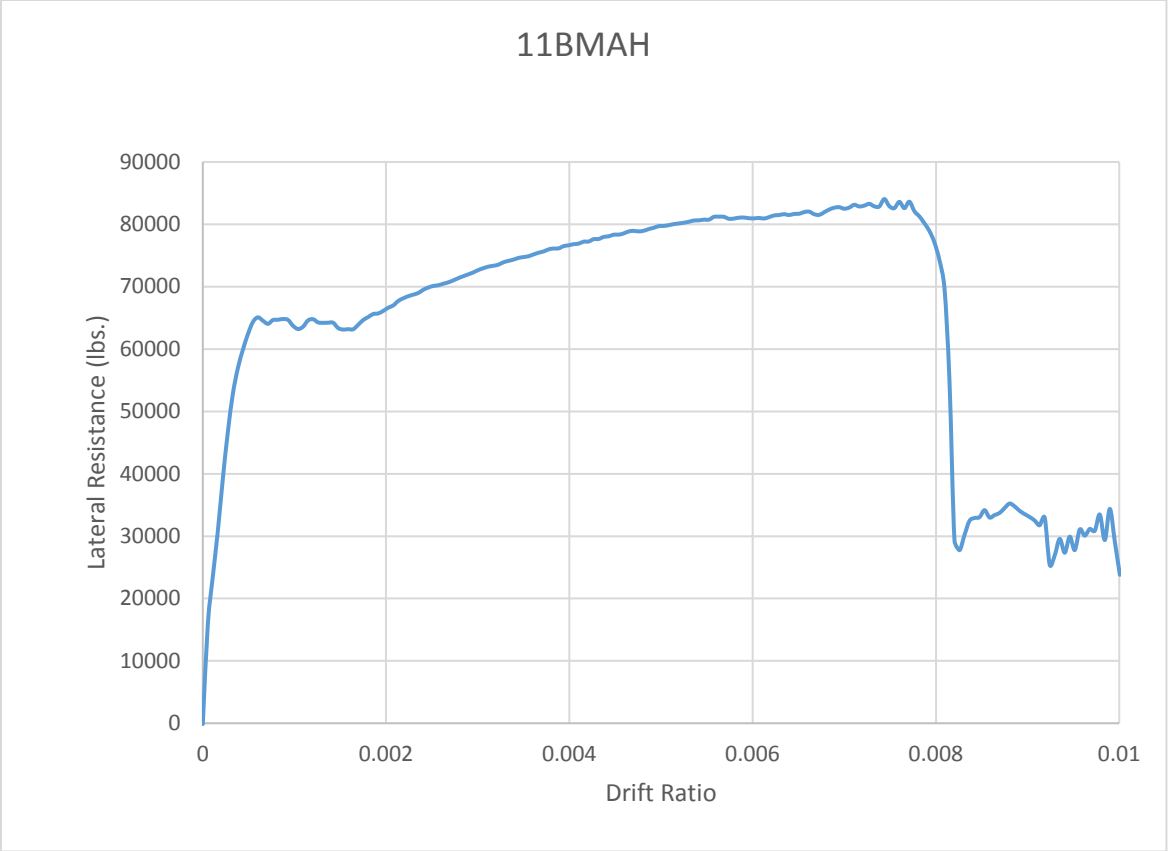

Figure 8-1 Pushover analysis of archetype 11BMAH.

Table 8-1 Pushover Analysis Results

Arch ID	μ_t	Ω
11BMAH	3.06	1.76
11BMAL	3.22	1.36
11BMIH	4.81	3.48
11BMIL	3.10	2.60
21BMAH	8.19	2.58
21BMAL	2.99	1.93
21BMIH	12.04	4.98
21BMIL	4.70	3.63
22BMAH	6.14	1.30
22BMAL	3.43	1.02
22BMIH	5.18	2.71
22BMIL	4.36	1.98

8.3.2 Time History Analysis

Each model of the archetype wall was analyzed with the 44 time history records. The spectral intensity was increased until half the time history records caused an archetype to collapse. Due to the thousands of analyses that were conducted, only a few are shown herein. Figure 8-2 shows the response of archetype 11BMAL subject to the NORTHR/MUL279 time history record at a spectral intensity of 2.21 greater than the MCE. Appendix D presents the other time history analyses results for this intensity and archetype. Similar results were obtained for all analyses, and similar to what is shown in Figure 8-2, collapse of the wall was due to the drift ratio. Table 8-2 gives the CMR for each archetype.

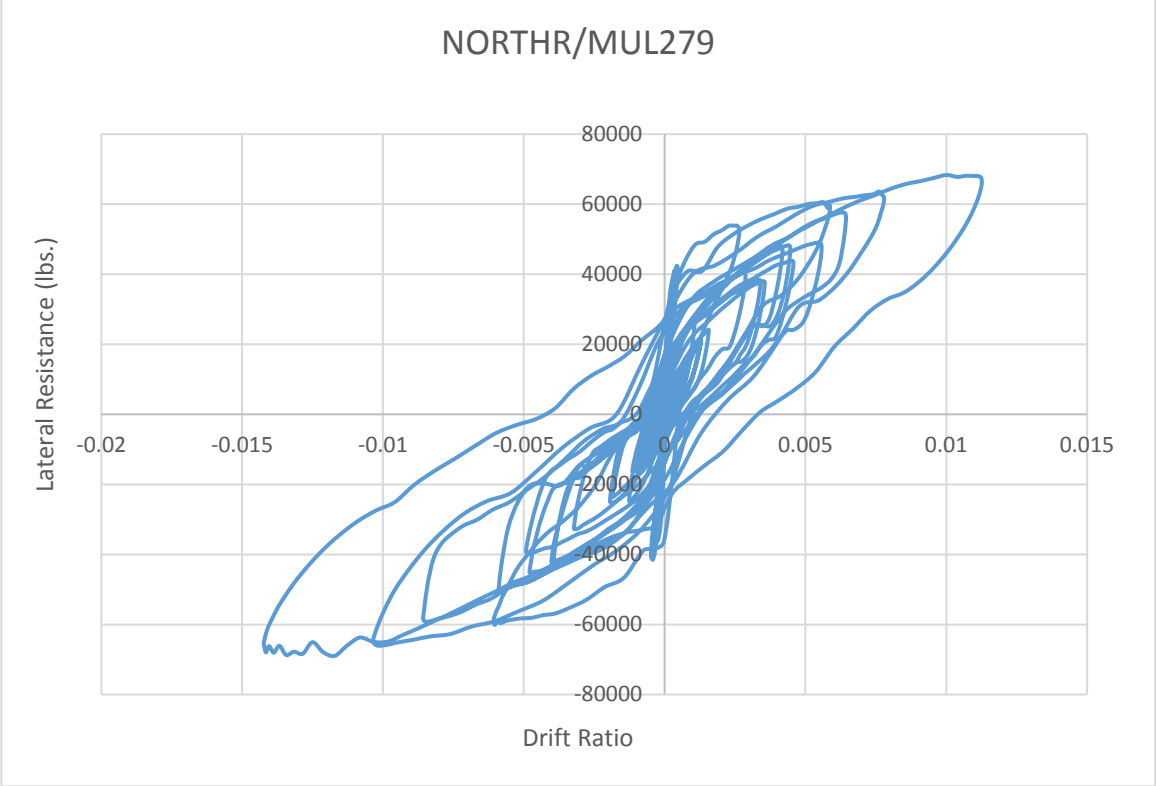

Figure 8-2 Time history analysis of archetype 11BMAL.

Table 8-2 Collapse Margin Ratio

Arch ID	CMR
11BMAH	2.53
11BMAL	2.48
11BMIH	3.12
11BMIL	2.98
21BMAH	2.75
21BMAL	2.67
21BMIH	4.21
21BMIL	3.85
22BMAH	2.61
22BMAL	2.53
22BMIH	3.35
22BMIL	3.26

8.3.3 Summary of Performance Evaluation

To meet the specified criteria, individual archetypes must have an adjusted collapse margin ratio exceeding the acceptable collapse margin ratio related to a 20% collapse probability. The average performance group adjusted collapse margin ratio then must exceed the acceptable collapse margin ratio related to a 10% collapse probability. Table 8-3 gives the evaluation results for individual archetypes and the mean of each performance group. In all cases the dry-stack system met the specified criteria.

8.3.4 Seismic Parameters

As all archetypes and performance group met the chosen value of 2, such value is the accepted response modification factor for dry-stack walls with surface coating.

The system overstrength factor, Ω_0, is the largest average overstrength factor, Ω, from the performance groups, which is 3.72 from performance group 3. However, the system overstrength factor is limited to 1.5 times the R factor or 3.5, with an overall maximum of 3. Due to these limitations, the system overstrength factor for dry-stack walls with surface coating is 3.

Table 8-3 Evaluation Results

Performance Group 1										
Arch ID	Layout	# of stories	Gravity Load	μ_t	Ω	CMR	SSF	ACMR	Acceptable ACMR	Pass/Fail
11BMAH	1	1	high	3.06	1.76	2.53	1.08	2.73	1.90	Pass
21BMAH	2	1	high	8.19	2.58	2.75	1.14	3.14	1.90	Pass
22BMAH	2	2	high	6.14	1.30	2.61	1.12	2.92	1.90	Pass
MEAN of Performance Group					1.88			2.93	2.65	Pass
Performance Group 2										
Arch ID	Layout	# of stories	Gravity Load	μ_t	Ω	CMR	SSF	ACMR	Acceptable ACMR	Pass/Fail
11BMAL	1	1	low	3.22	1.36	2.48	1.08	2.68	1.90	Pass
21BMAL	2	1	low	2.99	1.93	2.67	1.08	2.88	1.90	Pass
22BMAL	2	2	low	3.43	1.02	2.53	1.08	2.73	1.90	Pass
MEAN of Performance Group					1.44			2.76	2.65	Pass
Performance Group 3										
Arch ID	Layout	# of stories	Gravity Load	μ_t	Ω	CMR	SSF	ACMR	Acceptable ACMR	Pass/Fail
11BMIH	1	1	high	4.81	3.48	3.12	1.10	3.43	1.90	Pass
21BMIH	2	1	high	12.04	4.98	4.21	1.14	4.80	1.90	Pass
22BMIH	2	2	high	5.18	2.71	3.35	1.10	3.69	1.90	Pass
MEAN of Performance Group					3.72			3.97	2.65	Pass
Performance Group 4										
Arch ID	Layout	# of stories	Gravity Load	μ_t	Ω	CMR	SSF	ACMR	Acceptable ACMR	Pass/Fail
11BMIL	1	1	low	3.10	2.60	2.98	1.08	3.22	1.90	Pass
21BMIL	2	1	low	4.70	3.63	3.85	1.10	4.24	1.90	Pass
22BMIL	2	2	low	4.36	1.98	3.26	1.09	3.55	1.90	Pass
MEAN of Performance Group					2.74			3.67	2.65	Pass

Surprisingly, the overstrength factor was greater than the response modification factor. This indicates that when using the response modification factor the design would remain within the elastic region and not in the non-linear portion. Though unusual, this is observed for other systems. For example, ordinary reinforced masonry shear walls have an R value of 2 and Ω value of 2.5. The overstrength is generally higher than the response modification factor in systems made from brittle material such as concrete. By keeping the system in the elastic range it helps to ensure that brittle failure and collapse does not occur.

The deflection amplification factor, C_d, is calculated using the R value by equation 8-1.

$$C_d = \frac{R}{B_I} \tag{8-1}$$

where B_I is a coefficient from Table 18.6-1 of ASCE (ASCE 2010). Usually a B_I value of 1.0 is acceptable, and in general, this factor should be calculated for long-period archetypes (FEMA 2009). As no long period archetypes exist for the system analyzed, herein, B_I is assumed to be 1.0, which results in a C_d factor for dry-stack walls with surface coating of 2.

8.4 Near-Field Record Evaluation

As a case study, the Near-Field set was used to evaluate the performance of one archetype. Archetype ID 11BMIL was chosen to be evaluated as it had one of the highest adjusted collapse margin ratios from the analysis performed using the Far-Field set. The results from this analysis are shown in Table 8-4. Similar results from the evaluation of the Near-Field set were found for all structures that were evaluated (FEMA 2009). The adjusted collapse margin ratio was lower when evaluating the Near-Field set compared to the Far-Field set. This indicates that different seismic parameter should be used when designing buildings in locations close to fault lines. Further research is needed to determine if a modification factor could be applied or if the adjustment is system dependent.

Table 8-4 Evaluation Results of Near-Field Set

Arch ID	Layout	# of stories	Gravity Load	μ_t	Ω	CMR	SSF	ACMR	Acceptable ACMR	Pass/Fail
11BMIL	1	1	low	3.10	2.60	2.65	1.08	2.86	1.90	Pass

9 CONCLUSIONS

The analysis of dry-stack masonry with surface bond was examined for its shear capacity and its ability to resist seismic forces following the methodology of FEMA P-695 *Quantification of Building Seismic Parameters*. This led to the following conclusions:

1. The shear capacity of dry-stack masonry with surface bond is dependent on both the shear reinforcement and the surface bond. The masonry units provide little resistance to shear.

2. Dry-stack masonry with surface bond does not meet the requirements that are outlined for Seismic Category D in the FEMA P-695 procedure. This is due to the high-ductility demand placed on short-period archetypes, the lower ductility capacity of shorter walls, and the need to be conservative on shorter walls due to lack of research on collapse of low-rise buildings.

3. The seismic response of dry-stack masonry with surface bond is similar to that of traditional masonry to Seismic Category D.

4. Dry-stack masonry with surface bond does not meet the requirements that are outlined for Seismic Category C. However, with additional testing to reduce uncertainty, dry-stack masonry with surface bond would be able to meet the requirements of Seismic Category C.

5. Dry-stack masonry with surface bond met the requirements outlined for Seismic Category B, indicating that the system can be used for seismic category A and B regions.
6. The response modification factor, R, of 2, a system overstrength factor, Ω_0, of 3, and a displacement amplification factor, C_d, of 2, are the values to be used when designing dry-stack masonry with surface bond.

9.1 Contributions

This research has led to several contributions. These include:

1. Testing of the shear capacity of dry-stack masonry with surface bond. Prior to this research little to no research had been conducted on the shear capacity, or the ability of dry-stack masonry to resist lateral forces.
2. Proposed design equations for evaluating the shear capacity of dry-stack masonry with surface bond as shown in equations 9-1 to 9-4. Currently, dry-stack masonry with surface bond is designed using empirical methods that are highly conservative and limits the regions where it can be used.

$$\boldsymbol{\phi V_n = (V_{nsb} + V_{ns} + V_{ng})\gamma_g * \phi} \quad (9\text{-}1)$$

$$\boldsymbol{V_{ng} = 2.25 A_{ng}\sqrt{f'_g}} \quad (9\text{-}2)$$

$$\boldsymbol{V_{nsb} = 2.25 A_{nsb}\sqrt{f'_{sb}} + 0.25 P_u} \quad (9\text{-}3)$$

$$\boldsymbol{V_{ns} = 0.5\left(\frac{A_v}{s}\right) f_y d_v} \quad (9\text{-}4)$$

3. Developed a method for accounting for the surface bond of dry-stack masonry when using finite element analysis based on the joint strength.
4. Developed seismic parameters for dry-stack masonry with surface bond.

9.2 Recommendations for Future Research

To improve upon the research that has been completed, several recommendations for future research are proposed. These include:

1. Additional research on the shear capacity of dry-stack masonry with surface bond. Several variables should be explored; these include: various aspect ratios, various amounts of shear reinforcement, various gravity loads, various shear reinforcement spacing, various thicknesses of the surface bond, and using 1 reinforcement bar compared to bundled bars.
2. Further research to determine when low-rise buildings, especially masonry buildings collapse. Currently, it is difficult to assess when low-rise buildings collapse. The little research that exists, suggests that low-rise buildings have a higher deflection capacity and will not collapse even after failure.
3. Develop standards for testing surface bond. The development of standards would limit the variability that currently exists for the surface bond. These standards should attempt to standardize water-cement ratio, compressive strength testing, and workability of the surface bond.
4. Research should be conducted on the use of the Near-Field earthquake set. Currently only the Far-Field set is used for determining the seismic parameters, and the Near-Field set has been shown to result in lower collapse margin ratios.
5. Research should be conducted on normalizing the earthquake record set by the peak ground acceleration. The peak ground velocity correlates with the failure of long period buildings, while the peak ground acceleration correlates with the

failure of low period buildings. Currently, no information is available on the reason the peak ground velocity is used instead of the peak ground acceleration.

6. Research should be conducted on determining uncertainty from test data, model, and design requirements. Current methodology is somewhat subjective instead of quantitative.

REFERENCES

American Concrete Institute (ACI). *Building Code Requirements for Structural Concrete ACI 318-14*. American Concrete Institute, Farming Hills, MI 2014.

Anand, K., & Ramamurthy, K. (2000, June). Development and Performance Evaluation of Interlocking-Block Masonry. Journal of Architectural Engineering, 45-51.

Anand, K., & Ramamurthy, K. (2003). Laboratory-Based Productivity Study on Alternative Masonry Systems. Journal of Construction Engineering and Management, 237-242.

ASCE. 2010. Minimum Design Loads for Buildings and Other Structures. ASCE/SEI Standard 7-10.

ASTM Standard 1437 "Standard Test Method for Flow of Hydraulic Cement Mortar," American Society for Testing and Materials, ASTM International, West Conshohocken, PA, www.astm.org

ASTM Standard C1019 "Standard Test Method for Sampling and Testing Grout," American Society for Testing and Materials, ASTM International, West Conshohocken, PA, www.astm.org

ASTM Standard C109 "Standard Test Method for Compressive Strength of Hydraulic Cement Mortars (Using 2-in or Cube Specimens)," American Society for Testing and Materials, ASTM International, West Conshohocken, PA, www.astm.org

ASTM Standard C1314 "Standard Test Method for Compressive Strength of Masonry Prisms," American Society for Testing and Materials, ASTM International, West Conshohocken, PA, www.astm.org

ASTM Standard C140 "Standard Test Methods for Sampling and Testing Concrete Masonry Units and Related Units," American Society for Testing and Materials, ASTM International, West Conshohocken, PA, www.astm.org

ASTM Standard C143 "Standard Test Method for Slump of Hydraulic-Cement Concrete," American Society for Testing and Materials, ASTM International, West Conshohocken, PA, www.astm.org

ASTM Standard C1717 “Standard Test Methods for Conducting Strength Tests of Masonry Wall Panels,” American Society for Testing and Materials, ASTM International, West Conshohocken, PA, www.astm.org

ASTM Standard C1552 “Standard Practice for Capping Concrete Masonry Units, Related Units and Masonry Prims for Compression Testing,” American Society for Testing and Materials, ASTM International, West Conshohocken, PA, www.astm.org

ASTM Standard C230 “Standard Specification for Flow Table for Use in Tests of Hydraulic Cement,” American Society for Testing and Materials, ASTM International, West Conshohocken, PA, www.astm.org

ASTM Standard E519 “Standard Test Method for Diagonal Tension (Shear) in Masonry Assemblages,” American Society for Testing and Materials, ASTM International, West Conshohocken, PA.

Baker, J.W. and Cornell, C.A., 2006, “Spectral Shape, Epsilon and Record Selection,” Earthquake Engineering and Structural Dynamics, 34 (10), pp. 1193-1217

Bennati, S., Nardini, L., and Salvatore, W. (2005). “Dynamic Behavior of a Medieval Masonry Bell Tower. II: Measurement and Modeling of the Tower Motion.” J. Struct. Eng., 10.1061 (ASCE) 0733-9445 (2005) 131:11 (1656), 1656-1664.

Bosiljkov, V., Totoev, Y. Z., and Nichols, J. M. 2005. “Shear modulus and stiffness of brickwork masonry: An experimental perspective.” Struct. Eng. Mech., 20(1), 21–43.

Brandow, G., Ekwueme C., & Hart G. (2015). *2012 Design of Reinforce Masonry Structures*. Concrete Masonry Association of California and Nevada. Citrus Heights, CA.

Calderini, C., Cattari, S., & Lagomarsino, S. (2010). The Use of the Diagonal Compression Test to Identify the Shear Mechanical Parameters of Masonry. Construction and Building Materials, 677-685.

Chaimoon, K., and Attar, M. M. (2007). “Modeling of Unreinforced Masonry Walls under Shear and Compression.” Engineering Structures Vol. 29, Issue 9, 2007.

Computer Program VecTor 2 version 3.8, (University of Toronto, 2011)

Dhanasekar, M., and Haider, W. (2008) “Explicit Finite Element Analysis of Lightly Reinforced Masonry Shear Walls.” Computers and Structures Vol 86, Issues 1-2, January 2008.

Dizhur, D., & Ingham, J. (2013). Diagonal Tension Strength of Vintage Unreinforced Clay Brick Masonry Wall Panels. Construction and Building Materials, 418-427.

Eligehausen, R., Popov, E., and Bertero, V. 1983. "Local Bond Stress-Slip Relationship of Deformed Bars under Generalized Excitations", Report No. UCB/EERC-83/23, Earthquake Engineering Center,University of California, Berkeley

Elmapruk, J. (2010). Shear Strength of Partially Grouted Squat Shear Walls. Washington State University.

Elmenshawi, A., Sorour, M., Mufti, A., Jaeger, L., and Shrive, N. (2010). "Damping Mechanisms and Damping Ratios in Vibrating Unreinforced Stone Masonry." Engineering Structures, Vol. 32 Issue 10, 3269-3278, Oct 2010.

FEMA P695: Quantification of Building Seismic Performance Factors, Federal Emergency Management Agency, Washington, D.C., June 2009

Fonseca, F., & Murray, E. (2012). Axial Capacity of Dry-Stacked ENDURA Masonry Walls. 15th International Brick and Block Masonry Conference.

Gabor, A., Ferrier, E., Jacquelin, E., & Hamelin, P. (2006). Analysis and Modelling of the In-Plane Shear Behavior of Hollow Brick Masonry Panels. Construction and Building Materials, 308-321.

Ghanem, G. M., Essawy, A. S., and Hamid, A. A. (1992). "Effect of steel distribution on the behavior of partially reinforced masonry walls." Proceedings of the 6th Canadian Masonry Symposium, vol. 1, 365–376. Saskatoon, SK, Canada.

Haach, V.G., Vasconcelos, G., and Lourenco, P.B. (2014). "Study of the behavior of reinforced masonry wallets subjected to diagonal compression through numerical modelling". 9th International Masonry Conference, 2014.

Hall, J. F. (2006), Problems encountered from the use (or misuse) of Rayleigh Damping. Earthquake Engr. Struct. Dyn., 35: 525–545.

Hognestad, E. (1951). "A study on combined bending and axial load in reinforced concrete members." Univ. of Illinois Engineering Experiment Station, Univ. of Illinois at Urbana-Champaign, IL, 43-46.

Hines, T. (1994, February 1). Using Dry-Stacked Concrete Masonry for Affordable Construction. Masonry Construction.

ICC-ES Legacy Report, "IMSI Insulated Reinforced Masonry Wall System", ICC Evaluation Services, Inc. ER-4997, 2001.

International Code Council (ICC). (2012). 2012 international building code. Country Club Hills, Ill: ICC.

Irtem, E., Turker, K., and Hagul, U. (2007). "Causes of Collapse and Damage to Low-Rise RC Buildings in Recent Turkish Earthquakes." J. Perform. Constr. Facil., 1061/ASCE 0887-3828(2007)21:5(351), 351-360.

Lotfi, H.R., and Shing, P.B. (1991). "An Appraisal of Smeared Crack Models for Masonry Shear Wall Analysis." Computers and Structures Vol. 41, No3. Pp 413-425, 1991.

Lourenco, P., and Ramos, L. (2004, May). "Characterization of Cyclic Behavior of Dry Masonry Joints." Journal of Structural Engineering, 779-786.

Magnese, G. and Calvi, G.M (1997) "In-Plane Seismic Response of Brick Masonry Walls." Earthquake Engineering & Structural Dynamics, 1091-1112.

Maleki, M. (2008). Behaviour of Partially Grouted Reinforced Masonry Shear Walls under Cyclic Reversed Loading. Ph.D. thesis, McMaster University, Hamilton, ON, Canada.

Marfia, S., and Sacco, E. (2001). "Modeling of Reinforced Masonry Elements." International Journal of Solids and Structures. Volume 38, June 2001.

Marzahn, G. (1999). "Investigation on the initial settlement of dry-stacked masonry under compression." LACER No. 4, Institute of Massivbau and Baustoff Technology, Leipzig Univ., Germany, 253–269.

Marzahn, G., and König, G. (2002). "Experimental Investigation of Longterm Behavior of Dry-Stacked Masonry." J. Masonry Soc., 20(1), 9–21.

Masonry Standards Joint Committee (MSJC), *Building Code Requirements for Masonry Structures,* TMS 402-13/ACI 530-13/ASCE 5-13, The Masonry Society, Boulder, CO, 2013

Matsumura, A. (1987). "Shear strength of reinforced hollow unit masonry walls—differences between partially grouted walls and fully grouted walls." Proceedings of the 4th North American Masonry Conference. Los Angeles.

Matsumura, K. (1992). "On the Intensity Measure of Strong Motions Related to Structural Failures." Earthquake Engineering, Tenth World Conference. Madrid, Spain.

Minaie, E. (2009). Behavior and Vulnerability of Reinforced Masonry Shear Walls. Ph.D. thesis, Drexel University, Philadelphia.

Mwafy, A.M, and Elnashai, A.S (2001). "Static Pushover versus Dynamic Collapse Analysis of RC Buildings." Engineering Structures, Vol 23 Issue 5, 407-424, May 2001.

National Institute of Standards and Technology (NIST) (2010). Evaluation of the FEMA P-695 Methodology for Quantification of Building Seismic Performance Factors (NIST GCR 10-917-8), prepared by the NEHRP Consultants Joint Venture for the National Institute of Standards and Technology. Gaithersburg, Maryland:NIST.

Nolph, S. (2010). "In-Plane Shear Performance of Partially Grouted Masonry Shear Walls." Washington State University, Pullman, WA.

Palermo, D., and Vecchio, F.J., 2002, "Behaviour and Analysis of Reinforced Concrete Walls Subjected to Reversed Cyclic Loading." Publication No. 2002-01, Department of Civil Engineering, University of Toronto, 351 pp.

Park, R., Priestley, M.J.N. and Gill, W.D. (1982). "Ductility of Square Confined Concrete Columns" Journal of the Structural Div., ASCE, 108 (4), 929-50.

Priestley, M.J.N, Calvi, G.M., Kowalsky, M.J. *Displacement-Based Seismic Design of Structures*. IUSS Press, Italy, 978-88-6198-000-6, 2007.

Ramamurthy, K., and Nambiar, E. (2004). "Accelerated Masonry Construction: Review and Future Prospects." Progress in Structural Engineering and Materials, 1-9.

Schultz, A. E. (1996a). "Seismic resistance of partially–grouted masonry shear walls." Worldwide Advances in Structural Concrete and Masonry, 211–222. American Society of Civil Engineers (ASCE).

Schultz, A. E. (1996b). "Seismic resistance of partially–grouted masonry shear walls." Proceedings of the 11th World Conference on Earthquake Engineering, 1221. Acapulco, Mexico.

Schultz, A. E., Hutchinson, R. S., and Cheok, G. C. (1998). "Seismic performance of masonry walls with bed joint reinforcement." Structural Engineers World Congress Proceedings, T119-4. San Francisco.

Shedid, M.T., Drysdale, R.G., and El-Dakhakhni, W.W. (2008). "Behavior of Fully Grouted Reinforced Concrete Masonry Shear Walls Failing in Flexure: Experimental Results." J. Struct. Eng, 134(11), 1754-1767.

Shing, P., Noland, J., Klamerus, E., and Spaeh, H. (1989). "Inelastic Behavior of Concrete Masonry Shear Walls." *J. Struct. Eng.*, 115(9), 2204–2225.

Shing, P.B., Schuller, M.P, Hoskere, V.S, and Carter, E. (1990a) "Flexural and Shear Response of Reinforced Masonry Walls." American Concrete Institute Structural Journal, Farmington Hills, MI, Vol 87, No. 7, November-December 1990a.

Shing, P.B., Schuller, M.P, and Hoskere, V.S. (1990b). “In-Plane Resistance of Reinforce Masonry Shear Walls.” American Society of Civil Engineers Structural Journal, Reson, VA, Vol 116. No. 3, March 1990b.

SouthWest Management (2014). “ENDURA Design Tables.” Orem, UT.

Stavridis, A., and Shing, P.B. (2010). “Finite-Element Modeling of Nonlinear Behavior of Masonry-Infilled RC Frames.” Journal of Structural Engineering, Volume 136, Issue 3, March 2010.

Sveinsson, B. I., McNiven, H. D., and Sucuoglu, H. (1985). “Cyclic loading tests of masonry single piers, vol 4–additional tests width height to width ratio of 1.” Tech. Rep. UCB/EERC–85/15, University of California, Berkeley, CA.

Thanoon, W., Jaafar, M., Abdul Kadir, M., Abang Ali, A., Trikha, D., & Najm, A. (2004). “Development of an Innovative Interlocking Load Bearing Hollow Block System in Malaysia.” Construction and Building Materials, 445-454.

Tomaževic, M., and Weiss P. (1994). Seismic Behavior of Plain- and Reinforced-Masonry Buildings.” Journal of Structural Engineering, Volume 120 Issue 2, February 1994.

Tomazevic, M. (1998). “Earthquake-Resistant Design of Masonry Buildings.” Imperial College Press, Covent Garden, London.

Uang, C. (1991). “Establishing R (or Rw) and Cd Factors for Building Seismic Provisions”. Journal of Structural Engineering, 19-28.

Vecchio, F.J. and Collins, M.P., 1986. "The Modified Compression Field Theory for Reinforced Concrete Elements Subject to Shear." ACI Journal Vol. 83, No. 2, pp. 219-231.

Vecchio, F.J. and Collins, M.P., 1993. "Compression Response of Cracked Reinforced Concrete", ASCE Journal of Structural Engineering, Vol. 119, No. 12, pp. 3590-3610.

Vermeltfoort ATh, Van der Pluijm R. “Strength and Deformation Properties of Masonry to be used in Computer Calculations. In: Proceedings of the 9th IBMaC. 1991. P. 244-52.

Voon, K.C. and Ingham, J.M (2006). “Experimental In-Plane Shear Strength Investigation of Reinforced Concrete Masonry Walls.” Journal of Structural Engineering, 400-408.

Wong, P.S., Vecchio, F.J, and Trommels, H. (2002). *VecTor 2 & FormWorks User’s Manual*. Second Edition. University of Toronto, Canada.

A OUT-OF-PLANE TESTING

Out-of-plane flexural tests were performed on 8, 8 ft. by 8 ft. walls. In addition to the walls tested, testing was conducted on the various components used in the construction of the walls.

A.1 Component Testing

The same component testing that was done for the diagonal-tension test was also done for the out-of-plane flexural tests.

A.1.1 Grout

The grout was made and tested in the same manner as outlined in the Diagonal-Tension test section. Results from the compression testing are summarized in Table A-1, which also lists the corresponding walls.

Table A-1 Grout Prism Compressive Strength Results

Wall	Prism	Area (in^2)	Max Force (lbs.)	Compressive Strength (psi)
3&4	22	16.5	70885	4291
3&4	23	16.6	68930	4152
3&4	24	17.4	72100	4147
5,6,7,& 8	25	16.9	71410	4238
5,6,7,& 8	26	17.2	67075	3894
5,6,7,& 8	27	16.8	67555	4030

A.1.2 Mortar

The mortar was made and tested in the same manner as outlined in the Diagonal-Tension test section. Results from the compression testing are summarized in Table A-2. The mortar was only used on walls 7 and 8.

Table A-2 Mortar Cube Compressive Strength Results

Cube	Area (in^2)	Max Force (lbs.)	Compressive Strength (psi)
7	4.1	28545	7030
8	4.2	27683	6653
9	4.1	28505	6952

A.1.3 Surface Coating

The surface coating was made and tested in the same manner as outlined in the Diagonal-Tension test section. Results from the compression testing are summarized in Table A-3 along with their corresponding walls.

Table A-3 Surface Coating Compressive Strength Results

Wall	Cube	Area (in^2)	Max Force (lbs.)	Compressive Strength (psi)
Flexural 1, 2, 3, & 4	v	4.1	24050	5923
Flexural 1, 2, 3, & 4	w	4.0	22115	5474
Flexural 1, 2, 3, & 4	x	4.1	22025	5345
Flexural 5, 6, 7, & 8	y	4.1	30455	7501
Flexural 5, 6, 7, & 8	z	4.0	28905	7190
Flexural 5, 6, 7, & 8	aa	4.1	29080	7127

A.1.4 Masonry Prism Compressive Strength

The masonry was made and tested in the same manner as discussed in the Diagonal-Tension test section. Results from the compression testing are summarized in Table A-4 along with their corresponding walls.

Table A-4 Masonry Prism Compressive Strength Results

Wall	Prism	Area (in^2)	Max Force (lbs.)	Compressive Strength (psi)
Flexural Wall 1, 2, 3, & 4	NN	33.1	47610	1436
Flexural Wall 1, 2, 3, & 4	OO	33.0	48982	1485
Flexural Wall 1, 2, 3, & 4	PP	32.2	41517	1291
Flexural Wall 1, 2, 3, & 4	QQ	52.0	81791	1573
Flexural Wall 1, 2, 3, & 4	RR	52.7	95212	1808
Flexural Wall 1, 2, 3, & 4	SS	52.5	89293	1702
Flexural Wall 5, 6, 7, & 8	TT	31.6	43852	1388
Flexural Wall 5, 6, 7, & 8	UU	32.7	43527	1332
Flexural Wall 5, 6, 7, & 8	VV	33.0	49023	1486
Flexural Wall 5, 6, 7, & 8	WW	52.5	89628	1708
Flexural Wall 5, 6, 7, & 8	XX	51.1	82947	1622
Flexural Wall 5, 6, 7, & 8	YY	53.0	91100	1719

A.2 Wall Construction

The walls were built on a steel channel with the rebar needed for the varying configurations welded to the bottom of the channel. There were 4 configurations that were tested: ungrouted, grouted vertically every 4 ft. and horizontally every 4 ft., grouted vertically every 2 ft. and horizontally every 4 ft., and grouted vertically every 4 ft. and horizontally every 4 ft. with thin mortar layer between each course. The configuration of each wall can be seen in Table A-5. Visual representation of the layout can be seen in Figure A-1 where the grey areas represent the grout cells.

Table A-5 Wall Configurations

Wall	Grout Pattern	Thin Mortar
#1	Ungrouted	
#2	Ungrouted	
#3	4'x4'	
#4	4'x4'	
#5	2'x4'	
#6	2'x4'	
#7	4'x4'	X
#8	4'x4'	X

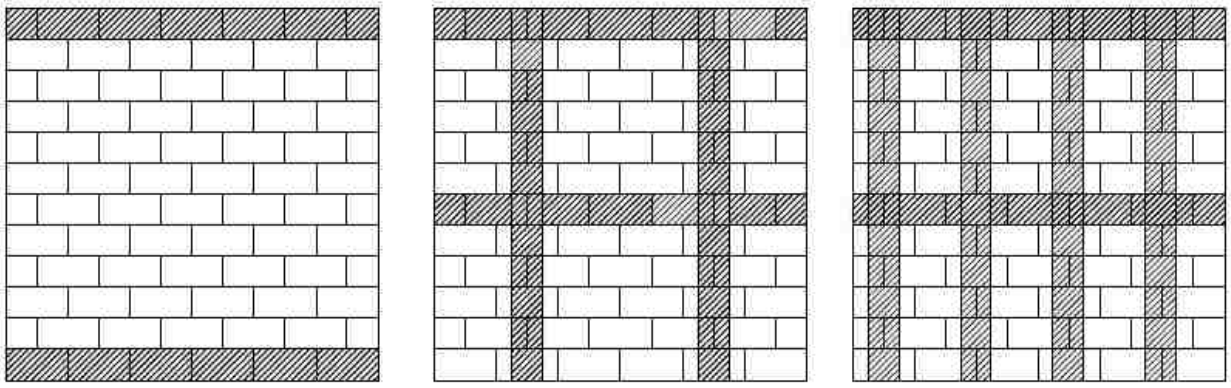

(a) Ungrouted **(b) 4' x 4'** **(c) 2' x 4'**

Figure A-1 Wall configurations for out-of-plane flexural test.

Similar to the in-plane shear tests that ungrouted walls were in fact grouted on the top and bottom course. This was done so that small amounts of rebar could be welded to the steel channel and connect to the wall for easy of transport and to insure the wall stayed connected to the apparatus during testing.

A.3 Test Setup

A W 12x64 that was 10 ft. in length was attached to the strong floor with steel bars that were post tensioned. 3 steel plates were welded across the steel beam and steel clevises were

welded to the top of the plates. This was to pin the bottom steel channel that the walls were built upon. A steel channel was also placed on top of the wall and bolted through the top grout layer on both sides. On top of this channel steel plates had been welded to act as pick points and other plates to weld more clevises to. These clevises were then pinned to a stiffened C 8x13.5. This c channel was then bolted to W 8x31 steel columns through slotted holes. The slotted were chosen to facilitate moving the wall in and out and to allow for and deformation of the wall with adding as little shear possible.

The walls were then loaded by a 100 kip actuator. To distribute the load C 8x11.5 channels were welded to a plate and connected through bolts to the actuator. These channels were 8.5 ft. in length and were placed at third points at the wall or at 2 ft. 8 in. and at 5 ft. 4 in. These channels were long enough to run the whole length of the wall with a little extra, and the 8 in. channel width was chosen to distribute the load evenly and without causing crushing in the concrete blocks. Figure A-2 shows the design of the test setup and Figure A-3 shows pictures of the actual test setup.

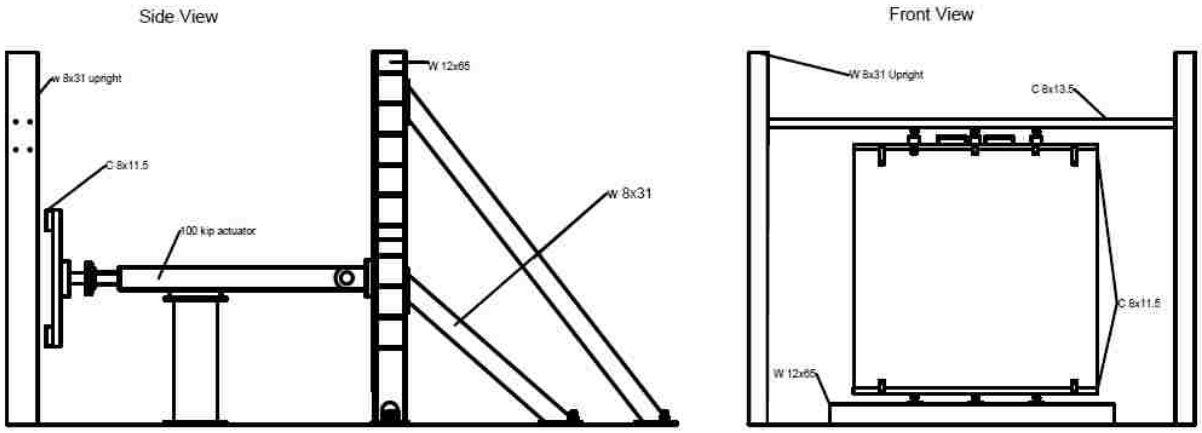

Figure A-2 Design for test setup of out-of-plane flexural test.

(a) Whiffle frame.

(b) Testing frame.

(c) Clevsis attached to bottom of wall channel.

(d) Clevises attached to top channel.

Figure A-3 Pictures of test setup.

A.4 Instrumentation and Testing Protocol

The out-of-plane displacement and load was measured during the test. The load was taken from the computer system connected to the calibrated actuator. Load was applied to the walls at a displacement rate of 0.1875 in. per min.

The displacement was taken from 10 linear variable differential transformers (LVDTs). The LVDTs were placed with 3 at 2 ft. from the bottom of the wall each being placed 2 ft. apart from each other and 2 ft. from the sides of the walls. At 4 ft. from the bottom of the wall 4

LVDTs were placed with 2 of them being 16 in. away from the edge of the wall and the other 2 on the sides of the actuator 2 ft. in from the other LVDTs. The final 3 LVDTs were placed 2 from the top of the wall each being 2 ft. apart from each other and 2 ft. away from the edge of the wall. Readings were taken every 0.5 seconds during testing. Figure A-4 shows a visual representation of where the LVDTs were placed, where the red dots are the spots were the LVDTs were placed.

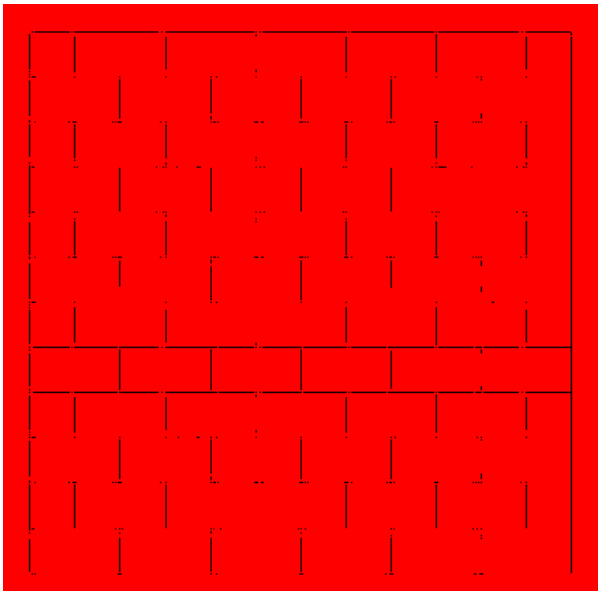

Figure A-4 Instrumentation for out-of-plane flexural test.

General test results are shown in Table A-6. In the results shown the max load in psi was found by taking the maximum load from the actuator and dividing it by the area of the steel channels. The actual moment was found using equation A-1.

$$M_u = w * h * f * a \quad \text{(A-1)}$$

where M_u is the moment in the center of the wall, w is the width of the area being considered in this case 12 in., h is the height of the channel or 8 in., f is the max load in psi, and a is the spacing between the top or bottom of the wall to the steel channel or 32 in.

Table A-6 General Results for Out-of-Plane Flexural Test.

Wall	Configuration of walls	Max Load (lbs)	Max Load (psi)	Actual Mu (lb-in/ft)
1	ungrouted	1069	0.7	2148
2	ungrouted	1274	0.8	2559
3	4'x4'	10974	7.2	22045
4	4'x4'	9834	6.4	19754
5	2'x4'	15285	10.0	30704
6	2'x4'	13499	8.8	27116
7	4'x4' thin mortar	10435	6.8	20961
8	4'x4' thin mortar	13287	8.7	26690

A.5 Wall 1

Wall 1 was an ungrouted wall with no apparent defects prior to testing. During testing intermediate cracking could be heard but no visible damage was seen until the max load of 1069.1 lbs. was reached. At the point of max load a crack opened up just below the bottom third point where load had been applied. In addition a smaller crack 2 courses from the top opened and the wall was unable to resist load. Figure A-5 shows the load in psi vs displacement of the middle of the wall for this test. Figure A-6 shows pictures of the wall after failure.

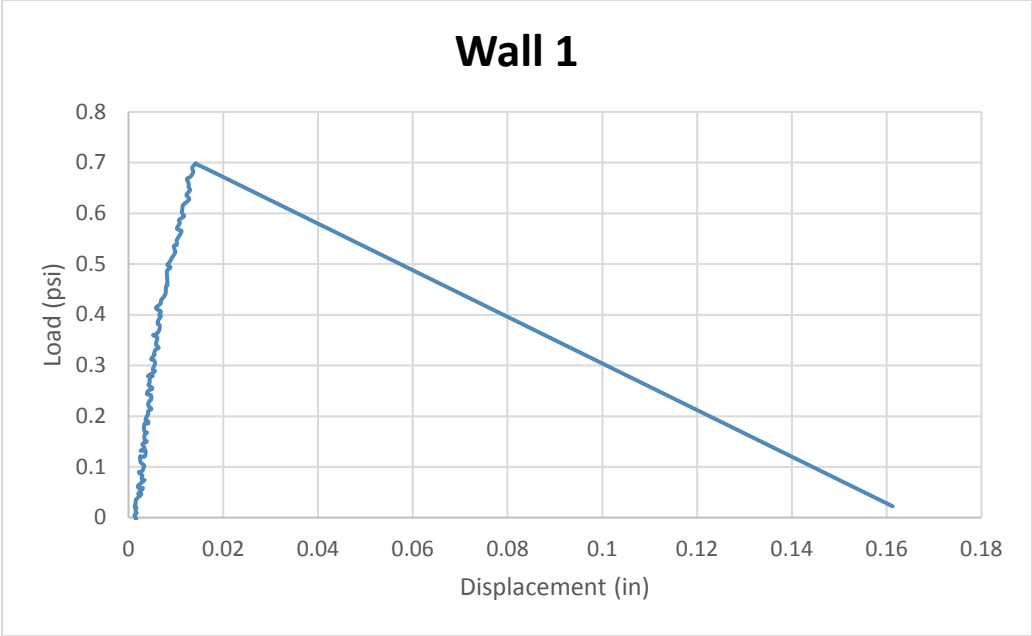

Figure A-5 Load vs displacement wall 1.

(a) Overall appearance. **(b) Crack below third point** **(c) Crack at top of wall.**

Figure A-6 Pictures of wall 1 after failure.

A.6 Wall 2

Wall 2 was an ungrouted wall that had no apparent defects prior to testing. At around 500 lbs. partial delamination of the surface bond from the wall was observed. At max load of 1274 lbs. sudden failure occurred and a crack opened up just under the bottom third point where

load was applied. Figure A-7 shows the load in psi vs displacement of the middle of the wall. Figure A-8 shows pictures of the wall after failure.

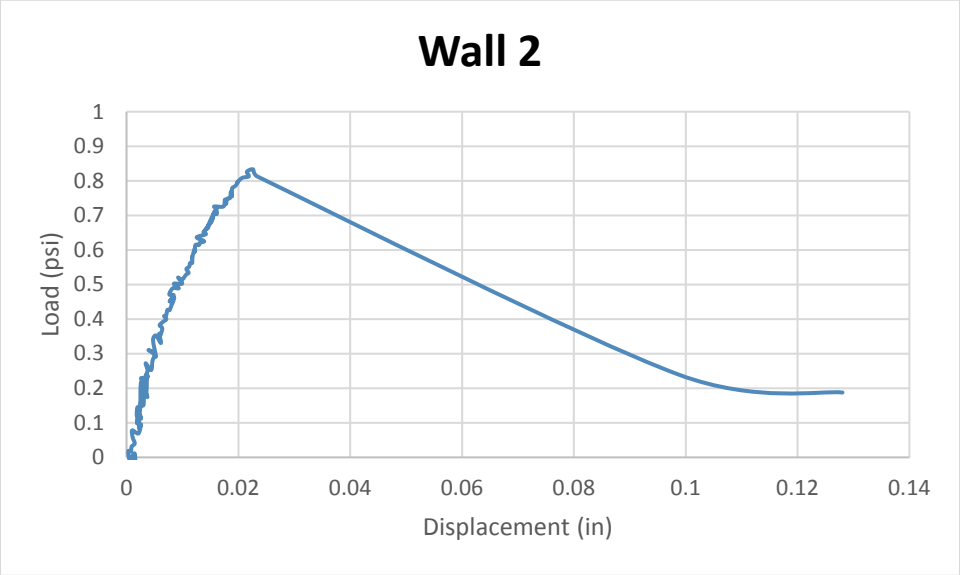

Figure A-7 Load vs displacement curve for wall 2.

(a) Overall view. **(b) Crack below third point.** **(c) Delamination.**

Figure A-8 Failure in wall 2.

A.7 Wall 3

Wall 3 was grouted every 4 ft. vertically and every 4 ft. horizontally. Prior to testing there were some hairline cracks in the middle of the wall that propagated horizontally. These cracks were only through the surface layer and did not penetrate through the structural layer and were not considered important in the outcome of the test.

The load steadily increased until around 6,000 lbs. when the outside webs of the blocks cracked. This lowered the load being resisted slightly but then load continued to increase. Around 7,000 lbs. cracks appeared horizontally between each course layer. This cracks continued to widen until the max load was reached at 10974.4 lbs. At this point the whole wall shook and then a big opening appeared just below the bottom third point of the wall. Figure A-9 shows the load in psi vs displacement of the middle of the wall. Figure A-10 shows pictures of the wall after failure.

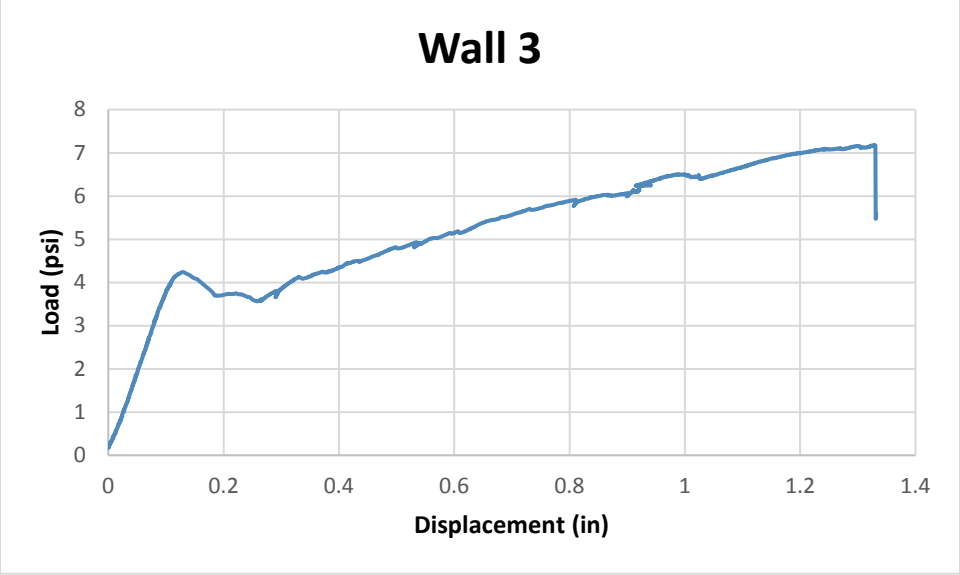

Figure A-9 Load displacement curve for wall 3.

(a) Cracks in webs. **(b) Overall view.** **(c) Horizontal cracks.**

Figure A-10 Failure in wall 3.

A.8 Wall 4

Wall 4 was grouted every 4 ft. horizontally and 4 ft. vertically. No apparent defects were seen prior to testing. The loading increased steadily until around 7,500 lbs. when the outside webs at the bottom of the wall cracked. The wall resisted less load but then continued to increase again. Around 8,500 lbs. horizontal cracks began to appear at every course. When it reached max load of 9833.6 lbs. a sudden failure at the top course occurred with a large opening. At this point the wall lost the ability to resist almost all load. Figure A-11 shows the load vs. displacement of the middle of the wall. Figure A-12 shows pictures of wall 4 after failure.

A.9 Wall 5

Wall 5 was grouted horizontally every 4 ft. and vertically every 2 ft. Small hairline cracks were visible in the surface coat but did not enter into the structural coat and were not considered important to the results of the test.

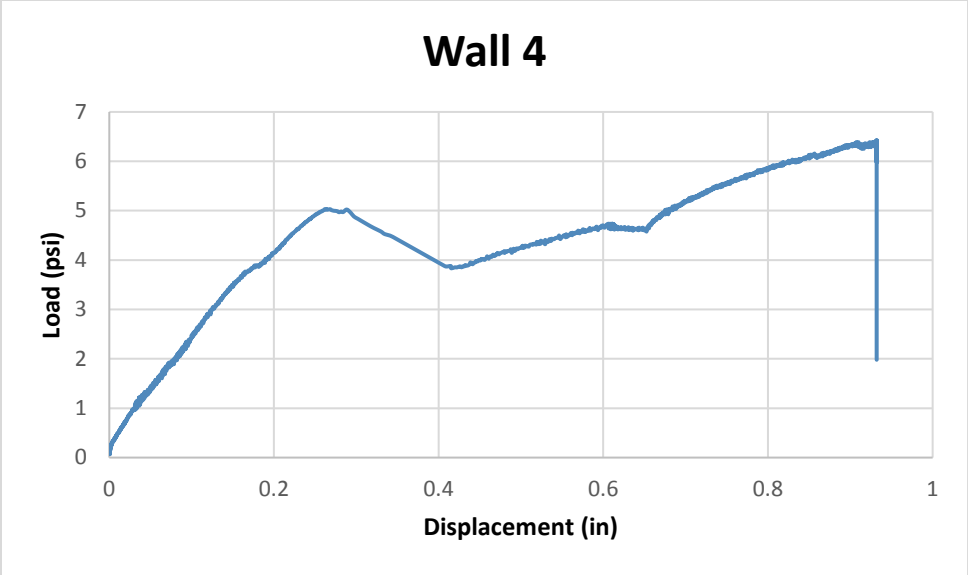

Figure A-11 Load vs displacement curve of wall 4.

(a) Overall view **(b) Crack at top of wall.** **(c) Cracking through webs.**

Figure A-12 Failure in wall 4.

The load steadily increased with small cracking noises being heard. At around 9,000 lbs. the outside webs cracked. After a small decline in the load the load continued to increase steadily until it reached its max load of 15,284.9 lbs. At the max load cracks appeared two courses from the bottom and opened a significant amount. The wall was unable to resist load

after this. However, after the load was taken off the wall the openings closed up. Figure A-13 shows the load vs displacement graph for the middle of the wall. Figure A-14 shows pictures of the wall after failure.

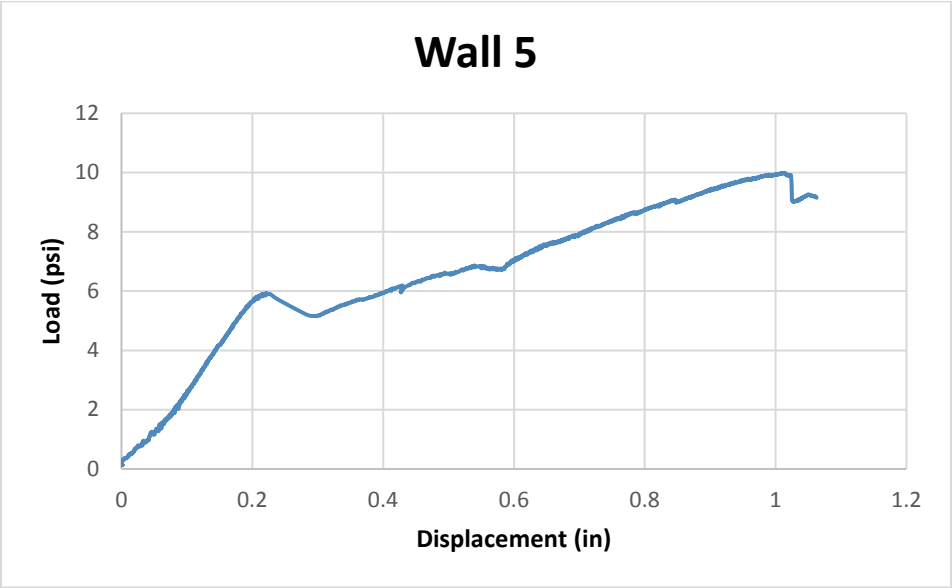

Figure A-13 Load-displacement curve for wall 5.

(a) Cracking in webs. **(b) Cracking at bottom of wall.** **(c) No visible cracks in top of wall.**

Figure A-14 Failure in wall 5.

A.10 Wall 6

Wall 6 was grouted every 4 ft. horizontally and every 2 ft. vertically. No apparent defects were noticed prior to testing. Load increased steadily until around 9,000 lbs. when the outside webs cracked. At 10,000 lbs. small cracks became visible between course layers. Load continued to increase until max load at 13,498.6 lbs. At this point a large opening cracked open just below the top course, and the wall was unable to resist the load. Figure A-15 shows the load displacement graph for the middle of the wall. Figure A-16 shows pictures of the wall after failure.

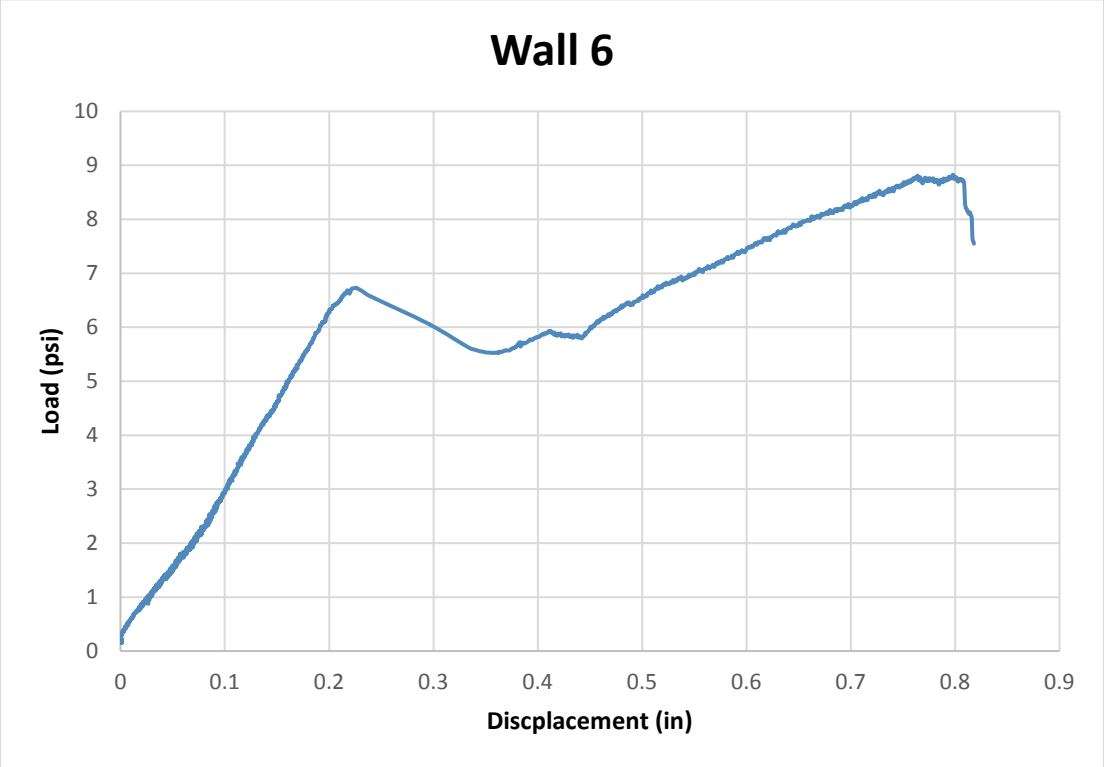

Figure A-15 Load-displacement curve for wall 6.

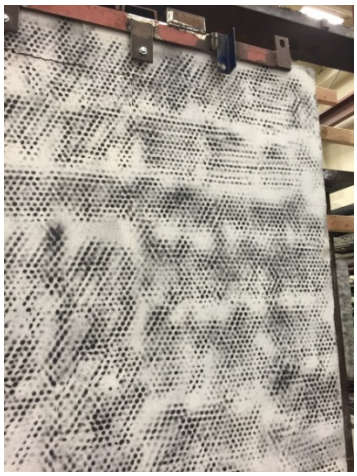

(a) Cracks in webs. **(b) Crack in top course.** **(c) Typical horizontal cracking.**

Figure A-16 Failure in wall 6.

A.11 Wall 7

Wall 7 was grouted every 4 ft. horizontally and 4 ft. vertically. In addition, a thin layer of mortar was used between each course layer. Prior to testing at each course layer small bulges and cracking was noticed and is attributed to the thin layer of mortar. Each of these was minor and not considered significant to the test being performed.

At testing the load steadily increased and unlike previous tests the outside webs of the wall did not break. Around 5,000 lbs. cracking could be heard and small cracks began to appear on the face of the wall. At 7,000 lbs. these cracks propagated horizontally until there were horizontal cracks between each course layer. The load continued to increase until the maximum load of 10434.7 lbs. when a large opening between the top two courses opened up with propagating cracks downward. At this point the wall was unable to continue resisting load. Figure A-17 shows the load vs displacement graph for the middle of the wall. Figure A-18 shows pictures of the wall after failure.

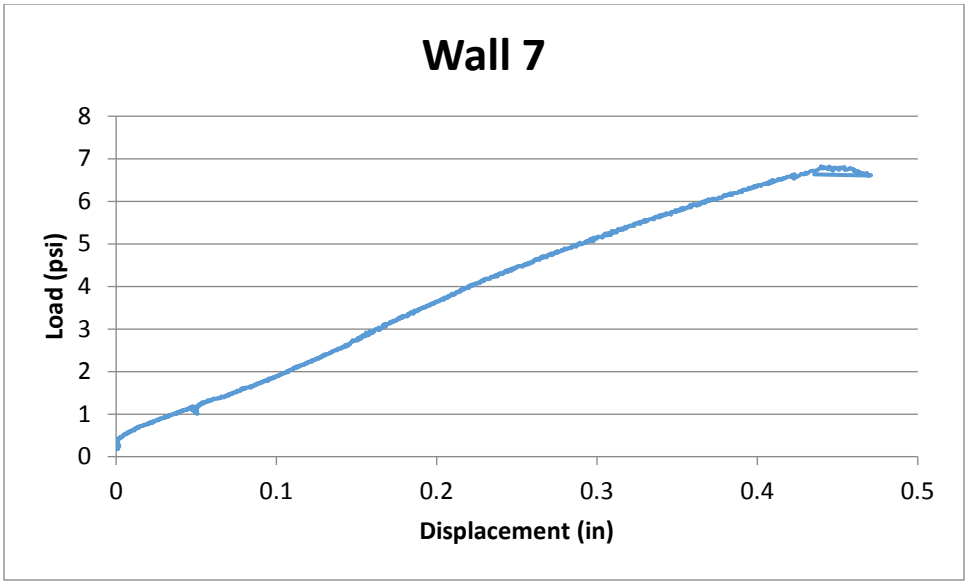

Figure A-17 Load-displacement curve for wall 7

(a) No cracking in webs. **(b) Crack through top course.**

Figure A-18 Failure in wall 7.

A.12 Wall 8

Wall 8 was grouted every 4 ft. horizontally and 4 ft. vertically. In addition a thin layer of mortar was laid between each grout layer. Hairline cracks were noticed before testing between

each course layer but only penetrated through the surface layer and were not considered significant to the testing.

During testing load continued to increase steadily until about 10,000 lbs. when the outside webs cracked. This resulted in a slightly smaller load that continued to increase. About 12,000 lbs. cracks appeared between each course layer that continued to propagate across the whole horizontal layer. At the max load of 13,286.8 lbs. an opening between the top 2 course layers appeared and the wall was unable to resist load. Figure A-19 shows the load vs displacement graph at the middle of the wall. Figure A-20 shows pictures of the wall after failure.

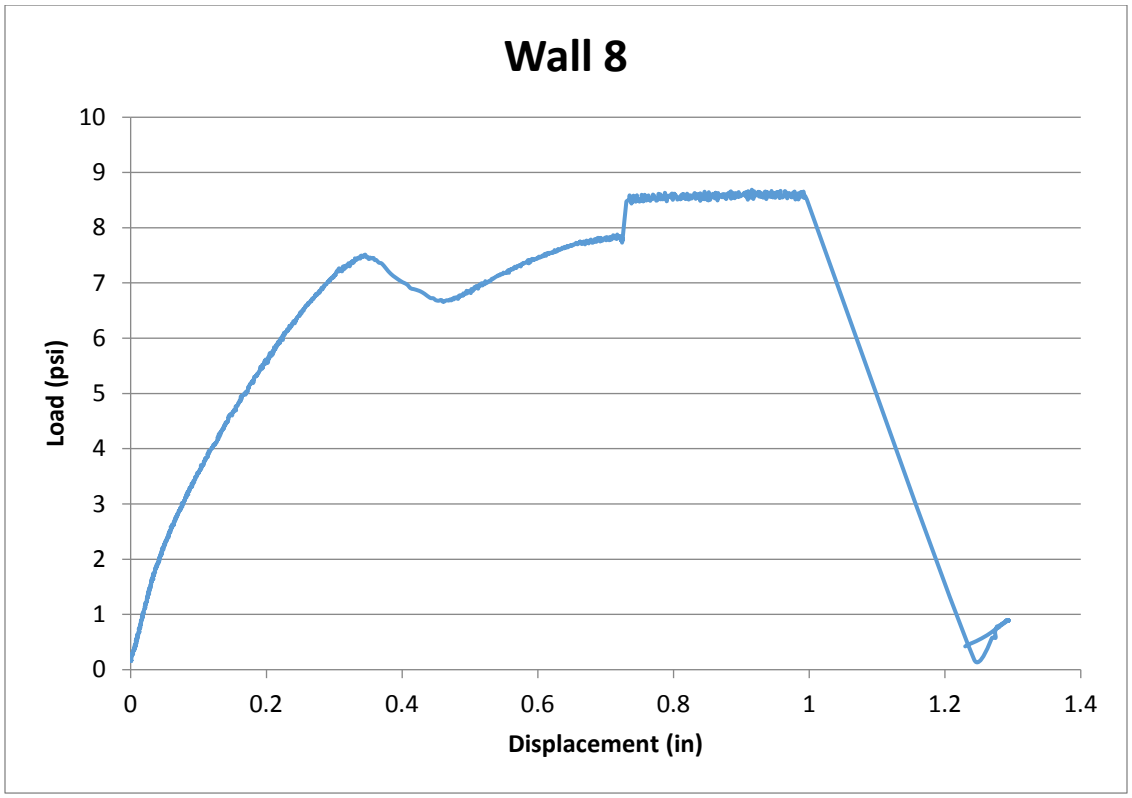

Figure A-19 Load-displacement curve for wall 8.

(a) Overall view. **(b) Cracks in webs.** **(c) Opening in top.**

Figure A-20 Failure in wall 8.

B SAMPLE CALCULATIONS

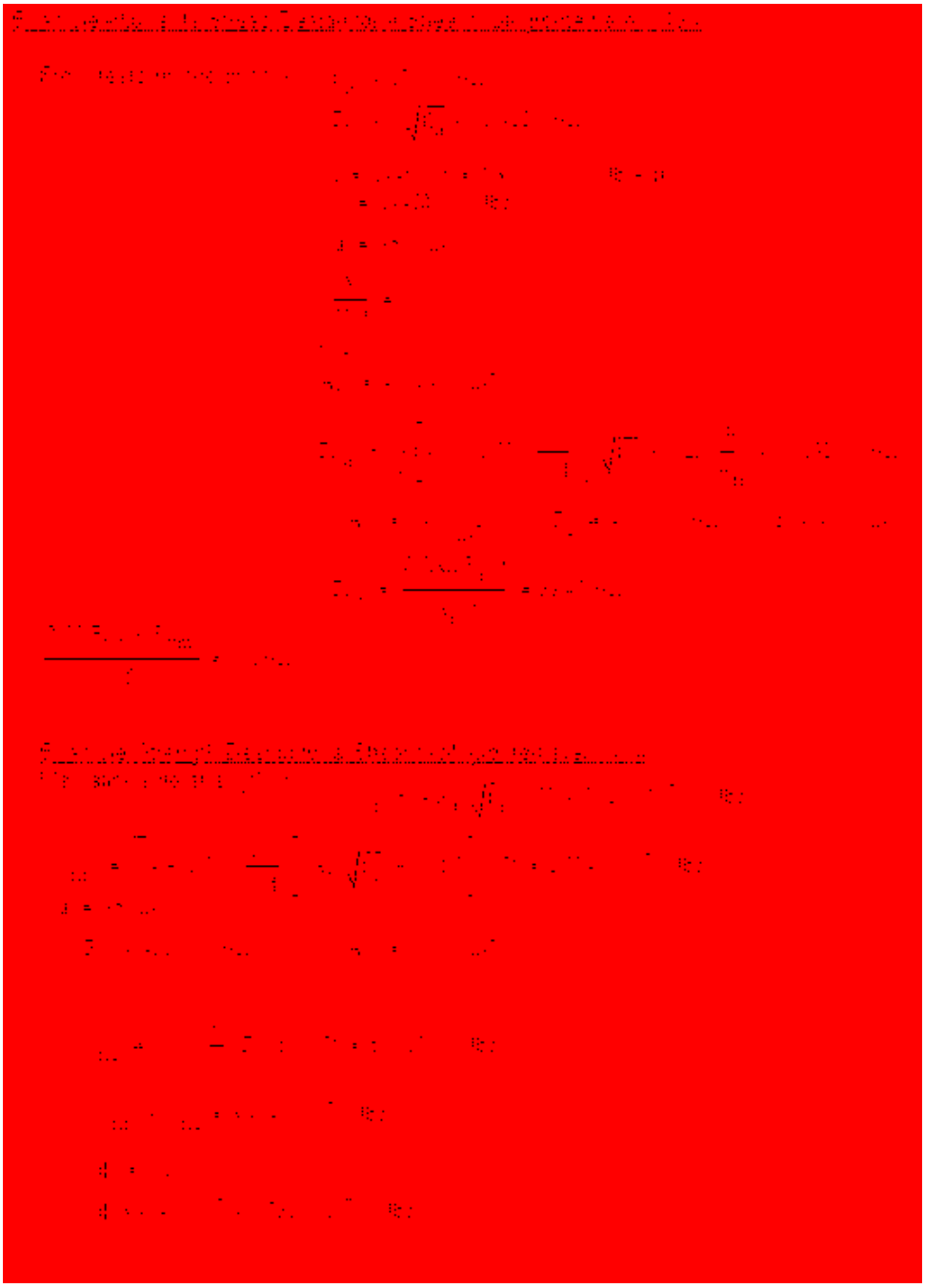

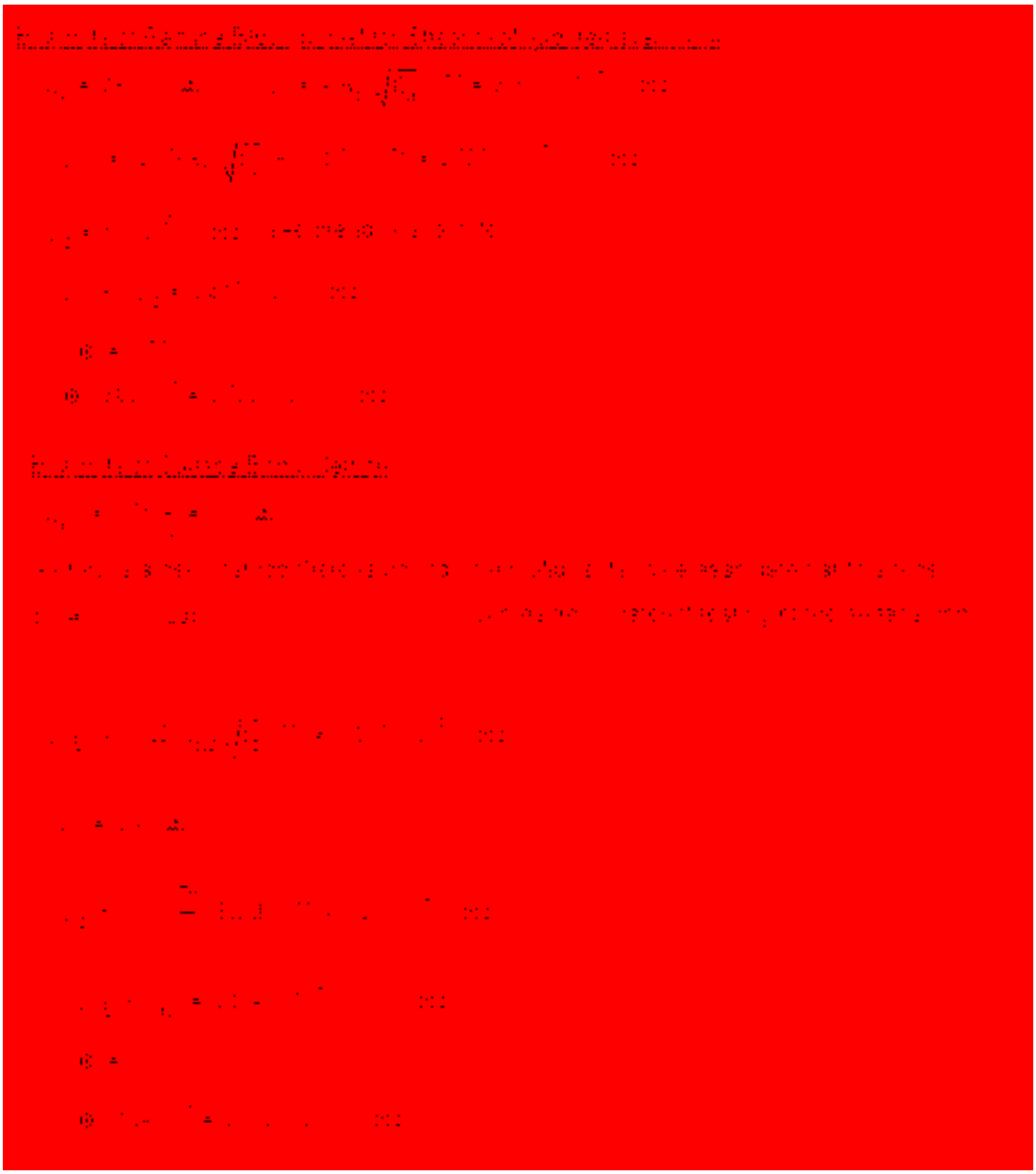

C PUSHOVER ANALYSIS

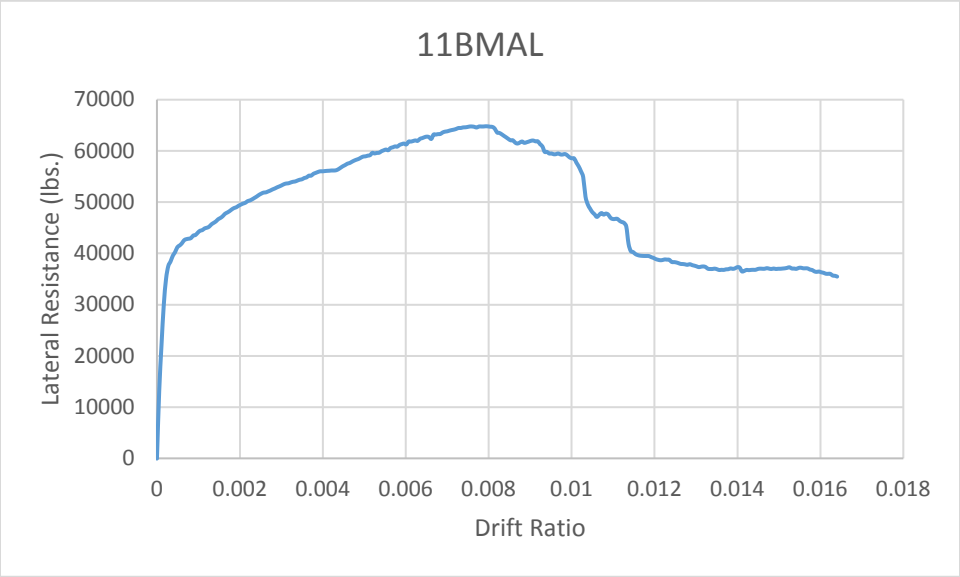

Figure C-1 Pushover analysis of 11BMAL

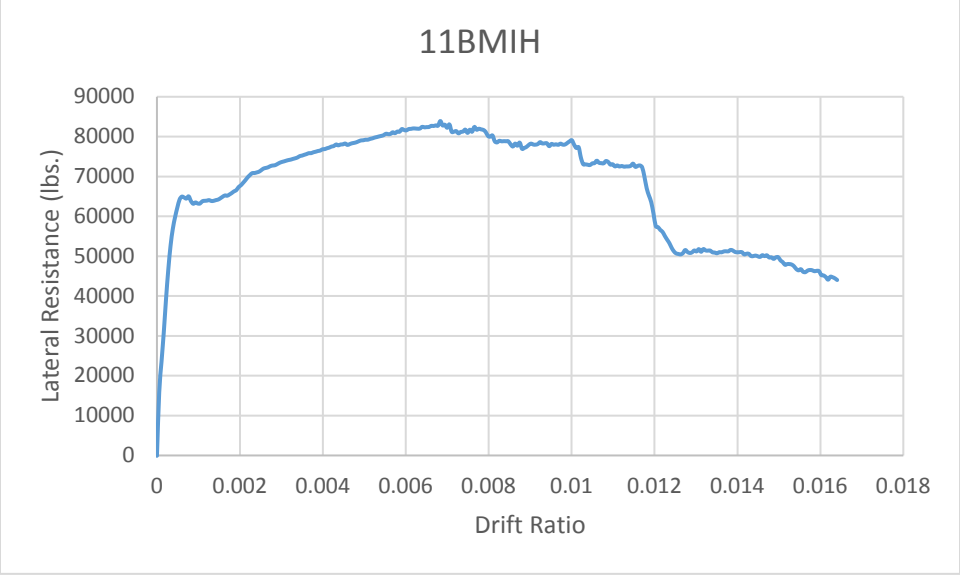

Figure C-2 Pushover analysis of 11BMIH.

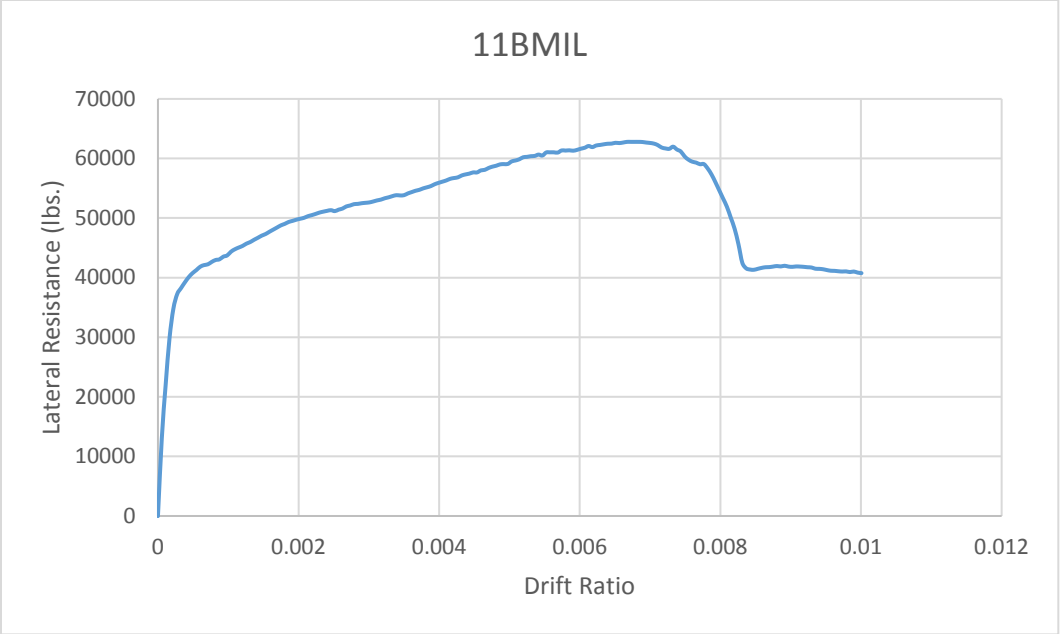

Figure C-3 Pushover analysis of 11BMIL.

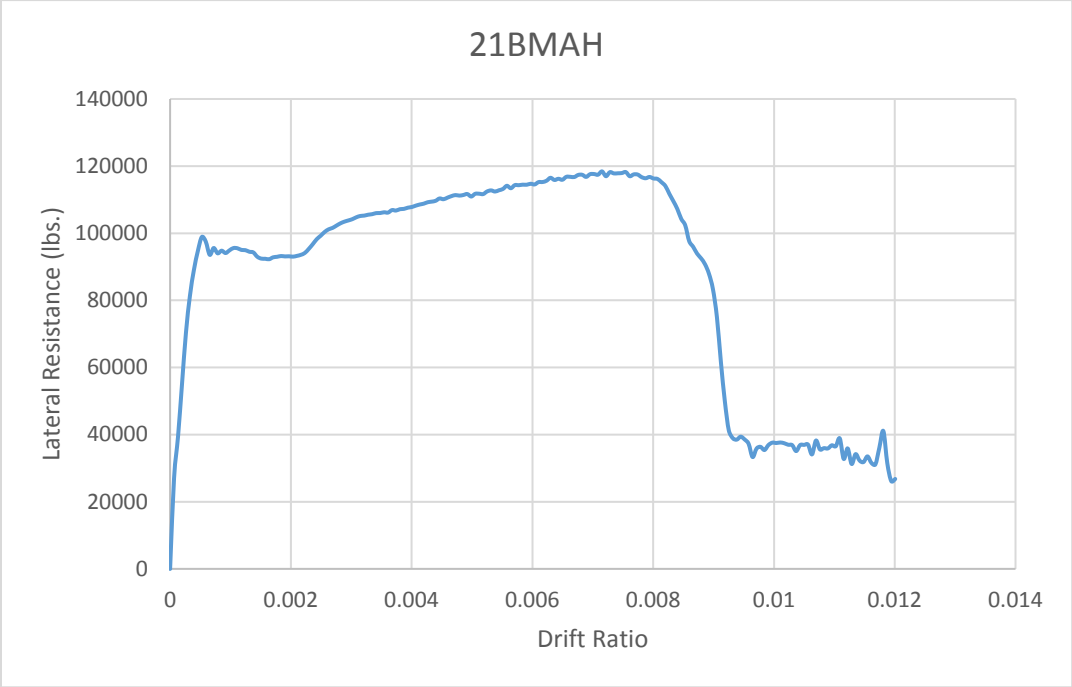

Figure C-4 Pushover analysis of 21BMAH.

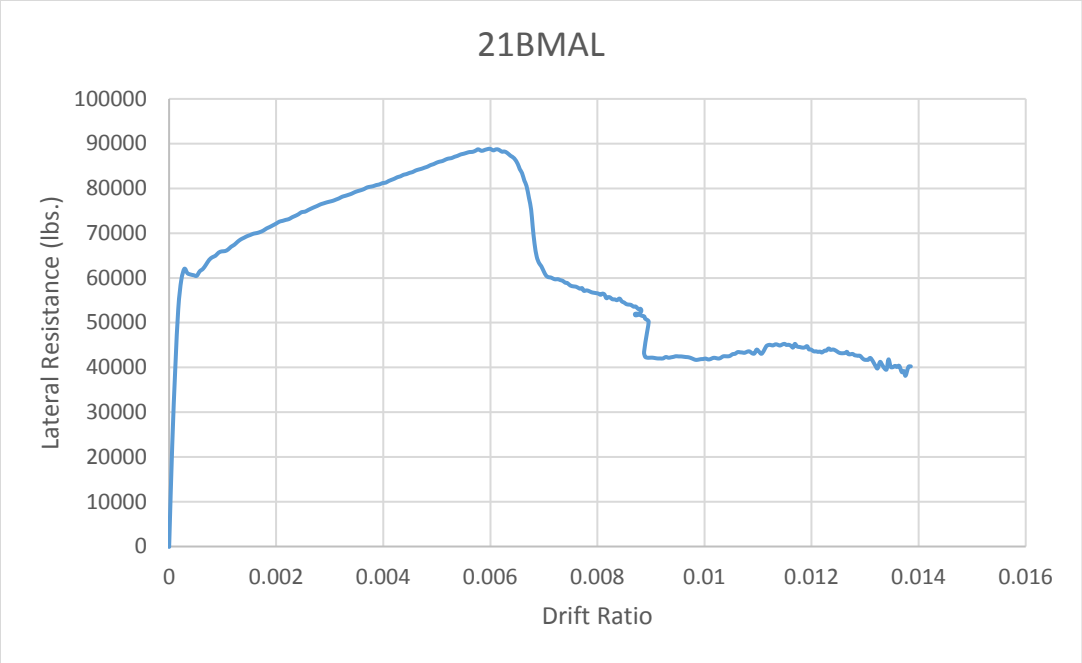

Figure C-5 Pushover analysis of 21BMAL.

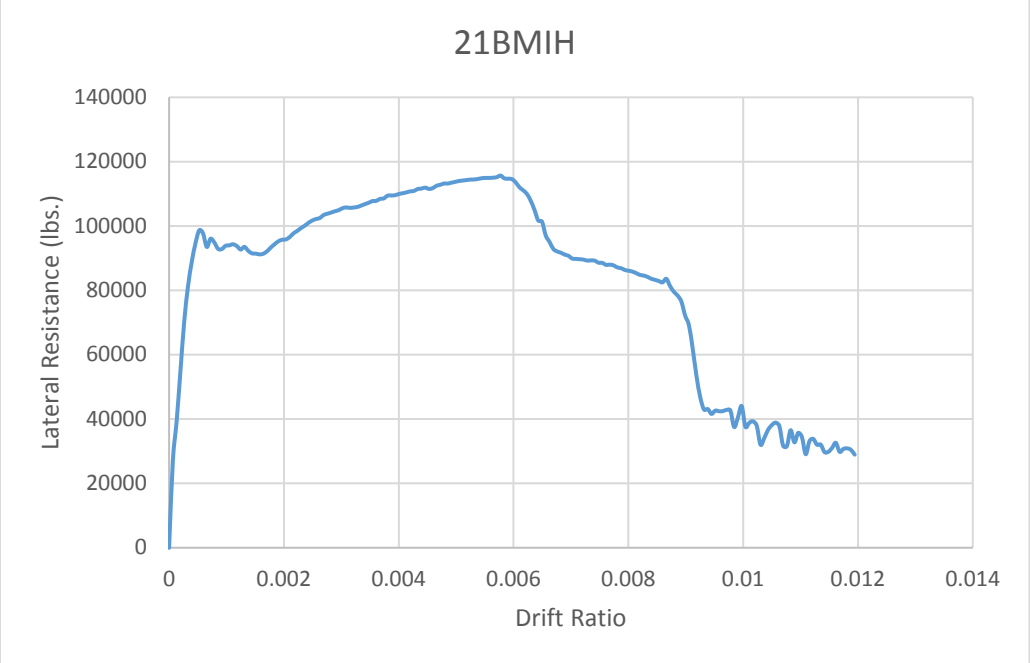

Figure C-6 Pushover analysis of 21BMIH.

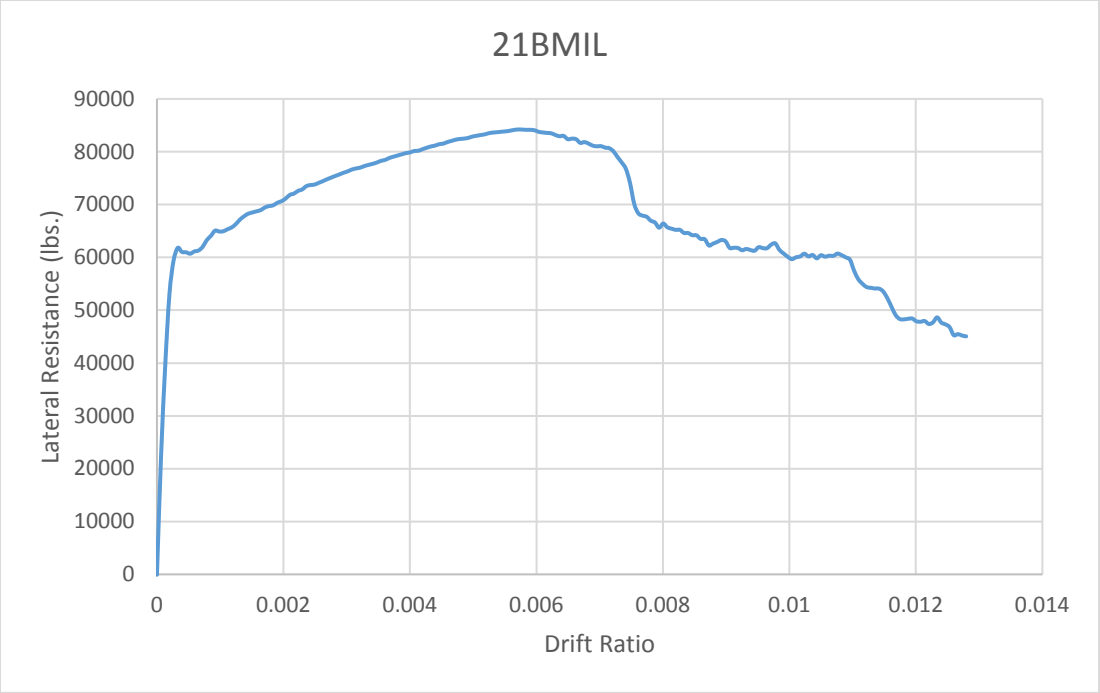

Figure C-7 Pushover analysis of 21BMIL.

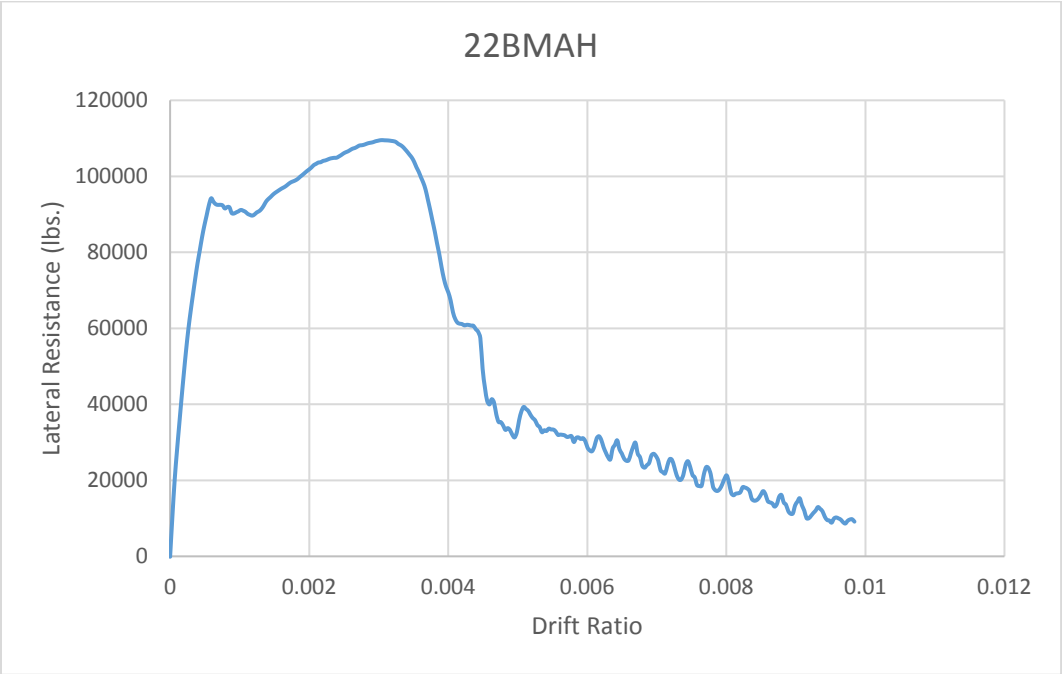

Figure C-8 Pushover analysis of 22BMAH.

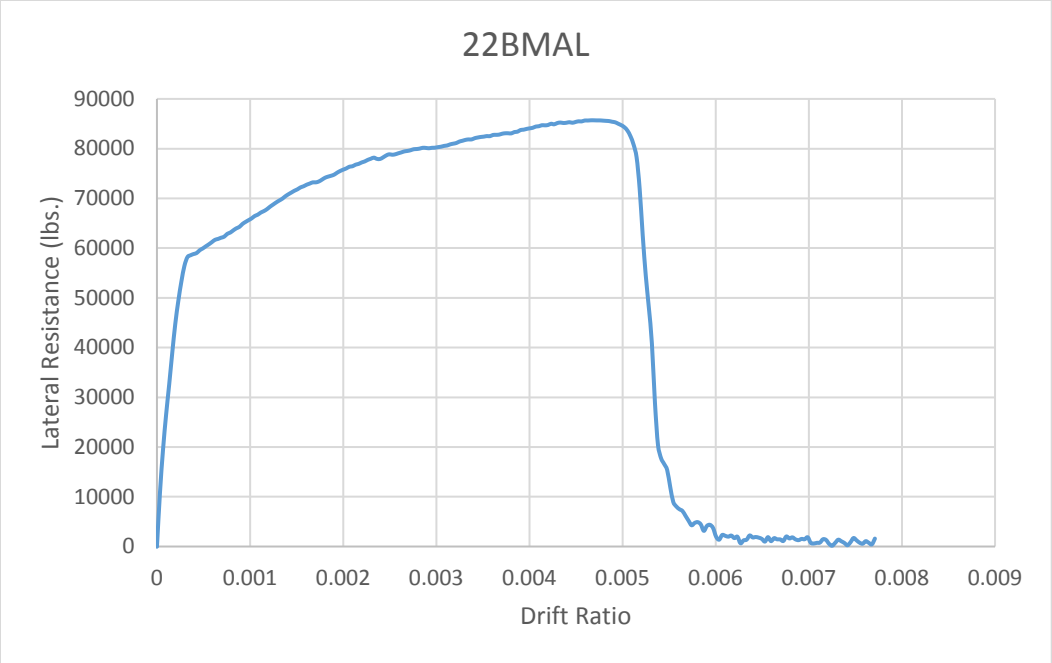

Figure C-9 Pushover analysis of 22BMAL.

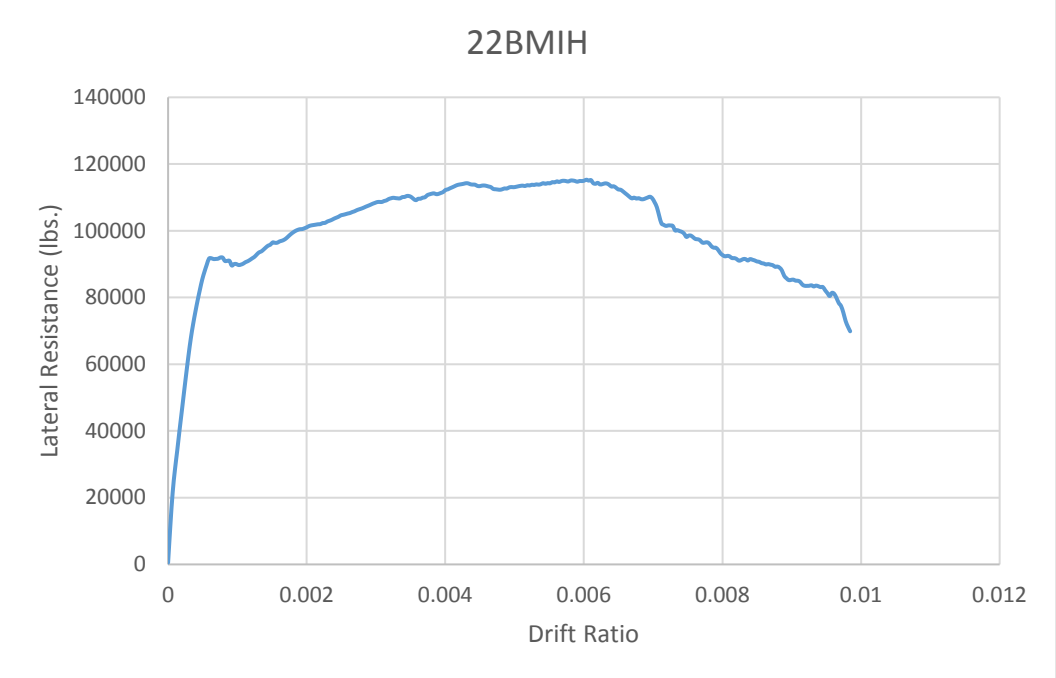

Figure C-10 Pushover analysis of 22BMIH.

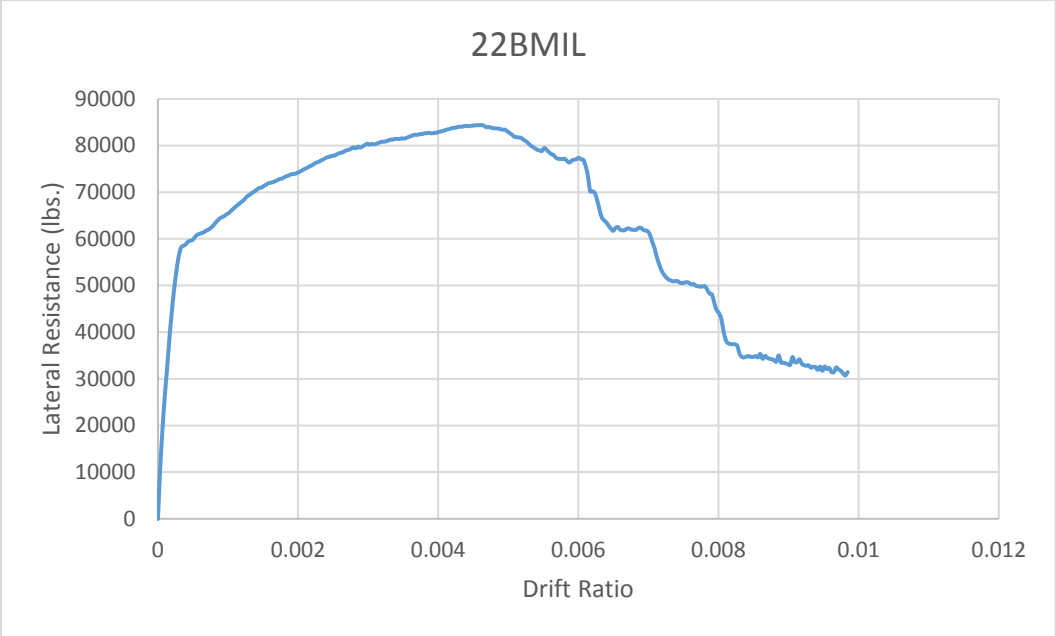

Pushover analysis of 22BMIL.

D TIME HISTORY ANALYSIS OF 11BMAL AT INTENSITY 2.21

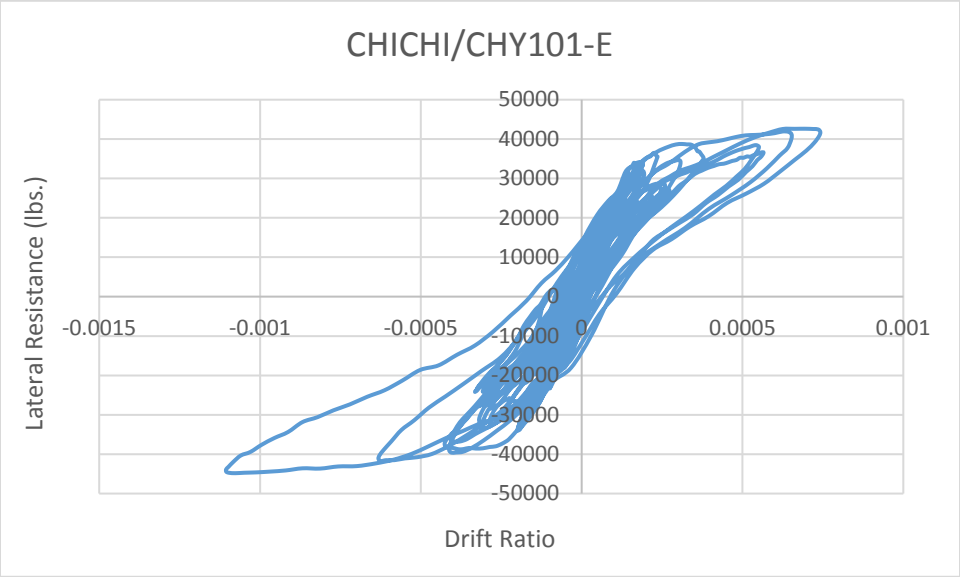

Figure D-1 Time history analysis of archetype 11BMAL using CHICHI/CHY101-E.

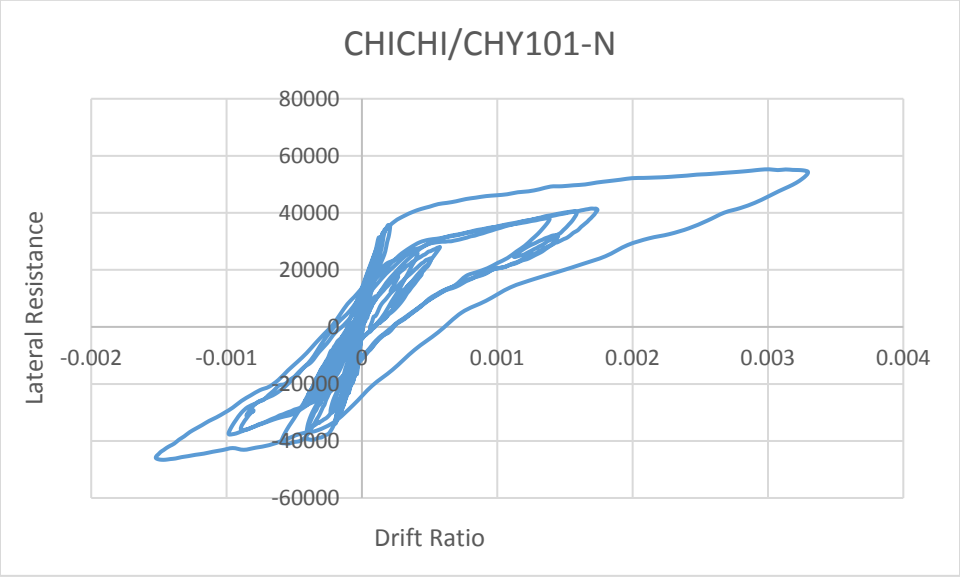

Figure D-2 Time history analysis of archetype 11BMAL using CHICHI/CHY101-N.

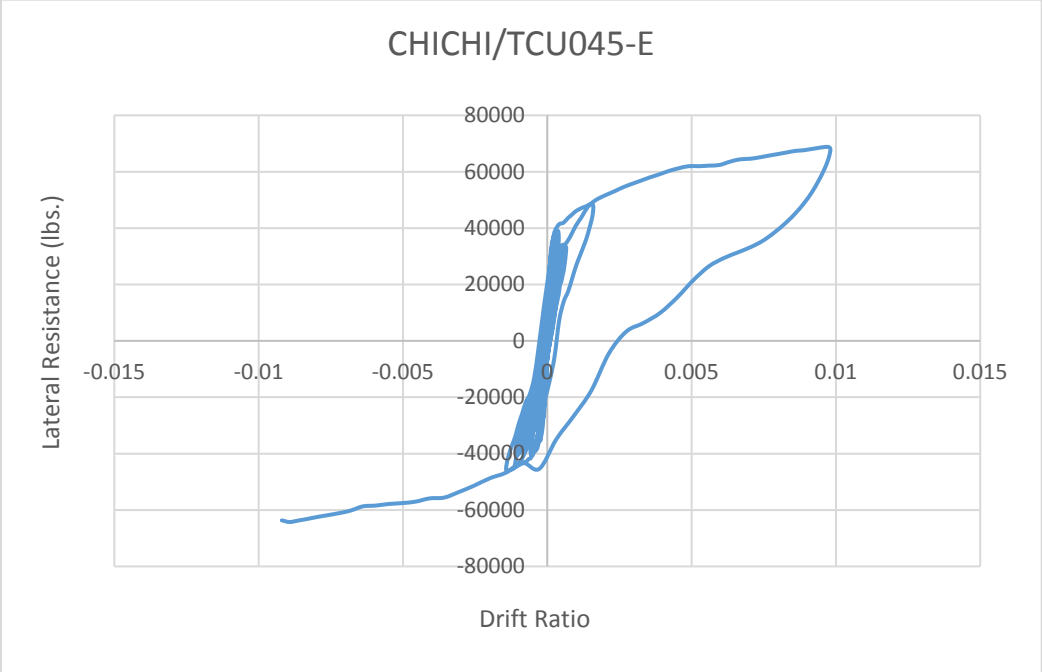

Figure D-3 Time history analysis of archetype 11BMAL using CHICHI/TCU045-E.

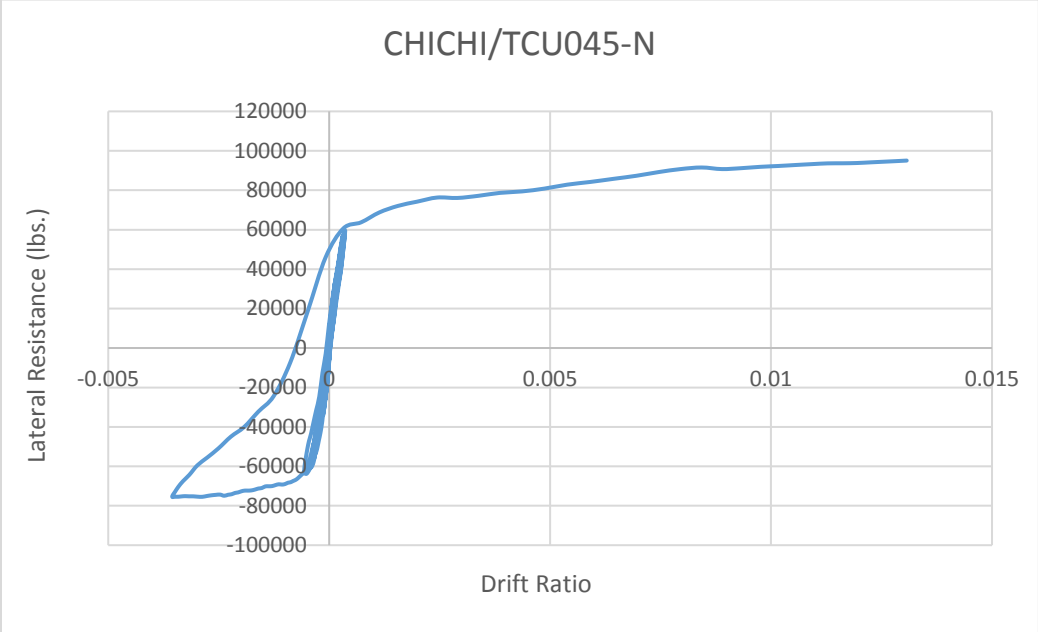

Figure D-4 Time history analysis of archetype 11BMAL using CHICHI/TCU045-N.

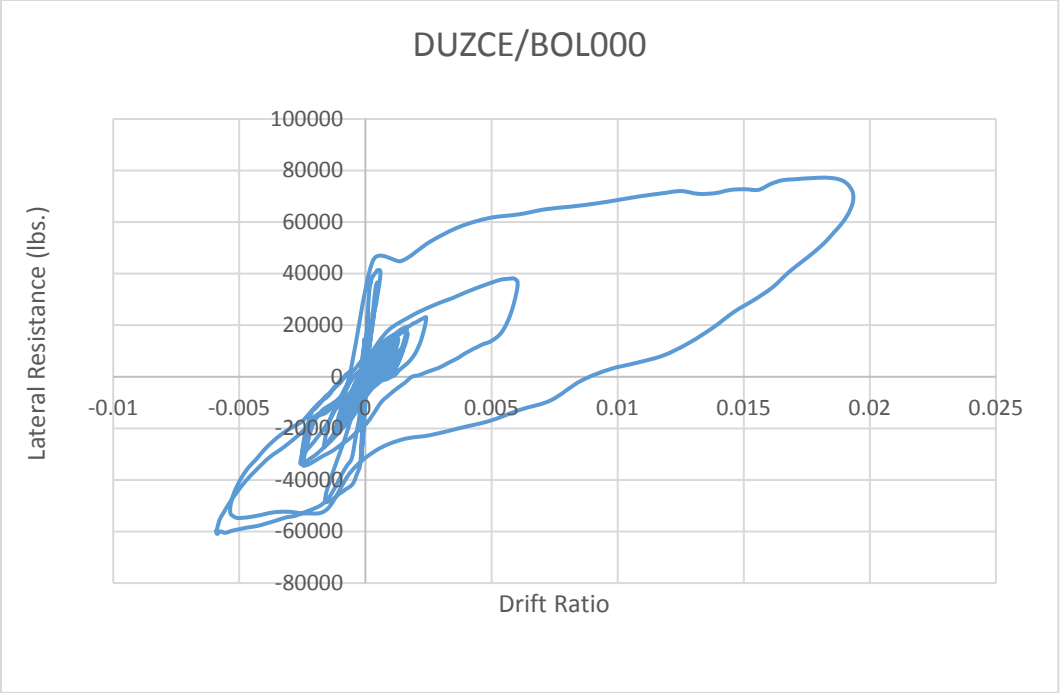

Figure D-5 Time history analysis of archetype 11BMAL using DUZCE/BOL000.

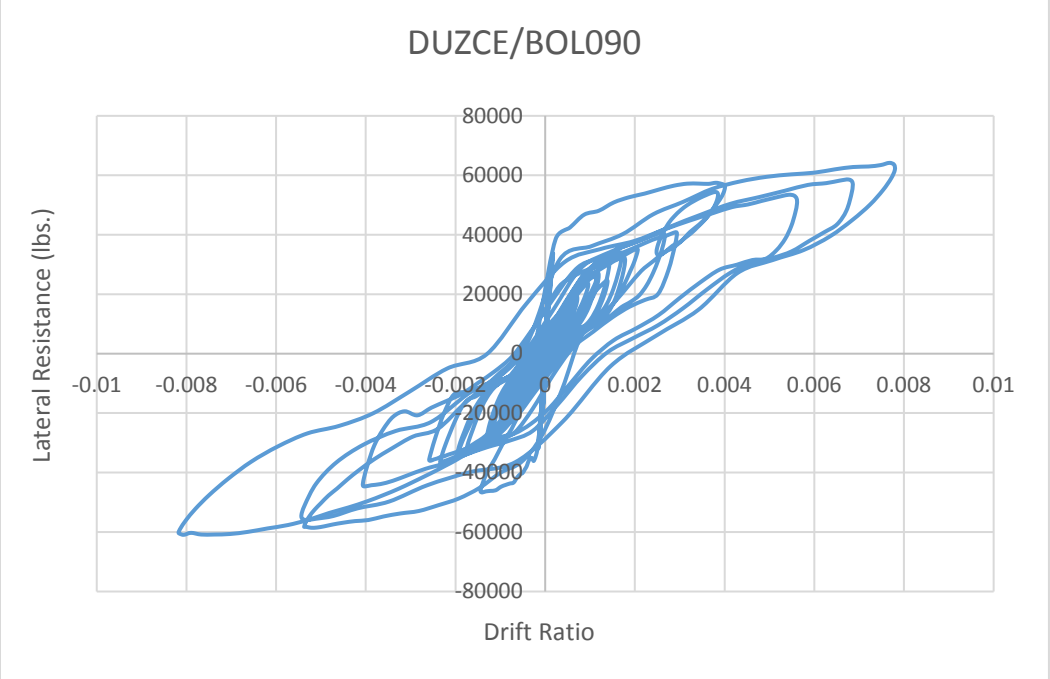

Figure D-6 Time history analysis of archetype 11BMAL using DUZCE/BOL090.

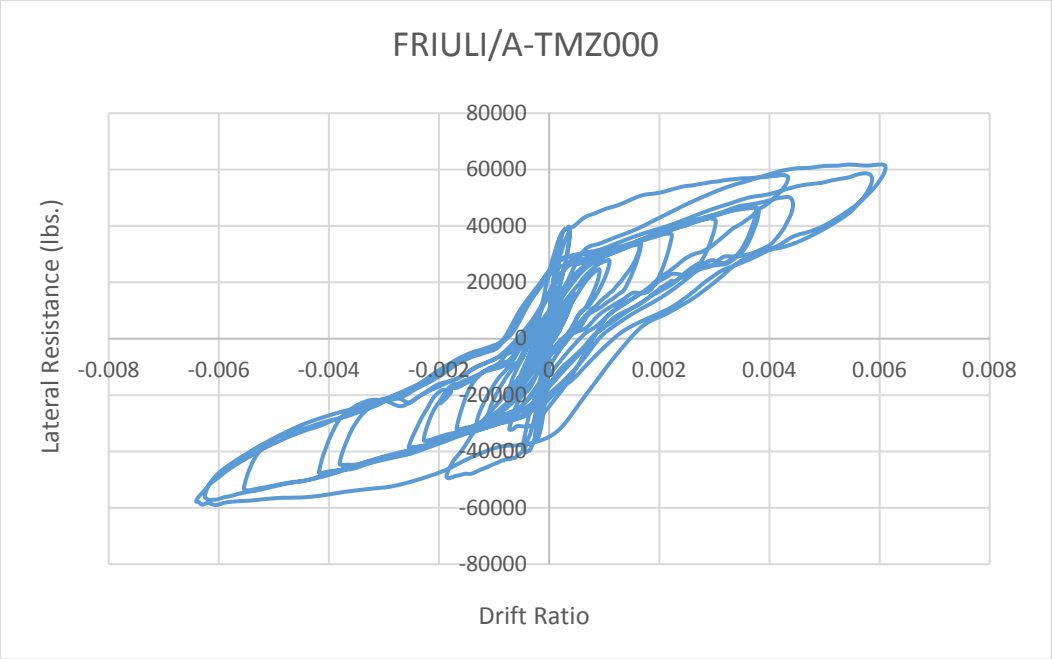

Figure D-7 Time history analysis of archetype 11BMAL using FRIULI/A-TMZ000.

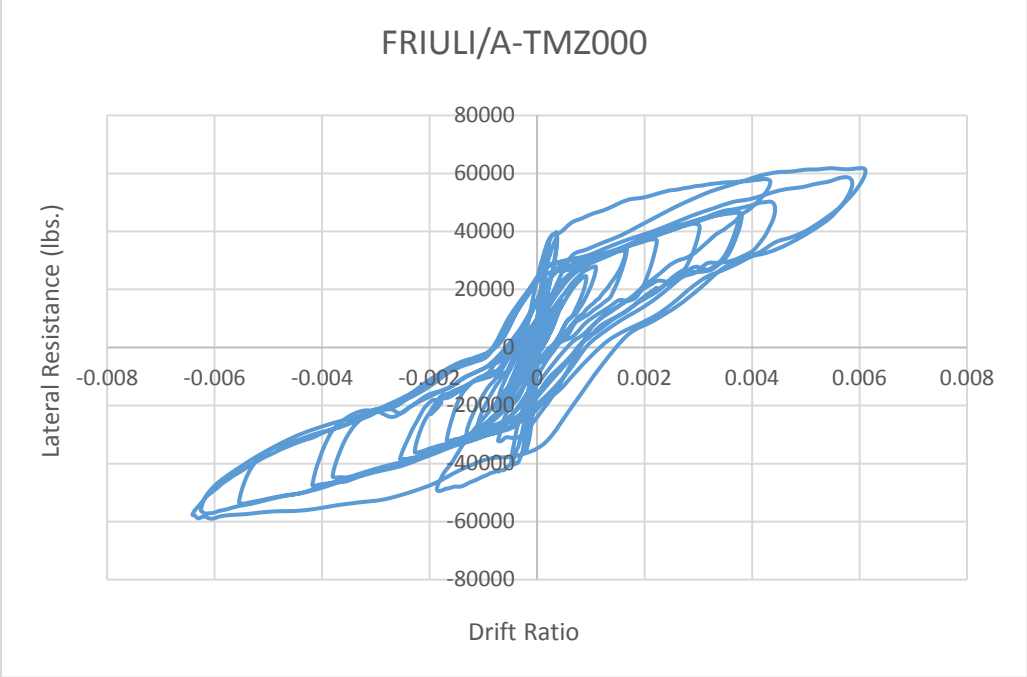

Figure D-8 Time history analysis of archetype 11BMAL using Friuli/A-TMZ000.

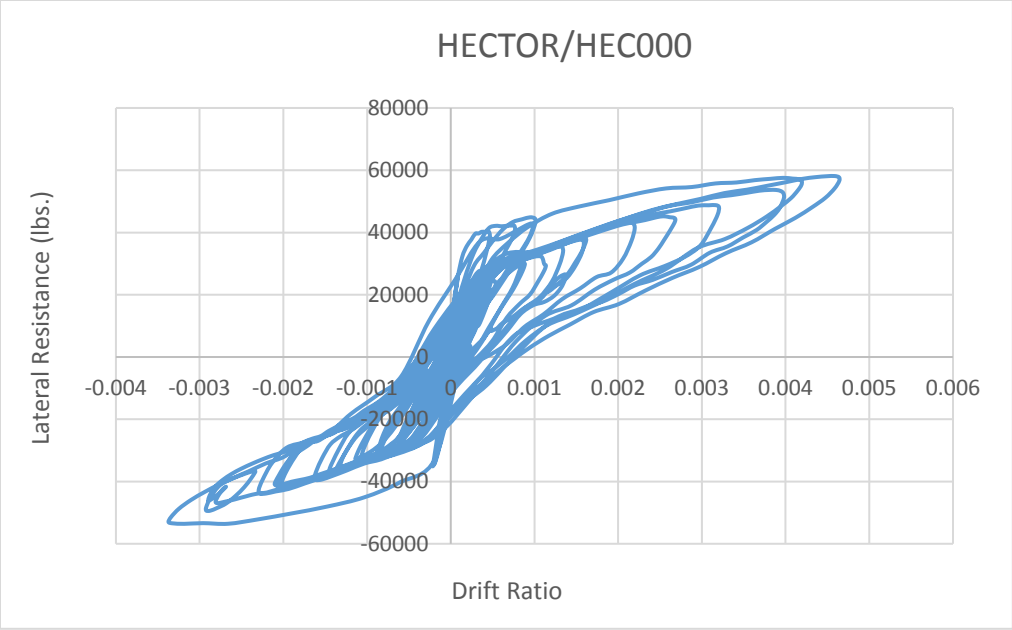

Figure D-9 Time history analysis of archetype 11BMAL using HECTOR/HEC000.

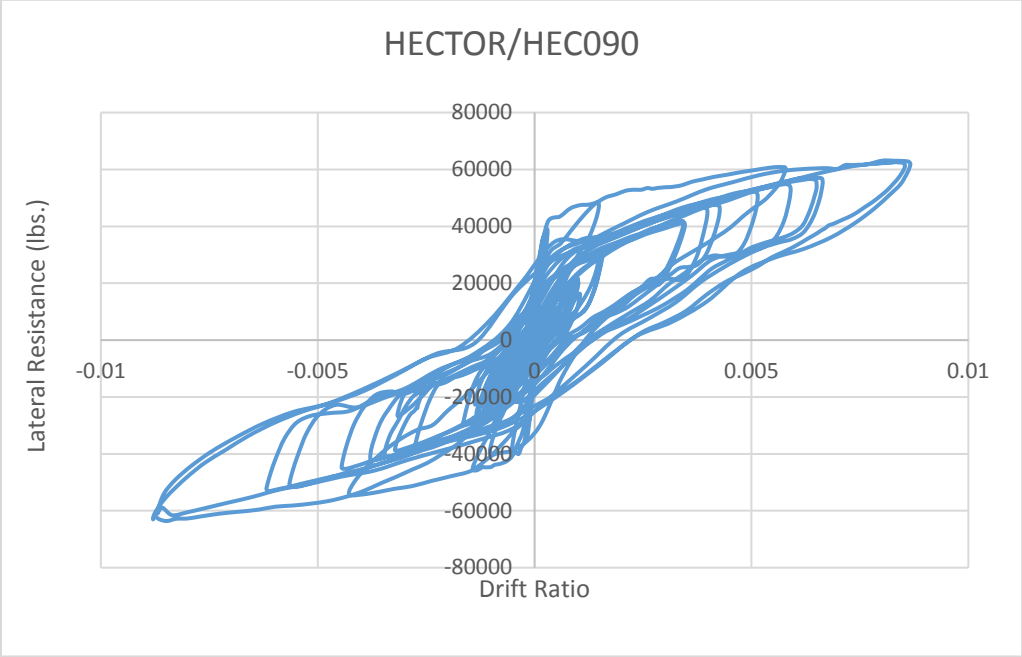

Figure D-10 Time history analysis of archetype 11BMAL using HECTOR/HEC090.

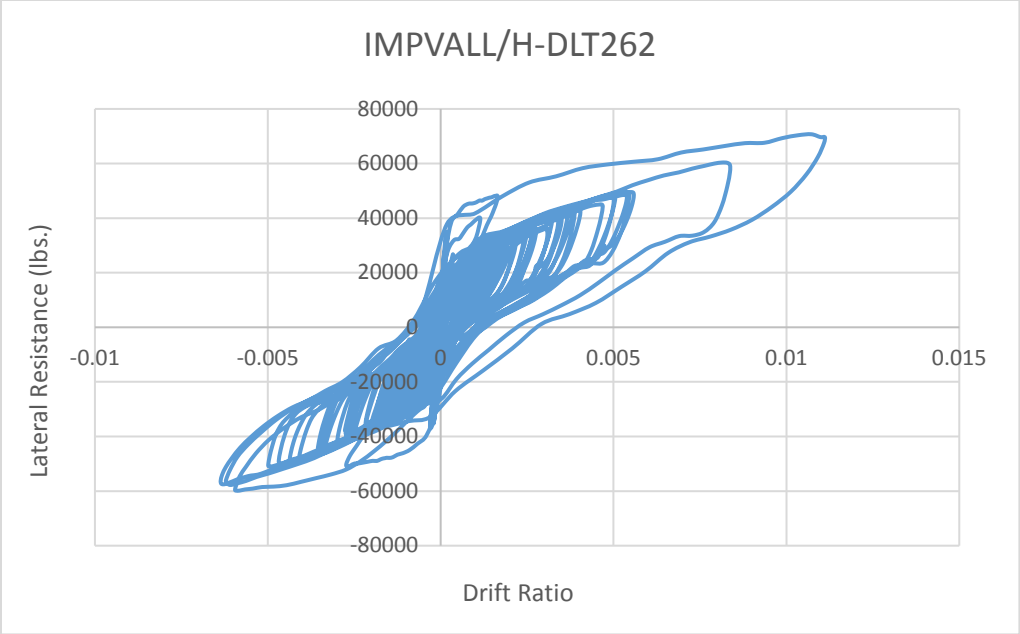

Figure D-11 Time history analysis of archetype 11BMAL using IMPVALL/H-DLT262.

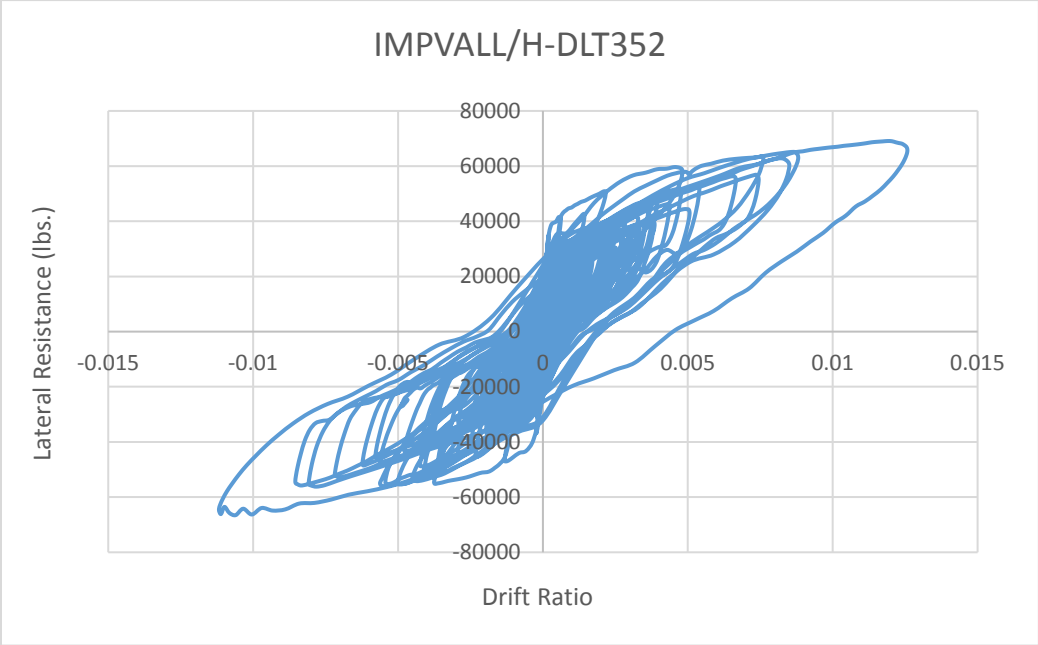

Figure D-12 Time history analysis of archetype 11BMAL using IMPVALL/H-DLT352.

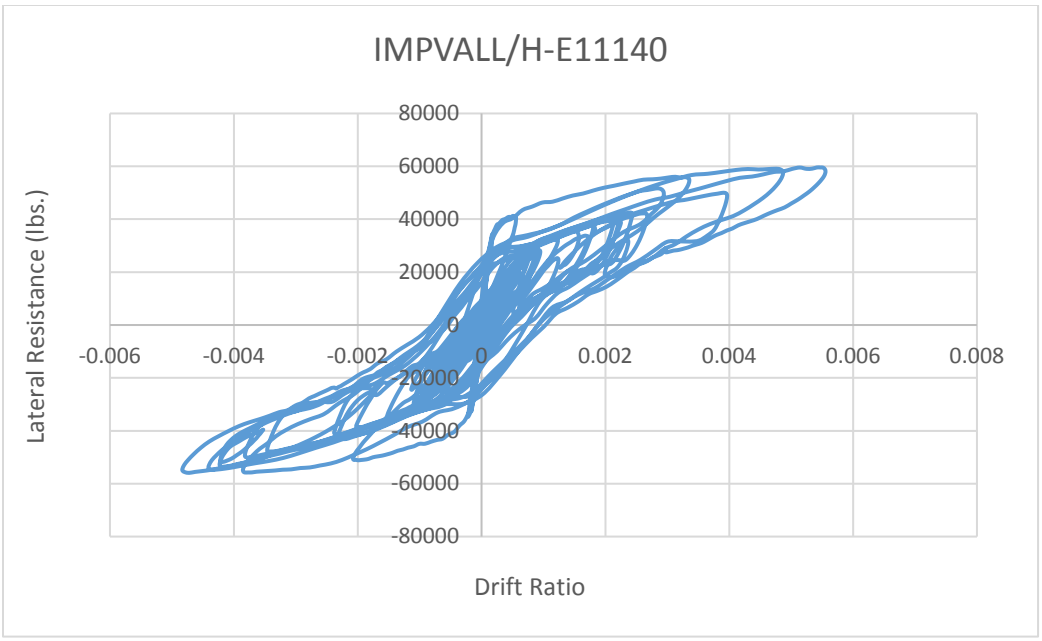

Figure D-13 Time history analysis of archetype 11BMAL using IMPVALL/H-E11140.

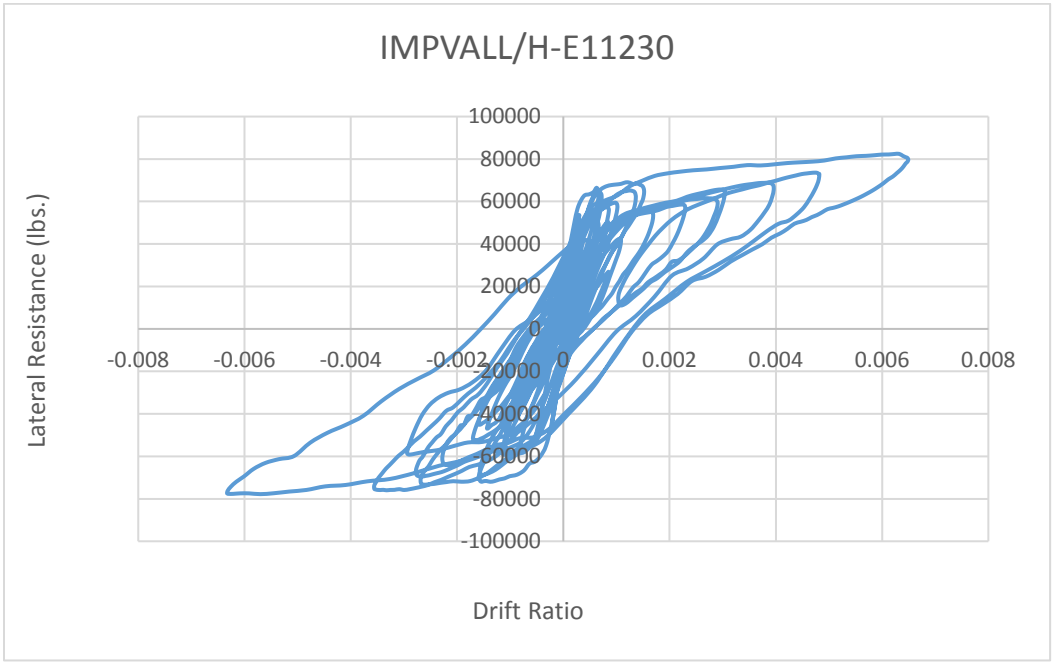

Figure D-14 Time history analysis of archetype 11BMAL using IMPVALL/H-E11230.

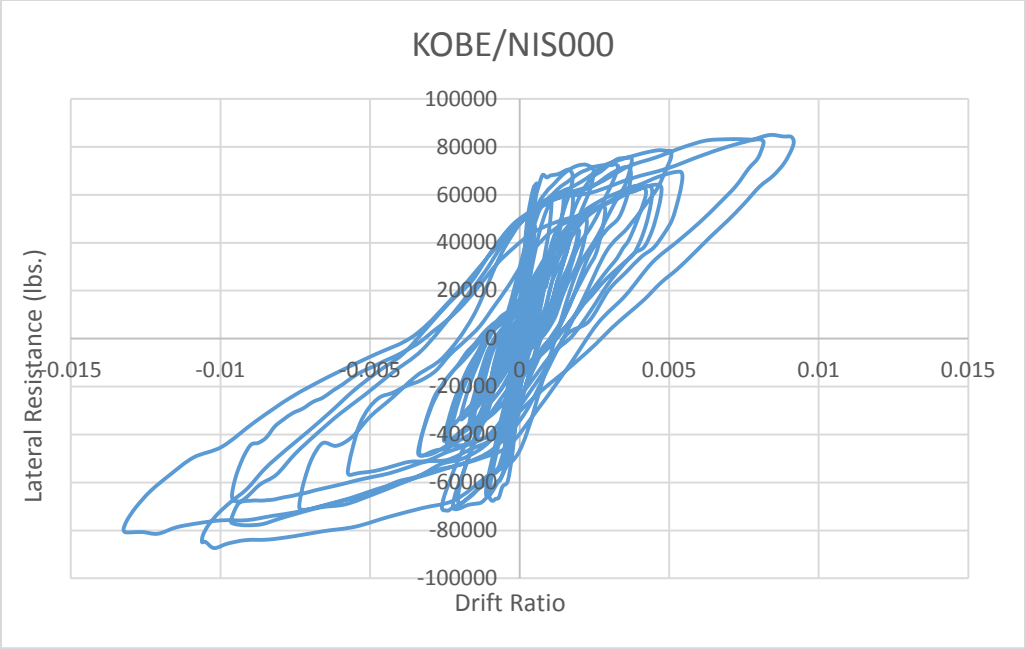

Figure D-15 Time history analysis of archetype 11BMAL using KOBE/NIS000.

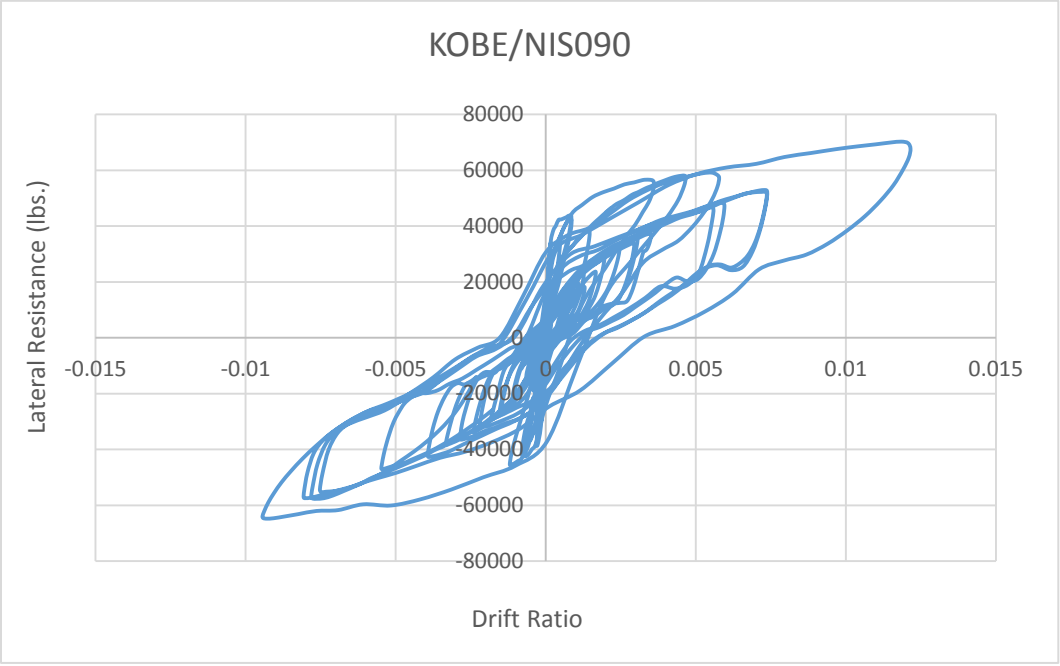

Figure D-16 Time history analysis of archetype 11BMAL using KOBE/NIS090.

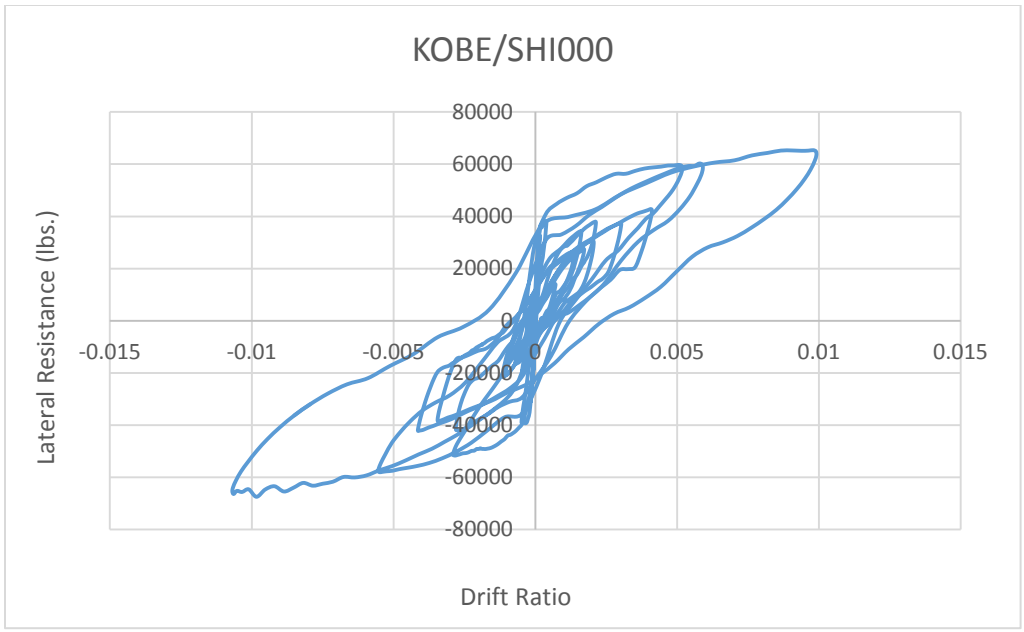

Figure D-17 Time history analysis of archetype 11BMAL using KOBE/SHI000.

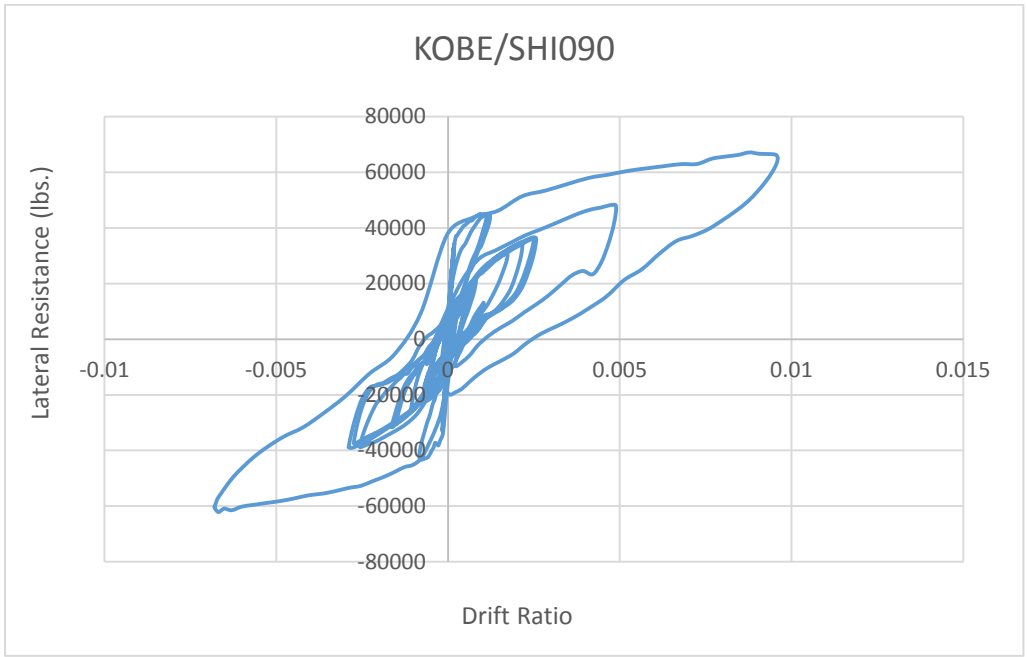

Figure D-18 Time history analysis of archetype 11BMAL using KOBE/SHI090.

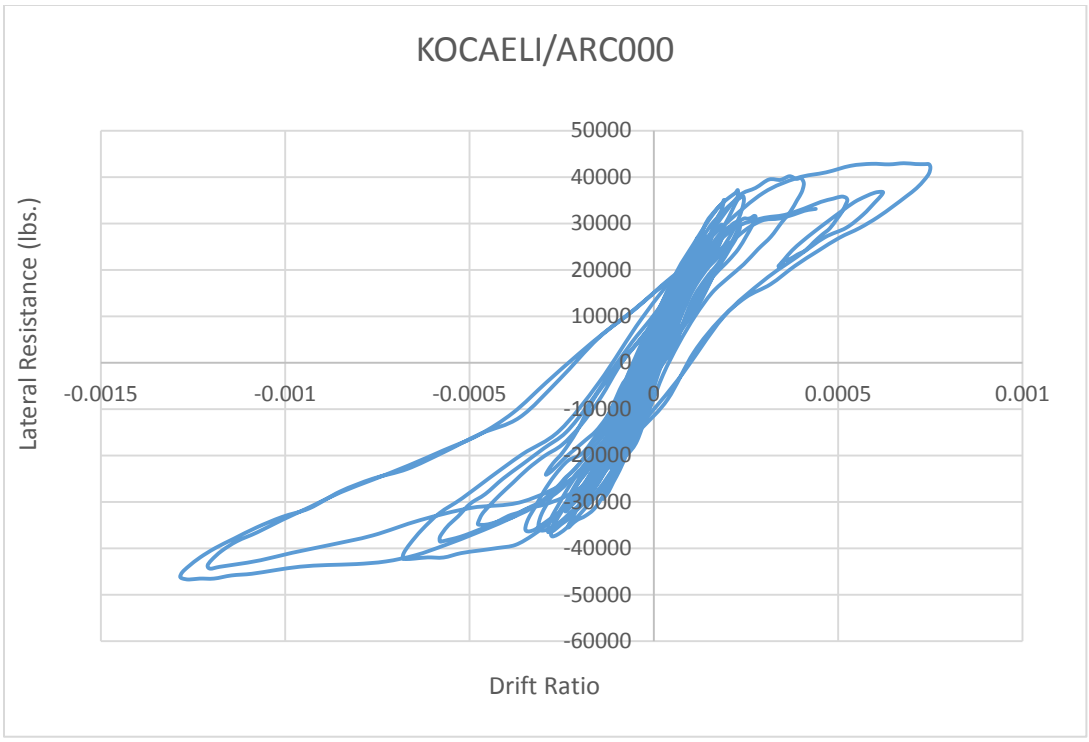

Figure D-19 Time history analysis of archetype 11BMAL using KOCAELI/ARC000.

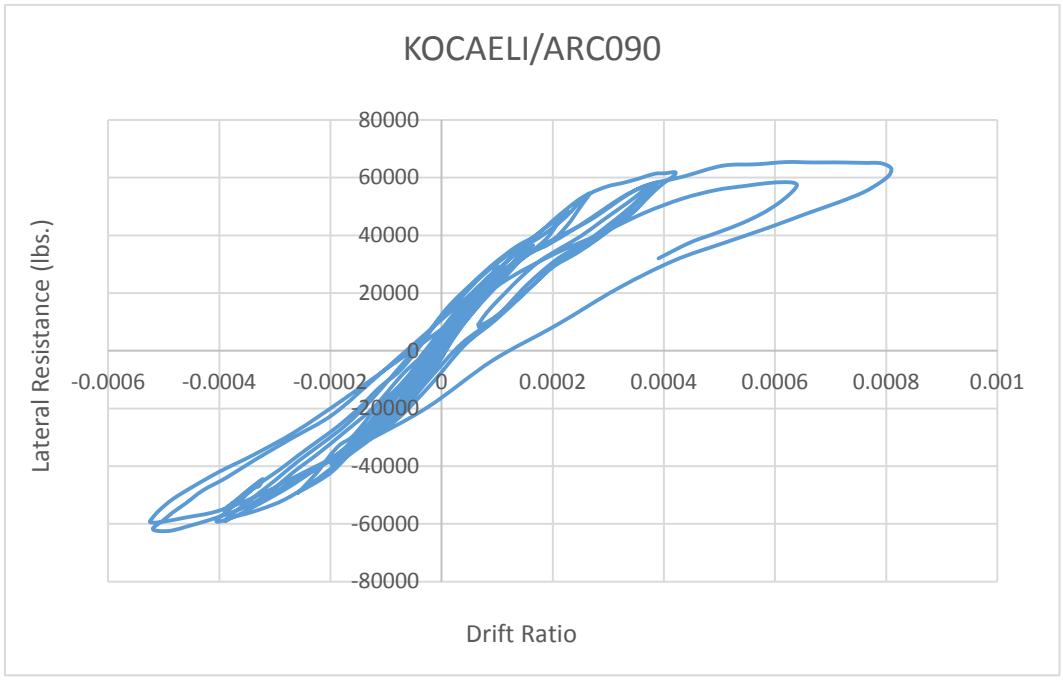

Figure D-20 Time history analysis of archetype 11BMAL using KOCAELI/ARC090.

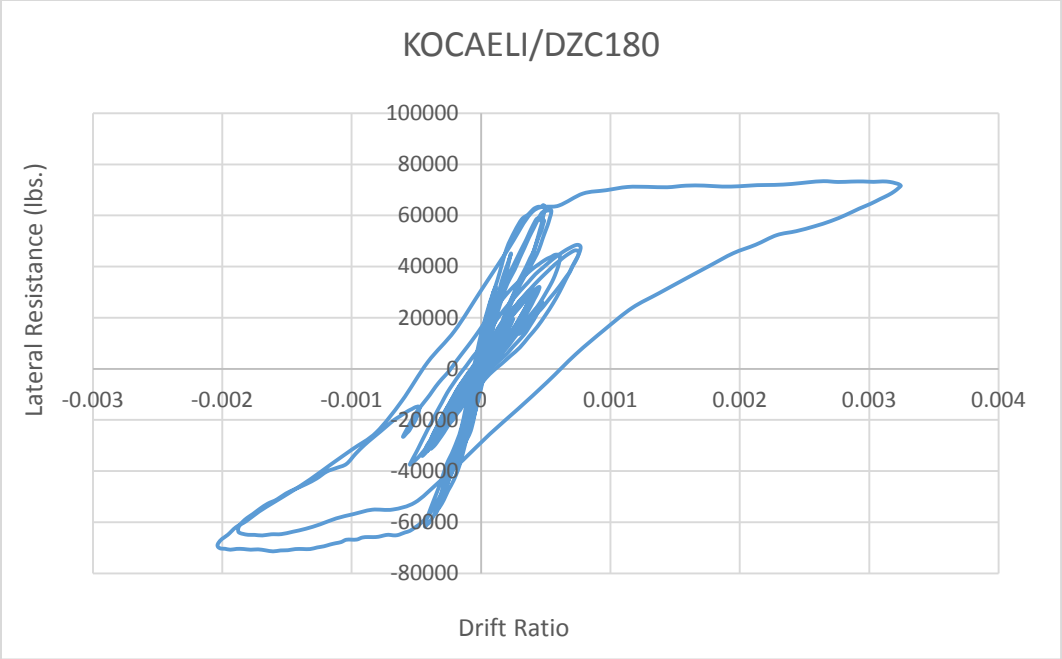

Figure D-21 Time history analysis of archetype 11BMAL using KOCAELI/DZC180.

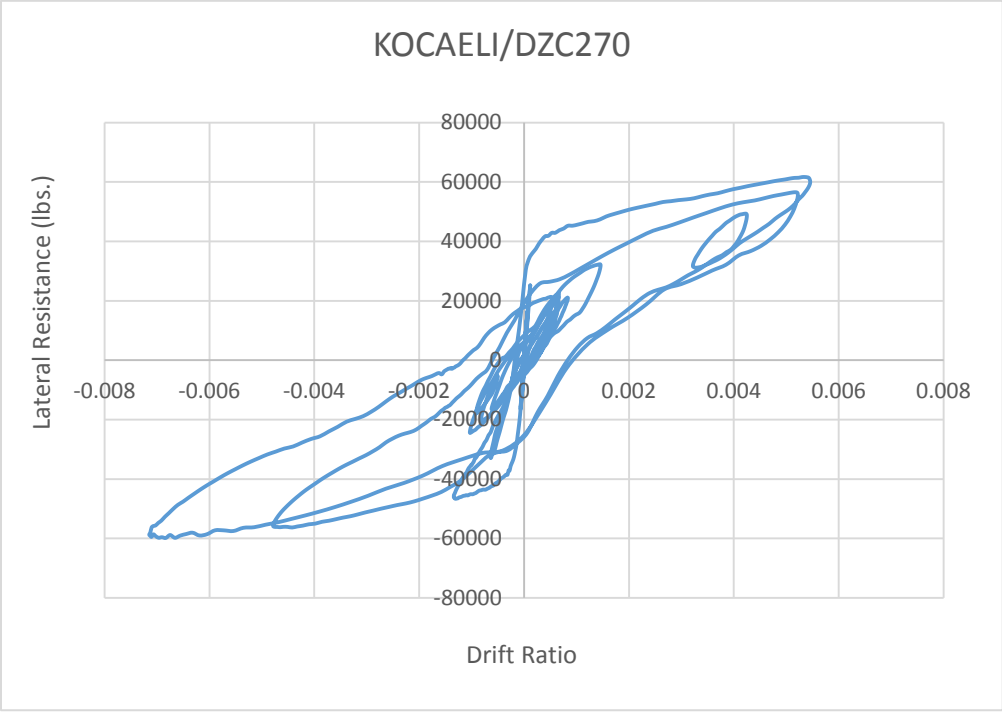

Figure D-22 Time history analysis of archetype 11BMAL using KOCAELI/DZC270.

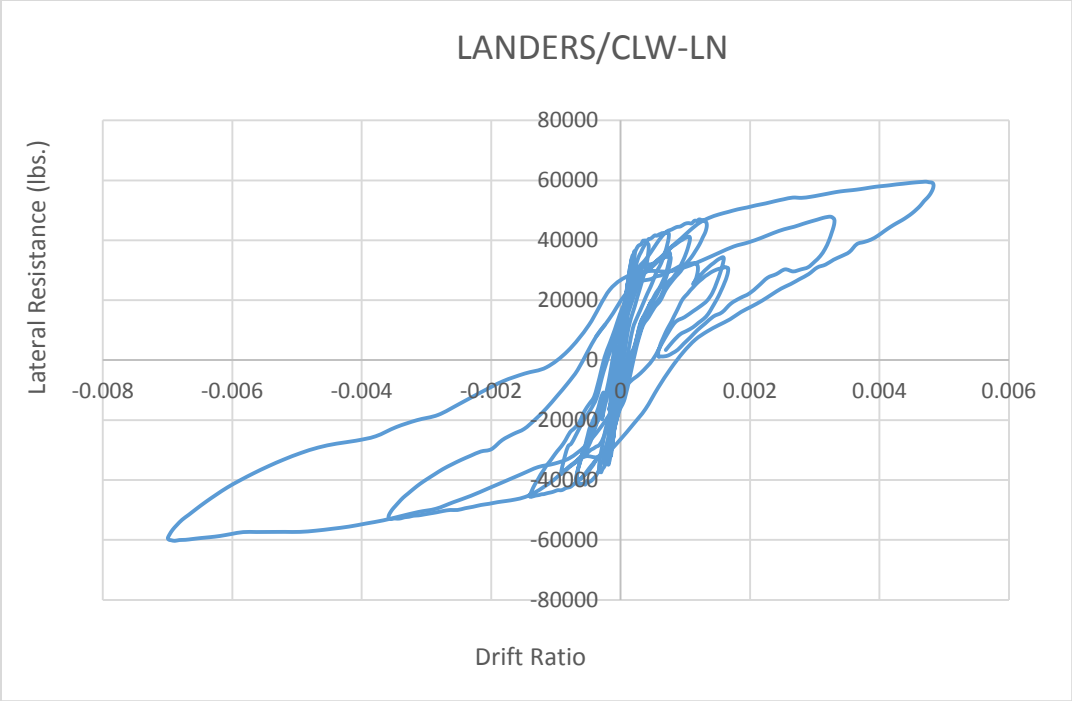

Figure D-23 Time history analysis of archetype 11BMAL using LANDERS/CLW-LN.

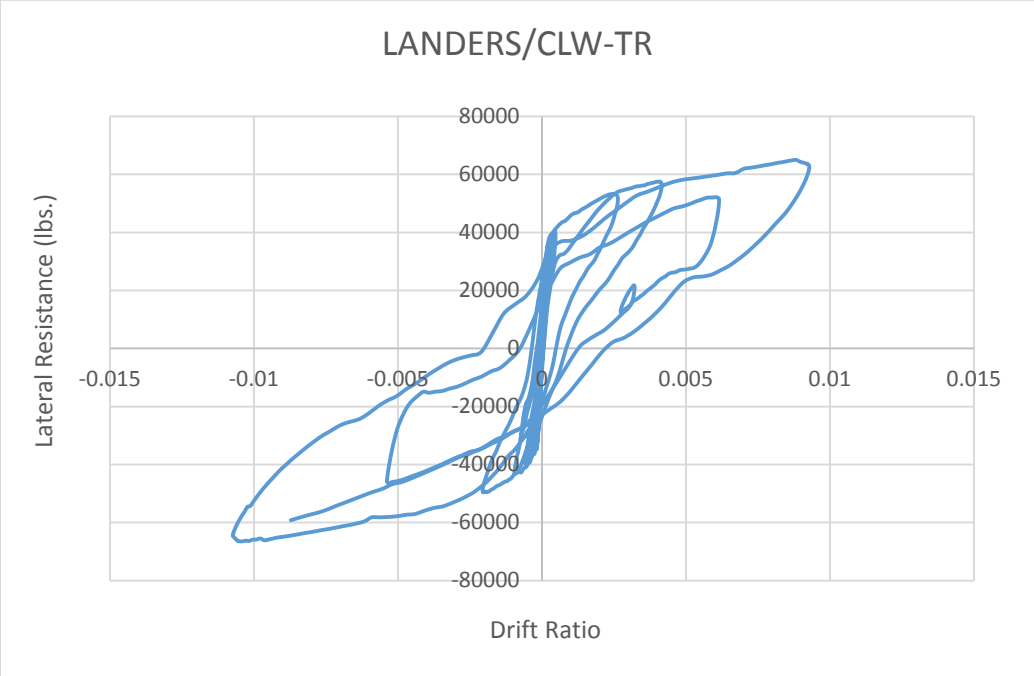

Figure D-24 Time history analysis of archetype 11BMAL using LANDERS/CLW-TR.

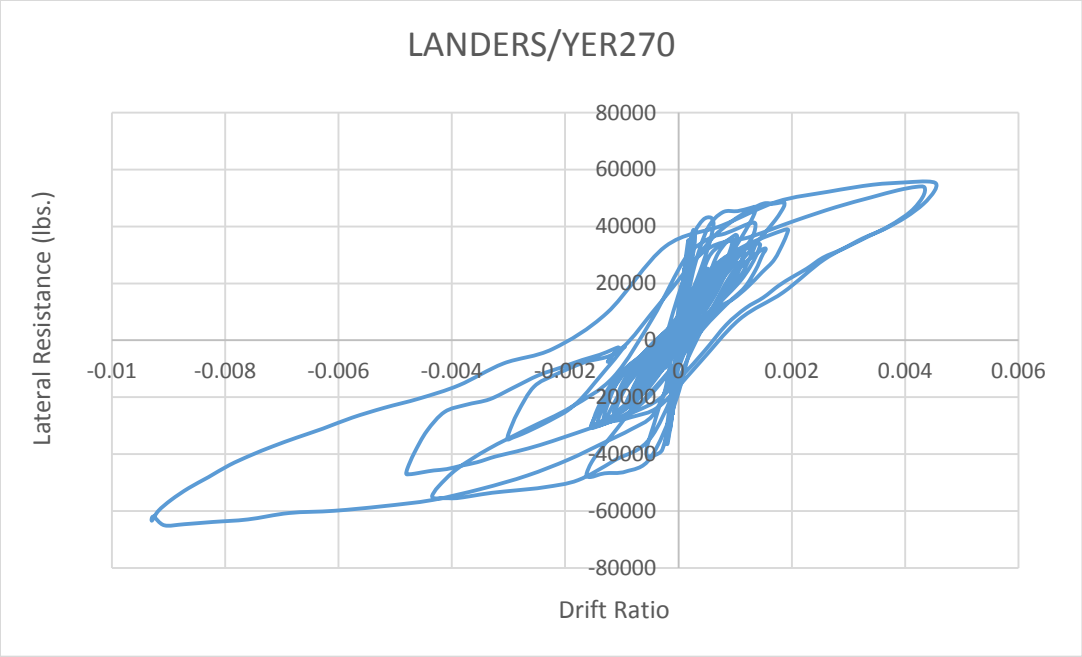

Figure D-25 Time history analysis of archetype 11BMAL using LANDERS/YER 270.

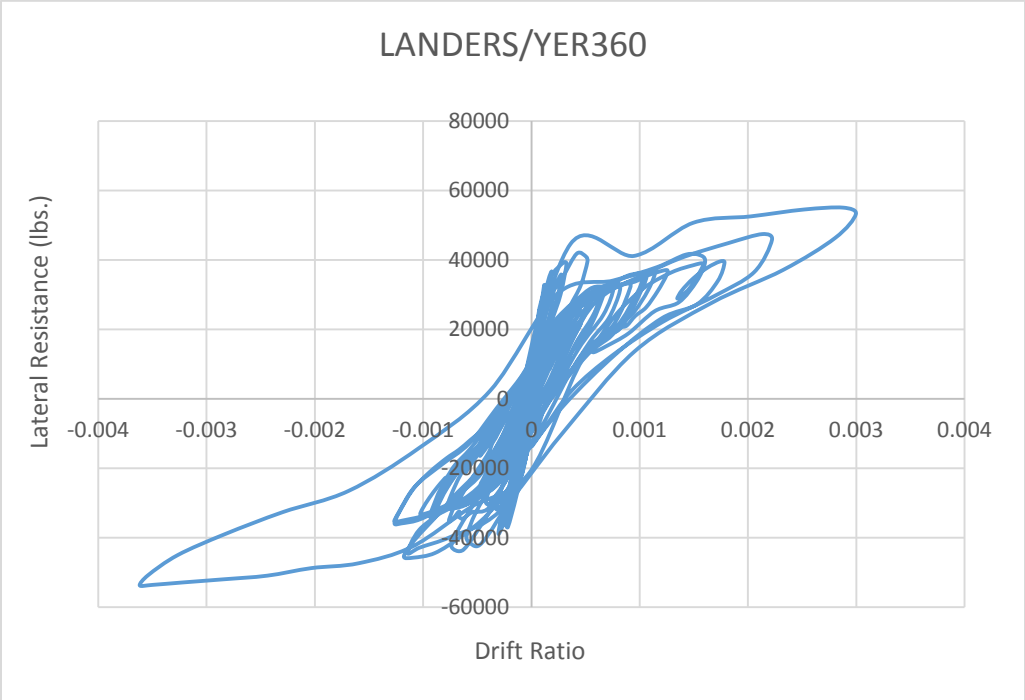

Figure D-26 Time history analysis of archetype 11BMAL using LANDERS/YER360.

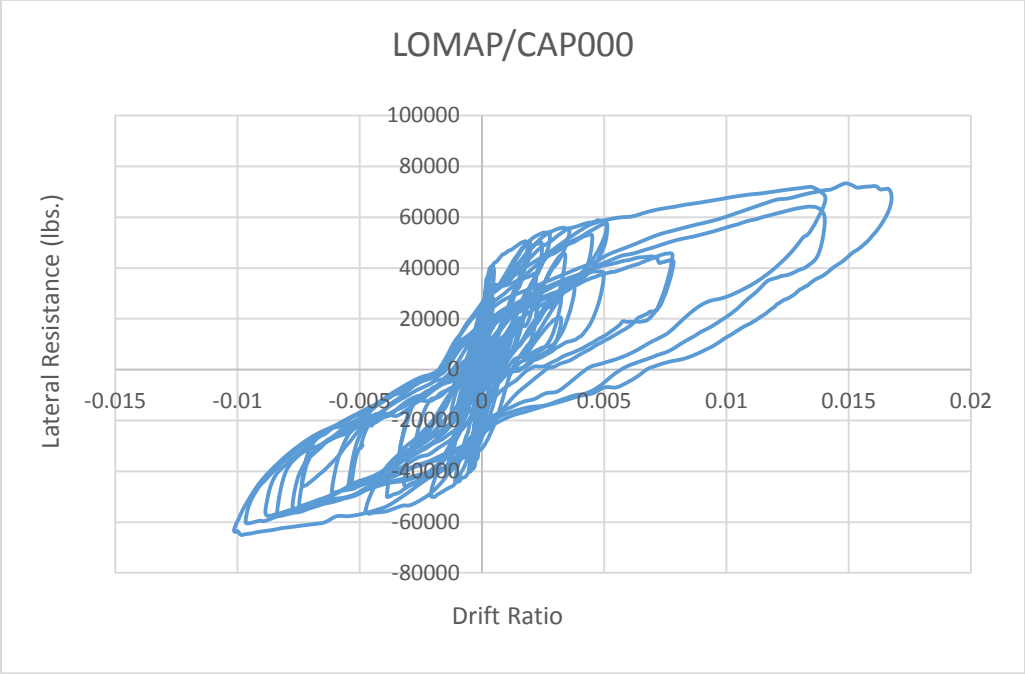

Figure D-27 Time history analysis of archetype 11BMAL using LOMAP/CAP000.

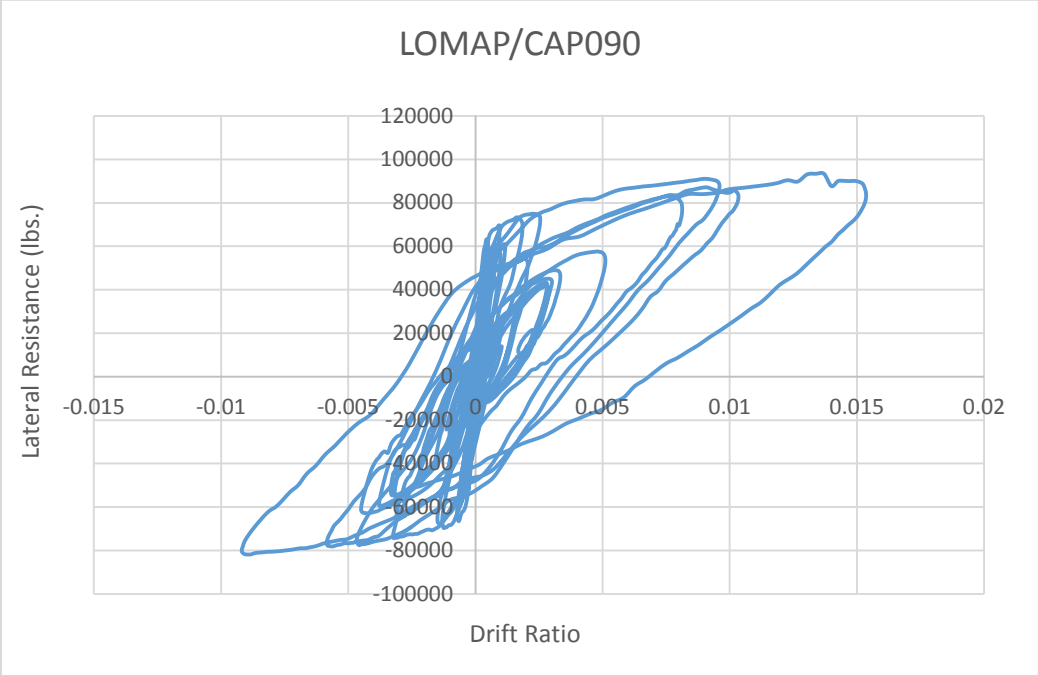

Figure D-28 Time history analysis of archetype 11BMAL using LOMAP/CAP090.

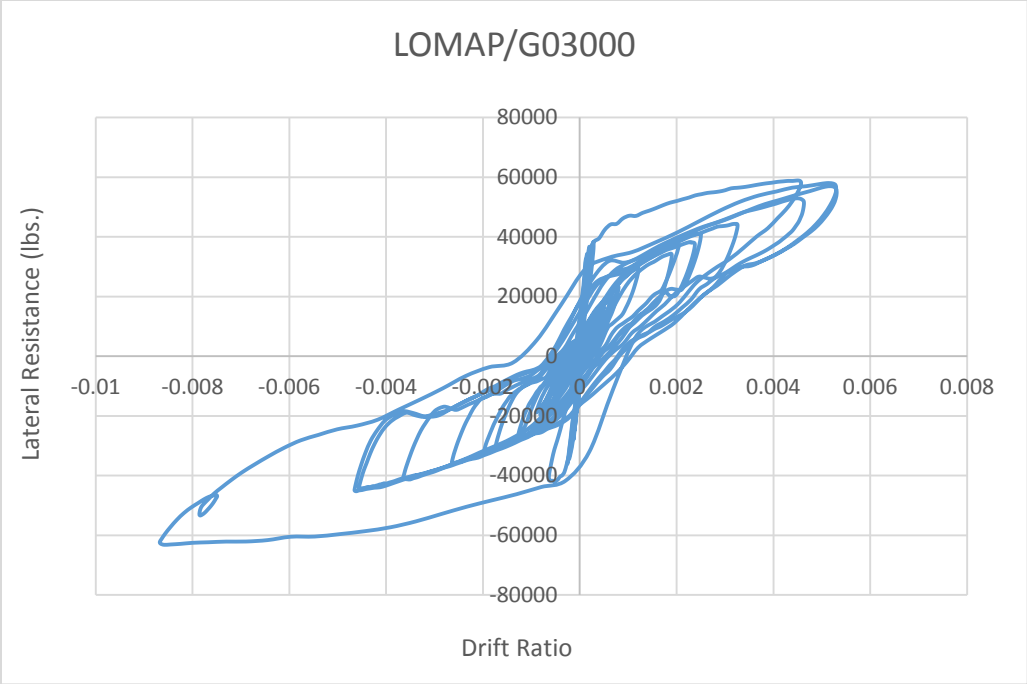

Figure D-29 Time history analysis of archetype 11BMAL using LOMPAP/G03000.

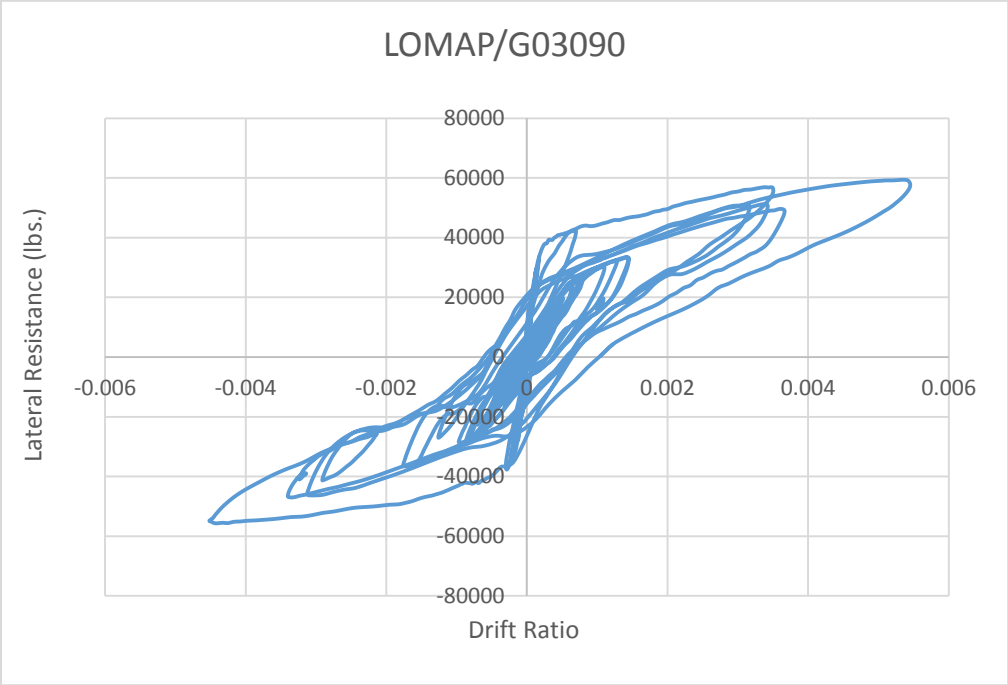

Figure D-30 Time history analysis of archetype 11BMAL using LOMAP/G03090.

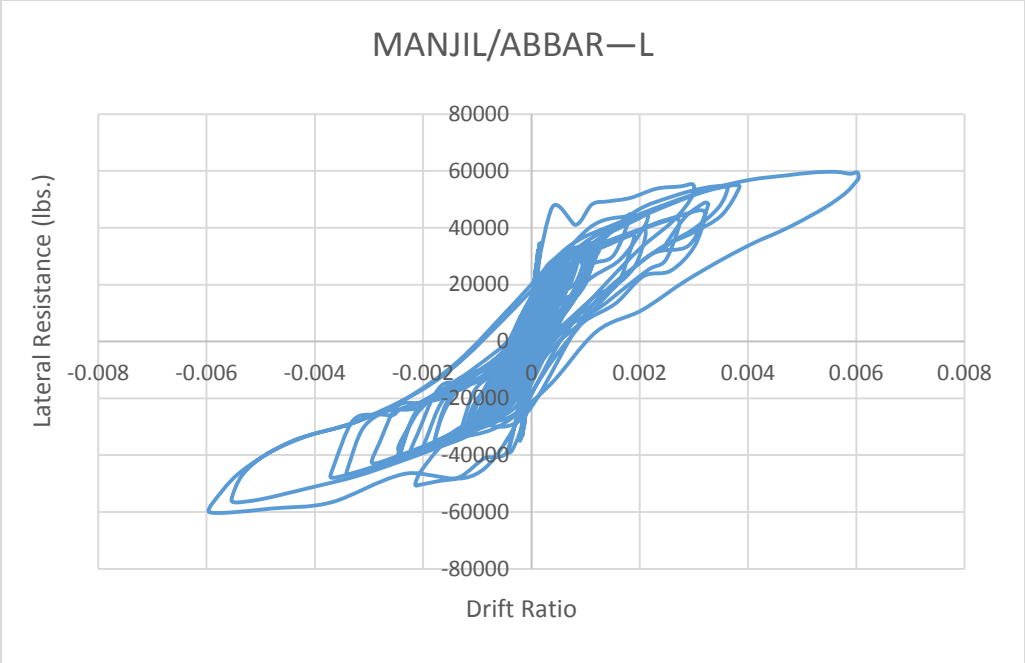

Figure D-31 Time history analysis of archetype 11BMAL using MANJIL/ABBAR--L.

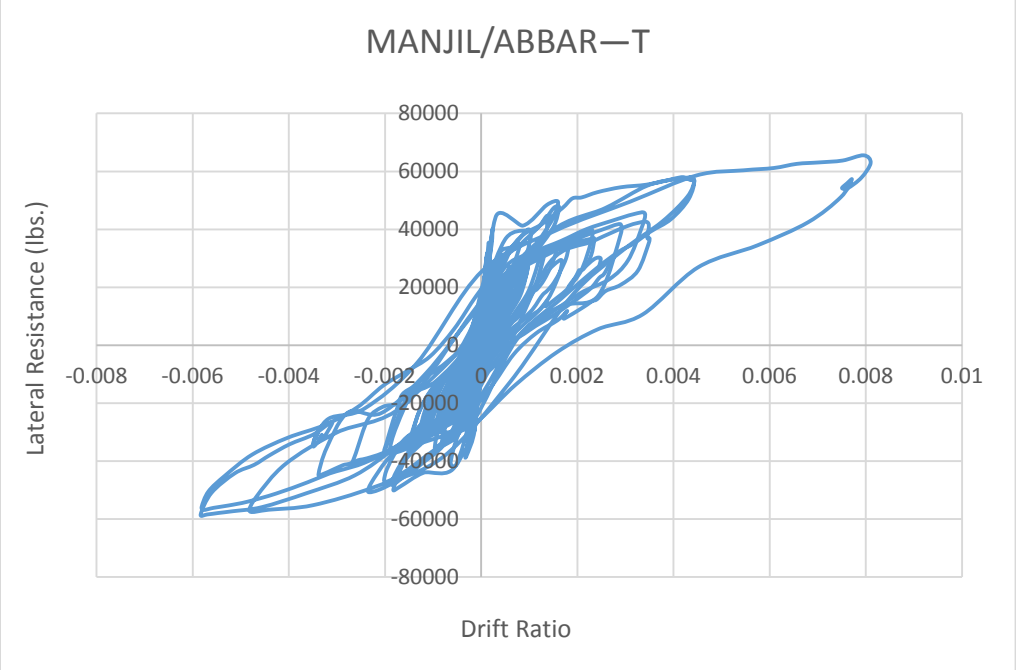

Figure D-32 Time history analysis of archetype 11BMAL using MANJIL/ABBAR--T.

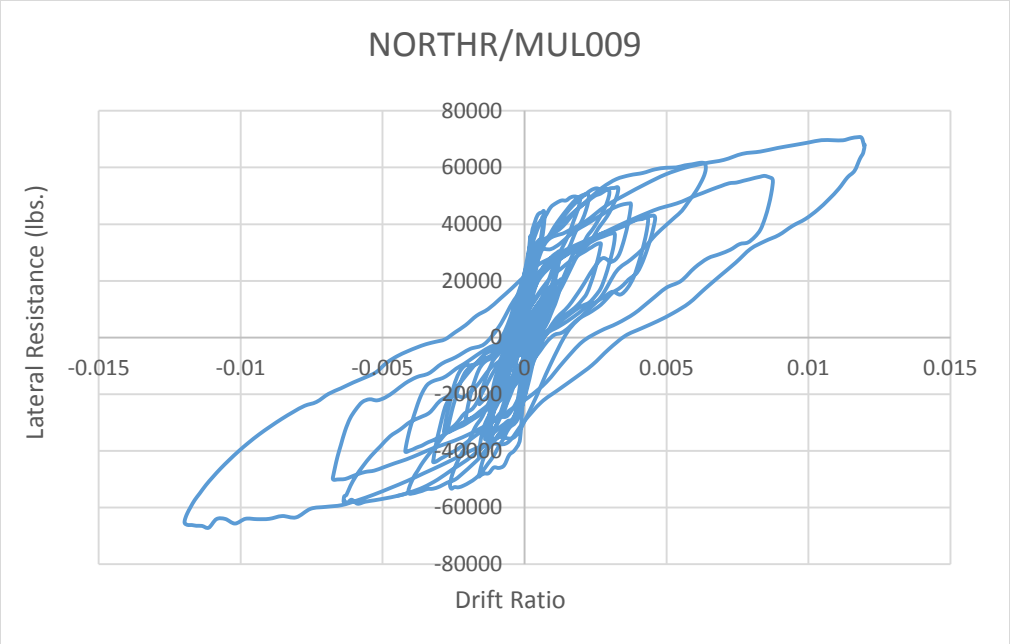

Figure D-33 Time history analysis of archetype 11BMAL using NORTHR/MUL009.

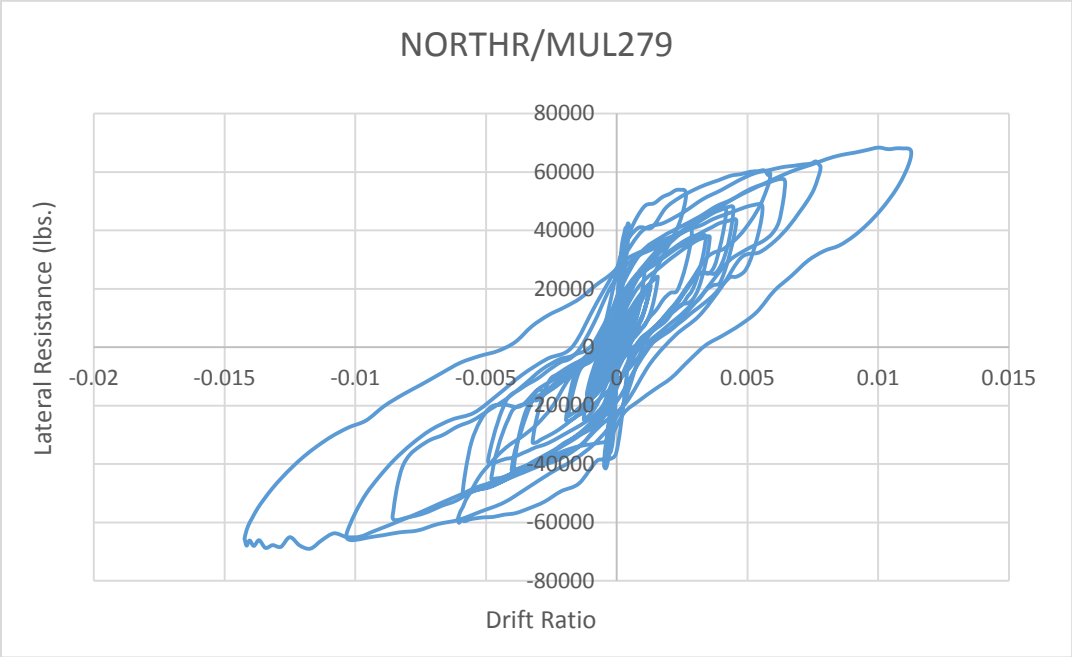

Figure D-34 Time history analysis of archetype 11BMAL using NORTHR/MUL279.

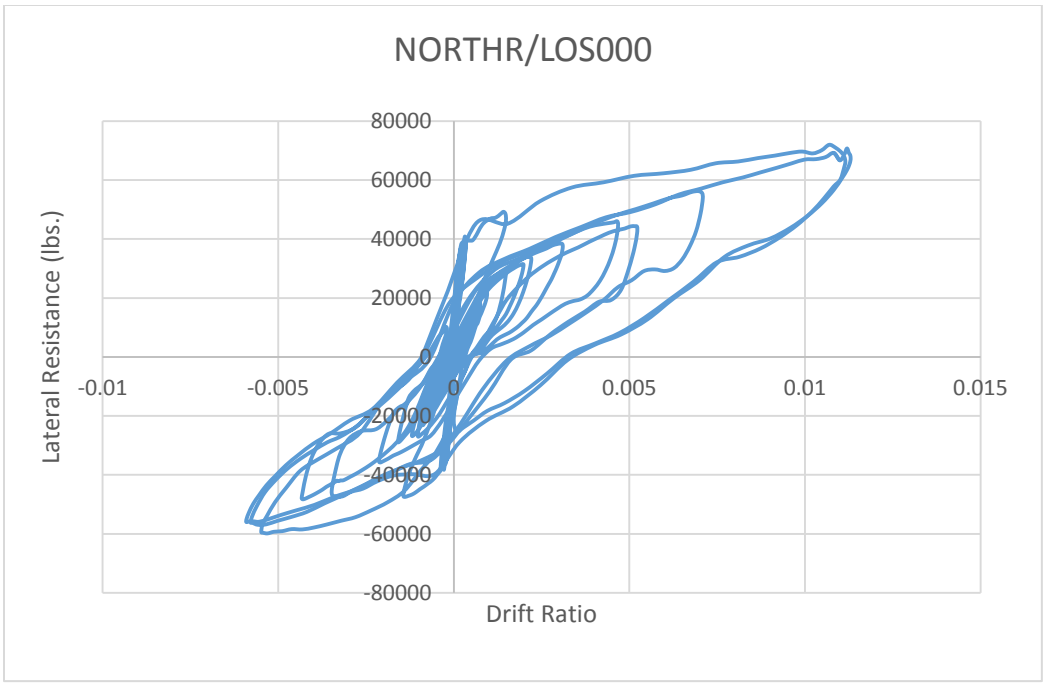

Figure D-35 Time history analysis of archetype 11BMAL using NORTHR/LOS000.

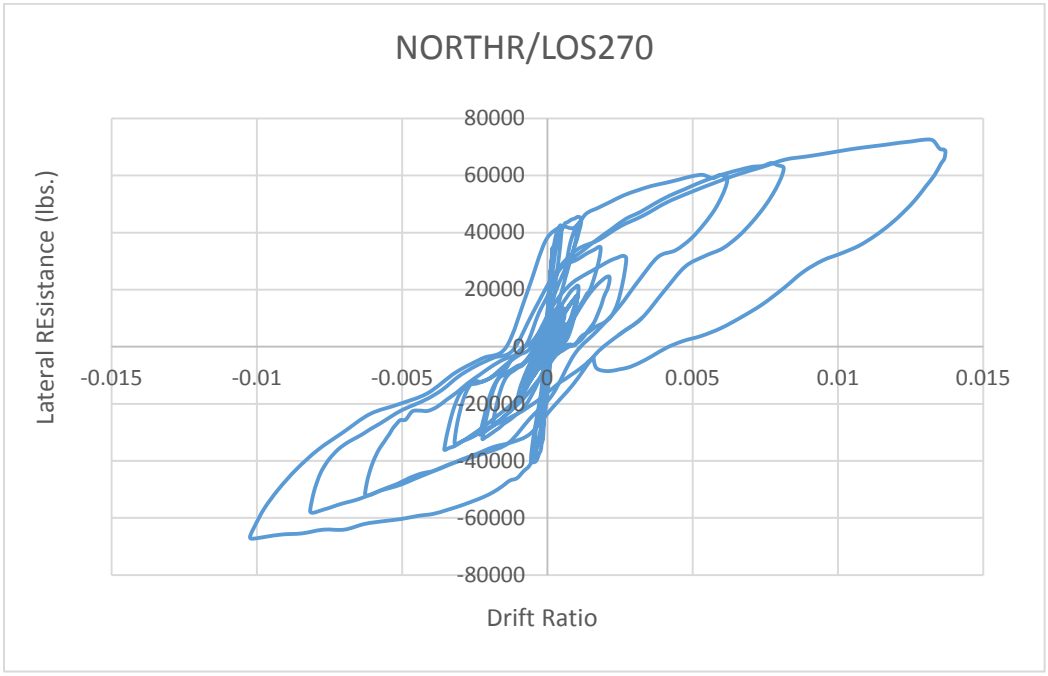

Figure D-36 Time history analysis of archetype 11BMAL using NORTHR/LOS270.

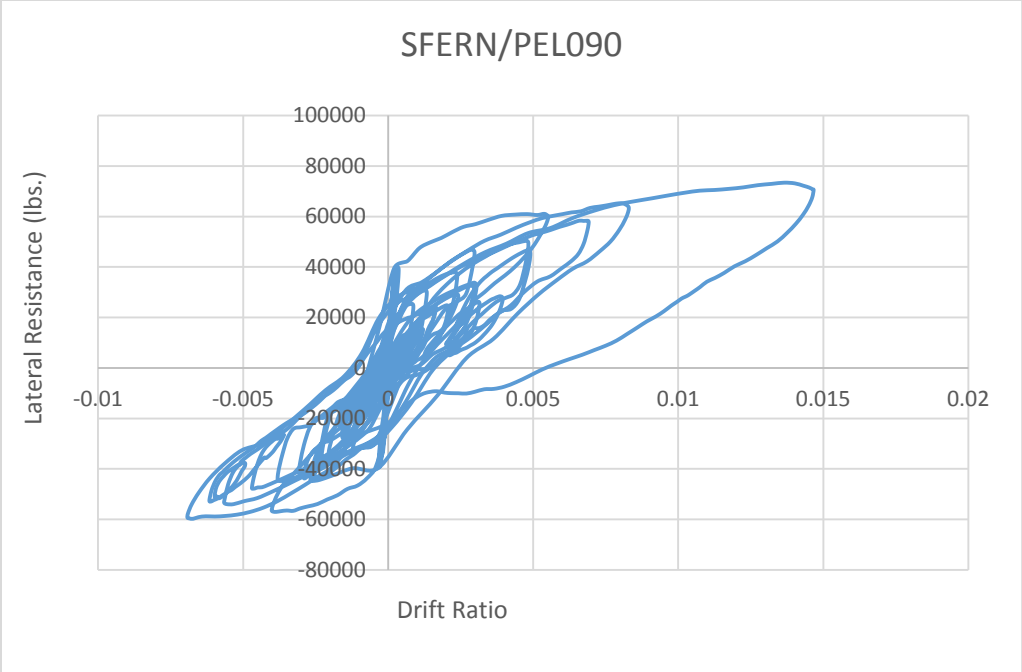

Figure D-37 Time history analysis of archetype 11BMAL SFERN/PEL090.

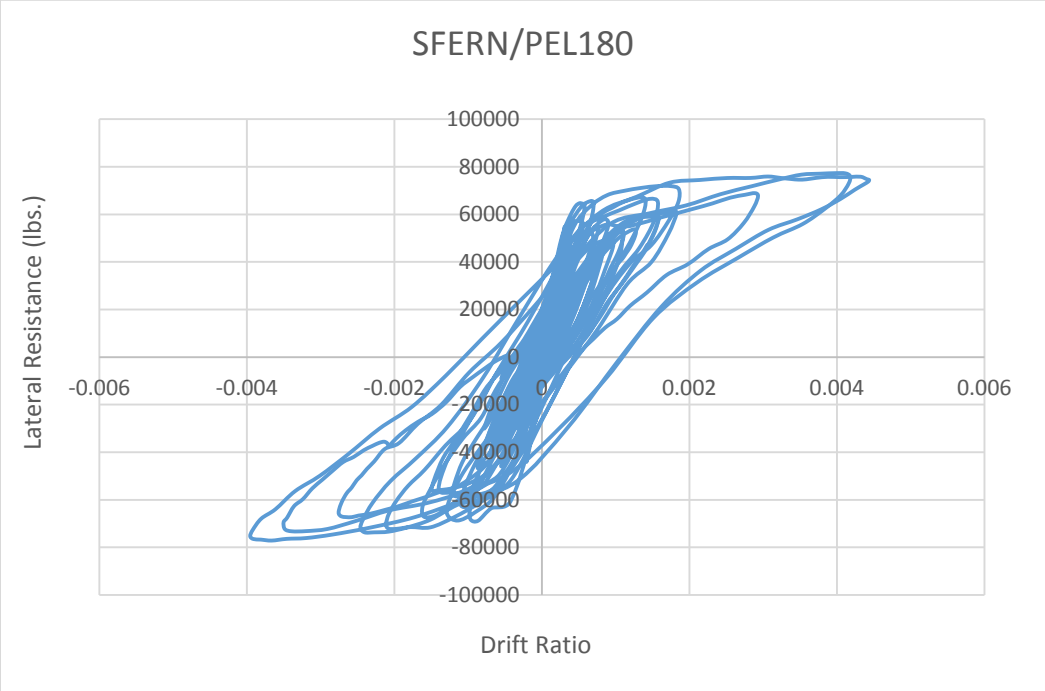

Figure D-38 Time history analysis of archetype 11BMAL SFERN/PEL180.

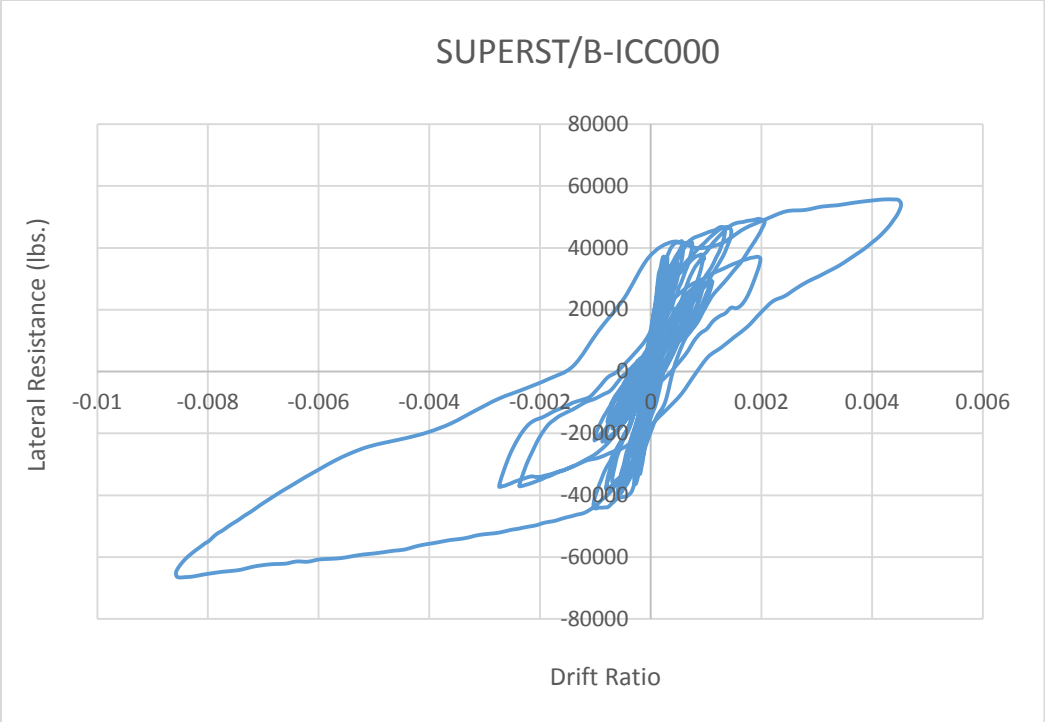

Figure D-39 Time history analysis of archetype 11BMAL using SUPERST/B-ICC000.

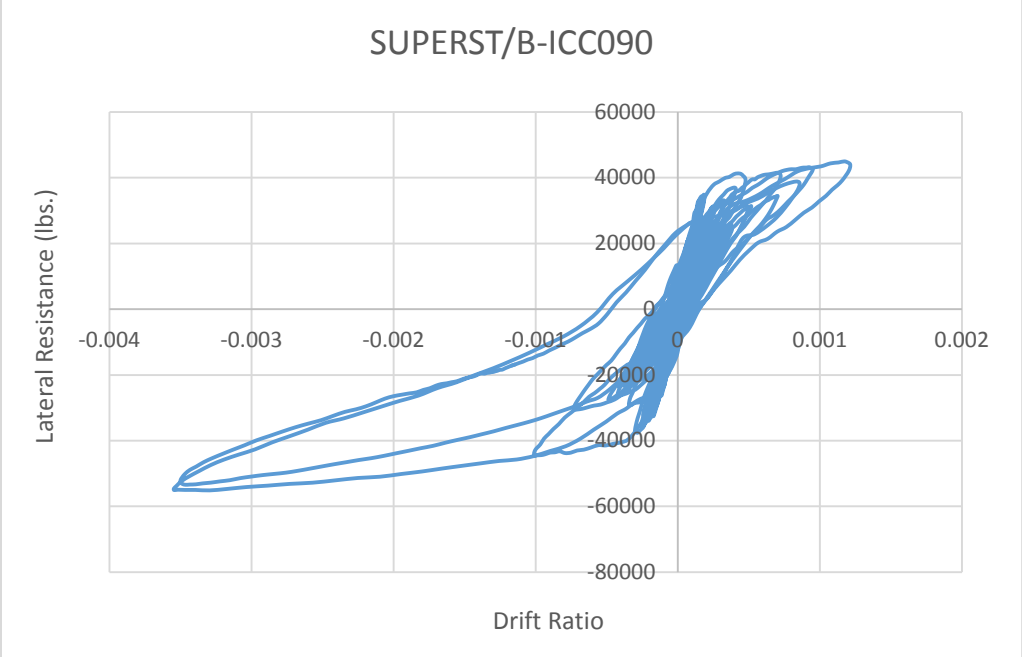

Figure D-40 Time history analysis of archetype 11BMAL using SUPERST/B-ICC090.

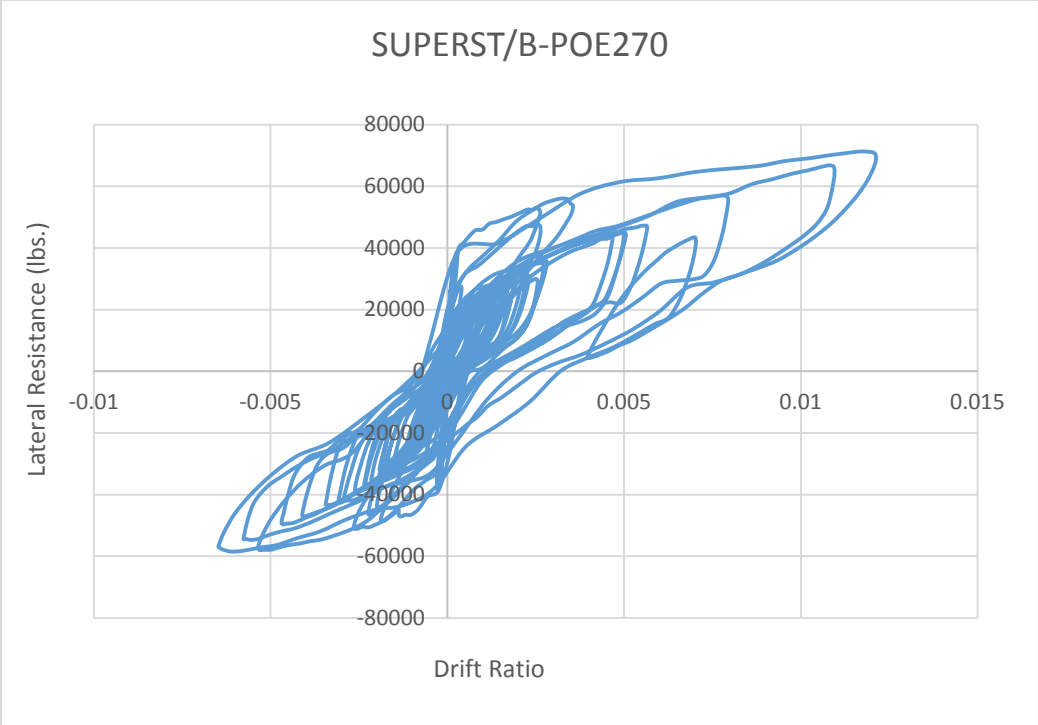

Figure D-41 Time history analysis of archetype 11BMAL using SUPERST/B-POE270.

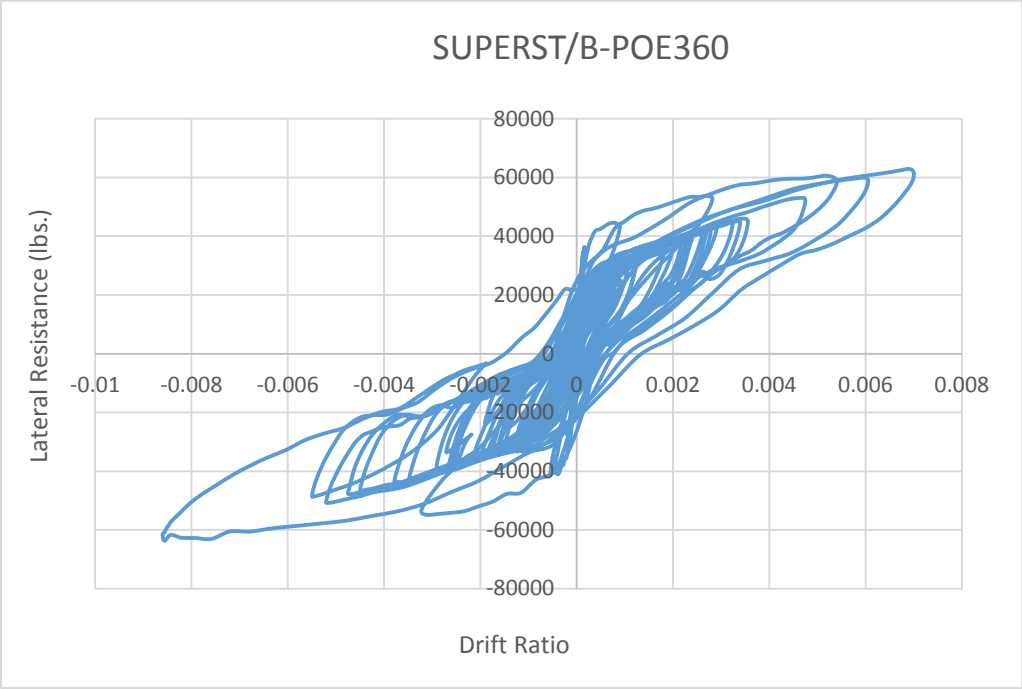

Figure D-42 Time history analysis of archetype 11BMAL using SUPERS/B-POE360.